RATIONAL DESIGN STRATEGIES FOR REDOX FLOW BATTERIES

by

Bertrand J. Neyhouse

Bachelor of Science in Chemical Engineering, Ohio University, 2018

Submitted to the Department of Chemical Engineering
in partial fulfillment of the requirements for the degree of

Doctor of Philosophy in Chemical Engineering

at the

MASSACHUSETTS INSTITUTE OF TECHNOLOGY

June 2023

Author ....
Bertrand J. Neyhouse
Department of Chemical Engineering
May 9th, 2023

Certified by ....
Fikile R. Brushett
Associate Professor of Chemical Engineering
Thesis Supervisor

Accepted by ....
Patrick S. Doyle
Robert T. Haslam Professor of Chemical Engineering
Singapore Research Professor
Chair, Committee for Graduate Students

Rational Design Strategies for Redox Flow Batteries

by

Bertrand J. Neyhouse

Submitted to the Department of Chemical Engineering on 9 May 2023, in partial fulfillment of
the requirements for the degree of
Doctor of Philosophy in Chemical Engineering

Abstract:

Global decarbonization of the energy sector necessitates development of storage technologies to mediate the inherent intermittency of renewable resources. Electrochemical systems are well-positioned to support this transition with redox flow batteries (RFBs) emerging as a promising grid-scale platform, as their unique architecture offers decoupled energy / power scaling, simplified manufacturing, and long service life. Despite these favorable characteristics, current embodiments remain prohibitively expensive for broad adoption, motivating the development of new electrolyte formulations (e.g., redox molecules, supporting salts, solvents) and reactor materials (e.g., electrodes, flow fields, membranes) to meet performance and cost targets for emerging applications. While many next-generation materials offer performance improvements, they must carefully balance complex tradeoffs between power / energy density, cycling stability, energy efficiency, and capital costs. This multifaceted parameter space frustrates the articulation of unambiguous design criteria, as the relationships between constituent material properties and cell performance metrics are not yet well-understood.

In this thesis, I address these knowledge gaps by advancing theoretical and experimental methods that support the rational design of RFBs. First, I develop an in-line electrochemical sensor to measure electrolyte concentrations during RFB operation, providing insight into the dynamics of flow cell cycling. Second, I introduce an analytical zero-dimensional modeling framework for describing RFB cycling behavior, enabling facile simulation of charge / discharge behavior and device performance metrics. I then further simplify this approach by deriving closed-form expressions, facilitating the use of spreadsheet models for cycling simulations. Third, I apply these models to assess design tradeoffs for two-electron materials, demonstrating marked performance limitations. Finally, I leverage the analytical zero-dimensional framework to develop a new technique—compositionally unbalanced symmetric cell cycling—for characterizing crossover rates in redox flow cells. Broadly, the methods developed in this work have the potential to advance foundational understanding in RFB design and operation, leading to more rigorous selection criteria for candidate materials and ultimately supporting more robust, cost-competitive, and durable grid-scale energy storage.

Thesis Supervisor: Fikile R. Brushett
Title: Associate Professor of Chemical Engineering

Acknowledgements:

I am immensely grateful to so many people who have contributed to my journey as a scientist and to the work involved in this thesis. First, I want to acknowledge my advisor, Fik, for providing me the academic freedom to explore these challenging research topics over the past four years while offering critical insight, feedback, and direction. Beyond his contributions to my research, Fik has helped me develop as a stronger leader, research mentor, and science communicator. I am looking forward to continuing our personal and professional relationship in the years to come. I also want to thank my thesis committee members, Zach and Karthish, for encouraging me to think about the broader context and insights of my research and especially for providing valuable career guidance throughout the past several years.

Within this thesis, I want to specifically acknowledge the research contributions of Kevin Tenny, Aman Kaur, the late Susan Odom, Jonathan Lee, Alexis Fenton Jr., Robert Darling, and James Saraidaridis. I am grateful to members of the Brushett Group, past and present, for their technical guidance and for encouraging such a supportive, collaborative, and inspiring research environment—Jeffrey Kowalski, Michael Orella, McLain Leonard, Katharine Greco, Alexis Fenton Jr., Kara Rodby, Kevin Tenny, Charles Wan, Lauren Clarke, Weiran Gao, Aditya Limaye, Alex Quinn, Chris Mallia, Nick Matteucci, Katelyn Ripley, Trent Weiss, John Vergados, Isabella Caruso, Cindy Wong, Anish Sukumar, Jesse Hinricher, Anne Neiderdraenk, Yasser Ashraf-Gandomi, Madhu Majji, Amira Alazmi, Lingping Kong, and Javit Drake. I also want to thank the undergraduate researchers who I have had the opportunity to mentor—Will Exson, Destinee Hung, Jonathan Lee, Dien Nguyen, and Nick Price. I have learned so much working alongside you all and have grown significantly as a research advisor.

I am grateful to have learned from and worked alongside those I had the opportunity to collaborate with throughout my time at MIT, including Matteo Gigli, Rahul Jha, Anton Perera, Giorgio Baggi, Daniel Dailey, Malsha Suduwella, Zhiming Liang, Harrison Cassady, Michael Hickner, Michael Gerhardt, Jiangjin Liu, Adam Weber, Zhiwei Yang, Mariam Pogosova, Nikita Akhmetov, Nikolai Ovsyannikov, Natalia Gvozdik, Vasily Artemov, Mikhail Pugach, Keith Stevenson, Kyle Lennon, the late James Swan, Lily Robertson, Ilya Shkrob, Xiaoting Fang, Lu Zhang, Gengyu Tian, Michael Thielke, Carlos Mingoes, and Ana Sobrido.

Beyond research, I had numerous opportunities to contribute to organizations at MIT, including the ChemE Communication Lab, the ChemE Graduate Student Advisory Board (GSAB), and the MIT Science Policy Review, and I am grateful to everyone I had the fortune of working alongside. I want to specifically acknowledge Caitlin Stier for providing me the opportunity to join the Comm Lab as a first-year graduate student and for teaching me so much about science communication, education, and mentoring.

I am so fortunate to have the love of my family and words alone cannot capture their importance nor their impact. My partner, Hannah, is a pillar of strength, compassion, and unconditional love, supporting me through the challenges of this Ph.D. and making every day full of joy. My parents, who always pushed me to pursue my passions, supported my dreams, and fostered my interest in math and science, have shaped me into who I am, and I will be forever grateful for their love and encouragement. My brothers, Arend and Jimmy, have been and continue to be amazing role models in my life, and I deeply cherish their friendship and guidance.

Table of Contents:

List of Figures:

List of Tables:

I. Introduction

The need for advancing renewable energy technologies such as wind and solar energy has driven scientists and policymakers alike to expand efforts to deliver reliable, clean energy across the globe.[1–3] While we can harness immense amounts of energy from the sun and our environment, renewable energy production and energy demand are significantly misaligned.[4,5] Thus, in order to make use of this energy and deliver it to the public, we must develop reliable energy storage systems that can store energy during peak production and deliver energy during peak demand. Electrochemical energy storage (EES) has long been sought after as a clean, efficient platform for storing energy, owing to the faster charge/discharge rates and direct conversion between chemical and electrical energy.[6,7] Perhaps the prototypical EES systems, both lithium-ion batteries and fuel cells have undergone decades of research and innovation, placing them at the forefront of commercial energy storage.[8–11] Although they have been thoroughly developed, they are not without their limitations and drawbacks. For example, fuel cells suffer from large capital costs associated with storing and delivering gases (H_2 and O_2).[12] On the other hand, lithium-ion batteries are limited by the coupling of energy and power – in order to pack more energy into a battery, the size of the electrodes must be made larger, concomitantly increasing power.

In order to combat limitations faced by these EES systems, redox flow batteries (RFBs) have emerged in recent years as a promising alternative for energy storage at the grid-scale.[13] Unlike traditional solid-state batteries (e.g. lithium-ion) that store charge in their electrodes, RFBs store charge in electrolytes that are held in external tanks and pumped through an electrochemical cell during charge and discharge. Through this architecture, RFBs decouple energy and power (**Figure I-1**)—energy can be manipulated by changing the size of the tanks and concentration of active species and power can be manipulated by changing the size and performance characteristics of the electrochemical cell.[13–15] Additionally, these characteristics give rise to modular construction, simplified maintenance, and long service lives, all of which may contribute to a more robust energy storage platform. The vanadium RFB remains the state-of-the-art, owing to its singular active material that can access multiple oxidations states—V^{2+}, V^{3+}, VO^{2+}, VO_2^+—within the electrochemical stability window of water, yielding high long-term stability and suitable energy / power characteristics for grid storage applications. However, the high and volatile capital cost of the vanadium pentoxide precursor as well as other system components stifles the practical utility and economic prospects of vanadium-based RFBs, prompting research efforts to focus on potentially more sustainable platform chemistries.

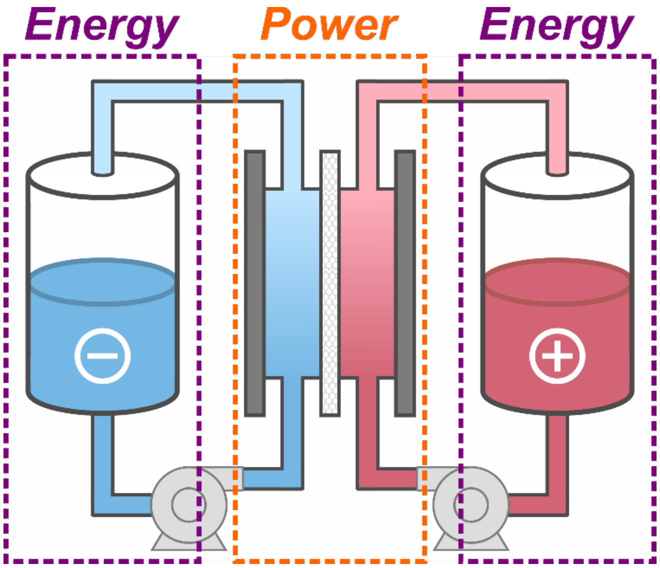

Figure I-1. *Graphical depiction of redox flow batteries, highlighting the decouple energy / power scaling.*

Notably, the past decade has seen exciting advances, including the emergence of engineered molecules (e.g., redox-active organics, metal-centered coordination complexes) whose physical and electrochemical properties can be tuned through molecular functionalization.[16–18] While such materials offer a new means of tuning RFB performance metrics, they also present new complexities for device operation, which include managing an array of parasitic processes (e.g., active species crossover, molecular decay, component degradation, side reactions) that result in heightened capacity fade and reduced cycling efficiencies.[19] The degradation of individual components dictates system maintenance schedules and operating expenses, as routine repairs and replacements are feasible but adversely impact profitability over the service life of the battery.[20,21] However, performance losses in such complex systems are often rooted in a multitude of confounding factors, which are difficult to decouple experimentally and/or to replicate in isolation.[16,22–24] Thus, understanding failure modes requires diagnostic tools that can monitor RFB components under conditions that resemble practical embodiments and modeling frameworks that can interpret these performance losses and connect them to fundamental material characteristics.[25]

In this introductory chapter, we discuss present experimental methods for characterizing materials for RFB applications and review theoretical approaches for connecting those material properties to performance characteristics, focusing primarily on considerations around redox electrolytes and membranes / separators. First, we introduce techniques for characterizing active species, discussing standard electrochemical methods for evaluating candidate materials and limitations to their applicability. Next, we present common methodologies for assessing membranes / separators both through ex situ and emerging in situ diagnostics. Finally, we provide an overview of modeling approaches that aim to improve fundamental understanding of RFB performance and operation, comparing the merits of different theoretical frameworks and focusing on those used for long-duration cycling. Throughout this chapter, we highlight limitations in current experimental workflows and theoretical frameworks—which presently obscure deeper understanding of long-duration performance—to motivate the development of new approaches presented in this thesis.

1. *From the synthesis vial to the full cell: Chemical and electrochemical methods for characterizing redox flow battery materials*

The overarching goal of materials research for RFBs is for newly-developed compounds to operate in a full cell for extended time with performance metrics similar to those envisioned for cost-competitive practical embodiments. While flow cell testing remains a critical step in the pipeline from discovery science to electrochemical product, it is non-trivial in practice. Performance losses in such complex systems arise from a multitude of confounding factors (e.g., electrode and membrane degradation, crossover, evaporation, molecular decay), which prevents the establishment of quantitative and unambiguous connections between the properties of individual components and the overall cell behavior. Flow cells also require considerable material quantities to operate at application-relevant concentrations and scales, and performance systems can take hours to assemble and days to weeks to cycle. Alternatively, by first analyzing components in isolation, at smaller scale, and under well-controlled conditions, researchers can identify potential shortcomings before investing significant time and materials. Further, properties extracted from these studies can inform structure-function relationships that are invaluable to materials discovery.[26,27] Using knowledge gained from experiments at near-ideal conditions as a foundation, deliberate, step-wise progress can be made toward full cell operation by identifying, understanding, and mitigating sources of performance loss.

The purpose of this section is to outline a systematic approach for advancing new materials from synthesis to full cell implementation using various physicochemical and electrochemical techniques along the way. While there exist some established practices for individual experimental procedures,[28] to the best of our knowledge, there is no connective and detailed framework for evaluating new materials in the context of RFB systems. To this end, we introduce foundational characterization methods with a focus on key determinable properties and their relative importance to RFB performance.

1.1. Assessing next-generation redox electrolytes

In general, we endeavor to develop electrolytes possessing disparate redox potentials that are either high (posolytes) or low (negolytes); rapid electrochemical kinetics and diffusivity; permanent stability; and high solubility in all relevant oxidation states. In pursuit of these design goals, researchers seek to synthesize compounds that exhibit some, if not all, of these desired properties. However, there are almost always tradeoffs between properties, and target property sets may vary from system to system as dictated by techno-economic analyses and design specifications. Molecular engineering campaigns may also consider other valuable features such as crossover tolerance, multi-electron capacity, synthetic ease, low molecular weight, and non-toxicity, provided the underlying compound already possesses other essential properties. Notably, many of these properties are not solely dependent on the redox couple but also on the supporting electrolyte, the electrodes, and the membrane. Of these components, the supporting electrolyte choice is the most closely tied to development of charge-storage materials. While aqueous systems are limited to water as the solvent, non-aqueous systems can employ a range of solvents (e.g., acetonitrile, dimethylformamide, propylene carbonate), each of which can profoundly influence the redox potential, diffusivity, kinetic rates, material stability, and voltage stability window.

Regardless of the target criteria, the process for developing new redox electrolytes requires careful evaluation of their key properties to enable quantitative comparison between candidates and inform design of next-generation materials. **Figure I-2** offers a roadmap for developing new redox electrolytes, reflecting an iterative design-synthesize-characterize-learn process to guide materials discovery. A guiding principle behind the proposed scheme is the importance of experimental ordering—moving from left to right in **Figure I-2**, chemical and electrochemical characterizations become increasingly time and materials intensive as they approach more realistic

RFB conditions. These conditions also impose restrictions on results as experimental complexities introduce new sources of error and inconsistency. Note that, although this process is outlined for materials synthesized in-house, if materials are purchased from vendors or simply explored in new electrolyte formulations, the electrochemical methods described here are still applicable.

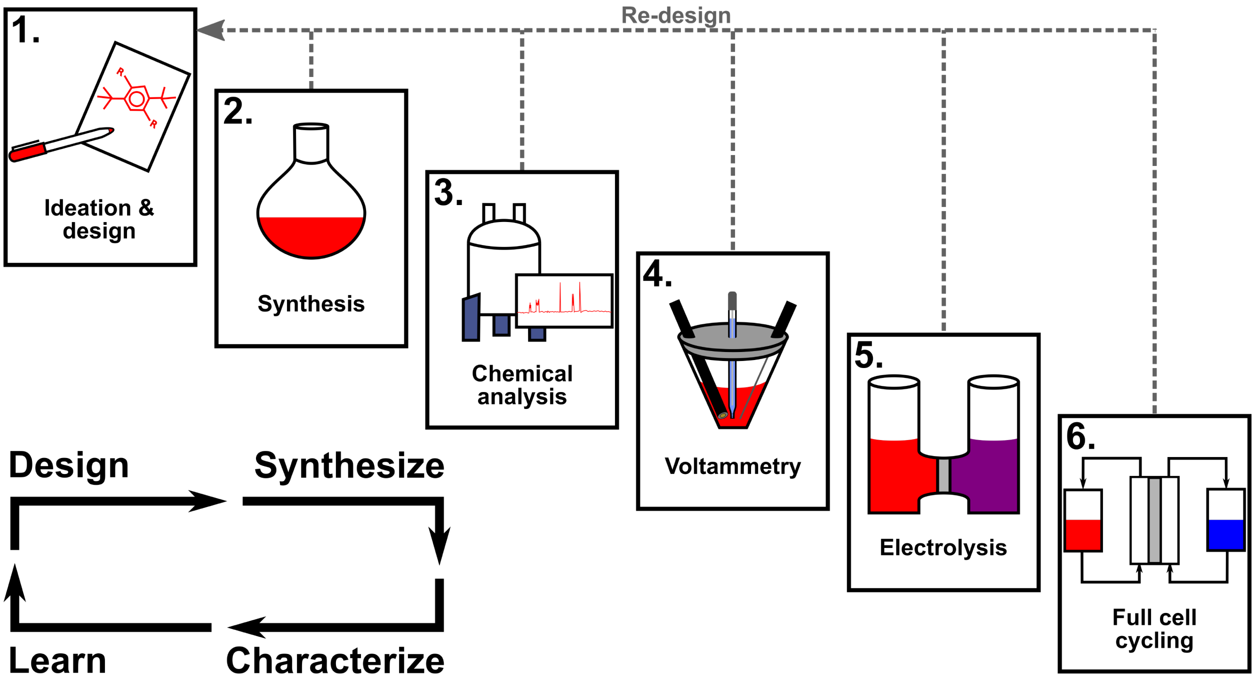

Figure I-2. *Roadmap for transitioning charge-storage materials from synthesis to full cell testing, emphasizing experimental ordering in an iterative design-synthesize-characterize-learn framework.*

First and foremost, synthesizing new active materials requires a baseline series of chemical characterizations to validate structural and chemical properties as well as product purity. Though beyond the scope of this chapter, spectroscopic techniques (e.g., mass spectrometry, infrared spectroscopy (FT-IR), nuclear magnetic resonance spectroscopy (NMR)) evince that the target compound has been generated and can also provide insight into various underlying molecular properties that influence electrochemical behavior. Further, many useful physicochemical measurements can elucidate simple (solubility, viscosity, density, conductivity) and advanced (solvation, aggregation) solution properties which impact electrochemical responses. In particular, the active species solubility is directly proportional to charge storage capacity and can be measured both in pure solvent and in appropriate electrolyte, the latter providing a more application-relevant metric. If the molecule can be prepared in multiple oxidation states, its solubility should be measured in all states accessible during cell operation. With chemical descriptors as a foundation, subsequent electrochemical experiments, the focus of this chapter, assess the key properties (i.e., redox potential, kinetics, diffusivity, stability) that influence full cell performance. Chemical and electrochemical techniques are not, however, mutually exclusive, as coupled spectroscopic data (e.g., NMR, FT-IR, ultraviolet-visible spectroscopy (UV-Vis), electron paramagnetic resonance spectroscopy (EPR)) can provide additional insight into the electrochemical behavior and stability through both in situ and ex situ measurements.[29]

Electrochemical methods span a wide array of cell configurations, electrode arrangements, and current-voltage inputs, each with advantages and disadvantages for characterizing solution-phase redox-active materials. Arguably the simplest and most routine approaches, especially for RFB materials, are those employing voltammetry in three-electrode cells, with cyclic voltammetry (CV) being a near-universal standard. These techniques are robust and powerful, allowing quantitative evaluation of redox potential, electrochemical kinetics, and diffusion rates as well as qualitative insight into stability and decay mechanisms.[30] However, voltammetry is not well-suited for quantification of the long-term stability of a molecule in its charged state or for evaluation of its cyclability. This requires the use of electrolysis to (1) convert the molecule to its charged state and monitor its decay and (2) cycle the molecule between charged and discharged states to monitor capacity fade.[31] Finally, and only with an understanding of key material properties, tests can be conducted in a flow cell, providing a more thorough interpretation of cycling behavior beyond proof-of-concept studies. In subsequent sections, we explore the use of several foundational electrochemical techniques with particular attention to interpreting data in the context of RFB performance.

1.1.1. Voltammetry in three-electrode cells

A nearly ubiquitous analytical technique in electrochemistry and electrochemical engineering, voltammetry is built on decades of experimental and theoretical research, and is an essential tool for characterizing redox electrolytes used in RFBs. At its core, voltammetry applies a controlled voltage waveform to a working electrode and measures the resulting current from electrochemical reactions in solution. The working electrode is typically a planar disk (e.g., glassy carbon, gold, platinum) while a high surface area wire, coil, or mesh serves as a counter-electrode to complete the circuit and facilitate the flow of current. These electrodes are polished and cleaned before and between experiments to provide a pristine, smooth surface for electrochemical reactions and limit the effects of fouling and impurities. In a three-electrode cell, the working electrode is polarized relative to a reference electrode, which maintains a stable redox potential by leveraging a well-defined electrochemical reaction housed in an isolated environment that is separated from the electrolyte by a glass frit or selective separator.

Although relatively simple in practice, CV possesses a wealth of information about electrochemical reactions that can be used to characterize thermodynamic, kinetic, and transport properties of a redox electrolyte (**Figure I-3**), which, in turn, can provide insight into its performance and viability for a full cell. In CV, the working electrode potential varies linearly with time according to the scan rate, and as electrochemical reactions proceed, a diffusion boundary layer forms near the surface as the reactant is consumed. This boundary layer grows with time, and its structure is dependent on the diffusivity and kinetics of the redox reaction while its thickness is dictated by the scan rate. As such, the resulting current is a product of the interplay between kinetics and mass transfer, and their relative contributions are prescribed by the scan rate. **Figure I-3a** provides an exemplar CV experiment for an electrochemically quasireversible (vide infra), single electron transfer redox couple, outlining the key features which enable quantitative evaluation of electrochemical properties. In most cases, CV is performed using multiple scans to evaluate cycle-to-cycle stability and a range of scan rates to quantify the kinetic rate constant and diffusion coefficient. In the proceeding sections, we describe the information that can be extracted from such measurements in the context of redox electrolytes for flow batteries. For a comprehensive discussion of this subject matter, the interested reader is encouraged to study the work by Elgrishi et al. as well as relevant textbooks on voltammetry and electrochemistry fundamentals.[32–35] In addition, Wang et al. provide an excellent perspective on protocols for determining kinetic parameters for RFB materials, which may serve as a more targeted reference for such measurements.[36]

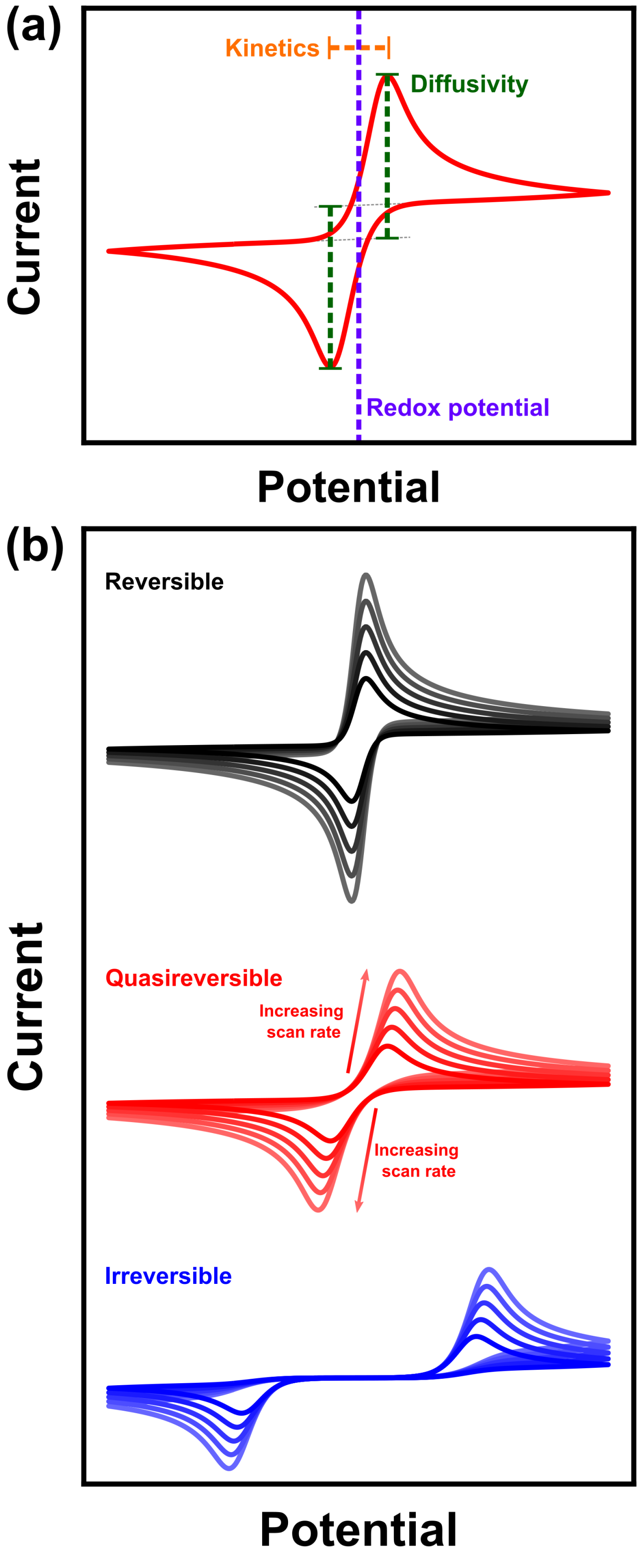

Figure I-3. *Exemplar CVs for a one-electron transfer reaction, highlighting (a) available quantitative information (shown for a quasireversible redox couple) and (b) varying kinetic regimes and the effect of scan rate. CVs were simulated using Bio-Logic EC-Lab software.*

In CV, the formal redox potential is usually approximated by measuring the average potential between the oxidative and reductive peak potentials, $E_{1/2}$ (V vs reference), but can be made more accurate by accounting for variant species diffusion coefficients.[34] It should be noted that, in many cases, the equilibrium and formal redox potentials can vary with supporting electrolyte composition. For example, in the case of certain aqueous organic materials, electrochemical reactions are proton-coupled and consequently dependent on pH, introducing a proton concentration term into the Nernst equation.[37,38] Hence, the pH dependence of the equilibrium potential can provide useful insight into the nature of the electron transfer mechanism in accordance with the Nernst equation. Conversely, in most non-aqueous systems, the active species does not react directly with the supporting salt and therefore the equilibrium potential is less sensitive to these conditions and is dominated by the active species and solvent.

The 'reversibility' of a molecule is often referenced in the literature, but its definition conflates distinct chemical and electrochemical behavior that should be carefully distinguished. The 'chemical reversibility' is a measure of stability, describing the propensity for a species to remain stable following electron transfer and subsequently return to its initial state. Thus, if there are undesired chemical or electrochemical reactions that follow the desired electrode reaction(s), this will adversely impact the chemical reversibility. In contrast, the 'electrochemical reversibility' is a measure of the ratio between the rates of charge transfer and mass transfer, which are respectively described by the kinetics of the electrochemical reaction at the electrode surface and the diffusive fluxes of reactants to the electrode surface (**Figure I-3b**). Charge transfer rates are directly proportional to the reaction kinetics and are often represented by a heterogeneous rate constant (k_o) that is chiefly dependent on the redox couple and the electrode surface. Mass transfer rates are proportional to the molecular diffusivity of the reactant species in the bulk electrolyte and the boundary layer thickness adjacent to the electrode surface, the latter of which can be controlled by the scan rate. The electrochemical reversibility is directly related to the peak-to-peak separation—the potential difference between the oxidative and reductive peak currents—and can be determined by performing CV at varying scan rates.

In general, CV cannot quantify kinetic rate constants for electrochemically reversible reactions—often, changes in the peak-to-peak separation cannot be completely dissociated from ohmic losses. For faster quasireversible reactions, kinetic constants can still be extracted, but variations in these values are anticipated to have a minor impact on RFB performance, as facile kinetics correspond to low charge transfer resistances which minimally contribute to voltage losses. For both slower quasireversible and irreversible reactions, kinetic analyses in three-electrode assemblies provide insight into charge transfer characteristics at ordered, planar surfaces, but quantitative translation to RFB performance may not be possible, as flow cells utilize carbon-fiber based electrodes with more disordered and spatially-variable surface chemistry and morphology[39] Despite these limitations in evaluating heterogeneous rate constants, such information remains insightful when considering sources of loss at the cell-level; however, we note that redox couples with slow kinetics on planar surfaces should not be automatically disqualified as candidate materials. Indeed, canonical RFB chemistries such as vanadium and iron-chromium exhibit quasireversible or irreversible kinetics on most model surfaces but remain leading technology embodiments. There are numerous methods for tailoring the surface area and chemistry of porous electrodes to promote electrochemical reaction rates, and similar approaches can address charge transfer limitations in new materials.

The peak current in a CV reflects the mass transfer limiting current, and as such, is directly related to the diffusion coefficient of the reactant and boundary layer thickness. However, in addition to diffusive fluxes, RFBs leverage bulk electrolyte convection to increase mass transfer rates. Convection enhances active species transport to the electrode surface and generates a steady state boundary layer, allowing the mass transfer rate to be described by a single mass transfer coefficient. Although flow regimes vary based on flow field design and electrode microstructure, the mass transfer coefficient can be related to the diffusion coefficient through empirical Sherwood number correlations and scales approximately with the square root of the diffusivity.[40] Still, the diffusion coefficient is one of several factors that contribute to the mass transfer rate, including electrode properties, flow velocity, as well as cell and electrode geometry. Given the many available engineering controls that govern mass transfer rates in RFBs and the weak dependence on diffusivity, changes in molecular diffusion coefficients must be on an order of magnitude to significantly impact mass transfer rates. Nevertheless, experimental diffusivity measurements are relatively simple to conduct and provide meaningful comparison between candidate compounds, making quantification worthwhile.

While CV is not conducive to evaluating the long-term stability of soluble redox-active species, the method can detect rapid decay processes and coupled chemical and electrochemical reactions occurring near the electrode surface, providing a qualitative assessment of chemical reversibility on shorter time scales. A common approach for determining the short-term stability of redox couples is to monitor the consistency of voltammogram shape over multiple consecutive cycles, as the appearance of additional peaks on subsequent scans evinces materials instability and evolution. However, if a material is stable on the timescale of a CV cycle (ca. 10s of seconds), extending from 10s to 100s of cycles does not provide much additional information because the measurement does not change bulk concentrations or access charged states for long periods of time, as might be expected in RFB operation. Changes in peak current can also be used to determine if the material experiences decay—for a chemically and electrochemically reversible redox couple, the ratio between peak currents should be approximately one; significant deviations from this value suggest that the amount of one species has decreased during the CV experiment and may imply instability. But considering the exact values of the peak current are dependent on diffusivity and scan rate as well as both the chemical and electrochemical reversibility, this metric is at best a qualitative descriptor.

Rotating disk electrode (RDE) voltammetry provides complimentary information to CV to quantify diffusivity and kinetics. Applying rotation to a planar electrode induces convective mass transport perpendicular to the electrode surface—the result is a steady mass transfer boundary layer that is well-described by the canonical theory of Levich.[33] Compared to CV, the direct control of mass transfer rates also enables a more complete method for quantifying the kinetic rate constant and transfer coefficients. In addition, RDE enables higher mass transfer rates than traditional CV, which in turn allows the evaluation of reactions with faster kinetics.

Microelectrodes provide another option for complementary electrochemical characterization of diffusivity and kinetics, leveraging a small electrode radius (~μm) to produce a steady state measurement. Unlike their macroelectrode counterparts, planar microelectrodes feature a diffusion boundary layer that exceeds the electrode radius. Hence, the boundary layer scales rapidly and diffusion is driven in both the axial and radial directions, resulting in a steady state current similar to that observed for RDE at low scan rates.[35] Further, because of the small electrode area, the current is much lower (~nA – μA), significantly diminishing the effects of ohmic losses.

1.1.2. Evaluating chemical stability

There are numerous ways in which RFB cells undergo capacity fade and performance loss, but one key pathway that plagues the development of redox electrodes is chemical decomposition. Determination of chemical stability requires evaluation of redox electrolytes in their charged state, which can be achieved either through electrolysis or via chemical oxidants, such as nitrosonium, or chemical reductants, such as hydrogen or alkali metals. These experiments commonly have several outcomes: measuring the stability of the active material in the charged state, confirming its cyclability, and, for unstable molecules, providing insight into decay processes. Stability can be evaluated using a few different electrochemical methods (**Figure I-4**), but, at the time of writing, there exist no standardized protocols and procedures. Thus, we discuss leading methodologies as well as their advantages and drawbacks, considering experimental complexity, equipment accessibility, operational limitations, and data interpretation.

For experiments designed to measure stability, other losses must be understood and managed both to enable unambiguous interpretation of results and to facilitate experimental conditions that mimic those of a practical embodiment. The use of high surface area electrodes and sufficient convective mixing can reduce kinetic and mass transfer resistances and facilitate higher current operation to improve accessed capacity at moderate overpotentials. Mass transfer limitations, which are dependent on electrolyte properties, cell geometry, and experimental conditions, set an upper bound on accessible capacity at any given charging rate, which influences the observed rate of decomposition. Most experiments apply galvanostatic cycling with potential limits, typically using charging times on the order of minutes to hours. Because species decay is a time-dependent process, capacity fade measured under galvanostatic conditions should be reported versus time, as opposed to the more commonly reported cycle number, in order to make data comparable despite different charging rates being used.[41] To overcome some of these reporting inconsistencies, Goulet and Aziz introduced potentiostatic operation as a means of assessing capacity fade.[31] By applying a sufficient overpotential to overcome kinetic limitations, the active species charge and discharge under mass transfer control, cycling almost fully between 0% state-of-charge (SOC) and 100% SOC each cycle. Further, these conditions alleviate the influence of ohmic losses due to variable cell resistance. Until standardized protocols are developed, validated, and widely-adopted by the community, the cycling conditions should be carefully selected and fully reported to enable comparison between different experiments in the interest of evaluating the merits of different redox couples and experimental apparatuses.

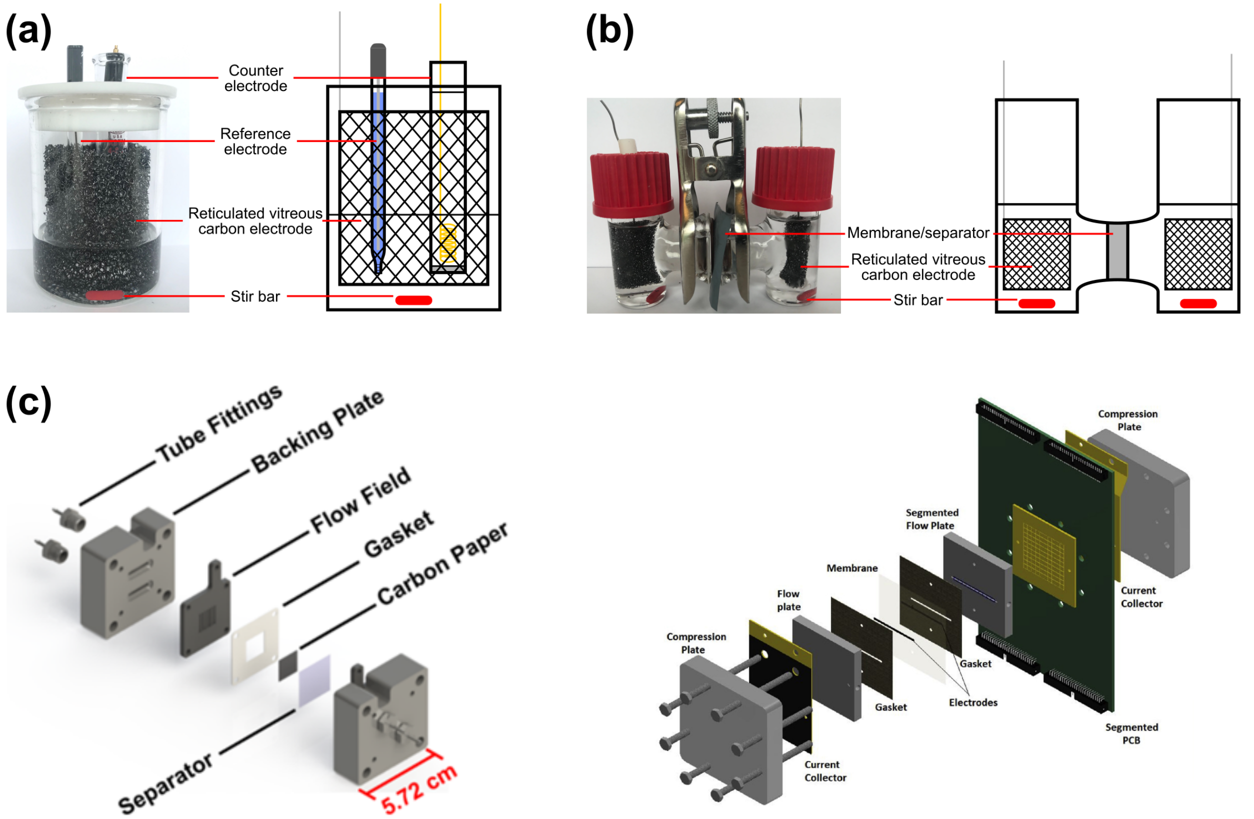

Figure I-4. *Schematics for electrochemical cell configurations used for evaluating chemical stability: (a) bulk electrolysis cell (purchased from BASi), (b) H cell, and (c) flow cells as shown by the Brushett Group*[42] *and the Mench Group.*[43] *Figures in (c) were reproduced with permission from Elsevier.*

Bulk electrolysis can be conducted in beaker-based or commercially available cells (**Figure I-4a**), making this technique easily implementable for most research laboratories. These experiments are especially conducive to stability screening, as they are conducted at low active species concentrations, requiring small quantities of active species (~mg) and relatively short cycling times. The electrolysis cell is equipped with a high surface area working electrode, typically reticulated vitreous carbon (RVC), an appropriate reference electrode, a fritted counter-electrode chamber, and a stir bar to promote mixing. Of particular interest, the reference electrode provides insight into the state of the electrolyte throughout cycling, revealing temporal changes to the charge/discharge profile that may suggest decomposition or evolution of the active species. Additionally, the glass frit slows the rate of species crossover, but the uncontrolled generation of solvent or salt decomposition products in the counter-electrode chamber eventually transport into the working electrode chamber and influence the measurement, setting a time limit on reliable data collection. Decomposition can be mitigated by using cyclable electrode or electrolyte components (e.g., stable redox couples, metal electrodes), but species crossover will inevitably lead to capacity fade. Similarly, transport through the reference electrode separator or glass frit can both contaminate the redox electrolyte and foul the reference electrode, causing the potential to drift. Difficulty in sealing bulk electrolysis cells may also lead to permeation of gas-phase impurities and/or solvent evaporation, accelerating capacity fade. In summary, these cells are easy to operate and enable relatively high experimental throughput, making them suitable for stability screening, but limitations arise for long-duration cycling.

Crossover in bulk electrolysis cells always results in capacity fade, preventing meaningful interpretation of longer duration cell cycling, especially for more stable materials. Instead of using a small, asymmetric counter-electrode chamber, an H cell design (**Figure I-4b**) may be used to eliminate capacity fade due to crossover.[26] In a symmetric H cell, the counter-electrode chamber is identical to the primary chamber except that the redox reactions proceed in opposite directions. Through this approach, capacity fade can be primarily attributed to active material decomposition, but coulombic efficiency may still be influenced by crossover-driven self-discharge reactions. Although glass frits are fairly common for mitigating crossover, these cells can leverage a range of membranes and separators, provided they are chemically compatible with the redox electrolyte and cycling conditions are selected to balance the relative trade-offs between conductivity and permeability. Functionally, the electrolytes can be prepared a priori if the redox couple is available in multiple oxidation states—in this case, both sides of the cell can be initially prepared identically at 50% state of charge (SOC). Alternatively, the working electrode chamber can be initially charged to 100% SOC through galvanostatic charging with a potentiostatic hold or potentiostatic charging, using a sacrificial electrolyte (e.g., a stable model compound) initially in the counter-electrode chamber. Once the working chamber is fully charged, the sacrificial electrolyte is removed from the counter-electrode chamber and replaced with a fresh electrolyte at 0% SOC and, if need be, a pristine electrode. Finally, these cells can be operated with or without a reference electrode in the working electrode chamber—while the reference electrode provides more accurate characterization of the working electrode potential, it also introduces a potential source of contamination. Overall, the symmetric H-cell approach provides a more accurate evaluation of long-duration stability, as compared to bulk electrolysis, with only minor increases in experimental complexity, making it the method of choice for many materials discovery laboratories.[26,44]

While useful for stability screening, the bulk electrolysis and symmetric H cells are limited to low active material concentrations, as the relatively low surface area of RVC, low mass transfer rates, and large electrode-to-electrode distances prevents the application of currents suitable for high concentration cycling. Flow cells (**Figure I-4c**) present more realistic experimental conditions as they improve convective transport, reduce ohmic resistance, and enable the use of higher surface area materials. The redox electrolytes are stored in reservoirs and pumped through the cell, permeating high surface area porous carbon electrodes (e.g., papers, cloths, felts). The resultant intra-electrode velocity yields mass transfer rates sufficient for high concentration cycling at reasonable current densities. Different flow field patterns (e.g., interdigitated, flow-through, serpentine) balance trade-offs between pressure losses through the cell and mass transfer. Instead of a glass frit, flow cells employ thin, flexible, and stable membranes or separators capable of withstanding the chemical and mechanical stresses inherent to device operation. The resulting compact design lowers the ohmic resistance, which could otherwise overload many potentiostats at high currents. A number of commercially available ion-exchange membranes and microporous separators can be used, and the most appropriate choice is dependent on the redox couples of interest and composition of the associated supporting electrolyte. Finally, with all components assembled, the cell must be sealed with appropriate gaskets and O-rings to prevent leakage and limit electrical contact resistance.

Similar to the H-cell, flow cells can operate in a symmetric configuration, often with volumetrically-unbalanced half-cells to more accurately assess capacity fade in the capacity limiting half-cell.[31] Symmetric flow cells offer an increasingly application-relevant understanding of the redox electrolyte behavior (e.g., higher concentrations, mass transfer control), but the increasing number of constituent components, necessary infrastructure, and active material quantities (~g) greatly increases experimental complexity. This convolutes understanding of the system physics and leads to additional error and complications. For example, introducing flow into an open system presents the opportunity for leaking and solvent evaporation as well as non-uniform electrolyte mixing. More subtle effects such as flow and current distribution through the electrode can further complicate performance evaluations. In addition, cell components such as the electrodes and separators may be susceptible to long-term degradation and performance loss, making it more difficult to distinguish failure modes. Wherever possible, electrodes and separators of known / demonstrated stability should be used, with the caveat that stability against new electrolytes is not guaranteed and should be verified. To understand the viability of new redox electrolytes, it is essential to understand their performance at high concentrations, but considering the confounding factors present in flow cells and high material demand, simpler cycling methods (i.e., bulk electrolysis and H cells) should be used to evaluate stability at low concentrations prior to applying this more complex technique.

The preceding techniques are well-equipped to evaluate the application-specific capacity fade of a redox electrolyte, but they alone cannot reveal the decay mechanism. Broadly, decay proceeds through two pathways – reversible decay refers to reactions such as self-discharge that result in recoverable capacity loss while irreversible decay refers to reactions that result in degradation of the active material. Species degradation can be tracked using ex situ, and in some cases in situ, chemical and electrochemical characterization tools (e.g., UV-vis, NMR, FT-IR, EPR, CV, microelectrodes) to identify decay products after cycling and enable determination of decay pathways via retrosynthetic analysis. By understanding the underlying principle reactions, these processes may be mitigated through molecular engineering of the active species or advanced electrolyte formulation (e.g., additives). Such mechanism-based approaches have been frequently implemented in the development of both redox-active organic molecules and metal-coordination complexes.[26,27]

Quantitative decay monitoring can further assess the underlying capacity fade rates and aid in the comparison of candidate compounds. Of particular importance is deconvoluting the contributions of reversible and irreversible decay in order to evaluate the portion of capacity fade that can be recovered through system-level processes such as electrolyte re-mixing and rebalancing. Quantitative measurements can be achieved through analytical techniques (e.g., UV-Vis, NMR, EPR) as well as electroanalytical techniques (e.g., CV, microelectrodes) by monitoring the time evolution of active species concentrations outside of a flow cell.[45] Each technique has unique advantages—chemical techniques enable facile compound identification while electrochemical techniques are better-suited for environments within operating cells—but the method of choice will depend on the properties and concentrations of the redox electrolyte. In addition to comparing candidate compounds, decay rates are also valuable in concert with quantitative structure-property relations to predict properties of new compounds and accelerate material development using machine learning models.[46]

1.2. Characterizing membranes for redox flow cells

An ideal membrane / separator would display high selectivity toward supporting ions as opposed to charge-storage species, typically by charge- and / or size-exclusion, however, most materials present tradeoffs.[47–50] Specifically, the chemical and microstructural characteristics needed to promote ionic conductivity and reduce ohmic losses often increase rates of active species crossover.[16] Further, species transport through microporous separators and ion-exchange membranes is complex, as the contributions of diffusion and electromigration are interrelated and depend on the material composition and microstructure, electrolyte formulation, dissolved species properties, and cell operating conditions (i.e., current density, cycling time).[48,51] Thus, assessing the extent of such tradeoffs necessitates thorough membrane / separator characterization under conditions that approximate those anticipated in practical RFBs.[28]

Typical membrane /separator characterization workflows (**Figure I-5**) evaluate thermodynamic and transport properties of the materials *ex situ* in the redox electrolyte of interest.[28] Soaking the membrane / separator in an electrolyte allows for the observation of swelling, which provides insight into the electrolyte uptake, which can increase the thickness and pore sizes while lowering the relative concentration of fixed ion sites in ion-exchange membranes. Additionally, such preliminary soaking tests can determine whether the membrane / separator is chemically compatible with the redox electrolyte, as dissolution and degradation may be visually observed. Subsequent leaching of active species from the membrane / separator into a solution of supporting electrolyte enables calculation of internal active species concentrations and thus determination of partitioning behavior.[52]

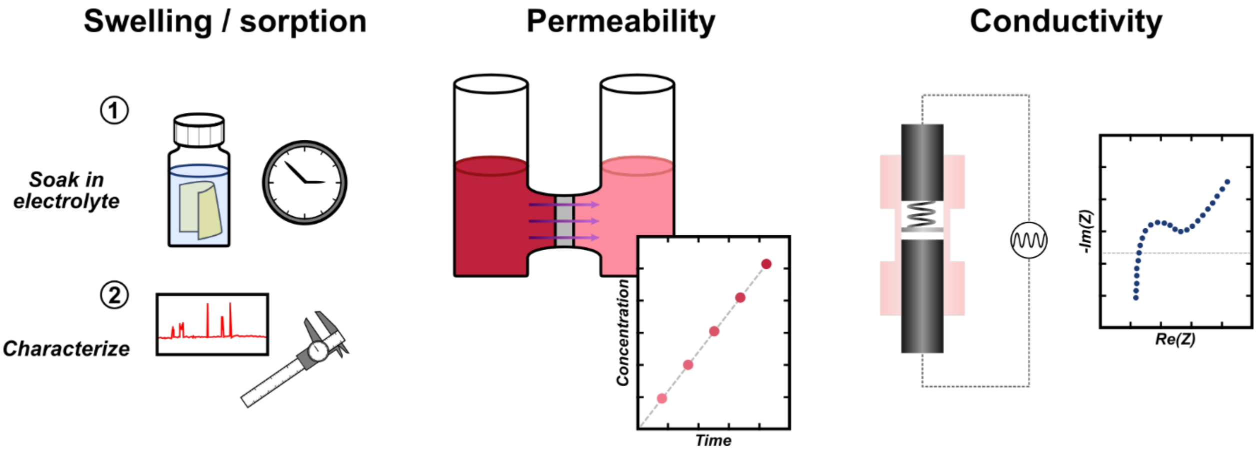

Figure I-5. *Graphical depiction of typical membrane characterization workflows, highlighting sorption / swelling, permeability (H-cell), and ionic conductivity (Swagelok cell) measurements.*

Active species permeability is directly associated with the diffusive crossover rate of active species, giving rise to both capacity fade and losses in coulombic efficiency. Accordingly, the diffusive flux is typically measured in an H-cell configuration whereby the transport rate is measured between two electrolytes separated by the membrane / separator—a permeate, containing only the supporting salt, and the retentate, containing the active species and supporting salt. Concentrations are monitored over time through electrochemical or spectroscopic methods to quantify the accumulation of active species in the permeate.[53] The change in concentration over time is then directly correlated to the diffusive flux to determine the permeability. Additionally, if the partition coefficient is calculated from sorption measurements, then the active species diffusivity within the membrane / separator can also be extracted from the permeability. More advanced spectroscopic methods (e.g., NMR, EPR) may also be applied in custom configurations to directly interrogate the membrane diffusivity.

Ionic conductivity reflects the total rate of ion transport through the membrane / separator and is thus associated with both voltaic efficiency (i.e., ohmic losses) and active species crossover via electro-migration. Comparing the active species permeability against the ionic conductivity defines the relative transport rates between supporting ions and active species, underscoring the membrane selectivity or transference.[54] Conductivity can be quantified with a range of techniques—the most common are four-point probes, which can measure either the in-plane conductivity through a direct contact measurement or the through-plane conductivity using a Devanthan-Stachurski cell architecture. Two-electrode cell architectures, including Swagelok cells[53] and conventional redox flow cells,[55] can be used to directly measure the resistance between the electrodes; additionally, the membranes may be stacked, and the slope of resistance versus thickness can be used to decouple the membrane resistance from the cell internal resistance. Some workflows may also assess other potentially useful characteristics, including the hydraulic permeability as well as the specific surface area and porosity, which provide insight into the pore-scale structure.

While an extensive suite of ex situ methods can yield valuable insights into structure-property characteristics of the membrane / separator, testing in representative cells is still necessary to both assess the efficacy of the material and evaluate its behavior under practical conditions—specifically, under applied current over long duration testing. Here, the membrane conductivity can be correlated to ohmic losses through cell diagnostics (e.g., electrochemical impedance spectroscopy, polarization) and cycling (e.g., voltaic efficiency). Conversely, extended cycling is necessary to monitor capacity fade and coulombic efficiency and interpret the role of permeability in determining cell performance. Additionally, post mortem materials testing can be applied to interrogate degradation modes as well as temporal evolution of the chemical structure and material properties. However, as noted already for active materials characterization (**Section 1.1**), performance characteristics measured within full cells are obscured by multiple confounding factors, obscuring unambiguous determination of failure modes and direct connections between the underlying material properties and RFB performance.

To address this gap, previous efforts have sought to develop new experimental tools for characterizing the influence of applied current density on species crossover. Sing and Meyers designed a four-chamber, three-electrode flow cell design—similar to an electrodialysis cell—to directly quantify individual models of active species transport within a single-electrolyte configuration (**Figure I-6**).[56] By measuring the active species concentration in the permeate streams, the steady-state fluxes from the positive electrode and negative electrode can be quantified as a function of current density, enabling interpretation of electric field effects on crossover. Note that a thicker membrane is typically used in the center of the cell to prevent crossover between the permeate cells. From this initial demonstration, others in the field have adopted this methodology for characterizing membrane / separator transport. Gandomi et al. applied this approach to study vanadium crossover and establish design rules for membrane selection,[57] and Darling et al. used the technique to quantify transference numbers for vanadium in aqueous RFBs,[58] for vanadium acetylacetonate in nonaqueous RFBs,[52] and for iron and chromium metal complexes in aqueous RFBs.[59]

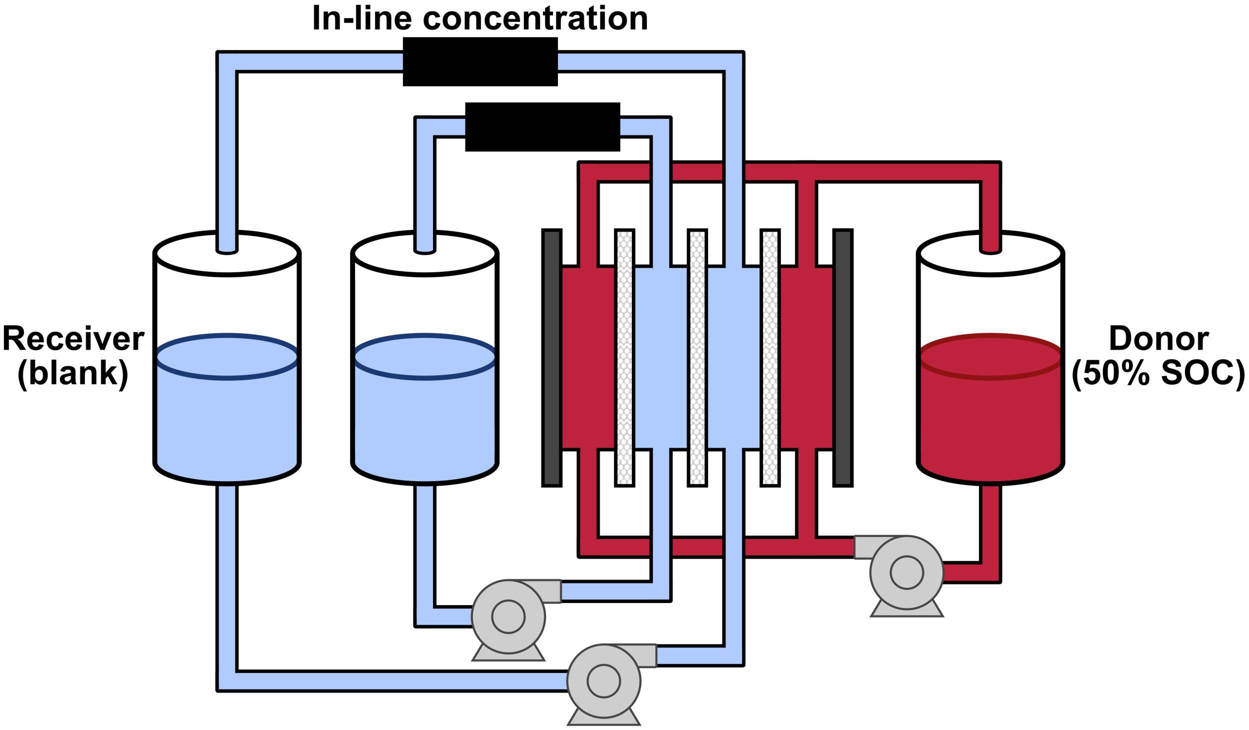

Figure I-6. *Graphical depiction of the four-chamber, three-membrane dialysis cell used for in situ measurement of membrane transport properties. Current is applied via reactions in the donor electrolyte, typically prepared at 50% state of charge (SOC), and ions are transported through the membrane / separator into the blank receiver solution containing supporting electrolyte. Redox species concentrations in the receiver solutions are measured using in-line concentration sensors (e.g., spectrophotometers).*

In addition to the dialysis approach, others have sought to develop alternative methodologies for characterizing the influence of applied current density on species transport. Luo et al. described a system containing four distinct redox flow cells and four electrolytes to study the impact of electric field on vanadium crossover across varying states of charge.[60] Vardner et al. used a single-pass configuration in a conventional redox flow cell to measure vanadium transport at different current densities by measuring the outlet concentrations from a blank permeate.[61,62] Despite the new insights offered by these advances, gaps remain in the accessibility, experimental throughput, and utility of these techniques. For instance, the four-chamber cell developed by Sing and Meyers[56] as well as the full cell architecture developed by Luo et al.[60] require periodic sampling or in-line monitoring to quantify crossover rates while the approach by Vardner et al.[61,62] requires collection and monitoring after each single-pass experiment. Further, while the architectures used here resemble redox flow cells, they differ in structure, design and/or operation, both challenging direct correlation to RFBs and stifling broader adoption in the field. Therefore, new approaches are needed to adequately characterize membranes / separators in flow cells that resemble practical embodiments.

2. Mathematical models for translating material properties to RFB performance

Deconvoluting the relationships between material properties and cell performance can require days / weeks of cycling for a single cell in addition to extensive materials characterization, which challenges rigorous and systematic experimental investigations.[28] Modeling can complement, augment, or even replace these studies by providing theoretical frameworks for interpreting cycling performance and for guiding the design of next-generation components and practical embodiments.[63] Cell, stack, and system models can span a range of length and time scales depending on the level of granularity required to describe the processes under consideration. Multi-dimensional expressions (i.e., 2D, 3D) are often necessary for describing relevant electrochemical and fluid dynamic processes in the microscopic detail needed to mirror experimental data and to represent the spatial dependence of performance-limiting factors. Conversely, lower-dimensional models (i.e., 0D, 1D) employ more generalized assumptions about the underlying physical processes and device geometries, sacrificing precision to reduce computational complexity and simulation time. These mathematical analyses often lend themselves to useful analytical formulations which can be readily adapted by practitioners.

Numerous implementations of 2D and 3D models have primarily sought to predict cell polarization behavior and interrogate relationships between the nuanced microstructural details of porous electrodes and achievable power density (i.e., kinetic, transport, distributed ohmic losses). The insights provided from such investigations have expounded foundational knowledge surrounding the role of electrode properties on performance and enabled the identification of optimal electrode geometries to balance voltage losses and hydraulic losses due to pumping. Further, various studies have been conducted to assess the role of flow field design on these characteristics, identifying idealized electrode-flow field combinations and deriving optimal, customized geometries. Often these studies rely on commercial multiphysics software (e.g., COMSOL) to construct and solve mass and momentum conservation equations, and while these tools are powerful for studying complex systems, they require expensive software packages and domain-specific user knowledge for effective implementation. Additionally, the numerical methods required to solve large systems of partial differential equations can stifle or significantly slow simulations, challenging prediction of long-duration with standard computing resources. While some efforts have applied data science tools (e.g., machine learning, neural networks) to reduce computational complexity, 2D and 3D models remain ill-suited for cell cycling applications.

Lower-dimensional models—in particular, zero-dimensional models—have found extensive use for assessing long-duration performance, simulating charge / discharge behavior, and predicting capacity fade rats. Seminal work by Skyllas-Kazakos and coworkers used simple models, accounting for Nernstian electrode potentials and diffusive crossover to contemplate the role of crossover in vanadium RFB cycling efficiency.[64,65] Others have expanded on this approach by incorporating more detailed descriptions of voltage losses and additional modes of crossover (e.g., migration, electro-osmosis).[66–70] Modak et al. described a zero-dimensional framework using the MATLAB Simulink package to assess the effects of flow distribution and species decay for the performance of an aqueous organic RFB.[71] Barton et al. combined a zero-dimensional cycling approach with a 1D porous electrode model to develop a vanadium RFB stack model, evaluating the role of shunt currents, pressure drop, and stack size on polarization and cycling performance for practical embodiments.

Despite the computational advantages engendered by simplifying the constitutive mass balances, these models continue to rely primarily on numerical methods to solve time-dependent ordinary differential equations. Many of the studies cited above report computational times beyond 60 s per cycle, meaning that simulating hundreds to thousands of cycles—which would be reasonable for practical implementations—could require hours of computation time for a single simulation. While these timeframes are likely sufficient for individual performance predictions and interpretation for targeted experimental systems, the expensive computation can hinder applications that require rapid simulations, including parameter estimation, process control, optimization, and broad parametric sweeps. To this end, Silcox et al. previously derived closed-form expressions for capacity fade as a function of cycle number in bulk electrolysis experiments, reporting a simple analytical model for evaluating redox species stability.[44] However, as the framework contemplated here only considers species decay in a single half-cell, the model is not broadly applicable to RFBs undergoing multiple failure modes and performance losses. Overall, while zero-dimensional models offer significant opportunities for enabling deeper understanding of long-duration RFB cycling performance, major gaps remain in the mathematical utility of these models, their computational accessibility, and their generalizability to full cells.

3. *Thesis outline*

A thorough understanding of the complex relationships between measurable material characteristics and flow cell behavior underpins the selection of candidate system components, providing crucial foundations for the rational design of RFBs. While a wide array of methodologies—both experimental and theoretical—can be leveraged for materials testing, the relationships between measured properties and long-duration, cell-level performance remain unclear. From an experimental perspective, few techniques exist for evaluating materials under conditions that resemble practical embodiments and assessing their evolution over time. From a modeling perspective, there are limited generalized frameworks for long-duration cell cycling that combine rapid computation and multiple decay pathways. To begin to address these shortcomings, this thesis develops experimental and theoretical approaches to navigate the complex relationships between material properties and cell performance (**Figure I-7**).

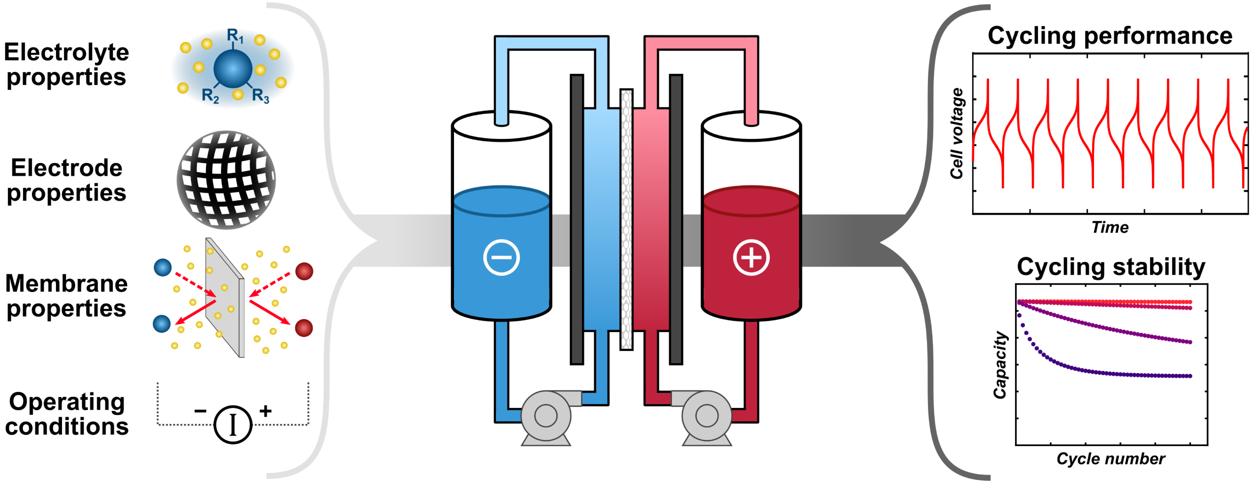

Figure I-7*. Graphical representation of the constitutive relationships between material properties and cell cycling performance which underpin rational design strategies for redox flow batteries.*

Chapter II investigates a flow-through, microelectrode-based sensor for continuously measuring species concentrations in flow cells, offering direct insight into the dynamic behavior or redox species during device operation. A gold microelectrode (working electrode) and platinum wire (pseudo-reference electrode) are sealed into a stainless-steel fitting (counter electrode), and three-electrode electroanalytical techniques (i.e., voltammetry, chronoamperometry) are performed to correlate steady-state current to concentration. To validate transport and thermodynamics that govern the sensing mechanism, we combine multiphysics simulation with *ex situ* experimental testing, confirming the device is capable of accurately determining individual species concentrations. We then evaluate the microelectrode sensor in a symmetric redox flow cell, demonstrating the utility of this approach for measuring *operando* concentrations, and discuss additional considerations for successful implementation (e.g., measurement protocol, material selection, flow cell design). Assembled from commercially available, off-the-shelf components, the sensor can be readily adopted by research laboratories and integrated into existing experimental workflows, making it a promising tool for studying flow battery materials.

Chapter III derives zero-dimensional, analytical expressions for mass balances and cell voltages under galvanostatic cycling, enabling direct connections between material / electrolyte properties, cell operating conditions, and resulting performance metrics (e.g., energy efficiency, capacity fade). To demonstrate the utility of this modeling framework, we highlight several representative considerations for RFB design, including upper bound estimation, active species decay, and membrane / separator conductivity-selectivity tradeoffs. We also discuss modalities for extending this framework to incorporate kinetic losses, distributed ohmic losses, and multiple spatial domains. **Chapter IV** expands on this framework by deriving closed-form expressions for key performance metrics and comparing the accuracy of these simplifications to the complete analytical model. The resulting closed-form model simplifies the computational structure and allows for spreadsheet modeling of cell cycling behavior, which we highlight by developing a simulation package in Excel. Importantly, because the mass balances are solved analytically in both **Chapters III** and **IV**, hundreds of cycles can be simulated in seconds, potentially facilitating detailed parametric sweeps, system optimization, and parameter estimation from cycling experiments. More broadly, this approach provides a means for assessing the impact of cell components that simultaneously influence multiple performance-defining processes, aiding in the elucidation of key descriptors and the identification of favorable materials combinations for specific applications.

Chapter V then applies zero-dimensional models to understand performance tradeoffs for two-electron compounds, which can enhance the energy density of RFBs yet suffer from diminished voltaic efficiency resulting from disparate redox potentials. To this end, we apply theoretical models to investigate the influence of the electron transfer mechanism and redox-active species properties on galvanostatic processes. First, we model chronopotentiometry at a planar electrode to understand how the electrochemical response and associated concentration distributions depend on thermodynamic and mass transport factors. Second, using a zero-dimensional galvanostatic charge / discharge model, we assess the effects of these key descriptors on performance (i.e., electrode polarization and voltaic efficiency) for a single half-cell. Finally, we extend the galvanostatic model to include two-electron compounds in both half-cells, demonstrating compounding voltage losses for a full cell. These results show that multi-electron compounds with disparate redox potentials are less attractive than those with concerted electron transfer—as such, we suggest new directions for molecular and systems engineering to improve the prospects of these materials for RFBs.

Chapter VI reports a facile method for assessing crossover directly in redox flow cells—compositionally unbalanced symmetric cell cycling (CUSCC). Based on conventional symmetric cell cycling, CUSCC imposes a concentration gradient between two chemically similar half-cells, inducing species crossover during galvanostatic cycling, which results in a characteristic "capacity gain" over time. We first develop a zero-dimensional model to describe fundamental processes that underpin the technique and examine the dependence of capacity gain on membrane / separator properties and operating conditions. Subsequently, we perform proof-of-principle experiments using $FeCl_2$ / $FeCl_3$ and Nafion^{TM} 117 as a representative system and demonstrate results consistent with those predicted from simulations. Finally, we use model fits of the capacity gain data to extract membrane transport parameters, obtaining similar values to those measured from ex situ techniques and thus validating the efficacy of this methodology. Overall, this chapter describes a promising new approach for characterizing species crossover and expands the testing toolbox for RFB development.

The thesis concludes by broadly highlighting the utility of the methods developed here for connecting material properties and RFB performance. We then discuss potential applications and extensions of this work to inspire future directions for the research community. Ultimately, the work outlined here supports the development of rational design strategies for RFBs, furthering their advancement for grid-scale storage applications and contributing to the grand challenge of sustainable energy.

II. A microelectrode-based sensor for measuring *operando* active species concentrations in redox flow cells

1. Background

Understanding modes of performance loss requires diagnostic tools that can monitor the RFB throughout its operating lifetime.[25] Such insights into the state of the system would allow researchers to interrogate mechanisms of component failure and operators to improve asset utilization and maintenance planning. The condition of the electrolyte is typically characterized by either its state of charge (SOC), which reflects the fraction of the total species concentration in the charged form, or state of health (SOH), which reflects the fraction of species available for electrochemical reaction compared against a reference concentration, typically defined as the concentration at the start of life.[25] There are numerous experimental methods that can be used to track SOC and SOH in RFBs, which vary depending on the electrolyte chemistry and the desired analytical information. Spectroscopic techniques, including spectrophotometry,[72,73] nuclear magnetic resonance spectroscopy,[29,74,75] electron paramagnetic resonance spectroscopy,[74,76,77] and infrared spectroscopy,[78,79] can enable quantitative measurements of the species concentration and, in some cases, elicit chemical information about the stability and decomposition products of different species within the electrolyte, but these typically require specialized hardware and infrastructure to be performed *in situ* or *operando*.[28] In lieu of more comprehensive chemical characterizations of the electrolyte, one can monitor physicochemical (e.g., density,[80] viscosity[81]) and electrochemical descriptors (e.g., conductivity,[82,83] open-circuit potential[84]) that in many instances correlate to electrolyte SOC. For example, in-line electrochemical cells can be used to measure the open circuit potential between the two electrolytes, which can be related to the overall SOC through equilibrium thermodynamic expressions.[85–87] Similarly, external reference electrodes can be introduced to measure the open circuit potential at a model electrode surface, which captures the equilibrium potential of each electrolyte independently, allowing determination of individual electrolyte SOCs.[84,88–90] The resultant SOC assessment from these techniques offers a cursory glance into the health of the electrolyte and the balance of charge between the two half-cells. However, these methods only describe the relative electroactive species concentrations, which presents inherent limitations in cases where performance decay is related to species crossover and decomposition, as these processes can lead to changes in the total concentrations in each half-cell.

Most methods for monitoring SOC only measure the ratio of species concentrations in different oxidation states; however, the magnitudes of these concentrations are necessary to determine the SOH and elucidate sources of performance loss (e.g., crossover, species decay, self-discharge). While concentration measurements are often more challenging, electroanalytical techniques are well suited to quantify electroactive species in redox systems.[91–93] For example, amperometric measurements have been performed on gas diffusion electrodes to measure vanadium (IV) and vanadium (V) concentrations; but despite the robust methodology, the protocol requires specialized equipment to prepare electrodes.[94] Microelectrode voltammetry has also been demonstrated as a viable method for characterizing electrochemical properties,[95,96] measuring redox species concentrations,[97] and assessing the decay of active materials *ex situ* in deterministically prepared electrolytes.[98] Microelectrodes have the distinct advantage of decoupling redox species concentrations, as their small active area enables steady-state voltammetric measurements at reasonably low scan rates (ca. 10 mV s^{-1}). Further, the resultant low currents minimize ohmic distortions and capacitive currents, enabling electrochemical measurements in more complex electrolytes, such as highly concentrated or low supporting salt environments.[33,99] However, typical three-electrode voltammetry experiments are challenging to perform *in situ*, as cross-contamination through the semi-permeable frit that separates the reference electrode fill solution from the surrounding electrolyte adversely impacts measurement reliability and longevity. Voltammetry is also commonly performed under either quiescent (e.g., cyclic voltammetry (CV)) or controlled hydrodynamic conditions (e.g., rotating disk electrodes), but non-uniform convection in the electrolyte reservoirs and redox flow cell can frustrate *operando* measurements. Microelectrodes were recently applied to monitor electrolyte SOC in RFBs using the ratio of steady state currents obtained from CV, but this implementation fell short of evaluating concentrations, owing to surface fouling and placement of the microelectrode directly in the electrolyte reservoir.[100] To enable high fidelity concentration measurements, the flow conditions around the electrode need to be uniform and consistent, and species transport must be well understood. Additionally, eliminating fouling necessitates judicious pairing of electrode materials and redox species alongside careful operation and maintenance.

In this work, we describe an in-line, flow-through microelectrode sensor (**Figure II-1**) for use as an *operando* diagnostic tool to measure redox species concentrations within a flow cell. The device leverages a three-electrode assembly to accurately quantify species concentrations via the steady-state current obtained through voltammetry and chronoamperometry. To provide a stable reference potential, the sensor uses a platinum (Pt) wire pseudo-reference electrode in place of a more standard fritted reference electrode to reduce cross-contamination and associated potential drift. We validate the proposed working principle using multiphysics simulations in an idealized domain and assess the measurement protocol using a model electroactive compound (*N*-(2-(2-methoxyethoxy)ethyl)phenothiazine, MEEPT)[42] prepared at varying SOCs. *Ex situ* measurements confirm the current is a linear function of concentration under steady flow conditions, indicating that the respective species concentrations can be determined using an empirical mass transfer coefficient, which is calibrated internally. As a proof-of-concept, we demonstrate the efficacy of this approach for measuring individual species concentrations during potentiodynamic operation by employing the microelectrode sensor in a symmetric redox flow cell containing MEEPT/MEEPT$^+$. Importantly, the device is readily assembled from commercial, off-the-shelf materials and can be easily integrated into existing experimental workflows, making it accessible to the research community.

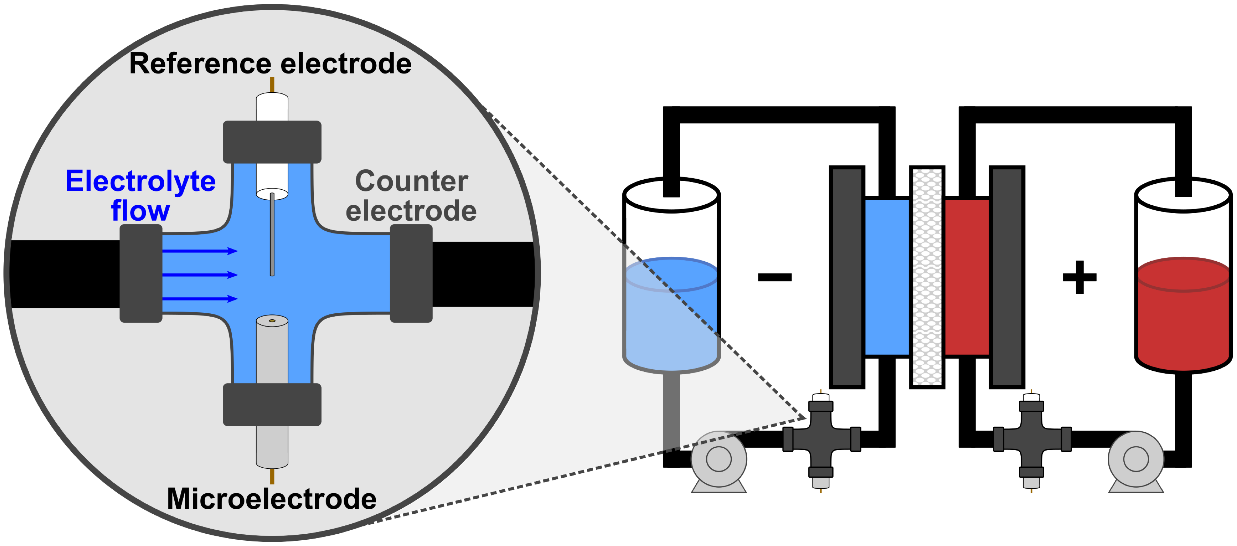

Figure II-1. *Graphical representation of the in-line, flow-through microelectrode sensor for measuring operando concentrations in RFBs. The device features a microelectrode as the working electrode, a Pt wire as the pseudo-reference electrode, and a stainless steel counter electrode, which also serves as the body of the cell.*

2. Experimental methods

All electrochemical experiments were conducted in a supporting electrolyte consisting of 500 mM tetraethylammonium tetrafluoroborate (TEABF$_4$, Gotion, > 99.9%) in propylene carbonate (PC, Gotion, > 99.9%). This composition was selected because of its wide electrochemical stability window and low volatility. MEEPT (TCI, > 98.0%) was used as the redox-active species. Oxidized MEEPT (MEEPT-BF$_4$) was prepared by chemical oxidation[101] via the addition of 1.05 molar equivalents of nitrosonium tetrafluoroborate (NOBF$_4$, Alfa Aesar, > 98%) in dichloromethane (Avantor, 99.9%), followed by precipitation with diethyl ether (Avantor, ACS reagent grade). The product was then precipitated twice from dichloromethane into diethyl ether to remove impurities and subsequently dried under vacuum to yield MEEPT-BF$_4$ at ca. 98% SOC, as confirmed by microelectrode voltammetry. All chemicals were used as-received, and electrolyte formulations were prepared a day in advance of use to ensure complete dissolution of solutes. Electrolyte viscosity was measured using a Viscolite V-700 vibrational viscometer probe and the density was calculated from the mass of a 20 mL solution prepared in a volumetric flask. Prior to use, electrodes were polished on a MicroCloth pad containing an aqueous slurry of 0.05 μm alumina powder (Buehler Ltd.), rinsed with deionized water (18.2 MΩ, Milli-Q), wiped with lens paper, rinsed with acetone (VWR, > 99.5%), and dried with compressed air. An argon-filled glovebox (MBraun Labmaster, $H_2O < 5$ ppm, $O_2 < 1$ ppm) with an ambient temperature of 26 ºC was used for chemical storage, solution preparation, and voltammetry measurements. The flow-through microelectrode sensor and symmetric flow cell cycling experiments were performed on the benchtop with the cell maintained in an in-house fabricated enclosure under an inert nitrogen atmosphere.

2.1. Pseudo-reference electrode measurements

Macroelectrode cyclic voltammograms were performed in triplicate at a scan rate of 100 mV s^{-1} using a VSP potentiostat (Bio-Logic) in electrolytes with a total MEEPT/$MEEPT^{+}$ concentration of ca. 10 mM and varying ratios of oxidized and reduced species to approximate different SOCs. Measurements were recorded with 100% *iR* correction based on the impedance measured at 200 kHz (Bio-Logic ZIR technique). The working electrode was a Pt disk (BASi, 99.95%, 3 mm diameter), the counter electrode was a Pt coil (BASi, 99.95%), and the pseudo-reference electrode was a Pt wire (BASi, 99.95%, 0.5 mm diameter). Microelectrode voltammetry measurements were performed in the same electrolytes using a CHI-630E potentiostat (CH Instruments, Inc.) at a scan rate of 10 mV s^{-1}. The working and counter electrodes were a 10 µm diameter gold (Au) disk microelectrode (BASi) and a Pt coil, respectively. The reference electrode was either a Pt wire or a fritted Li foil (Alfa Aesar, 99.9%) immersed in 1 M lithium tetrafluoroborate (Gotion, >99.9%) in PC.

2.2. Flow-through microelectrode sensor

The flow-through microelectrode sensor (**Figure II-2**) was constructed from commercial, off-the-shelf components (**Table II-1**) by integrating commercial electrodes into a 1/4” union cross (Swagelok, 316 stainless steel). The platinum pseudo-reference electrode was cut to ca. 1 cm length and fitted with 1/4” ferrules directly (**Figure II-3**). A 10-µm diameter Au disk microelectrode (BASi, 99.95%) was then inserted through ca. 1 cm of L/S 16 norprene tubing and fitted with 1/4" ferrules. The position of the tubing was adjusted such that the microelectrode surface was roughly even with the sides of the flow channel (**Figure II-3b**). The stainless-steel fitting itself served as the counter electrode, which was connected to the potentiostat by wrapping a piece of 110 copper wire (McMaster-Carr, 0.040”, 99.9%) around one side of the fitting. To introduce electrolyte flow, the fitting can use L/S 16 norprene tubing directly with 1/4" stainless steel ferrules, as shown in **Figure II-2**. To facilitate the use of different tubing sizes, additional reducing unions can be used; in the case of the L/S 14 norprene tubing used for cell cycling (vide infra), 1/4” to 3/16” reducing unions were placed at the inlet and outlet of the sensor, connected by a 1/4” tube adapter, as shown in **Figure II-3c**. During testing, the sensor was positioned vertically such that fluid enters from the bottom and exits from the top, ensuring that electrolyte completely fills the fitting. The total materials cost of the sensor was approximately $613 with the microelectrode being the largest contributor (ca. 69%). The cost could be reduced by using alternative suppliers or by manufacturing microelectrodes in-house.

For voltammetry experiments, ca. 20 mL of electrolyte containing 100 mM MEEPT/MEEPT$^+$ (ranging from 10 – 90% SOC) was continuously sparged with nitrogen (Airgas, 99.999%) and circulated between a 25 mL Pyrex® media bottle (Corning®) and the sensor through L/S 16 norprene tubing using a peristaltic pump (Masterflex L/S series, equipped with an Easy-Load II pump head) operating at variable flow rates. Voltammograms were recorded in triplicate at a scan rate of 10 mV s^{-1}. During *ex situ* testing, a pulse dampener was integrated upstream of the sensor to smooth out pressure oscillations from the peristaltic pump. Here, a 50 mL polypropylene syringe, filled with nitrogen, was connected to an additional 1/4” union tee (Swagelok, 316 stainless steel) by a short length (ca. 5 cm) of L/S 16 norprene tubing. For L/S 13 and L/S 14 tubing, additional 1/4” to 1/8” and 1/4” to 3/16” reducing unions (Swagelok, 316 stainless steel), respectively, were connected to the union tee to facilitate flow to the sensor.

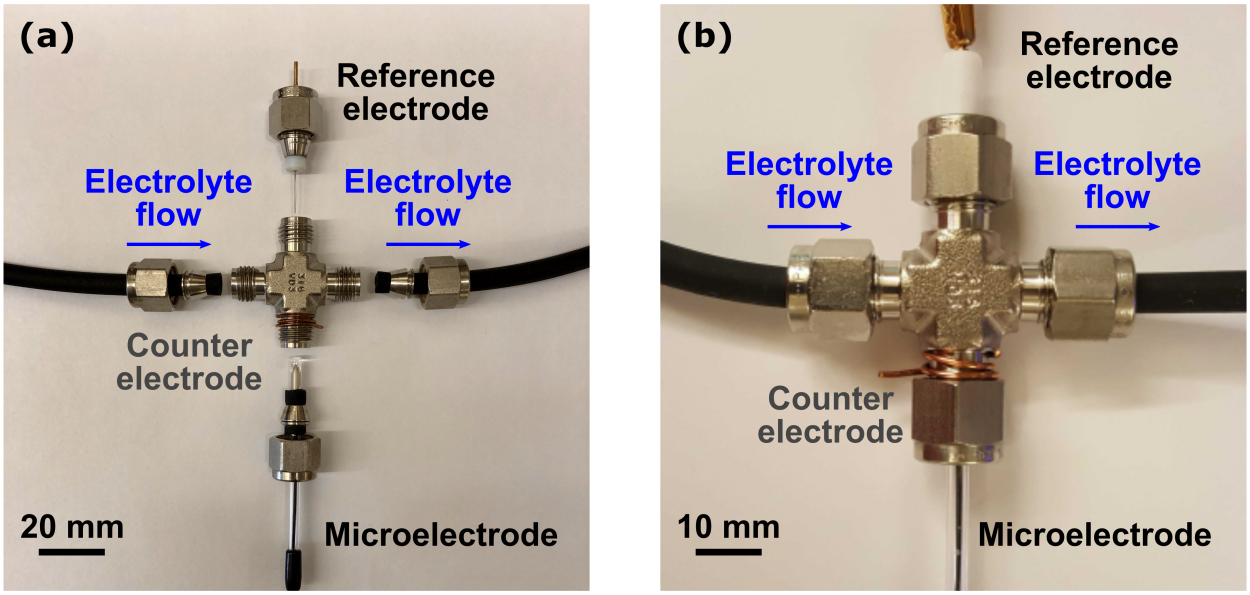

Figure II-2. *Photographs of the flow-through microelectrode sensor. (a) Exploded view depicting individual components, including the microelectrode, Pt wire pseudo-reference electrode, stainless steel body (counter electrode, connected by a copper wire), and ferrules for sealing the electrodes and tubing. (b) Fully assembled flow-through microelectrode sensor.*

Table II-1. *Constituent components used to assemble the flow-through microelectrode sensor.*

Component	Supplier	Part number	Estimated cost
10 µm gold microelectrode	BASi	MF-2006	$425
0.5 mm platinum wire	CH Instruments	CHI115	$79
1/4” union cross	Swagelok	SS-400-4	$48
1/4” to 3/16” reducing union (2)	Swagelok	SS-400-6-3	$30
1/4” tube adapter (2)	Swagelok	SS-4-TA-7-4RJ	$31

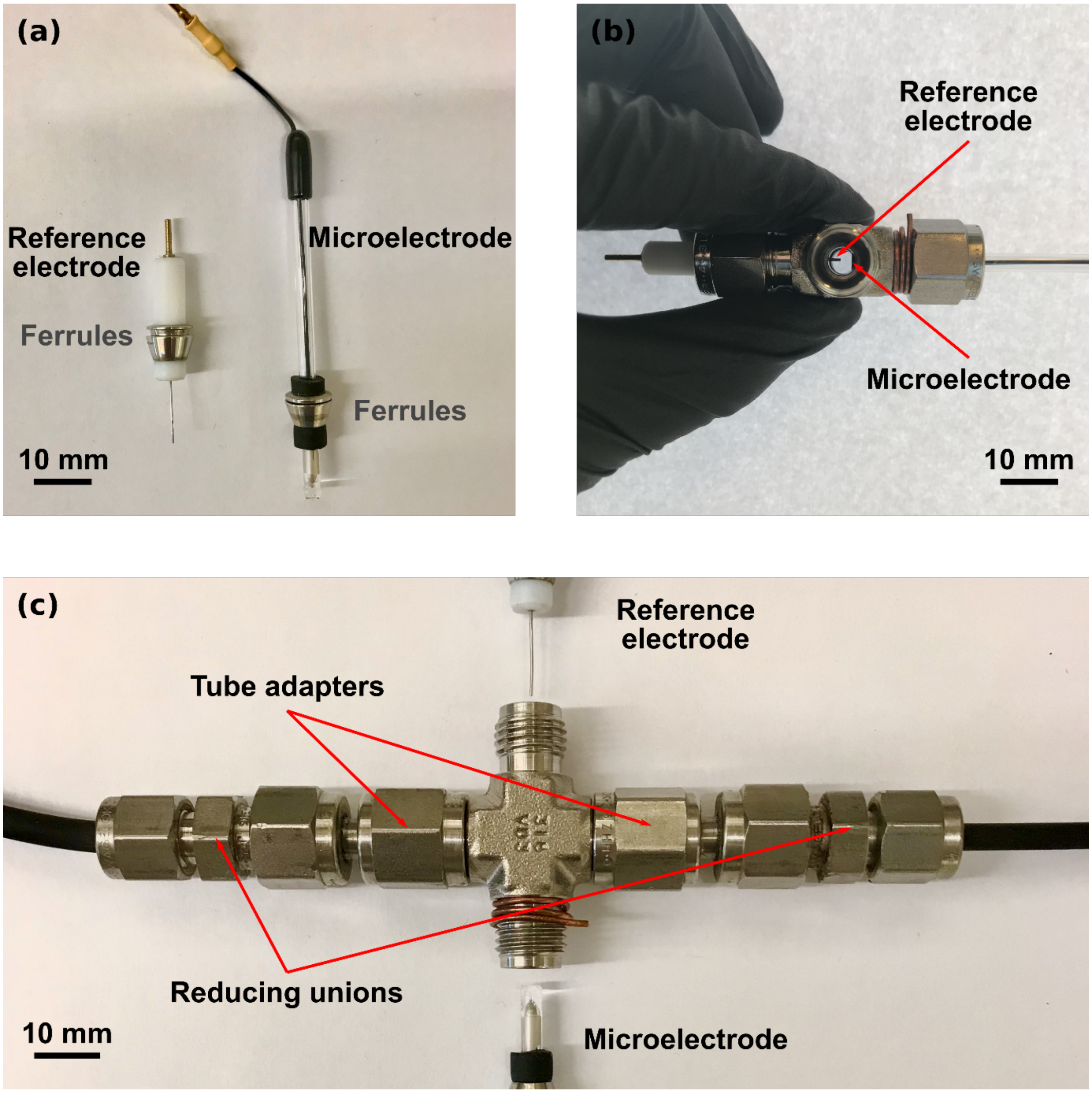

Figure II-3*. Photographs of the flow-through microelectrode sensor assembly: (a) Microelectrode and pseudo-reference electrode shown with ferrules. (b) Electrode placement in the flow channel. (c) Addition of reducing unions to facilitate different tubing sizes.*

2.3. *Operando* symmetric cell testing

Proof-of-concept *operando* cell cycling measurements were performed on the benchtop in a custom-built, small-volume flow cell.[102] A symmetric flow cell configuration was used with two identical electrolytes, each 15 mL, composed of 50 mM MEEPT, 50 mM MEEPT-BF_4, and 500 mM $TEABF_4$ dissolved in PC. The electrolytes were stored in 10 mL Savillex jars and delivered to the flow cell using a peristaltic pump through L/S 14 tubing at 20 mL min^{-1}. One side of the cell featured the flow-through microelectrode sensor while the other side featured an identical 1/4" union cross with 1/4” polytetrafluoroethylene (PTFE) plugs in place of the electrodes to balance electrolyte volumes and pressure across the separator. Both components were placed between the pump and the flow cell inlets, and additional 1/4” to 3/16” reducing unions were placed at the entrance and exit to make the sensor compatible with L/S 14 tubing. The sensor holds ca. 5 mL and thus accounts for excess electrolyte volume.

In the flow cell, one pristine AvCarb 1071 HCB carbon cloth (350 μm thickness, measured using a Mitutoyo 7300S caliper), with an area of 2.55 cm^2 (1.7 cm × 1.5 cm) and compressed by ca. 20% with PTFE gaskets of suitable thickness, was used as the electrode on each side of the cell. Interdigitated flow fields, milled in-house from Tokai G347B resin-impregnated graphite plates (3.18 mm thick, Tokai Carbon Co.), serve as current collectors and distribute electrolyte throughout the porous electrode.[103] An untreated Daramic 175 separator (175 μm thickness, measured using the aforementioned caliper) was used to mitigate crossover while maintaining sufficient ionic conductivity. In order to limit ingress of atmospheric oxygen and water into the system during cycling, the cell was kept inside a nitrogen-rich enclosure. Cells were preconditioned by circulating electrolyte through the system for 30 min to promote component wetting and bubble removal and subsequently cycled using a VSP potentiostat (Bio-Logic) at 10 mA cm^{-2} with voltage cutoffs of ± 0.5 V.

Active species concentrations were determined during cell cycling by using chronoamperometry to measure the microelectrode steady-state currents. Prior to cycling, a calibration was performed at 50% SOC by applying constant potentials of –0.35 V vs Pt for 10 s followed by +0.35 V vs Pt for 10 s to determine 1) the empirical mass transfer coefficients for oxidation and reduction and 2) the necessary time to reach steady state (< 1 s). Throughout cycling, chronoamperometry was performed every minute, applying the same sequence used for calibration. For both oxidation and reduction, the steady-state current was averaged over the last 9 s to calculate the final concentration.

2.4. Modeling and simulation

COMSOL Multiphysics® (v. 5.6) was used to perform the three-dimensional (3D) advection-diffusion simulations. The steady state *Laminar Flow* and *Transport of Diluted Species* modules were used to solve the fluid dynamic and mass-transfer equations, respectively, within the simplified 3D microelectrode sensor domain (**Figure II-4**). The fluid dynamic equations, as shown in their generalized form in **Equation (II.1)**, were solved alongside the continuity equation (**Equation (II.2)**).

$$\rho(\mathbf{u}\cdot\nabla)\mathbf{u}=\nabla\cdot\left(-p\mathbf{I}+\mu\left(\nabla\mathbf{u}+(\nabla\mathbf{u})^{T}\right)\right) \tag{II.1}$$

$$\rho\nabla\cdot\mathbf{u}=0 \tag{II.2}$$

ρ (kg m^{-3}) is the fluid density, $\mathbf{u}$ (m s^{-1}) is the velocity vector, p (Pa) is the pressure, $\mathbf{I}$ is the identity tensor, and μ (Pa s) is the fluid viscosity. Additionally, a symmetry boundary condition (**Equation**

(II.3)) was used on the microelectrode side to reduce the computational complexity, with other boundary conditions for the walls, the inlet, and the outlet shown in **Equations (II.4)**, **(II.5)**, and **(II.6)**, respectively.

$$\mathbf{u} \cdot \mathbf{n} = 0 \tag{II.3}$$

$$\mathbf{u} = 0 \tag{II.4}$$

$$-\int_{\text{inlet}} \rho \left(\mathbf{u} \cdot \mathbf{n} \right) d\mathrm{S} = \mathrm{w}^2 \, v \, \rho \tag{II.5}$$

$$\left(-p\mathbf{I} + \mu \left(\nabla \mathbf{u} + \left(\nabla \mathbf{u} \right)^T \right) \right) = 0 \tag{II.6}$$

n indicates the normal vector in either the x, y, or z spatial dimension, w (m) is the domain width, and v (m s^{-1}) is the scalar velocity. Similarly, the generalized mass transport equation solved in COMSOL® is shown in **Equation (II.7)**.

$$-D\nabla^2 c + \mathbf{u} \cdot \nabla c = 0, \tag{II.7}$$

D (m^2 s^{-1}) is the diffusion coefficient and c (mol m^{-3}) is the species concentration. Here, the wall with the microelectrode has a symmetry boundary condition (**Equation (II.8)**); the walls and the outlet are subject to a no-flux boundary condition (**Equation (II.9)**); the inlet has a Danckwerts boundary condition (**Equation (II.10)**); the electrode surface invokes a Dirichlet boundary condition, emulating a reactant-depleting event (**Equation (II.11)**).

$$\mathbf{n}\cdot\left(-D\cdot\nabla c+\mathbf{u}c\right)=0 \tag{II.8}$$

$$D\cdot\nabla c=0 \tag{II.9}$$

$$\mathbf{n}\cdot\left(-D\cdot\nabla c+\mathbf{u}c\right)=\mathbf{n}\cdot\left(\mathbf{u}c_0\right) \tag{II.10}$$

$$c_s=0 \tag{II.11}$$

c_0 and c_s (mol m^{-3}) are the bulk and microelectrode surface concentrations, respectively. The current is then derived from the species flux at the electrode surface (**Equation (II.12)**) with positive current corresponding to oxidation (e.g., oxidation of MEEPT).

$$I=-nF\int_{S_e}\mathbf{n}\cdot\left(D\left.\frac{\partial c}{\partial z}\right|_{z=0}\right)dS \tag{II.12}$$

n is the number of electrons transferred (here, $n = 1$), F (96485 C mol^{-1}) is the Faraday constant, and S_e (7.85×10^{-11} m^2) is the microelectrode surface area.

A schematic of the COMSOL® simulation domain is shown in **Figure II-4**, highlighting the three-dimensional flow domain, as well as a magnified rendering of the microelectrode surface. The width (x), length (y), and height (z) were set to 0.5, 1.0, and 0.5 mm, respectively. The x and y dimensions approximate the glass body housing the 10 µm diameter microelectrode. The z dimension is scaled to sufficiently capture gradients in the velocity and concentration. Note that we specified symmetry boundary conditions to reduce the computational intensity of the coupled advection-diffusion problem within this domain.

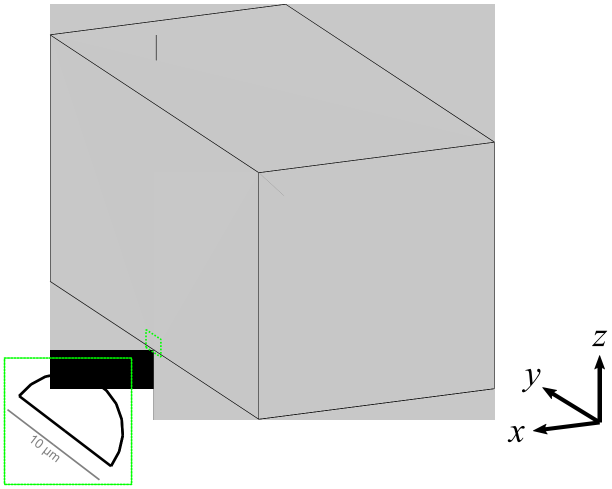

***Figure II-4**. The COMSOL® domain used in the simulation with half of the microelectrode diameter shown in the zoomed image. The microelectrode sits on the z = 0 plane and fluid flows in the y direction.*

Within the domain, we conducted a mesh study to limit inaccuracies in the numerical solvers without accruing large memory requirements. We applied the Paradiso solver with a relative tolerance of 1×10^{-3} and a maximum 100 iterations for the Newton non-linear method. Our approach was to specify a smaller mesh near the surface of the microelectrode, which is the region of interest for these simulations; whereas regions far from the microelectrode were allowed a coarser mesh. The minimum mesh size was set to 10^{-10} m, and the maximum value was varied between 5×10^{-8}, 1×10^{-7}, 5×10^{-7}, 1×10^{-6}, 5×10^{-6}, 1×10^{-5}, 5×10^{-5}, and 1×10^{-4} m to restrict the elements within the domain. A schematic of the mesh discretization is shown in **Figure II-5a**, revealing the smaller features near the electrode surface and larger elements farther away. To quantify the effect that the mesh size has on the simulation results, two metrics were monitored as the maximum mesh size was altered: the diffusive flux at the microelectrode surface and the concentration on a facsimile projection of the surface 1×10^{-7} m from the electrode. Next, the largest mesh size with the smallest deviation from the 5×10^{-8} m result was used for the simulations in the main text. These results are shown in **Figure II-5b**, with details on the final mesh properties described in **Table II-2**. Using the validated mesh, two parameter sweeps were performed, spanning values of v from $0 - 6 \times 10^{-2}$ m s^{-1} in increments of 0.5×10^{-2} m s^{-1} with c_0 specified at either 1, 5, 10, 25, 50, 100, or 200 mM. All simulations were completed on a 6-core laptop with 64 GB RAM and an Intel® Core™ i7-9750H CPUs (2.60 GHz) requiring ca. 4.75 h in total to compute all parametric combinations.

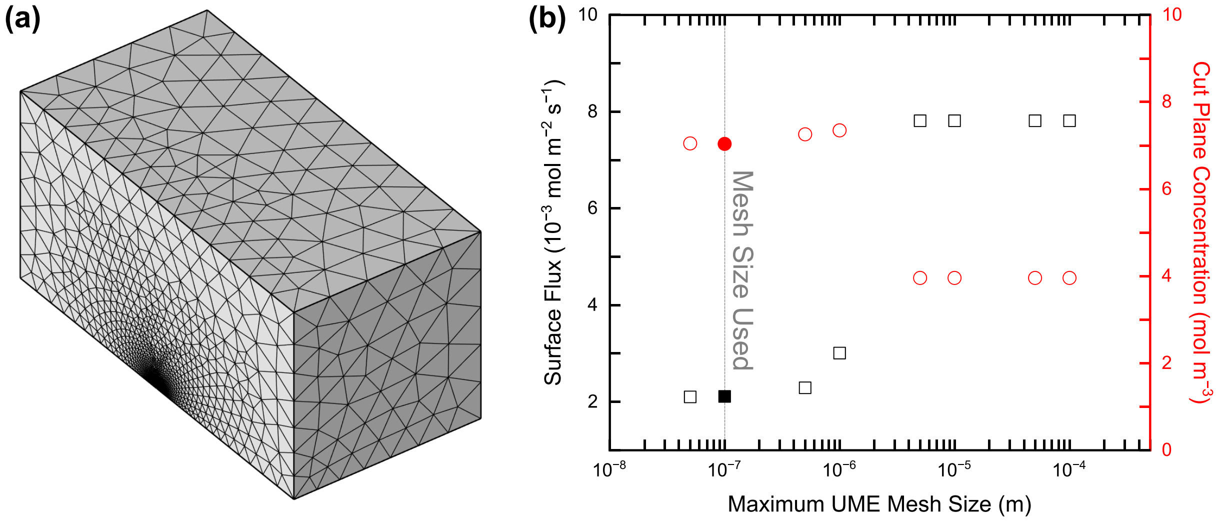

Figure II-5. *(a) The mesh used in the simulations, showing the changes in element size from the microelectrode surface to the domain. (b) The results of the mesh study, showing slight changes in the surface flux and the cut plane concentration when the maximum mesh size was set above* 10^{-7} *m for the microelectrode plane.*

Table II-2. *Final mesh geometry and statistics used in this study.*

Property	**Value**
Microelectrode maximum element size	1×10^{-7} m
Microelectrode minimum element size	1×10^{-10} m
Domain maximum element size	1×10^{-4} m
Domain minimum element size	1×10^{-10} m
Domain maximum growth rate	1.3
Number of elements	458087
Element volume ratio	8.654×10^{-11}
Mesh volume	2.5×10^{-10} m^3

3. Pseudo-reference electrode validation

Considering that standard reference electrodes rely on a well-defined redox chemistry isolated from the electrolyte of interest, species in this environment can leak through its separator (typically a porous glass frit), contaminating the RFB electrolyte and accelerating decay processes. Further, contamination of the isolated reference electrode chamber can poison the electrode and destabilize the potential, interfering with electrochemical measurements.[88] Using a pseudo-reference electrode, we can instead harness the chemistry of the electrolyte itself to yield a more stable potential for voltammetric and chronoamperometric measurements. In this case, the electrode is a Pt wire directly immersed in the electrolyte that measures the potential of the electrochemical processes occurring on the metal surface at equilibrium. While the potential of the reference electrode may shift with the SOC, we are primarily interested in the steady-state currents accessed by the microelectrode, and thus, if conducted properly, the precise value of the potential is inconsequential to the fidelity of the measurement. Here, we compare microelectrode voltammograms under varying SOC conditions for a nonaqueous redox couple, MEEPT/MEEPT$^+$, which is stable in both discharged and charged states, to establish the viability of this approach.

To quantify the pseudo-reference electrode potential, we first measure the potential of the Pt wire relative to the formal redox potential of MEEPT/MEEPT$^+$ using CV at a disk macroelectrode in deterministically prepared electrolytes with varying SOC (**Figure II-6a**). By calculating the average of the anodic and cathodic CV peak potentials to estimate the formal redox potential relative to the Pt wire, we can determine the relative potential of the pseudo-reference electrode as a function of electrolyte composition. As expected, the potential shifts in accordance with the Nernst equation, shown by **Eq. (II.13)** and **(II.14)**.

$$E = E^0 + \frac{RT}{nF}\ln\left(\frac{1-\mathrm{SOC}}{\mathrm{SOC}}\right) \tag{II.13}$$

$$\mathrm{SOC} = \frac{[\mathrm{MEEPT}^+]}{[\mathrm{MEEPT}]+[\mathrm{MEEPT}^+]} \tag{II.14}$$

Here, E (V) is the electrode potential, E^0 (V) is the formal potential, R (8.314 J mol^{-1} K^{-1}) is the universal gas constant, and T (K) is the absolute temperature. This form of the Nernst equation assumes ideal species activities, although activity coefficients may differ at higher electrolyte concentrations.[87] Given this robust understanding of the pseudo-reference electrode, we can apply it directly to conventional three-electrode measurements.

Next, we compare the microelectrode responses in the same electrolytes using either the pseudo-reference electrode or a more commonly used, fritted reference electrode (Li/Li$^+$). With the more traditional reference electrode (**Figure II-6b**), we only observe a vertical shift in the currents due to changing bulk concentrations which give rise to variable steady-state transport rates.[98] Under quiescent conditions, the plateau currents are related to the bulk concentration and the diffusion coefficient of the reacting species according to **Eq. (II.15)**.

$$I = \pm 4nFrc_0D \tag{II.15}$$

Here, r (5×10^{-6} m) is the microelectrode radius. Replacing the reference electrode with a pseudo-reference electrode introduces horizontal shifts in the curves as a function of electrolyte SOC (**Figure II-6c**), consistent with the anticipated changes in the reference electrode potential. At first, this may seem problematic for a voltammetric measurement; however, our key feature of interest is the steady-state currents, which are independent of the overpotential provided sufficiently positive or negative potentials are applied.

We note that some relevant electrolytes may exhibit undesired voltammetric features (e.g., sequential redox reactions, solvent / electrolyte decomposition) which could make accurately measuring extreme SOCs more difficult. These processes may also depend on the microelectrode surface chemistry; for example, noble metal electrodes (Au, Pt) often promote electrolyte decomposition more readily than carbon-based electrodes.[104] In such cases, fritted reference electrodes may still be integrated into this cell architecture and periodically cleaned to impose stricter control over the working electrode potential. While standard references are more common, those containing the RFB active species at 50% SOC may hinder contamination due to leaking.[88]

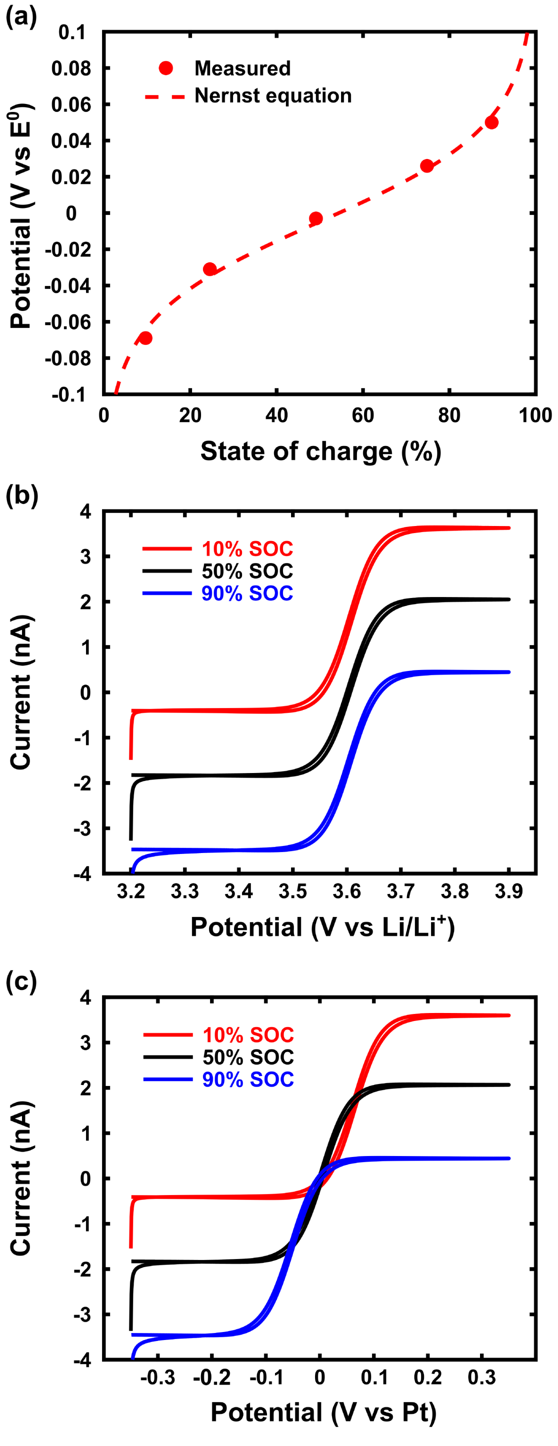

***Figure II-6**. Ex situ reference electrode potential measurements and microelectrode voltammograms measured at varying SOCs in electrolytes containing 10 mM MEEPT/MEEPT$^+$ and 500 mM TEABF$_4$ in PC. (a) Pt wire pseudo-reference electrode potential as a function of SOC shown alongside theoretical predictions from the Nernst equation. Measurements were performed in triplicate and the symbols exceed the size of error bars with one standard deviation. (b) Microelectrode voltammograms measured using a fritted Li / Li$^+$ reference electrode compared to (c) a Pt wire pseudo-reference electrode. Voltammograms were conducted on a 10 μm Au microelectrode at 10 mV s^{-1}. Positive currents correspond to MEEPT oxidation and negative currents correspond to MEEPT$^+$ reduction.*

4. Microelectrodes under flow

To provide theoretical foundations for the role of advection across the electrode surface, a COMSOL® model was designed as a simplification of the microelectrode sensor domain. By systematically varying the electrolyte composition and flow rate, this simulation platform provides a means to probe the working principles of the apparatus prior to experimental validation. For context, the linear velocities and electrolyte properties used in this model were chosen to mimic the range of conditions expected in the experimental cell. Average fluid velocities of 0 – 0.06 m s^{-1} correspond approximately to volumetric flow rates of 0 – 10^{-6} m^3 s^{-1} (0 – 70 mL min^{-1}) based on the channel diameter at the inlet and outlet (5×10^{-3} m). The following transport parameters were measured in electrolytes containing 100 mM MEEPT/$MEEPT^+$ at 50% SOC and 500 mM $TEABF_4$ in PC: $\mu = 3.96 \times 10^{-3}$ Pa s, ρ =1190 kg m^{-3}, and $D = 1.7 \times 10^{-10}$ m^2 s^{-1} for both the reduced and oxidized species (determined by microelectrode voltammetry and CV[34]).

The model generates a concentration profile, driven by advection and diffusion to the electrode surface, which allows for the determination of the steady-state current from the species flux. Plotting this current as a function of the electrolyte velocity (**Figure II-7a**), we observe a transition from diffusion-dominated transport at low fluid velocities to advection-dominated transport at high fluid velocities, scaling with the square root of the velocity, which is consistent with canonical models of fluid flow over a flat plate.[105] The non-linear scaling with respect to flow rate challenges prediction of the steady-state current via simple mathematical relationships and, in practice, the construction of an idealized planar surface with uniformly laminar flow and controlled mass transport is not feasible. However, theoretical predictions of the current as a function of concentration (**Figure II-7b**) show a linear dependence across all flow regimes, suggesting that the current can be predicted from an empirical mass transfer coefficient, k_m (m s^{-1}) at each flow rate, as indicated in **Eq. (16)**.

$$I = \pm nFk_m c_0 \tag{16}$$

Therefore, an ideal system is not a prerequisite to effectively measure concentration, and as long as consistent and stable flow can be maintained over the microelectrode surface, the steady-state current should be directly proportional to the reactant concentrations.

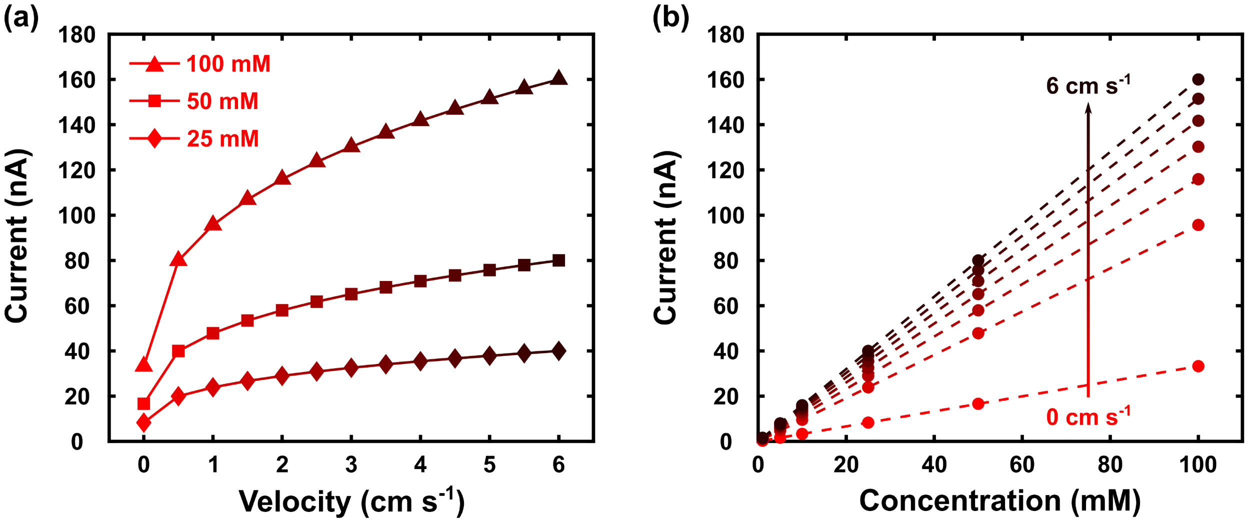

***Figure II-7**. COMSOL® simulations of the steady-state current to a disk microelectrode shown for a one-electron oxidation under varying electrolyte velocities and active species concentrations. (a) Current as a function of velocity for selected active species concentrations. (b) Linear relationship between current and concentration shown for electrolyte velocities ranging from 0 – 6 cm s^{-1} in increments of 1 cm s^{-1} and concentrations ranging from 1 – 100 mM. Dashed lines indicate linear fits with all $R^2 = 1$. All simulations were conducted using $D = 1.7 \times 10^{-10}$ m^2 s^{-1}, $\mu = 3.96 \times 10^{-3}$ Pa s, $\rho = 1190$ kg m^{-3}, and $r = 5 \times 10^{-6}$ m to mimic experimental conditions used in this work.*

To confirm these theoretical underpinnings prior to implementation in an operating flow cell with dynamically varying concentrations, we performed *ex situ* testing using deterministically-prepared electrolytes. We constructed the sensor (**Figure II-2**) from off-the-shelf components, sealing a 10 μm Au microelectrode and a Pt wire pseudo-reference electrode inside of a 1/4” stainless steel union cross, which served as the counter electrode. We then measured voltammograms of 100 mM MEEPT/MEEPT$^+$ electrolytes at 50% SOC to understand the microelectrode response to variable flow rates (**Figure II-8a** and **Figure II-8b**). Interestingly, the voltammograms display an oscillatory behavior that changes with flow rate, which may at first appear to be random noise due to boundary layer disruption. However, closer inspection of the experimental setup reveals that the oscillations are consistent with the frequency of the peristaltic pump, indicating that the microelectrode captures these subtle changes in flow rate. To confirm that these variations were due to the mode of fluid delivery rather than an artifact of the microelectrode environment, we sought to stabilize the flow by introducing a flow dampener upstream of the sensor (**Figure II-9**) to reduce the oscillations and yield a more consistent measure of the current.

Repeating the variable flow rate measurements, we find that at high flow rates (> 20 mL min^{-1}), and thus high rotational frequencies, the smoother flow profile yields a more constant steady-state current, which scales with increasing flow rate (**Figure II-11a**). The relationship between current and electrolyte velocity (**Figure II-10**) qualitatively follows the trends derived from **Figure II-7**, although, as expected, the magnitude of the current differs between the theoretical model and the experimental measurements with and without the pulse dampener. Considering the irregular channel geometry and pulsatile nature of the flow, these discrepancies are most likely the result of non-uniform velocity distributions throughout the measurement cell, which, in turn, lead to further deviations in transport phenomena from the flat plate contemplated in our model. It is important to reiterate that an idealized flow geometry is not required for high fidelity concentration measurements, and in all instances, the steady-state currents remain stable and are sufficient for this technique. The signal obtained under flow is also notably less sensitive to physical disturbances (e.g., walking by the experimental setup) as compared to microelectrode measurements in quiescent solutions. This suggests that the flow-through sensing approach imposes hydrodynamic conditions that impart greater stability in the local environment, providing measurements which are less susceptible to boundary layer disruptions.

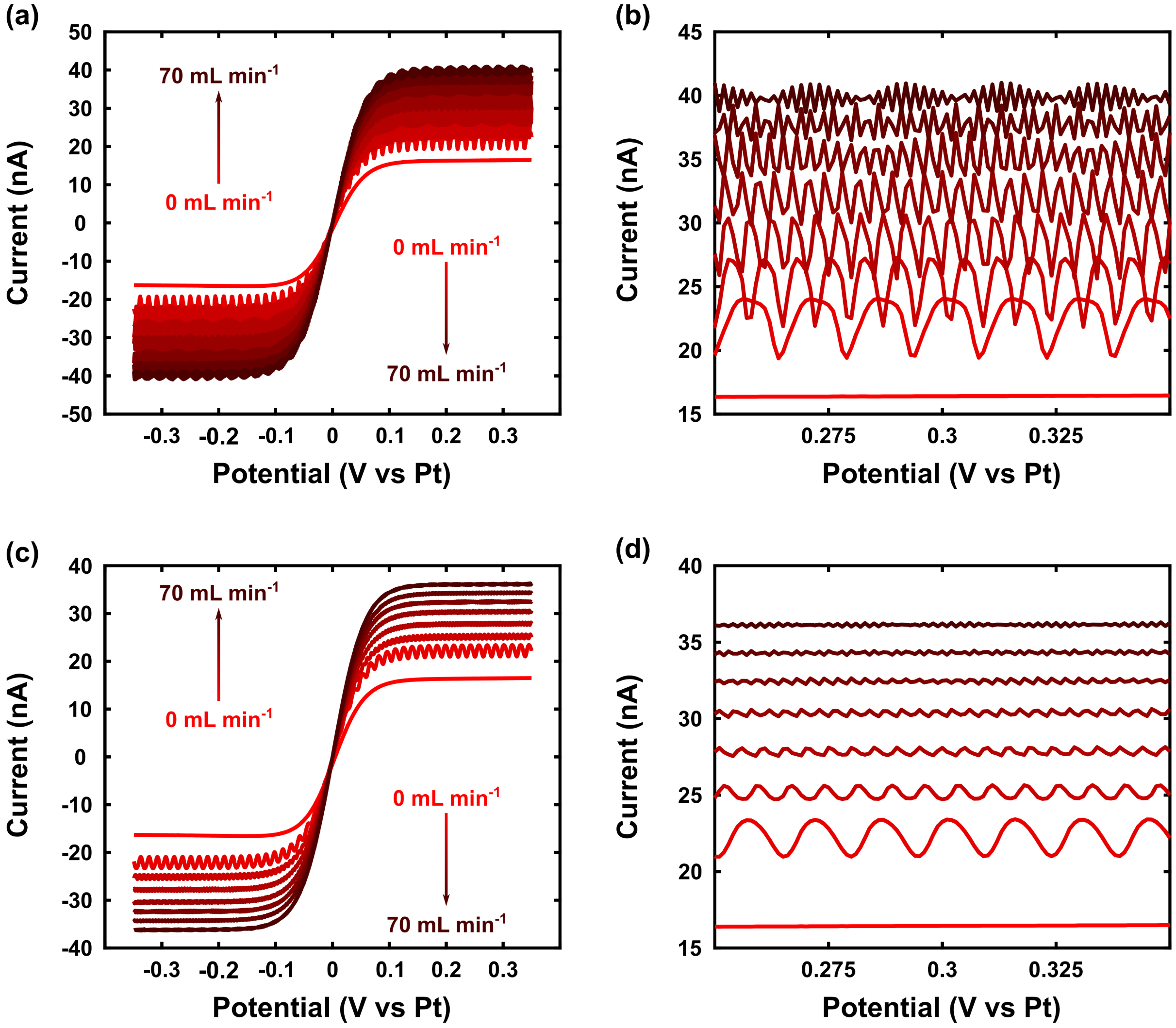

Figure II-8. *Experimental flow-through microelectrode measurements at variable flow rates for electrolytes containing 100 mM MEEPT/MEEPT*$^+$ *at 50% SOC and 500 mM TEABF*$_4$ *in PC. Microelectrode voltammograms measured (a, b) without and (c, d) with the pulse dampener. The positive steady state currents shown in (b) and (d) are similar to the negative steady state currents. All voltammograms were recorded at 10 mV s*$^{-1}$ *at flow rates ranging from 0 to 70 mL min*$^{-1}$ *in increments of 10 mL min*$^{-1}$.

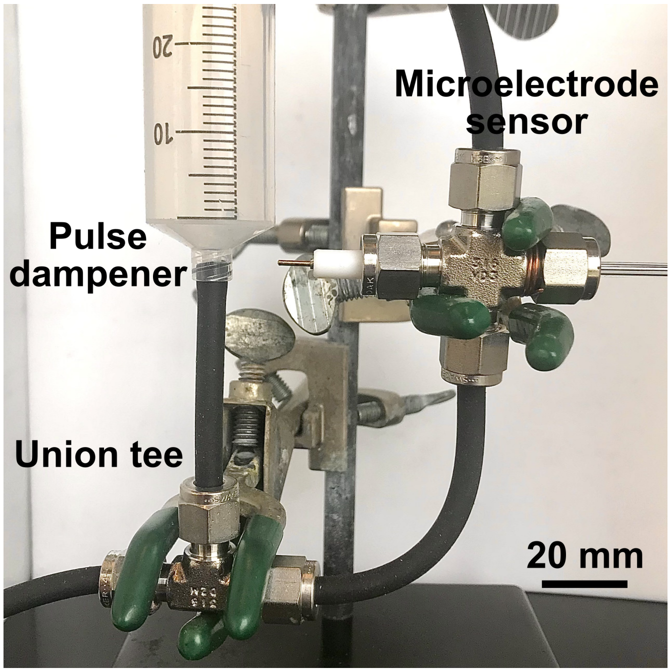

Figure II-9. *Photograph of the flow-through microelectrode assembly with a pulse dampener placed upstream of the sensor.*

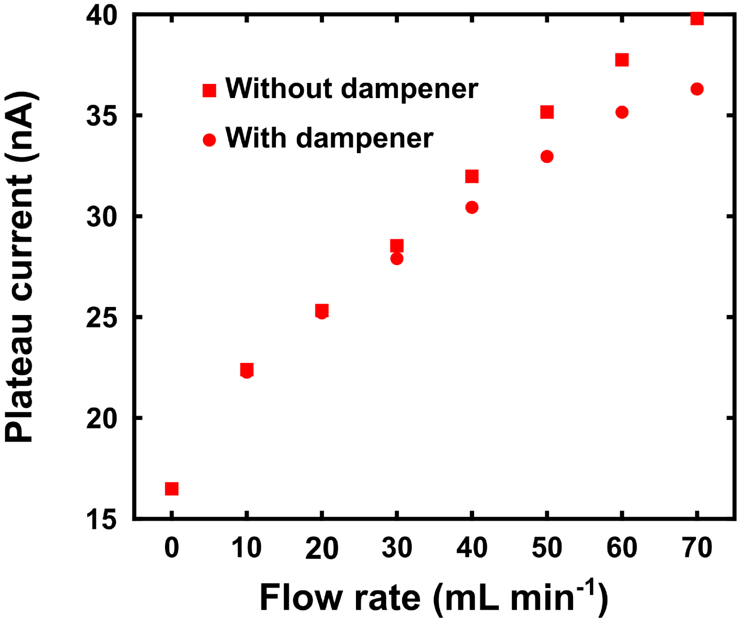

Figure II-10. *Average steady-state currents as a function of flow rate, shown with and without the pulse dampener. All voltammograms were recorded at 10 mV s^{-1} in electrolytes containing 100 mM MEEPT/MEEPT^{+} at 50% SOC and 500 mM TEABF$_4$ in PC. Plateau currents were measured by averaging the current over the last 50 mV of the plateau.*

To validate the concentration dependence and thus the working principle behind the sensor, we repeated these measurements at varying active species concentrations similar to those used in **Figure II-7b**. Specifically, the electrolytes contained the same total active species concentration (ca. 100 mM MEEPT/MEEPT$^+$) with differing ratios of oxidized and reduced species to approximate SOCs between 10 – 90%. Using the plateau currents obtained under quiescent conditions, we first calibrated the actual concentration of each species using **Eq. (II.15)**, again taking the diffusion coefficients to be 1.7×10^{-10} m^2 s^{-1}. **Figure II-11b** shows the resulting plateau currents as a function of the concentrations of MEEPT and MEEPT$^+$ with volumetric flow rates ranging from 0 – 70 mL min^{-1} and concentrations ranging from 10 – 90 mM. Although the empirical mass transfer coefficients differ from the model due to differences in the cell geometry and internal fluid dynamics, the linear dependence on the concentration is maintained across this range of SOCs, confirming the theoretical predictions and establishing the promise of this sensor. These measurements also demonstrate high accuracy with close linear fits ($R^2 > 0.999$) in all cases; however, the sensitivity and limit of detection will likely depend on the species concentrations, electrolyte flow rates, electrolyte properties, and instrumentation limits used in practice.

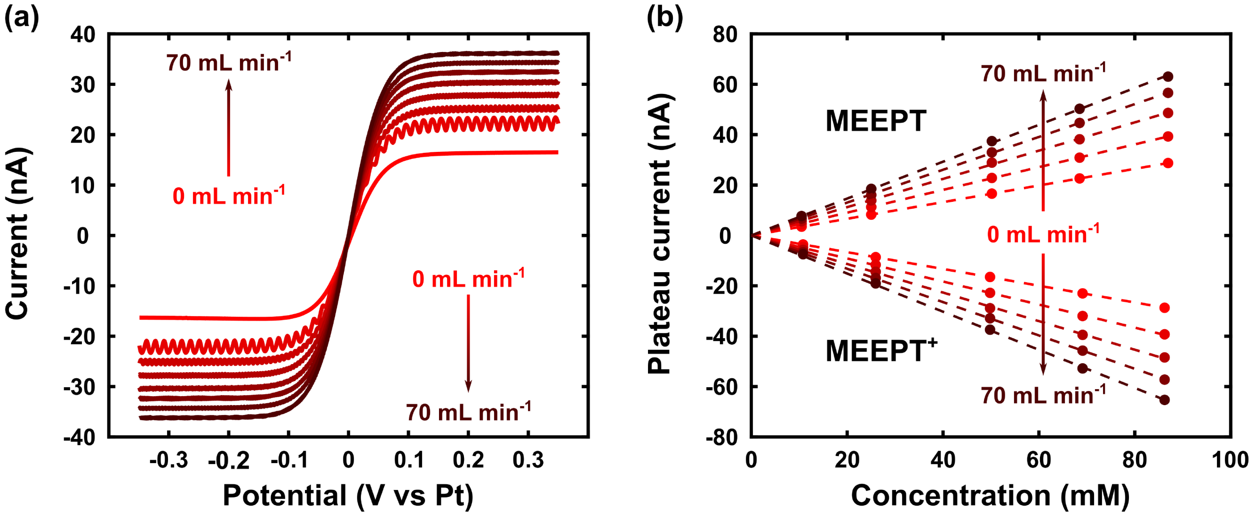

Figure II-11. *Experimental flow-through microelectrode measurements at variable SOCs and flow rates for electrolytes containing 100 mM MEEPT/MEEPT*$^+$ *and 500 mM TEABF*$_4$ *in PC at SOCs between 10 – 90%. (a) Microelectrode voltammograms in MEEPT/MEEPT*$^+$ *(50% SOC) measured at 10 mV s*$^{-1}$ *for flow rates ranging from 0 – 70 mL min*$^{-1}$ *in increments of 10 mL min*$^{-1}$*. (b) Average steady-state currents as a function of MEEPT and MEEPT*$^+$ *concentration taken from voltammograms measured at 0, 10, 30, 50, and 70 mL min*$^{-1}$ *in electrolytes prepared at 10, 25, 50, 75, and 90% SOC. Measurements were performed in triplicate and the symbols exceed the size of error bars with one standard deviation. Dashed lines indicate linear fits with all R*^{2} *> 0.999.*

5. *Measuring concentrations in a redox flow cell*

Finally, with the sensor performance validated externally, we conducted *operando* measurements to establish a proof-of-concept for this measurement platform. Specifically, we cycled the same redox couple, MEEPT/MEEPT$^+$, in a symmetric flow cell configuration.[42,102] Both electrolytes were prepared at 50% SOC with 100 mM total active species concentration and circulated through the cell at 20 mL min^{-1} under galvanostatic conditions at 10 mA cm^{-2} with potential limits of ± 0.5 V. The microelectrode sensor was used without the pulse dampener to mitigate pressure imbalances across the separator and placed between the pump outlet and flow cell to continuously sample the inlet concentrations. Although the sensor applies current directly to the electrolyte, because both the working and counter electrodes are present in the same electrolyte, the reactions are anticipated to be equal and opposite, negating any net changes in SOC from the measurement. Additionally, while we anticipate that the stainless steel counter electrode will remain stable under the conditions explored in this work, it may require the use of conductive carbon coatings or compatible, polymer-based fittings (with an integrated counter electrode) for highly oxidative electrolytes.

Rather than performing a full linear or CV sweep, which require several minutes to collect data at sufficiently low scan rates, we perform chronoamperometry at sufficiently positive or negative applied potentials to ensure only the steady-state currents are captured, requiring ca. 20 s (**Figure II-12**). Considering the reference electrode potential varies with SOC, it is important to ensure the overpotentials are high enough to achieve mass transfer limiting conditions without encountering additional redox processes (e.g., oxidation of MEEPT$^+$). Based on our validation of the reference electrode potential (**Figure II-6a**), we apply potentials of ± 0.35 V vs Pt. During cycling, these potentials are each held for a total of 10 s, and after achieving steady state (< 1 s), the current is averaged over the last 9 s to yield a final value. Initially, a calibration is performed using the same procedure and a known electrolyte composition to calculate the empirical mass transfer coefficient via **Eq. (16)**, which is subsequently used to measure concentrations during cell cycling. As discussed above, the mass transfer coefficient is a function of the electrolyte flow rate, cell geometry, and tubing size, but as these parameters remain unchanged throughout cycling, this coefficient need only be determined once immediately prior to use. It should also be noted that the approach outlined here assumes a constant viscosity across the system lifetime and across all electrolyte SOCs, as variable electrolyte viscosity can influence the species diffusivity and fluid dynamics which impact the empirical mass transfer coefficient. While such conditions are not anticipated based on our initial validation (**Figure II-11b**), this may be a consideration if more concentrated electrolytes are used, necessitating additional calibrations at different SOCs.[102,106,107]

We initially contemplated two possible architectures for this sensor: 1) a bleed stream, continuously sampling the electrolyte reservoir of the flow cell, and 2) in-line with the cell inlet stream, continuously sampling the electrolyte entering the flow cell. Of the two configurations, we found the in-line measurement to be less disruptive, as the bleed stream displaces significant volumes of electrolyte from the fluidic circuit between the cell and reservoir. While this displacement was incompatible with our current experimental setup given the small electrolyte volumes (ca. 15 mL per half-cell), it may have greater value in larger embodiments with increased electrolyte volumes.

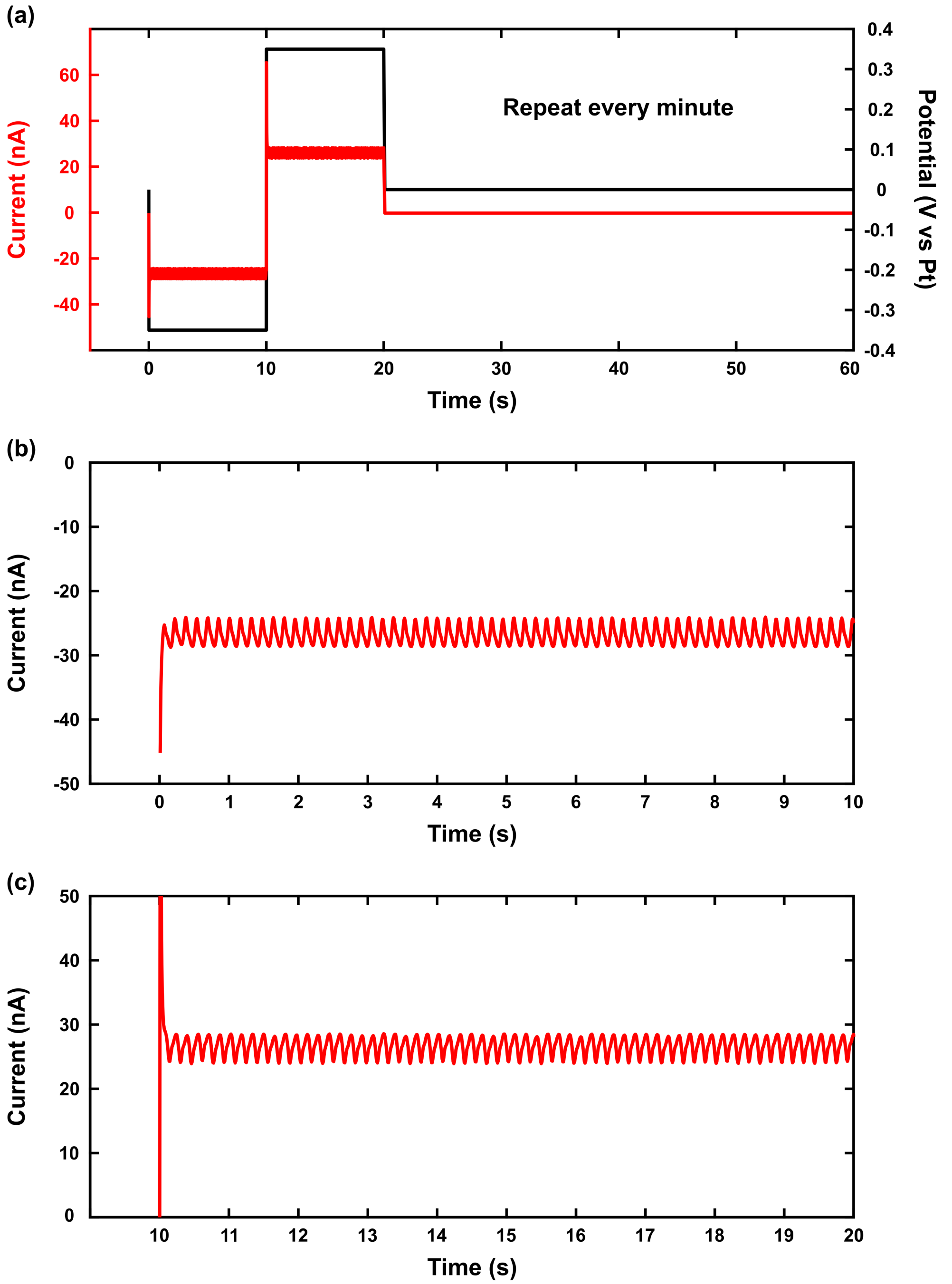

Figure II-12. *Chronoamperometry sequence applied for measuring operando species concentrations in the proof-of-concept symmetric cell cycling experiment. A reductive potential (–0.35 V vs Pt) is applied for 10 s followed by an oxidative potential (+0.35 V vs Pt) for 10 s, and this sequence is repeated once per minute. (a) Both the applied potential and current response for the full minute, (b) expanded view of the reductive current, and (c) expanded view of the oxidative current. Data shown prior to cell cycling at 20 mL* min^{-1} *in an electrolyte containing 100 mM MEEPT/*$MEEPT^{+}$ *at 50% SOC and 500 mM* $TEABF_4$ *in PC.*

Figure II-13a shows the potentiometric charge/discharge profiles for the flow cell, which are typical of a symmetric cycling experiment, while **Figure II-13b** shows the corresponding concentration profiles, which align with the variations in cell voltage. As expected, the measured concentrations change linearly with time because galvanostatic operation imposes a constant reaction rate to the electrolyte. Further, the cell exhibited negligible capacity fade with near 100% coulombic efficiency throughout cycling (**Figure II-14**), which is consistent with the stable species concentrations measured by the sensor as well as with prior literature.[42] From the applied current, we can directly quantify the charge passed over time (i.e., coulomb counting) in each half-cell, and, through Faraday's Law, relate that to the concentrations measured by the sensor (**Figure II-13b**).[80] While this method is not analytically precise and does not capture additional transient processes such as crossover and decomposition, it can serve as an additional semi-quantitative check of the anticipated sensor performance. Indeed, comparing this approximation with the experimental results shows good agreement; however, there are minor deviations between the two methods (**Figure II-15**), which we tentatively attribute to a combination of incomplete mixing in the reservoirs, inexact electrolyte volumes, and crossover effects. Given the limitations of coulomb counting, we expect that the sensor more accurately quantifies species concentrations within an operating redox flow cell, and taken together, these results represent a successful proof-of-concept demonstration.

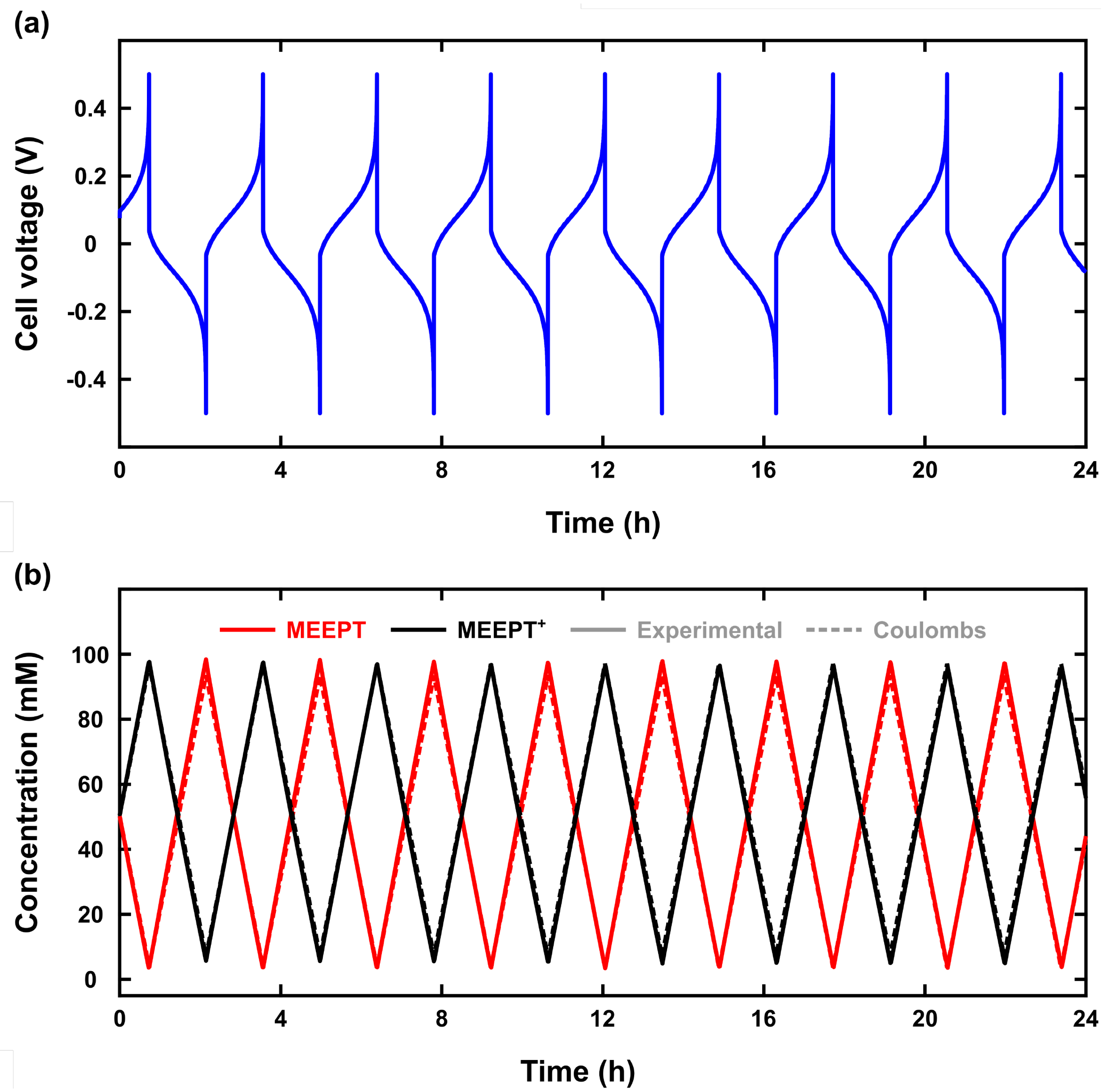

Figure II-13. *Proof of concept experiment for integration of the microelectrode sensor into a symmetric redox flow cell containing 100 mM MEEPT and MEEPT-BF$_4$, initially at 50% SOC, flowing at 20 mL min^{-1} and cycled at 10 mA cm^{-2}. (a) Cell voltage as a function of time and (b) corresponding species concentrations determined using the flow-through microelectrode sensor. The experimentally measured concentration is compared with concentration predictions derived from coulomb counting.*

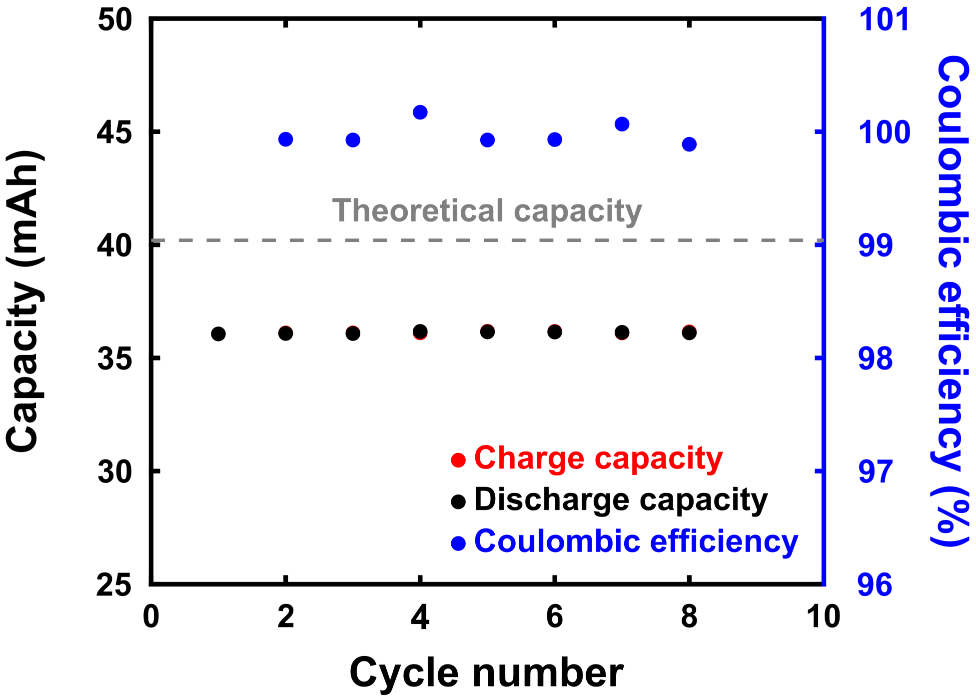

Figure II-14. *Capacities and coulombic efficiency measured during symmetric redox flow cell cycling. The flow cell was cycled at 10 mA cm*$^{-2}$ *and contained 100 mM MEEPT/MEEPT*$^{+}$*, initially at 50% SOC, flowing at 20 mL min*$^{-1}$.

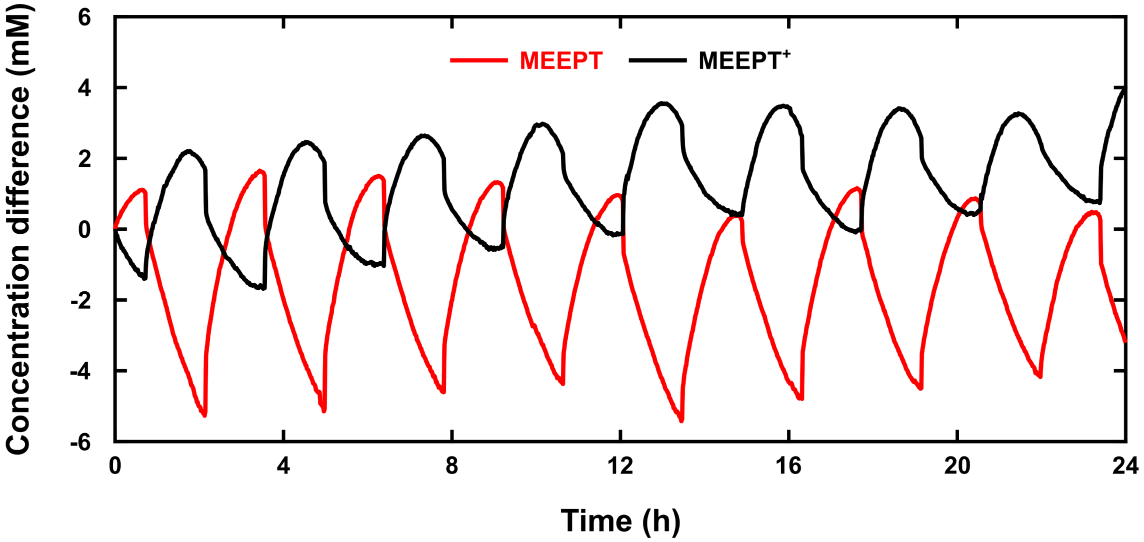

Figure II-15. *Differences between the concentrations measured using the flow-through microelectrode sensor and the concentration predictions obtained by coulomb counting. The concentration difference is calculated by subtracting the experimentally measured values from the theoretically predicted values shown in* ***Figure 6b*** *in the main text.*

To interrogate the stability of the electrode surface over the course of cell cycling, we maintained a control electrolyte, identical to that used for cycling, inside the glovebox. Because the composition and SOC of this electrolyte should remain constant, any changes in the voltammetric signal reflect changes to the microelectrode. Comparing voltammograms before and after cycling (**Figure II-16a**), we observe negligible changes in the measured current, confirming that the Au microelectrode was stable throughout the experiment. However, when we conducted a similar cycling experiment using a Pt microelectrode subjected to the same chronoamperometry conditions, we observed a marked decrease in the voltammetric steady-state currents in the control electrolyte (**Figure II-16b**). Considering that similar decreases were observed for both plateaus and that the signal was recoverable via polishing, this fouling is likely the result of losses in the electrochemically active surface area.[98,100] Further, as we did not observe fouling when the electrode is simply immersed in the same electrolyte at 50% SOC for 24 h, we posit that this reduction in surface area is a product of the duration and frequency of the potential holds. In this work, the current was measured every minute to elicit the dynamic concentrations during cycling, but applications such as SOH assessments, species decay monitoring, and crossover detection may demand less frequent measurements. As a result, they may be more resilient to the effects of fouling and thus can more readily integrate this sensing platform. In general, the design and implementation of microelectrode sensing schemes will require careful selection of electrode – active species pairs that demonstrate minimal fouling and undesired redox reactions; but where such combinations may not exist, the reliability of the signal can still be reasonably maintained by subjecting the surface to less frequent and shorter polarizations. The signal can also be periodically recovered by either polishing or replacing the fouled electrode. Finally, while the auxiliary materials selected for these experiments (i.e., pseudo-reference electrode, counter electrode) appear stable for these testing conditions, other chemistries and/or extended testing durations may also necessitate alternate material sets.

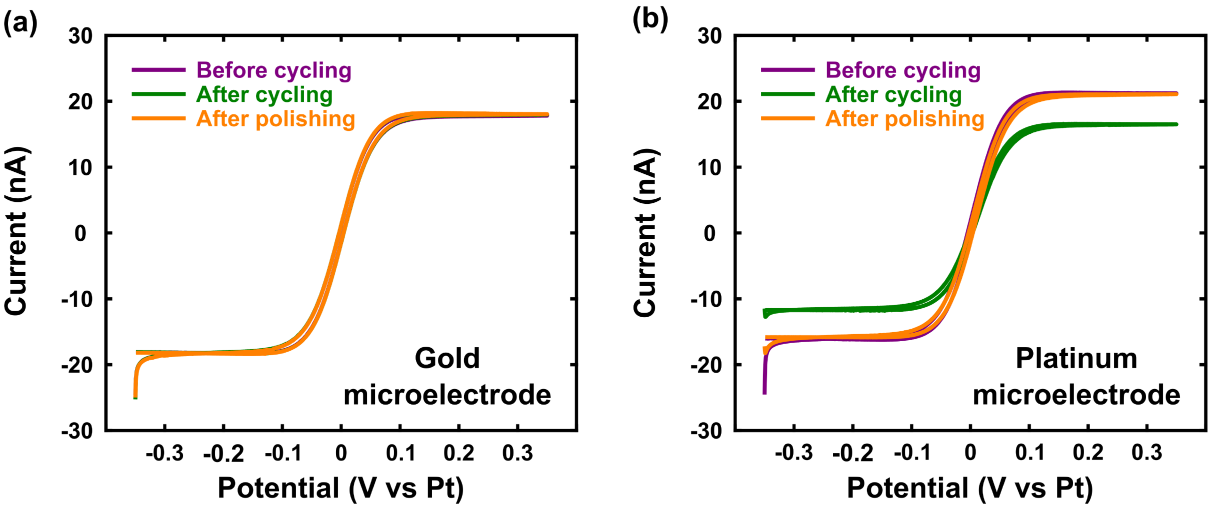

Figure II-16. *Microelectrode voltammograms taken before and after symmetric cell cycling experiments for (a) the Au microelectrode and (b) the Pt microelectrode. Both electrodes were then polished and the voltammogram was repeated. All voltammograms were recorded in the glovebox at 10 mV s*$^{-1}$ *in electrolytes containing 100 mM MEEPT/MEEPT*$^{+}$ *at 50% SOC and 500 mM TEABF*$_4$ *in PC. Note that the currents for Pt are slightly more positive than those for Au due to minor differences in the as-prepared electrolyte.*

6. Conclusions

We successfully demonstrated a flow-through, microelectrode-based electrochemical sensor for measuring *operando* active species concentrations in redox flow cells. The flow cell sensor was assembled from off-the-shelf components obtained from commercial suppliers and investigated through *ex situ* and *operando* testing as well as multiphysics simulation. The theoretical and experimental results establish the fundamental underpinnings of sensor operation; namely, under controlled hydrodynamic conditions and constant flow rates, the steady-state currents are linearly dependent on redox species concentrations. Symmetric flow cell cycling provides a proof-of-concept validation that the sensor is capable of continuously and accurately measuring SOC and SOH during cell operation. Considering its ease of implementation into existing experimental workflows, the sensor has broad potential utility in research and commercial technologies for monitoring component stability during cell cycling, particularly when quantifying the impact of redox species decomposition and/or crossover. While the device is functional in practice, the sensing mechanism can be further improved by better controlling flow through cell engineering such that steady-state transport may be predicted by power-law models as opposed to empirical internal calibrations.

7. List of symbols

Roman symbols

c	Concentration (mol m^{-3})
c_0	Bulk concentration (mol m^{-3})
c_s	Concentration at microelectrode surface (mol m^{-3})
D	Diffusivity (m^2 s^{-1})
E	Electrode potential (V)
E^0	Formal potential (V)
F	Faraday constant (96,485 C mol^{-1})
I	Current (A)
$\mathbf{I}$	Identity matrix (–)
k_m	Mass transfer coefficient (m s^{-1})
$\mathbf{n}$	Unit normal vector (–)
n	Number of electrons transferred (–)
p	Pressure (Pa)
r	Microelectrode radius (m)
R	Ideal gas constant (8.314 J mol^{-1} K^{-1})
S_e	Microelectrode surface (m^2)
SOC	Electrolyte state of charge (–)
T	Temperature (K)
$\mathbf{u}$	Velocity vector (m s^{-1})
v	Scalar velocity (m s^{-1})
w	Domain width (m)
z	Coordinate axis orthogonal to the microelectrode surface (m)

Greek symbols

μ	Viscosity (Pa s)
ρ	Density (kg m^{-3})

III. Connecting material properties and redox flow cell cycling performance using zero-dimensional models

1. *Background*

Zero-dimensional models have shown particular value for explaining flow battery cycling performance.[44,64,66–71,108] These formulations describe time-dependent changes in redox species concentrations and ignore spatial variations, sacrificing microscopic precision for solvability. Further, zero-dimensional models can easily incorporate parasitic processes (e.g., molecular decay, crossover) which lead to evolving charge / discharge profiles, capacity fade, and diminished efficiencies. Despite these simplifications, the numerical methods used to solve the time-dependent differential equations remain computationally expensive and, because they scale with the cell lifetime, simulations of long-duration performance scenarios can become prohibitively slow. For example, several previously reported zero-dimensional models require ca. 30 – 120 s to generate a single charge-discharge cycle on laptop computers, meaning that longer simulations (tens to hundreds of cycles) would take hours of computation time.[66,108,109] This may be feasible for specific uses, but it discourages systematic modeling for extended cycling scenarios and parametric studies. While numerical implementations are necessary for certain instances,[71,108] a range of cell architectures and operating conditions can be described by constitutive equations with analytical solutions. The development of analytical expressions that describe cycling behavior can drastically reduce the mathematical complexity of simulating durational performance in RFBs, potentially making such models more accessible to researchers with diverse technical backgrounds and varying computational resources.

Here, we develop an analytical framework for modeling galvanostatic cycling behavior in redox flow cells to illuminate the relationships between component material / electrolyte properties, cell operating conditions, and electrochemical performance. First, we derive explicit, analytical representations in the absence of capacity fade mechanisms to estimate upper bounds of accessible charge storage capacity and voltaic efficiency under idealized conditions where ohmic and mass transport losses dominate. Second, we introduce active species decay and self-discharge to simulate capacity fade in the absence of crossover. We then connect this expression to experimental observations in diagnostic flow cell architectures used to assess molecular decay rates. Third, we assess the impact of membrane selectivity and conductivity on capacity retention and energy efficiencies, illustrating the complex interplay of property combinations that govern species crossover over extended periods of cell cycling. Fourth and finally, we discuss modalities to further expand on this framework, including the incorporation of kinetic losses, non-uniform reaction distributions, and multiple spatial domains.

While prior reports have sought to develop and validate zero-dimensional models against cell cycling data,[44,66,71] we pursue a more general approach, focusing on the derivation, implementation, and overall utility of this modeling framework. Therefore, we contemplate questions that are of broad interest and importance to RFB cycling rather than address specific hypotheses surrounding a particular redox chemistry or device configuration. As such, we do not conduct an exhaustive parametric sweep of all adjustable variables but instead present representative analyses that emphasize the versatility of these models. Consequently, the results provided here validate several previously reported experimental observations and offer new considerations for individual component selection and cell design. We note that the simplified set of analytical expressions outlined here is relevant for a wide range of existing and emerging RFB chemistries, enabling the determination of more meaningful design guidelines for next-generation materials at an earlier stage of development and reducing the need for time- and materials-intensive experimental campaigns. Additionally, rapid computation times could facilitate the integration of cycling models into more complex mathematical frameworks, including techno-economic assessments,[20,47,110] process control and optimization,[111–113] parameter estimation from experimental systems,[114] and synthetic data generation for machine learning,[115,116] making this approach valuable for a broad swath of researchers.

2. *Zero-dimensional cycling model*

Here, we introduce a generalized, zero-dimensional modeling framework to describe galvanostatic cycling in a redox flow cell. Initially, we introduce mass balance equations associated with the individual charged and discharged species (**Section 2.1**). Subsequently, we discuss modes of homogeneous active species decay (**Section 2.2**) and membrane crossover (**Section 2.3**) to define source and loss terms, and derive analytical solutions (**Section 2.4**) to the associated mass balance equations. Then we introduce electrochemical expressions to describe the cell voltage (**Section 2.5**) and relevant cell cycling metrics (**Section 2.6**). Finally, we discuss model implementation, including the software and hardware used to perform cell cycling simulations (**Section 2.7**). This model invokes the following overarching assumptions: (1) all processes occur at constant temperature (i.e., isothermal); (2) all domains are well-mixed such that species concentrations are uniform throughout; (3) operating conditions and electrolyte / flow cell properties remain constant throughout cycling; and (4) all redox reactions proceed through a one-electron transfer without chemical / electrochemical intermediates. All other assumptions will be described within the context of specific models and equations.

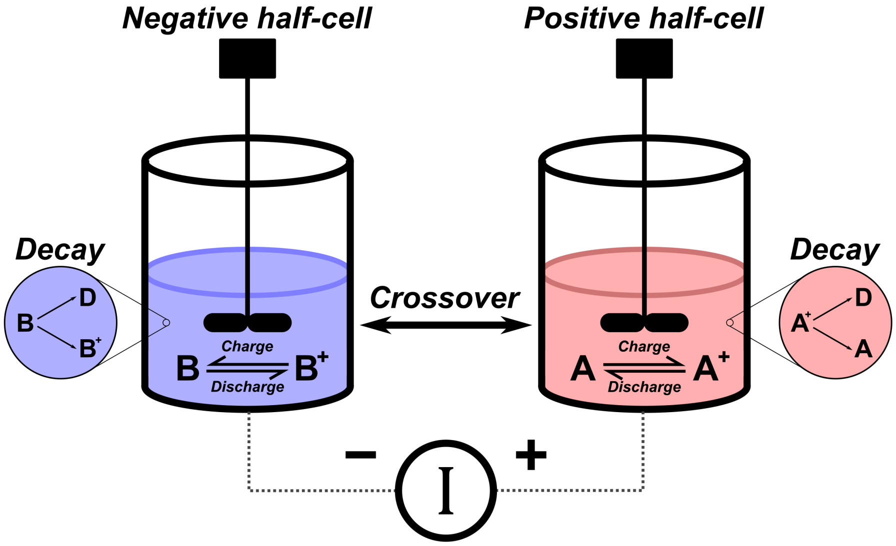

Figure III-1. *Representative modeling domain explored in this work.*

2.1. Reaction mass balances

In this modeling framework, we consider two species, A and B, undergoing one-electron half-reactions shown in **Equations (III.1)** and **(III.2)**.

$$A \rightleftharpoons A^{+} + e^{-} \tag{III.1}$$

$$B \rightleftharpoons B^{+} + e^{-} \tag{III.2}$$

A and A^{+} are treated as the positive electrolyte (posolyte) redox couple and undergo charge / discharge in the positive half-cell while B and B^{+} are treated as the negative electrolyte (negolyte) redox couple and undergo charge / discharge in the negative half-cell. Here, A and B^{+} reflect the discharged states while A^{+} and B reflect the charged states. Note that the nominal charges associated with A^{+} and B^{+} describe only their relative states of charge; however, the ionic charge of each species, z_j, may be any value (e.g., –2, –1, 0, +1, +2) such that $z_{A^{+}} = z_{A} + 1$ and $z_{B^{+}} = z_{B} + 1$.

Broadly, zero-dimensional cycling models rely on solving mass balances for each species in the system; here, we assume that both half-cells are well-mixed and that the reaction takes place uniformly throughout the electrolyte volume. Hence, each reactor half-cell, electrolyte reservoir, and connecting tubing are treated as one continuous domain, resembling two stirred tank reactors as represented schematically in **Figure III-1**. The mass balance for each species can be generally described by **Equation (III.3)** where the time, t (s), is measured from the beginning of each half-cycle (i.e., charge or discharge) and the applied current, I (A), is positive for the charging half-cycle and negative for the discharging half-cycle.

$$\frac{dC_j^{\infty,h}}{dt} = s_j^h \frac{I}{V^h F} + \sum R_j^h \tag{III.3}$$

V^h (m^3) is the total electrolyte volume in half-cell h (either the positive or negative electrolyte), $C_j^{\infty,h}$ (mol m^{-3}) is the bulk concentration of species j in half-cell h, s_j^h is the stoichiometric coefficient for the faradaic reaction (**Table III-1**), F (96,485 C mol^{-1}) is the Faraday constant, and $\sum R_j^h$ (mol m^{-3} s^{-1}) represents the sum of the source / sink terms for species j, which comprise the chemical decomposition reactions and crossover taking place in each half-cell. Stoichiometric coefficients for the charged species, A^+ and B, are excluded from the opposing half-cells, as the electrochemical potentials in those environments preclude their formation, meaning $C_{A^+}^{\infty,-} = 0$ and $C_B^{\infty,+} = 0$ at all times.

All of the mass balance equations are subject to an initial condition given by **Equation (III.4)**

.

$$C_j^{\infty,h}(t=0) = C_j^{o,h} \tag{III.4}$$

$C_j^{o,h}$ (mol m^{-3}) is the initial concentration of species j at the beginning of the half-cycle. For example, the initial concentration at the beginning of the discharge step will equal the final concentration at the end of the charge step.

Table III-1. Electrochemical reaction stoichiometric coefficients in each half-cell.

	Positive half-cell	Negative half-cell
s_A^h	–1	0
$s_{A^+}^h$	1	---
s_B^h	---	1
$s_{B^+}^h$	0	–1

2.2. Homogeneous active species decay

Homogeneous decay processes associated with unstable redox active materials lead to capacity fade and reduced energy efficiencies.[23] Following the approach of Silcox *et al.*, we contemplate two mechanisms for decay—self-discharge and irreversible degradation.[44] Homogeneous self-discharge (**Equations (III.5)** and **(III.6)**) is assumed to proceed by the charged active species (A^+ or B) reacting with the supporting electrolyte (supporting salt + solvent), contaminants, or wetted cell components and reverting to their discharged state.

$$A^+ \xrightarrow{f_{A^+}k_{d,A^+}} A \tag{III.5}$$

$$B \xrightarrow{f_B k_{d,B}} B^+ \tag{III.6}$$

Here, k_{d,A^+} and $k_{d,B}$ (s^{-1}) are the overall decay rate constants of A^+ and B, respectively. f_{A^+} and f_B (dimensionless) are the respective fractions of A^+ and B that decay via self-discharge. Note that while self-discharge is nominally a redox reaction, the electron is assumed to be irrecoverable. Irreversible degradation (**Equations (III.7)** and **(III.8)**) occurs when the charged active species (A^+ or B) decomposes to form any number of non-redox-active products, generally denoted as D.

$$A^{+} \xrightarrow{\left(1-f_{A^{+}}\right)k_{d,A^{+}}} D \tag{III.7}$$

$$B \xrightarrow{\left(1-f_{B}\right)k_{d,B}} D \tag{III.8}$$

Here, we assume that the decay products are benign and thus do not interfere with subsequent cell operation. Additionally, while there are certainly more complex decay mechanisms (e.g., dimerization,[117–119] protonation / deprotonation reactions,[24,120] formation of new electroactive products[121]) that may be considered for specific chemistries, we assume first-order homogeneous kinetics as this simplifies subsequent mathematical treatments and has precedence in earlier studies.[44]

2.3. Membrane crossover

The species transport model chosen for membrane crossover follows the work of Darling *et al.* who derived steady-state fluxes, accounting for diffusion, migration, and electro-osmotic convection terms.[48] The active species flux through the membrane, N_j, subject to Dirichlet boundary conditions on either side of the membrane, is shown in **Equations (III.9)** and **(III.10)**. Here, the flux is defined as positive for transport from the negative electrolyte to the positive electrolyte.

$$N_j = \frac{D_j^m K_j}{l_m} \gamma_j \left(\frac{C_j^{\infty,-} \exp(\gamma_j) - C_j^{\infty,+}}{\exp(\gamma_j) - 1} \right) \tag{III.9}$$

$$\gamma_j = -\left(\frac{z_j F}{\sigma_m RT} + \frac{\xi}{\nu C_{\text{site}} D_j^m F} \right) \frac{I l_m}{A_m} \tag{III.10}$$

D_j^m ($\mathrm{m^2\ s^{-1}}$) is the diffusion coefficient of species *j* through the membrane, K_j (dimensionless) is the membrane sorption coefficient of species *j*, l_m (m) is the membrane thickness, γ_j is a dimensionless flux parameter for species j, σ_m (S m^{-1}) is the membrane conductivity, R (8.314 J mol^{-1} K^{-1}) is the universal gas constant, T (K) is the absolute temperature, and A_m (m^2) is the geometric membrane area which is equivalent to the geometric area of the electrochemical cell. For an ion-exchange membrane, ξ (dimensionless) is the electro-osmotic coefficient, ν (dimensionless) is the molar ratio of solvent to fixed ion sites in the membrane, and C_{site} (mol m^{-3}) is the concentration of fixed ion sites in the membrane.

Because the flux is linear with respect to the bulk species concentrations, **Equation (III.9)** can be conveniently expressed in terms of first-order "crossover rate constants", $k_{c,j}^{-}$ and $k_{c,j}^{+}$ (s^{-1}), according to **Equation (III.11)**.

$$\frac{N_j A_m}{V^+} = k_{c,j}^{-} C_j^{\infty,-} - k_{c,j}^{+} C_j^{\infty,+} \tag{III.11}$$

To integrate membrane fluxes into the species mass balances, crossover-induced self-discharge reactions (**Equation (III.12)**) are assumed to occur instantaneously, consuming charged species at both membrane-electrolyte interfaces.[48]

$$A^+ + B \rightarrow A + B^+ \tag{III.12}$$

As a result, the concentration of charged species (A^+ and B) will always remain at zero in the opposite electrolyte. Finally, both crossover and species decay can be expressed as source terms, as shown in

Table *III-2*. Note that for symmetric chemistries, where the same parent compound is used on both sides of the battery but at different oxidation states (e.g., V^{2+}/V^{3+} and V^{4+}/V^{5+} on the negative and positive sides of the vanadium RFB, respectively), the comproportionation reactions differ from **Equation (III.12)**, as species undergo additional changes in oxidation state upon crossover, altering the form of the source terms.[66]

***Table III-2**. Active species source terms, including both species decay and crossover.*

	Positive half- cell	Negative half-cell
$\sum R_A^h$	$f_A k_{d,A^+} C_{A^+}^{\infty,+} + k_{c,A}^- C_A^{\infty,-} - k_{c,A}^+ C_A^{\infty,+} + k_{c,B}^- C_B^{\infty,-}$	$\left(-k_{c,A}^- C_A^{\infty,-} + k_{c,A}^+ C_A^{\infty,+} + k_{c,A^+}^+ C_{A^+}^{\infty,+}\right)\frac{V^+}{V^-}$
$\sum R_{A^+}^h$	$-k_{d,A^+} C_{A^+}^{\infty,+} - k_{c,A^+}^+ C_{A^+}^{\infty,+} - k_{c,B}^- C_B^{\infty,-}$	---
$\sum R_{B^+}^h$	$k_{c,B^+}^- C_{B^+}^{\infty,-} - k_{c,B^+}^+ C_{B^+}^{\infty,+} + k_{c,B}^- C_B^{\infty,-}$	$f_B k_{d,B} C_B^{\infty,-} + \left(-k_{c,B^+}^- C_{B^+}^{\infty,-} + k_{c,B^+}^+ C_{B^+}^{\infty,+} + k_{c,A^+}^+ C_{A^+}^{\infty,+}\right)\frac{V^+}{V^-}$
$\sum R_B^h$	---	$-k_{d,B} C_B^{\infty,-} + \left(-k_{c,B}^- C_B^{\infty,-} - k_{c,A^+}^+ C_{A^+}^{\infty,+}\right)\frac{V^+}{V^-}$

2.4. Mass balance analytical solutions

The introduction of species decay and crossover results in a coupled system of time-dependent differential equations, which can be solved analytically for galvanostatic cycling.[122] Because each of the source terms are first order, the mass balances can be expressed as a vector differential equation (**Equations (III.13)**) with initial conditions given by **Equation (III.14)**.

$$\frac{d}{dt}\mathbf{C} = \mathbf{b} - \mathbf{K}\mathbf{C} \tag{III.13}$$

$$\mathbf{C}(t=0) = \mathbf{C}^{\mathbf{o}} \tag{III.14}$$

C (mol m^{-3}) is a column vector containing the 6 bulk species concentrations of interest ($C_A^{\infty,+}$, $C_{A^+}^{\infty,+}$, $C_{B^+}^{\infty,+}$, $C_{B^+}^{\infty,-}$, $C_B^{\infty,-}$, $C_A^{\infty,-}$), **b** (mol m^{-3} s^{-1}) is a column vector containing constant reaction terms, **K** (mol m^{-3} s^{-1}) is a matrix containing the first-order rate constants, and $\mathbf{C}^{\mathbf{o}}$ (mol m^{-3}) is a column vector containing the initial concentrations. The general solution to this differential equation is shown in **Equation (III.15)**.

$$\mathbf{KC} = \mathbf{b} - \exp\left(-\mathbf{K}t\right)\left(\mathbf{b} - \mathbf{KC}^{\mathbf{o}}\right) \tag{III.15}$$

Because **K** is a positive semi-definite matrix,[122] the solution can be written in terms of the eigenvalues and eigenvectors of **K** according to **Equation (III.16)**.

$$\mathbf{\Lambda U}^{-1}\mathbf{C} = \mathbf{U}^{-1}\mathbf{b} - \exp\left(-\mathbf{\Lambda}t\right)\left(\mathbf{U}^{-1}\mathbf{b} - \mathbf{\Lambda U}^{-1}\mathbf{C}^{\mathbf{o}}\right) \tag{III.16}$$

U (dimensionless) and **Λ** (s^{-1}) are the eigenvector and diagonal eigenvalue matrices of **K**, respectively. Performing a coordinate transform ($\boldsymbol{\theta} = \mathbf{U}^{-1}\mathbf{C}$, $\boldsymbol{\theta}^{\mathbf{o}} = \mathbf{U}^{-1}\mathbf{C}^{\mathbf{o}}$, and $\boldsymbol{\beta} = \mathbf{U}^{-1}\mathbf{b}$) results in a system of linear equations for $\boldsymbol{\theta}$, as shown by **Equation (III.17)**, which can be expressed in terms of its individual elements according to **Equation (III.18)**.

$$\boldsymbol{\theta} = \mathbf{\Lambda}^{-1}\boldsymbol{\beta} - \mathbf{\Lambda}^{-1}\exp\left(-\mathbf{\Lambda}t\right)\left(\boldsymbol{\beta} - \mathbf{\Lambda}\boldsymbol{\theta}^{\mathbf{o}}\right) \tag{III.17}$$

$$\theta_i = \frac{\beta_i}{\lambda_i} - \left(\frac{\beta_i}{\lambda_i} - \theta_i^o\right)\exp(-\lambda_i t) \tag{III.18}$$

θ_i (mol m^{-3}), θ_i^o (mol m^{-3}), β_i (mol m^{-3} s^{-1}), and λ_i (s^{-1}) are the i^th^ element of **θ**, **θ^o^**, **β**, and **Λ**, respectively. Finally, the concentration vector may be obtained by transforming the resulting solution (**Equation (III.19)**).

$$\mathbf{C} = \mathbf{U}\boldsymbol{\theta} \tag{III.19}$$

2.5. Electrochemical thermodynamics and cell voltage

If the kinetics of the redox processes are sufficiently facile, then the electrode reactions can be assumed to occur instantaneously; thus, the electrode surfaces are always at equilibrium and the two electrode potentials can be described by the Nernst Equation (**Equations (III.20)** and **(III.21)**). Here, we assume ideal solution conditions such that concentrations may be used in place of activities.

$$\Phi_1^+ = E^{o,+} - \frac{RT}{F}\ln\left(\frac{C_A^s}{C_{A^+}^s}\right) \tag{III.20}$$

$$\Phi_1^- = E^{o,-} - \frac{RT}{F}\ln\left(\frac{C_B^s}{C_{B^+}^s}\right) \tag{III.21}$$

Φ_1^+ and Φ_1^- (V) are the electrode potentials for the positive and negative electrodes, respectively; $E^{o,+}$ and $E^{o,-}$ (V) are the formal redox potentials for the positive and negative redox reactions (**Equations (III.1)** and **(III.2)**, respectively); and C_j^s (mol m^{-3}) is the surface concentration of species *j*.

Assuming there is sufficient electrolyte flow, the species fluxes can be described by convective mass transport and related to the total current according to **Equation (III.22)**.

$$\frac{I}{FA_{ed}} = -s_j^h k_{m,j}\left(C_j^{\infty,h} - C_j^s\right) \tag{III.22}$$

A_{ed} (m^2) is the accessible interfacial surface area of the electrode and $k_{m,j}$ (m s^{-1}) is the convective mass transfer coefficient. In turn, this expression can be rearranged to describe the surface concentrations in terms of the bulk concentration using **Equation (III.23)**.

$$C_j^s = C_j^{\infty,h} + \frac{I}{FA_{ed}s_j^h k_{m,j}} \tag{III.23}$$

The mass transfer coefficients are generally treated as empirical values, which can either be determined experimentally or predicted from the operating parameters, electrolyte and electrode properties, and flow characteristics using dimensionless correlations. While there are a number of correlations that could be invoked,[123,124] we adopt a model described by Barton *et al.* and developed for an interdigitated flow field (**Equation (III.24)**) due to its consistency with our simulation conditions (*vide infra*).[125]

$$k_{m,j} = 0.018\left(\frac{Q}{n_{ch}l_{ch}l_e\varepsilon}\right)^{0.68}\left(\frac{\rho}{\mu}\right)^{0.18}\left(D_j^{\infty}\right)^{0.5}\left(d_f\right)^{-0.32} \tag{III.24}$$

Q ($\mathrm{m^3\ s^{-1}}$) is the volumetric flow rate, n_{ch} is the number of flow channels, l_{ch} (m) is the length of each flow channel, l_e (m) is the electrode thickness, ε (dimensionless) is the electrode porosity, ρ ($\mathrm{kg\ m^{-3}}$) is the electrolyte density, μ (Pa s) is the electrolyte viscosity, D_j^{∞} ($\mathrm{m^2\ s^{-1}}$) is the bulk diffusion coefficient of species j, and d_f (m) is the electrode fiber diameter.

Electrical resistances (e.g., contact resistance, wiring, electrodes) and ionic resistances (e.g., electrolyte conductivity, membrane conductivity) result in ohmic losses, as greater driving forces (voltages) are needed to pass charge through the electrochemical cell at a given rate (current). In many advanced flow cells, the membrane resistance, R_m (Ω), is the dominant contributor to ohmic losses, while additional contact resistances, R_c (Ω), tend to be minor.[47] The membrane resistance is related to the membrane conductivity according to **Equation (III.25)**.

$$R_m = \frac{l_m}{A_m\sigma_m} \tag{III.25}$$

Assuming the various ionic and electronic resistances are constant and obey Ohm's Law, the full cell voltage, E_{cell} (V) can be described using **Equation (III.26)**.

$$E_{\mathrm{cell}} = E^{o,+} - E^{o,-} + I\left(R_m + R_c\right) - \frac{RT}{F}\ln\left(\frac{\left(C_A^s\right)\left(C_{B^+}^s\right)}{\left(C_{A^+}^s\right)\left(C_B^s\right)}\right) \tag{III.26}$$

While not considered here, some aqueous systems exhibit pH differences across the membrane, giving rise to Donnan potentials that may also alter the cell voltage.[86]

2.6. Cycling performance metrics

The metrics typically used to describe durational cell cycling performance are the charge and discharge capacities as well as the cycling efficiencies (i.e., coulombic efficiency, voltaic efficiency, energy efficiency).[25] The capacity refers to the total amount of charge stored or released (**Equations (III.27)** and **(III.28)**).

$$Cap_c = \int_0^{t_c} I dt \tag{III.27}$$

$$Cap_d = -\int_0^{t_d} I dt \tag{III.28}$$

Here, Cap_c and Cap_d (C) are the charge and discharge capacities, respectively, and t_c and t_d (s) are the total charge and discharge times, respectively. Note that the negative sign in **Equation (III.28)** accounts for the change in direction of the current. The charge and discharge times are usually determined by a voltage cutoff for galvanostatic operation, which is based on either the point when the limiting current is approached (i.e., the cell voltage grows exponentially) or the point when a pre-determined cell voltage is reached (e.g., to prevent unfavorable side reactions). For the limiting current case, which is used throughout this work, t_c and t_d can be calculated as the minimum time for one of the reacting species surface concentrations to approach zero. For a pre-determined cell voltage, t_c and t_d can be determined by solving **Equation (III.26)** as discussed in **Section S2**.

The cycling efficiencies, defined here in their fractional forms, can be derived from the capacities and the cell voltage. The coulombic efficiency, CE, is the ratio between the discharge capacity and the charge capacity according to **Equation (III.29)**.

$$CE = \frac{Cap_d}{Cap_c} \tag{III.29}$$

The voltaic efficiency, VE, is defined as the ratio of the average discharge voltage to the average charge voltage according to **Equation (III.30)**.

$$VE = \frac{\overline{E}_d}{\overline{E}_c} = \frac{\frac{1}{t_d}\int_0^{t_d} E_{\text{cell}}\,dt}{\frac{1}{t_c}\int_0^{t_c} E_{\text{cell}}\,dt} \tag{III.30}$$

$\overline{E}_c$ and $\overline{E}_d$ (V) are the average charge and discharge voltages, respectively. Lastly, the energy efficiency, *EE*, is the multiplicative product of the voltaic and coulombic efficiencies according to **Equation (III.31)**.

$$EE = CE \times VE \tag{III.31}$$

2.7. Cycling performance metrics

All simulations were performed using MATLAB® R2021b on a Dell Latitude 7290 laptop computer with an Intel® Core™ i7-8650U processor (quad-core, 1.90 GHz) and a random-access memory of 16 GB. Eigenvalues and eigenvectors were calculated using the *eig* function, nonlinear algebraic equations were solved implicitly using the *fsolve* function, and numerical integration was performed using the *cumtrapz* function. To apply these models with relevant input parameters, all simulations are performed for a small-scale flow cell architecture with constant properties shown in **Table III-3**. We use this configuration because it is common in our laboratory and has been adopted by several others in the research community.[126–128] Thus, these conditions are representative of many studies in contemporary RFB literature, as experimental demonstrations exist for a wide range of materials, providing reliable engineering specifications and component properties. The device described here is a 2.55 cm^2 flow cell featuring porous carbon electrodes and interdigitated flow fields. To maintain consistency across results shown here, we use 10 mL of electrolyte with an initial active species concentration of 500 mM in both half-cells. Finally, we assume intermediate values for the fluid dynamic properties of each electrolyte. Note that the parameters chosen here are based on our own published data and common properties observed in the literature and therefore do not represent the breadth of the design space; however, the model may be easily adapted for other cell geometries, material sets, and electrolytes by adjusting the inputs to **Table III-3**. The current densities explored in this work (0 – 300 mA cm^{-2}) reflect a range of relatively low to moderately high charge / discharge rates used in experimental systems. Because we elect to start cycling with only the discharged species present (**Table III-3**), the current is initially positive during the first half-cycle (charging). The open-circuit voltages (OCV = $E^{o,+} - E^{o,-}$) used here span a range of possible RFB chemistries; voltages ca. 1 V are characteristic of aqueous cells whereas voltages ca. 2 – 3 V are characteristic of nonaqueous cells. For each cycle, the charge and discharge times are determined using the limiting current case; the concentrations and cell voltages are then calculated for 2000 evenly spaced time steps during each half-cycle. Considering that the cell voltage becomes infinite at $t = t_c$ and $t = t_d$, we replace the infinite voltage with an arbitrary, finite value that is well above or below the OCV (≥ 500 mV). Simulating each full cycle (charge and discharge) took ca. 0.05 s on the aforementioned computational resources.

Table III-3. *Constant properties for simulations performed in this study.*

Property[a]	Value	Reference
A_m	$0.000255\ \mathrm{m}^2$	102
n_{ch}	7	125
l_{ch}	0.016 m	125
l_e	0.00034 m	129
A_{ed}	$0.184\ \mathrm{m}^2$	129
ε	0.75	125,130
d_f	7×10^{-6} m	130
V^+, V^-	$1 \times 10^{-5}\ \mathrm{m}^3$	102
$C_A^{o,+}$, $C_{B^+}^{o,-}$	$500\ \mathrm{mol\ m}^{-3}$	---
$C_{A^+}^{o,+}$, $C_B^{o,-}$	$0\ \mathrm{mol\ m}^{-3}$	---
ρ	$1000\ \mathrm{kg\ m}^{-3}$	---
μ	1 Pa s	---
T	298 K	---

[a] Initial bulk concentrations are the concentrations at the beginning of the first half-cycle

3. *Evaluating performance upper bounds*

We begin by contemplating conditions where performance decay is negligible, which allows for the identification of upper bounds in accessible capacity and *EE*. Such bounding analyses enable simple correlations between electrochemical properties and performance metrics, which have practical utility for assessing design tradeoffs. For the idealized case where all species do not decay and do not crossover, $\sum R_j = 0$, and changes in concentration are driven entirely by the passage of current. As a result, following the first charging cycle, the capacity and *VE* do not vary from cycle to cycle and *CE* = 1. Here, we derive explicit analytical expressions for cycling performance metrics and demonstrate their value by connecting these outputs to more fundamental cell properties (e.g., cell resistance, mass transport rates, species redox potentials) and operating conditions.

For galvanostatic cycling, the current is constant, allowing the mass balances to be solved by integrating **Equation (III.3)** to yield **Equation (III.32)**.

$$C_j^{\infty} = C_j^{o} + \frac{s_j I}{V^h F} t \qquad \text{(III.32)}$$

Using the time-dependent concentration profiles, cell performance metrics can be expressed as shown in Table III-4. These explicit analytical equations provide a simplified means to explore how specific design factors contribute to performance. For example, they can be used to assess how a particular electrolyte composition and cell format will perform in the ideal case, establishing a baseline expectation for performance under a specified set of cycling conditions. As an illustrative example, the representative cycling behavior of a redox flow cell subjected to different current densities is shown in **Figure III-2a**. Here, increasing current density has the benefit of yielding greater power density and more rapid cycles, but at the expense of higher overpotentials and thus lower *VE*. Further quantifying these losses, **Figure III-2b** presents the resultant *VE* as a function of the applied current density and area-specific ohmic resistance ($\mathrm{ASR}_\Omega = A_m\,(R_c + R_m)$) for varying values of the OCV. Consistent with Figure III-2a, increasing current density imposes larger ohmic and mass transport losses, lowering the *VE*; here, ohmic losses are proportional to both the ASR_Ω and current density, resulting in a strong dependence on both parameters. Importantly, the *VE* increases significantly with higher OCV, suggesting that higher voltage redox chemistries, such as those enabled by nonaqueous electrolytes, can tolerate greater ASR_Ω while maintaining reasonable cycling efficiencies.

***Table III-4**. Performance metrics for galvanostatic cell cycling in the absence of molecular decay or species crossover.*

Performance metric	Analytical expression	
Charge capacity	$Cap_c = It_c$	(III.33)
Discharge capacity	$Cap_d = -It_d$	(III.34)
Coulombic efficiency[a]	$CE = 1$	(III.35)
Voltaic efficiency[b]	$VE = \dfrac{\overline{E}_d}{\overline{E}_c}$	(III.36)
Charge time[c]	$t_c = \min\left\{\dfrac{V^+F}{I}\left(C_A^o - \dfrac{I}{FA_{ed}k_{m,A}}\right), \dfrac{V^-F}{I}\left(C_{B^+}^o - \dfrac{I}{FA_{ed}k_{m,B^+}}\right)\right\}$	(III.37)
Discharge time[c]	$t_d = \min\left\{-\dfrac{V^+F}{I}\left(C_{A^+}^o + \dfrac{I}{FA_{ed}k_{m,A^+}}\right), -\dfrac{V^-F}{I}\left(C_B^o + \dfrac{I}{FA_{ed}k_{m,B}}\right)\right\}$	(III.38)

[a] After the initial cycle

[b] Analytical expressions for the average voltages are provided in **Section S3**

[c] Assumes the voltage cutoff is based on the limiting current condition

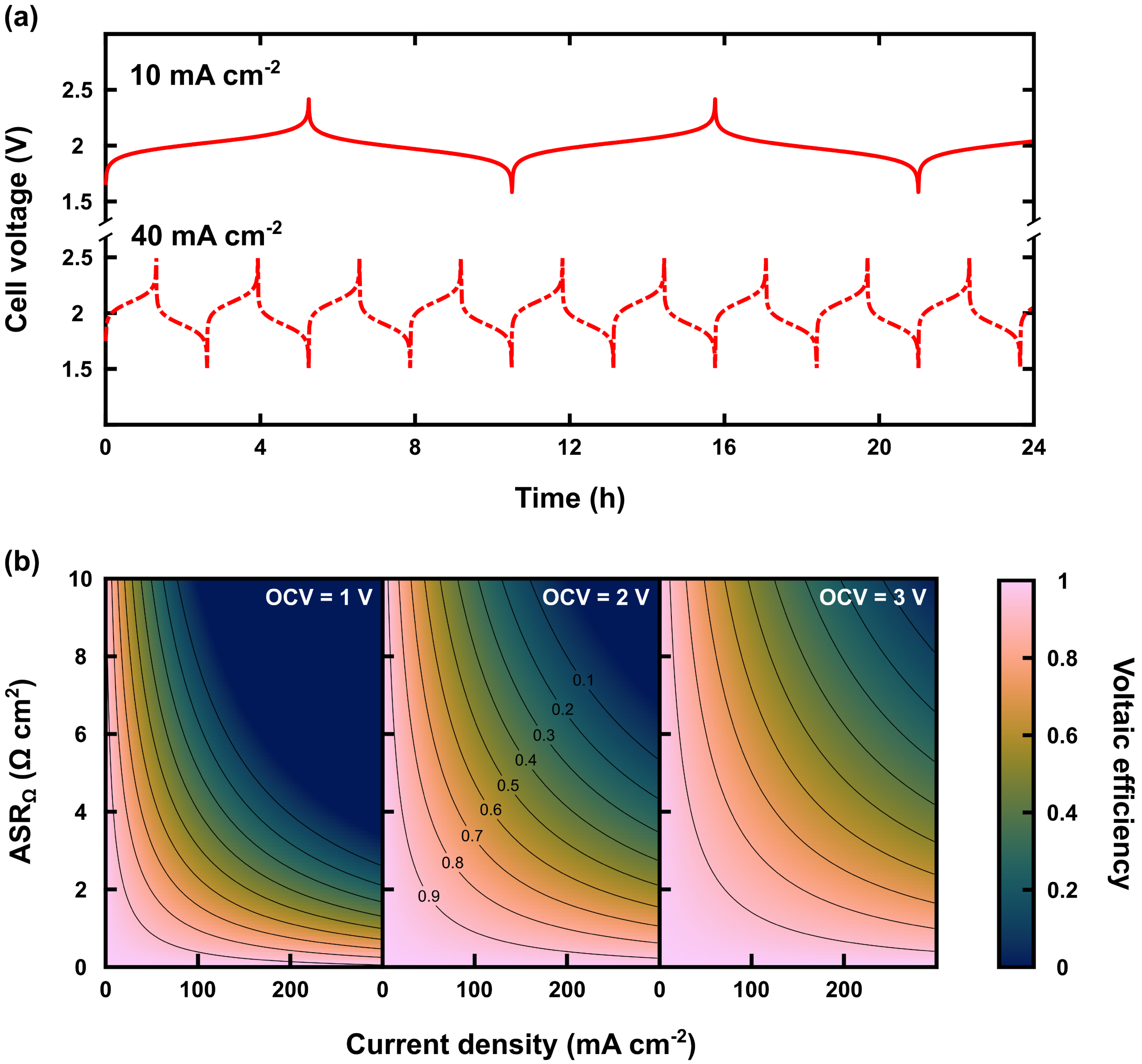

Figure III-2. *(a) Representative charge / discharge profiles for cycling in the absence of parasitic losses. (b) Voltaic efficiency (*VE*) as a function of the applied current density and cell area-specific ohmic resistance (ASR$_\Omega$) for electrolytes with varying open-circuit voltage (OCV). Black lines represent constant* VE *ranging between 0.1 – 0.9 in increments of 0.1. For all simulations,* Q *= 10 mL min^{-1} for both electrolytes and $D_j^\infty = 1 \times 10^{-9}$ m^2 s^{-1} for all species.*

These governing equations also enable the evaluation of more subtle connections between molecular properties and cell performance that can be difficult to disentangle from experiments. Such knowledge is useful in experimental design when considering suitable operating envelopes and in data interpretation when elucidating possible performance limitations. As a representative example, **Figure III-3** shows the combined effects of redox species diffusion coefficients on the accessible capacity for common ranges of current densities and flow rates used in experimental cells. Higher diffusion coefficients ($D_j^\infty = 10^{-10} - 10^{-9}$ m^2 s^{-1}) are typical of smaller redox species (e.g., inorganic ions, organic molecules, metal coordination complexes) whereas lower values ($D_j^\infty = 10^{-12} - 10^{-11}$ m^2 s^{-1}) are representative of larger macromolecular redox species (e.g., polymers,[131] colloids[132]). As expected, lower species mass transport rates reduce accessible capacity, setting effective upper bounds on useable current densities. For exceedingly slow mass transport, the applied current can exceed the limiting current, yielding zero accessible capacity. While high transport rates are desirable, enhancements in species diffusivity may have diminishing returns under conditions where the theoretical capacity is attainable through either decreasing the current density or increasing the volumetric flow rate. However, improvements in capacity utilization and cycling efficiencies must also be balanced with pumping losses, which scale with the pressure drop and volumetric flow rate. Relationships such as those explored in **Figure III-3** are relevant for balancing molecular engineering tradeoffs; the addition of substituent groups to redox molecules can shift redox potential, improve solubility / stability, and suppress crossover, albeit at the risk of reducing accessible capacity due to increasing molecular weight (lower diffusivity).[133]

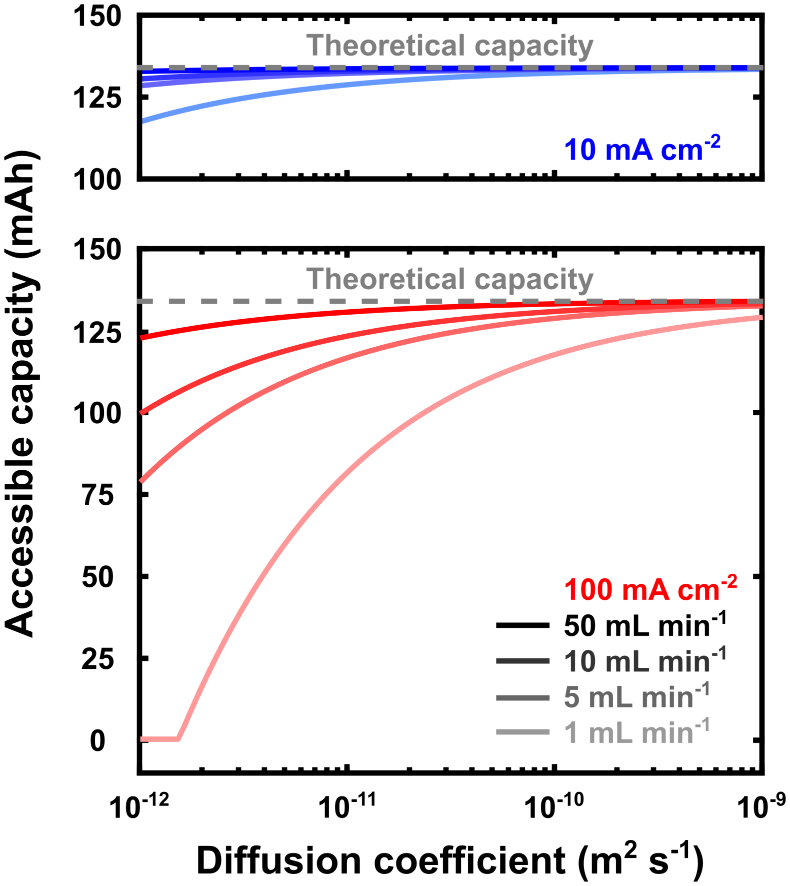

Figure III-3. *Accessible capacity as a function of the redox species diffusion coefficient for varying volumetric flow rates and current densities. The diffusion coefficients (* D_j^∞ *) are identical for all species.*

4. *Homogeneous active species decay*

Next, we consider the influence of species decomposition and self-discharge that hamper the development of high-voltage chemistries,[19,44,134] as increasingly positive / negative redox potentials are reflective of more reactive charged states. Consequently, improving species stability is of significant interest, and the identification and mitigation of decay processes is key to advancing new chemistries based on engineered organic molecules and metal-centered coordination complexes.[23] Modeling cell performance in the absence of additional parasitic processes (e.g., crossover) has practical value for experimental stability studies (e.g., bulk electrolysis, symmetric cell cycling) and for understanding the extent to which species decay may impact full cell performance. For example, time-dependent decay rates determined through *ex situ* methods can be combined with cycling models to predict performance prior to extensive cell testing. Conversely, cell cycling data may be paired with such models to estimate quantitative measures of decay kinetics.[44]

For galvanostatic cycling, the mass balances are decoupled such that simple, explicit expressions may be written for the bulk concentrations. Analytical solutions for the charged species are shown in **Equations (III.39)** and **(III.40)**.

$$C_{A^+}^{\infty} = \frac{I}{V^h F k_{d,A^+}} + \left(C_{A^+}^{o} - \frac{I}{V^h F k_{d,A^+}} \right) \exp\left(-k_{d,A^+} t\right) \tag{III.39}$$

$$C_{B}^{\infty} = \frac{I}{V^h F k_{d,B}} + \left(C_{B}^{o} - \frac{I}{V^h F k_{d,B}} \right) \exp\left(-k_{d,B} t\right) \tag{III.40}$$

These can then be substituted into mass balances for the discharged species to give **Equations (III.41)** and **(III.42)**.

$$C_A^\infty = C_A^o - \frac{I}{V^h F}\left(1 - f_{A^+}\right)t + f_{A^+}\left(C_{A^+}^o - \frac{I}{V^h F k_{d,A^+}}\right)\left(1 - \exp\left(-k_{d,A^+}t\right)\right) \qquad \text{(III.41)}$$

$$C_{B^+}^\infty = C_{B^+}^o - \frac{I}{V^h F}\left(1 - f_B\right)t + f_B\left(C_B^o - \frac{I}{V^h F k_{d,B}}\right)\left(1 - \exp\left(-k_{d,B}t\right)\right) \qquad \text{(III.42)}$$

Finally, the combined expressions for the bulk concentrations can be used with **Equations (III.23)** and **(III.26)** to compute the cell voltage and other cycling metrics. Because the surface concentrations are nonlinear with time, the charge and discharge times must be calculated by solving nonlinear algebraic equations for each half-cycle using either the limiting current condition or a voltage cutoff condition. Similarly, the *VE* (**Equation (III.30)**) requires numerical integration of the cell voltage.

To demonstrate the utility of the analytically-derived mass balances, we explore their use for describing cycling in symmetric cell architectures (i.e., the same redox species is present in both half-cells). Because these cells contain a single redox couple, the crossover fluxes are equal and opposite during charge and discharge, making the capacity fade primarily dependent on homogeneous decay.[135,136] To capture this behavior, we restrict the mass balances to a single half-cell (**Equations (III.39)** and **(III.41)**), which reflects the capacity-limiting side of the symmetric cell. **Figure III-4** shows predicted capacity fade for a range of decay rate constants, where the higher rate constants ($k_{d,A^+} > 10^{-7}$ s^{-1}) reflect relatively unstable active species and the lower rate constants represent more advanced chemistries. For context, state-of-the-art aqueous organic RFB redox couples exhibit capacity fade rates ca. 0.01% per day,[23] which correspond to k_{d,A^+} values of ca. 5×10^{-9} s^{-1} under the cycling conditions and assumptions used in this model. Thus, decay kinetics can be quantitatively translated to expected cycling lifetime in relevant experimental systems. While these results may be somewhat intuitive, the ability to predict capacity fade is relevant for experimental design (e.g., determining detection limits, experimental timeframes, and cycling conditions) and cell engineering.

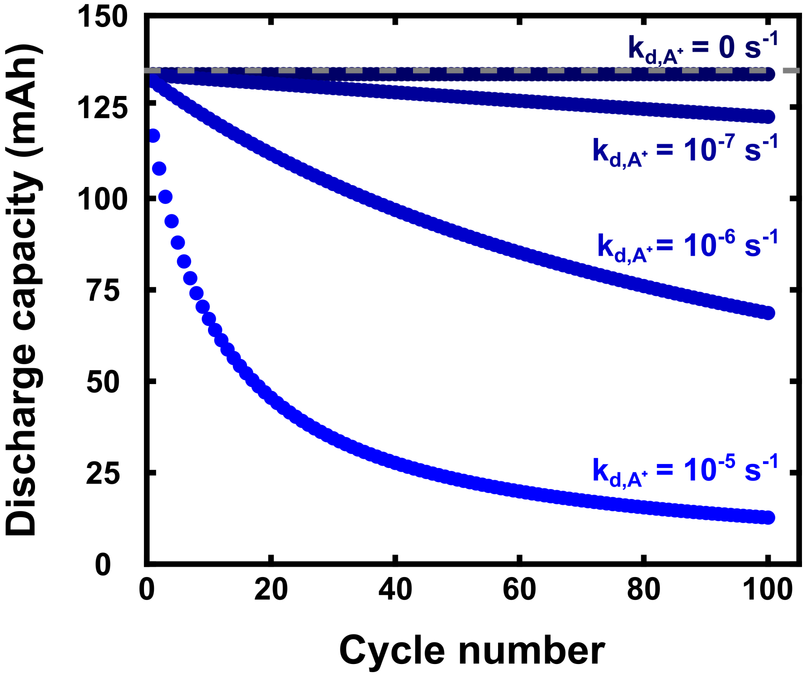

Figure III-4. *Discharge capacity as a function of cycle number for varying species decay rate constants in a symmetric cell. The gray dashed line indicates the theoretical capacity. For all simulations,* $I = 25.5$ *mA (10 mA cm*$^{-2}$*),* $f_{A^+} = 0.5$*,* $Q = 10$ *mL min*$^{-1}$ *for both electrolytes, and* $D_j^{\infty} = 1 \times 10^{-9}\ m^2\ s^{-1}$ *for all species.*

We also investigate the role of experimental cycling conditions on the apparent redox species stability; specifically, the applied current density alters the observed capacity fade when measured against cycle number as shown in **Figure III-5**. Considering homogeneous decay is a time-dependent process, the change in accessed capacity is dependent on the total cycling time (**Figure III-5b**) rather than the number of cycles (**Figure III-5a**). These model observations are consistent with previous experimental studies demonstrating this effect in bulk electrolysis experiments[41] as well as symmetric redox flow cells,[31] thus providing additional validation of such phenomena and further motivating the need for consistent testing and reporting metrics. Potential holds are sometimes included at the end of each galvanostatic step to access the full capacity of the electrolyte, providing a more consistent measure of the species stability such that it is not as strictly dependent on the charging rate.[31] This cycling profile can conceivably be emulated by alternating between equations that describe the galvanostatic process (**Equations (III.39) – (III.42)**) and equations that describe the potentiostatic process.

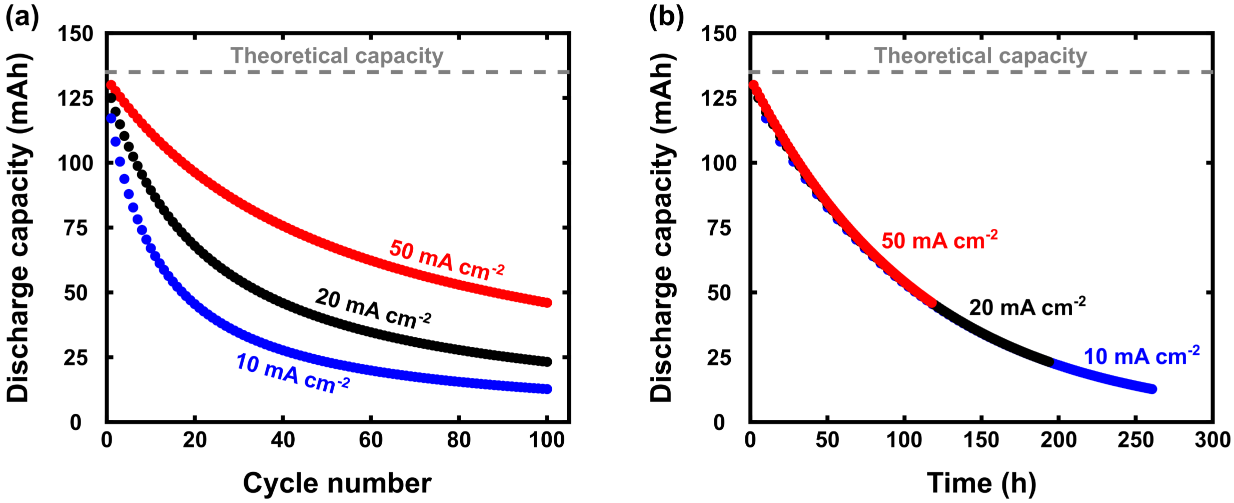

Figure III-5. *Discharge capacity as a function of (a) cycle number and (b) cycling time for varying current densities. For all simulations,* $k_{d,A^+} = 1 \times 10^{-5}\ s^{-1}$, $f_{A^+} = 0.5$, $Q = 10\ mL\ min^{-1}$ *for both electrolytes, and* $D_j^{\infty} = 1 \times 10^{-9}\ m^2\ s^{-1}$ *for all species.*

5. *Species crossover*

We now introduce active species crossover into the modeling framework to assess property tradeoffs for membranes / separators. For this analysis, we assume the charged species are chemically stable ($k_{d,A^+} = k_{d,B} = 0$), leading to a simplified derivation of the mass balances as detailed in **Appendix A**. While the added crossover terms obscure a concise, explicit representation, the resulting analytical expressions still enable rapid computation of the mass balances, allowing for facile performance comparisons across a range of input parameters. Solving for the time-dependent species concentrations requires evaluating the eigendecomposition of the rate constant matrix $\mathbf{K}$ during both charge and discharge, as the sign of the current changes. However, assuming transport properties in the membrane / separator do not change during cycling, these computations only need to be performed once at the outset. Using the eigenvalues and eigenvectors of $\mathbf{K}$, the vector $\boldsymbol{\theta}$ can be determined from **Equation (III.18)** and then transformed into the concentration vector using **Equation (III.19)**. Similar to the case of homogeneous species decay, the charge and discharge times must be determined by solving nonlinear algebraic equations at each half-cycle, either for the limiting current case or for the cutoff voltage case. The *VE*, in turn, can be determined by numerically integrating the resultant cell voltage.

Of particular interest is the comparison of different membrane / separator property combinations that govern crossover fluxes; specifically, tradeoffs between ionic conductivity of and redox species diffusivity through the membrane / separator give rise to variable capacity fade rates, voltage losses, and *EE*.[47] Using this framework, we can establish clear connections between these fundamental transport parameters and cell performance metrics. However, we again note that the purpose of this report is to highlight representative comparisons as opposed to providing a comprehensive sweep of parameter combinations. For simplicity, we neglect the electro-osmotic component of the flux ($\xi = 0$), set individual species diffusion coefficients equal to each other, assume the redox species share ionic charges (i.e., $z_A = z_B = 1$, $z_{A^+} = z_{B^+} = 2$), assume unity absorption ($K_j = 1$), and fix the membrane thickness ($l_m = 100$ µm).

Figure III-6 shows capacity fade and cycling efficiencies for variable diffusion coefficients and membrane conductivities which reflect typical property ranges observed across both aqueous and nonaqueous redox flow cells. As expected, higher diffusion coefficients yield faster crossover rates, resulting in increased capacity fade rates (**Figure III-6a**). The capacity initially decays rapidly before asymptotically approaching a steady value below 50% of the theoretical capacity, as mixing between the electrolytes slows diffusion (*vide infra*). Despite the marked capacity loss, the differing diffusion coefficients weakly impact the *EE*, as the *VE* remains largely unaffected and the *CE* only varies between ca. 95% – 99%.

Interestingly, membrane conductivity has a significant influence on both capacity fade and *EE* (**Figure III-6b**). Increasing conductivity reduces the driving force (i.e., potential drop) for ion migration, thus lowering crossover rates for ionic redox species, diminishing fade rates, and improving *CE*. Further, enhancing membrane conductivity lowers ohmic losses during cell charge and discharge, enhancing *VE*. Overall, this representative comparison suggests that membrane conductivity more strongly drives *EE* under these conditions. However, cycling stability requires the system to be reasonably tolerant to crossover-driven capacity fade, which can typically be achieved by using sufficiently-selective membranes or by generating compositionally-identical electrolytes on either side of the membrane via pre-mixing (i.e., spectator strategy).

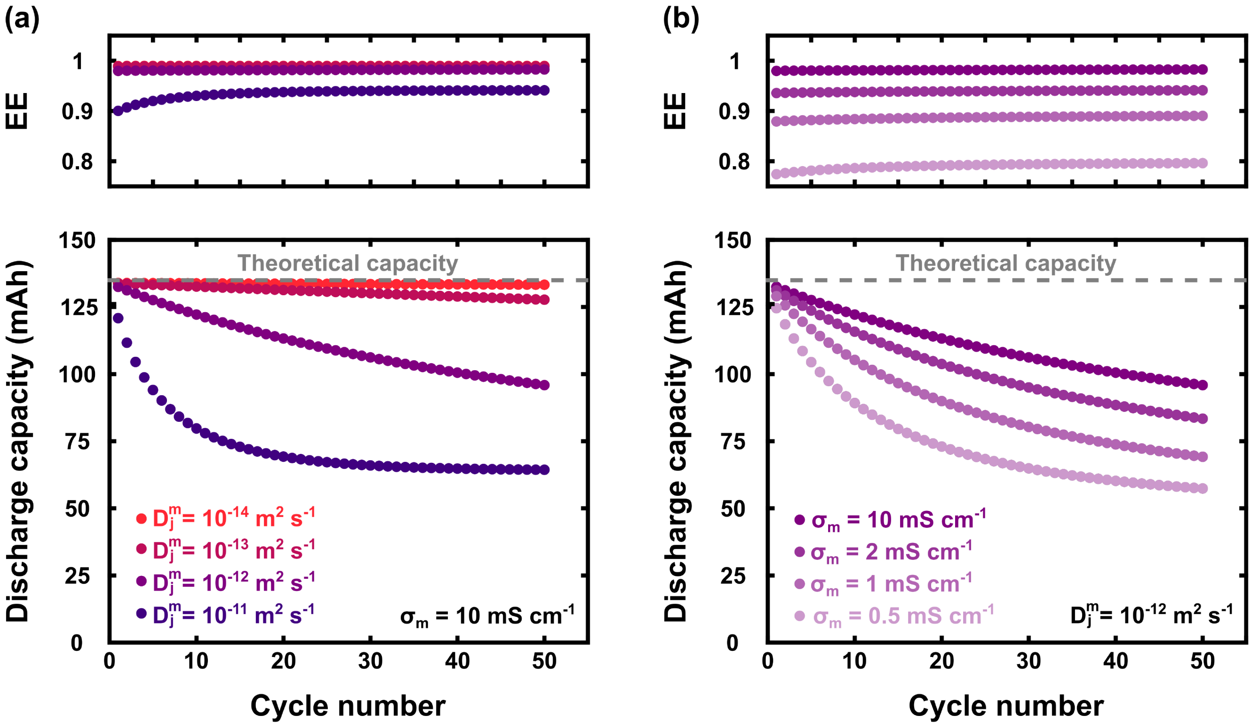

***Figure III-6**. (a) Discharge capacity and energy efficiency (*EE*) as a function of cycle number for varying redox species diffusion coefficients with constant conductivity ($\sigma_m = 10$ mS cm^{-1}). (b) Discharge capacity and* EE *as a function of cycle number for varying membrane conductivities with constant diffusion coefficients for all redox species ($D_j^m = 10^{-12}$ m^2 s^{-1}). For all simulations,* I *= 25.5 mA (10 mA cm^{-2}), OCV = 2 V, $C_A^{o,-} = C_{B^+}^{o,+} = 0$ mol m^{-3} for the first half-cycle,* l$_m$ *= 100 μm,* R$_c$ *= 0 Ω, $z_A = z_B = 1$, $z_{A^+} = z_{B^+} = 2$, $\xi = 0$, and* Q *= 10 mL min^{-1} for both electrolytes. For all species, $D_j^\infty = 1 \times 10^{-9}$ m^2 s^{-1} and* K$_j$ *= 1.*

Pre-mixing the positive and negative electrolytes can reduce diffusional driving forces for species crossover (i.e., pseudo-symmetry), which helps to maintain stable performance across the battery lifetime, albeit at the expense of achievable energy density, as mixing typically limits the solubility of either redox species.[21] Considering that relative differences in species-specific crossover rates can still lead to concentration imbalances, this strategy may not always yield perfect capacity retention over extended cycling. However, capacity can typically be recovered by re-mixing the electrolytes at some predetermined threshold, provided other irreversible decay mechanisms are negligible. Using this framework, we can examine factors that influence crossover-driven capacity fade for pre-mixed cells and predict scenarios where remediation may be required. To this end, **Figure III-7** highlights the influence of membrane conductivity and varying diffusion coefficients on capacity retention. Here, we fix $D_A^m = D_{A^+}^m$ and $D_B^m = D_{B^+}^m$ as a representative example, although we anticipate that deviation from this assumption will impact fade rates, which will further vary depending on other membrane-electrolyte properties (e.g., ionic charge, sorption coefficients) and cell operating conditions (e.g., applied current).

Despite the lower diffusional driving force due to pre-mixing, migration plays a sizeable role in the crossover rates, as the species flux is dependent on the magnitude of the electric field, which is augmented for less conductive membranes.[48] Differences in crossover rates lead to concentration imbalances that manifest as capacity fade; however, as the species concentrations evolve over time, the diffusive and migration fluxes eventually approach a steady state, leading to stable capacities well below the expected theoretical capacity. Similar effects have been reported in earlier experimental cell cycling studies, where more selective (i.e., lower conductivity, lower permeability) membranes displayed higher capacity fade rates.[137,138] Indeed, our model begins to shed further light on the theoretical underpinnings that govern these phenomenological observations, further underscoring the value of this framework for understanding performance characteristics.

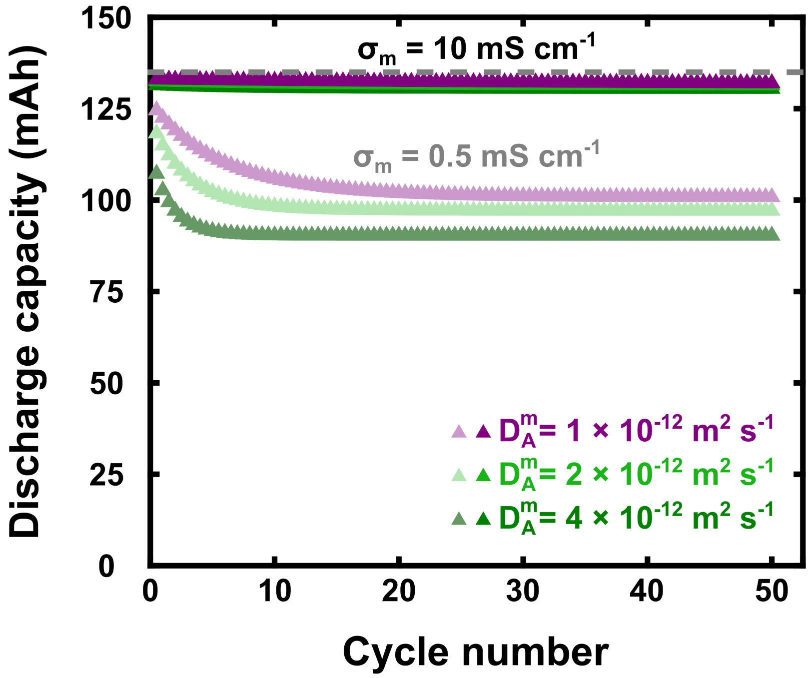

Figure III-7. *Discharge capacity as a function of cycle number for pre-mixed electrolytes with varying redox species diffusion coefficients* ($D_A^m = D_{A^+}^m$) *and varying membrane conductivities. The diffusion coefficients of* B *and* B$^+$ *are also identical and fixed at* $D_B^m = D_{B^+}^m = 10^{-12}$ m^2 s^{-1}. *The gray dashed line indicates the theoretical capacity. For all simulations,* I = 25.5 mA (10 mA cm^{-2}), $C_A^{o,-} = C_{B^+}^{o,+}$ = 500 mol m^{-3} *for the first half-cycle,* l_m = 100 μm, R_c = 0 Ω, $z_A = z_B = 1$, $z_{A^+} = z_{B^+} = 2$, $\xi = 0$, *and* Q = 10 mL min^{-1} *for both electrolytes. For all species,* $D_j^\infty = 1 \times 10^{-9}$ m^2 s^{-1} *and* $K_j = 1$.

6. Treatment of electrochemical kinetics

Thus far, we have contemplated redox couples, electrolyte formulations, and electrode combinations which obviate kinetic losses; however, several contemporary RFB chemistries (e.g., all-vanadium, iron-chromium) exhibit sluggish redox kinetics that contribute measurably to *VE*.[15] While the derivation of analytical solutions to the mass balances for galvanostatic cycling is the primary focus of this work, it is worth considering how predictions for the cell voltage and *VE* may be refined through extensions of this mathematical framework.

Describing increasingly complex kinetic and ohmic losses presents a tradeoff between accurate predictions of the cell voltage and tractable simulation times. However, the need for incorporating these features ultimately depends on the redox couple properties, electrolyte conductivities, as well as electrode microstructures and surface chemistry. For example, sluggish redox reactions may necessitate treatment of electrochemical kinetics whereas thicker electrodes (e.g., carbon felts) and low electrolyte conductivities may require consideration of distributed ohmic losses. To exemplify these differences, we explore models for Butler-Volmer kinetics and one-dimensional (1D) porous electrodes. We describe electrochemical kinetics using the Butler-Volmer equation, shown in **Equations (III.43)** and **(III.44)** using the formal redox potential and the standard rate constant.

$$i_n^+ = Fk_o^+\left(C_A^s\exp\left(\frac{\alpha_a^+F}{RT}\eta^+\right)-C_{A^+}^s\exp\left(\frac{-\alpha_c^+F}{RT}\eta^+\right)\right) \tag{III.43}$$

$$i_n^- = Fk_o^-\left(C_B^s\exp\left(\frac{\alpha_a^-F}{RT}\eta^-\right)-C_{B^+}^s\exp\left(\frac{-\alpha_c^-F}{RT}\eta^-\right)\right) \tag{III.44}$$

i_n^+ and i_n^- (A m^{-2}) are the interfacial current densities in the positive and negative half-cell, respectively; $k^{o,+}$ and $k^{o,-}$ (m s^{-1}) are the standard rate constants for the positive and negative redox couple, respectively; α_a^+ and α_a^- (dimensionless) are the anodic transfer coefficients for the positive and negative redox couple, respectively; α_c^+ and α_c^- (dimensionless) are the cathodic transfer coefficients for the positive and negative redox couple, respectively; η^+ and η^- (V) are the overpotentials in the positive and negative half-cell, respectively. The surface concentrations can be determined from convective mass transport (**Equation (III.23)**) to give a combined expression for the current-voltage relationship.

$$i_n^+ = \frac{Fk_o^+\left(C_A^\infty \exp\left(\frac{\alpha_a^+ F}{RT}\eta^+\right) - C_{A^+}^\infty \exp\left(\frac{-\alpha_c^+ F}{RT}\eta^+\right)\right)}{1+\frac{k_o^+}{k_{m,A}}\exp\left(\frac{\alpha_a^+ F}{RT}\eta^+\right)+\frac{k_o^+}{k_{m,A^+}}\exp\left(-\frac{\alpha_c^+ F}{RT}\eta^+\right)} \tag{III.45}$$

$$i_n^- = \frac{Fk_o^-\left(C_B^\infty \exp\left(\frac{\alpha_a^- F}{RT}\eta^-\right) - C_{B^+}^\infty \exp\left(\frac{-\alpha_c^- F}{RT}\eta^-\right)\right)}{1+\frac{k_o^-}{k_{m,B}}\exp\left(\frac{\alpha_a^- F}{RT}\eta^-\right)+\frac{k_o^-}{k_{m,B^+}}\exp\left(-\frac{\alpha_c^- F}{RT}\eta^-\right)} \tag{III.46}$$

The interfacial current densities are related to the overall current according to **Equation (III.47)**.

$$I = A_{ed} i_n^+ = -A_{ed} i_n^- \tag{III.47}$$

Under galvanostatic cycling conditions, the solutions to the mass balances are not influenced by the kinetics and thus determination of the cell voltage (**Equation (III.48)**) only requires solving two non-linear algebraic equations at each time point.

$$E_{\text{cell}} = E^{o,+} - E^{o,-} + I\left(R_m + R_c\right) + \eta^+ - \eta^- \tag{III.48}$$

Note that the kinetics of parasitic side reactions (e.g., solvent decomposition) cannot be treated explicitly within the given modeling framework, as nonlinearities in the mass balances would stifle analytical solutions. However, such processes could potentially be introduced by defining a generalized Faradaic efficiency.[139]

Additional losses associated with non-uniform reaction distributions through the electrode can also be treated by introducing porous electrode theory to describe overpotentials across the electrode-electrolyte interface. The overpotential can be expressed according to Milshtein et al. (**Equations (III.49) – (III.51)**) using the above kinetic expressions and assuming that the species concentrations are uniform throughout the electrode domain and that the electrode conductivity is significantly greater than the electrolyte conductivity.[103]

$$\frac{d^2\eta^h}{dx^2} = \frac{A_{ed}}{A_m l_e \kappa_{eff}} i_n^h(\eta^h) \tag{III.49}$$

$$\left.\frac{d\eta^+}{dx}\right|_{x=l_e} = \left.\frac{d\eta^-}{dx}\right|_{x=l_e} = 0 \tag{III.50}$$

$$-\left.\frac{d\eta^+}{dx}\right|_{x=0} = \left.\frac{d\eta^-}{dx}\right|_{x=0} = \frac{I}{A_m \kappa_{eff}} \tag{III.51}$$

Here, x (m) is the position in the electrode, where $x = 0$ corresponds to the membrane-electrolyte interface and $x = l_e$ corresponds to the electrode-current-collector interface, and κ_{eff} (S m^{-1}) is the effective electrolyte conductivity in the porous media. The cell voltage, in turn, can be determined according to **Equation (III.52)**.

$$E_{\text{cell}} = E^{o,+} - E^{o,-} + I\left(R_m + R_c\right) + \eta^+(0) - \eta^-(0) \tag{III.52}$$

Now, instead of solving nonlinear algebraic equations for the electrode overpotentials, **Equation (III.52)** requires the solution of second-order boundary value problems presented by **Equations (III.49) – (III.51)**; in this work, we solve these differential equations numerically using the *chebfun* package.[140] Note that the explicit consideration of electrolyte conductivity in the porous electrode model captures distributed ohmic losses throughout the reaction volume in addition to those considered earlier (R_c and R_m).

Figure III-8 shows discharge voltage profiles simulated in the absence of capacity fade using Nernstian behavior (**Equation (III.26)**), uniform Butler-Volmer kinetics (**Equation (S17)**), and 1D porous electrode kinetics (**Equation (S21)**). For both Butler-Volmer kinetics and the porous electrode, we explore different kinetic rate constants ($k_o^+ = k_o^- = 10^{-3}$, 10^{-5} cm s^{-1}) with typical outer-sphere, one-electron transfer coefficients ($\alpha_a^+ = \alpha_c^+ = \alpha_a^- = \alpha_c^- = 0.5$). For the porous electrode, we use relatively low effective electrolyte conductivities (κ_{eff} = 10 mS cm^{-1}) to accentuate disparities between the models. The relative times to generate each curve reflect the tradeoffs between accuracy and solvability; specifically, the Nernstian, uniform Butler-Volmer, and 1D porous electrode simulations required ca. 0.03 s, 5 s, and 13.5 min per cycle, respectively. While porous electrode theory refines the cell voltage calculation, the increase in computation time required to solve boundary value problems challenges simulations that span tens to hundreds of cycles. Moreover, in some instances, this refinement has diminishing returns; for example, redox couples with faster kinetics ($k^{o,+} = k^{o,-} > 10^{-3}$ cm s^{-1}) are well-described by Nernstian behavior under most conditions, so more detailed kinetic expressions only slightly improve the accuracy. Lastly, we note that although the 1D porous electrode refines ohmic losses resulting from the electrolyte and electrode, these could also be crudely approximated using the Nernstian or uniform Butler-Volmer expressions through the R_c parameter.

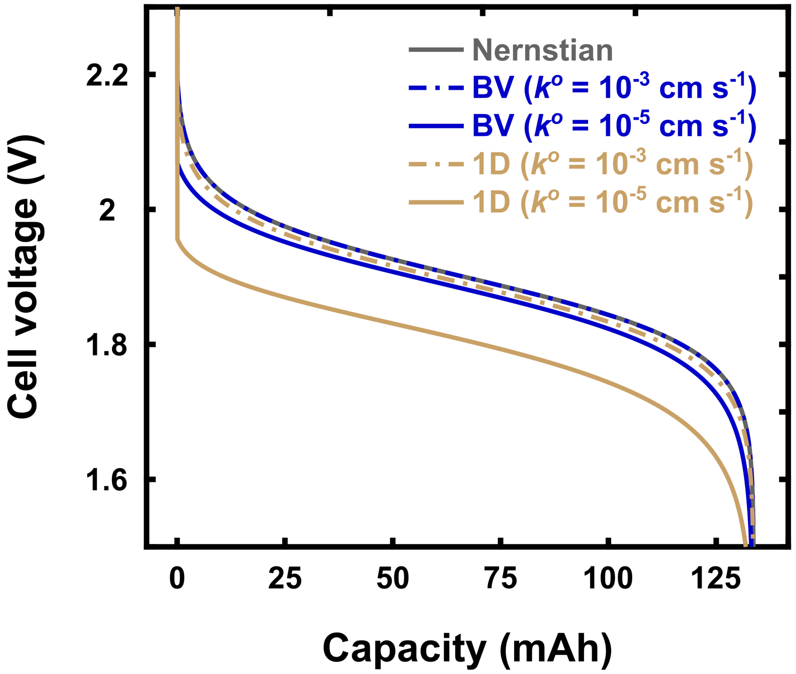

Figure III-8. *Discharge voltage profiles in the absence of capacity fade for varying methods of calculating the cell voltage: Nernstian behavior, uniform Butler-Volmer kinetics (BV), and one-dimensional porous electrode kinetics (1D). For all simulations,* $ASR_{\Omega} = 1\ \Omega\ cm^2$, $I = 255$ *mA (100 mA* cm^{-2}*),* $Q = 10$ *mL* min^{-1} *for both electrolytes, and* $D_j^{\infty} = 1 \times 10^{-9}\ m^2\ s^{-1}$ *for all species. For BV and 1D simulations,* $\alpha_a^+ = \alpha_c^+ = \alpha_a^- = \alpha_c^- = 0.5$ *and* $k^{o,+} = k^{o,-}$. *For 1D simulations,* $\kappa_{eff} = 10$ *mS* cm^{-1}.

7. Multiple electrolyte domains

This modeling framework also enables treatment of multiple spatial domains, which may be incorporated to better approximate cell behavior.[71] Thus far, we have treated each half-cell as a well-mixed, continuous domain with homogeneous reactions occurring throughout. While this assumption is analytically convenient and captures cycling behavior reasonably well, differences in residence times between the electrochemical cell, electrolyte reservoirs, and connecting tubing may introduce spatial variations in concentration.[66,71] These effects become more pronounced under conditions with high reactant conversion per pass (i.e., low flow rates and high current densities).

Fortunately, reactant flows manifest as first-order terms in the reactor mass balances, as material entering and leaving each domain is a linear function of the concentration and volumetric flow rate. For example, distinguishing the electrolyte storage tanks and redox flow cell yields the generalized mass balances shown in **Equations (III.53)** and **(III.54)**.

$$\frac{dC_j^{tk,h}}{dt} = \frac{Q}{V^{tk,h}}\left(C_j^{fc,h} - C_j^{tk,h}\right) + \sum R_j^{tk,h} \tag{III.53}$$

$$\frac{dC_j^{fc,h}}{dt} = \frac{Q}{V^{fc,h}}\left(C_j^{tk,h} - C_j^{fc,h}\right) + s_j \frac{I}{V^{fc,h}F} + \sum R_j^{fc,h} \tag{III.54}$$

Here, $C_j^{tk,h}$ and $C_j^{fc,h}$ (mol m^{-3}) are the bulk concentrations of species *j* in the tank and the flow cell, respectively; $V^{tk,h}$ and $V^{fc,h}$ are the electrolyte volumes in the tank and flow cell, respectively; $\sum R_j^{tk,h}$ and $\sum R_j^{fc,h}$ are loss terms in the tank and flow cell, respectively. Note that the loss terms in the tank comprise only species decay and self-discharge reactions whereas the loss terms in the flow cell also include crossover.

Combining the mass balances here results in a system of 12 coupled differential equations in contrast to 6 in the original formulation. However, solving this system of equations utilizes the same general strategy described in **Equations (III.13)** – **(III.19)** with volumetric flow rates incorporated into the matrix **K**. Thus, despite the small increases in computational complexity that arise with increasing spatial resolution, the presence of analytical solutions in more complex domains may still facilitate reductions in simulation time compared to numerical methods.

8. *Conclusions*

In this work, we derived a zero-dimensional model for galvanostatic cell cycling in a redox flow cell. This framework enables clear elucidation of the connections between cell material properties, operating conditions, and performance metrics, informing molecular, electrolyte, and cell design rules. To this end, we described several representative scenarios, characteristic in RFB research and development, that can be treated with varying degrees of analytical complexity. We showed that upper bound estimates for *VE*, accessible capacity, and cycling behavior may be obtained from explicit analytical equations. By incorporating redox species decay, we simulated the effects of decomposition and self-discharge on capacity fade for diagnostic symmetric cells. Treatment of species crossover allowed us to explore the role of membrane / separator conductivity-selectivity tradeoffs in predicting capacity fade and *EE* for asymmetric and pre-mixed (pseudo-symmetric) electrolytes. Lastly, we introduced modalities for including kinetic losses, distributed ohmic losses, and multiple spatial domains, highlighting routes for expanding this framework. Considering the relative simplicity and computational efficiency of the analytically-derived mass balances presented here, this approach is anticipated to be broadly useful for materials discovery, cell engineering and operation, as well as system-level techno-economic modeling.

9. List of symbols

Roman symbols

A_{ed}	Accessible surface area of the electrode (m^{2})
A_m	Geometric membrane area (m^{2})
ASR_{Ω}	Area-specific ohmic resistance (Ω m^{2})
$\mathbf{b}$	Constant reaction rate vector (mol m^{-3} s^{-1})
$\mathbf{C}$	Concentration vector (mol m^{-3})
$\mathbf{C^{o}}$	Initial concentration vector (mol m^{-3})
$C_j^{\infty,h}$	Bulk concentration of species *j* in half-cell *h* (mol m^{-3})
$C_j^{fc,h}$	Bulk flow cell concentration of species *j* in half-cell *h* (mol m^{-3})
$C_j^{o,h}$	Initial concentration of species *j* in half-cell *h* at the beginning of each half-cycle (mol m^{-3})
$C_j^{s,h}$	Electrode surface concentration of species *j* in half-cell *h* (mol m^{-3})
$C_j^{tk,h}$	Bulk tank concentration of species *j* in half-cell *h* (mol m^{-3})
C_{site}	Concentration of fixed ion sites in the membrane (mol m^{-3})
$\mathrm{Cap_c}$	Charge capacity (C)
$\mathrm{Cap_d}$	Discharge capacity (C)
CE	Fractional coulombic efficiency
d_f	Electrode fiber diameter (m)
D_j^{∞}	Diffusion coefficient of species *j* in the bulk (m^{2} s^{-1})
D_j^{m}	Diffusion coefficient of species *j* in the membrane (m^{2} s^{-1})
$E^{o,h}$	Formal redox potential in half-cell *h* (V)
$\overline{E}_c$	Average charging voltage (V)
$\overline{E}_d$	Average discharging voltage (V)
EE	Fractional energy efficiency
f_j	Fraction of *j* that decays via self-discharge
F	Faraday's constant (96485 C mol^{-1})
I	Applied current, denoted as positive for charging and negative for discharging (A)
$k_{c,j}^{h}$	Crossover rate constant for species *j* in half-cell *h* (s^{-1})
$k_{d,j}$	Decay rate constant for species *j* (s^{-1})
$k_{m,j}$	Mass transfer coefficient for species *j* (m s^{-1})
k_o^{h}	Standard rate constant in half-cell *h* (m s^{-1})
$\mathbf{K}$	Rate constant matrix (s^{-1})

K_j	Membrane sorption coefficient of species *j*
l_{ch}	Length of flow field channels (m)
l_e	Electrode thickness (m)
l_m	Membrane thickness (m)
n_{ch}	Number of flow field channels
N_j	Flux of species *j* through the membrane (mol m^{-2} s^{-1})
OCV	Open-circuit voltage (V)
Q	Volumetric flow rate (m^3 s^{-1})
R	Universal gas constant (8.314 J mol^{-1} K^{-1})
R_c	Additional ohmic resistances (Ω)
$R_j^{fc,h}$	Flow cell source term for species *j* in half-cell *h* (mol m^{-3} s^{-1})
R_j^h	Source term for species *j* in half-cell *h* (mol m^{-3} s^{-1})
$R_j^{tk,h}$	Storage tank source term for species *j* in half-cell *h* (mol m^{-3} s^{-1})
R_m	Membrane ohmic resistance (Ω)
s_j^h	Stoichiometric coefficient of species *j* in half-cell *h*
t	Time (s)
t_c	Charge time (s)
t_d	Discharge time (s)
T	Temperature (K)
$\mathbf{U}$	Eigenvector matrix of $\mathbf{K}$
$V^{fc,h}$	Flow cell volume in half-cell *h* (m^3)
V^h	Total electrolyte volume in half-cell *h* (m^3)
$V^{tk,h}$	Tank volume in half-cell *h* (m^3)
VE	Fractional voltaic efficiency
x	Position in the porous electrode (m)
z_j	Ionic charge of species *j*

Greek symbols

α_a^h	Anodic transfer coefficient in half-cell *h*
α_c^h	Cathodic transfer coefficient in half-cell *h*
β_i	i^{th} element of vector $\boldsymbol{\beta}$ (mol m^{-3} s^{-1})
$\boldsymbol{\beta}$	Transformed constant reaction rate vector (mol m^{-3} s^{-1})
γ_j	Dimensionless flux parameter

ε	Electrode porosity
η^h	Electrode overpotential in half-cell *h* (V)
θ_i	i$^{\text{th}}$ element of vector $\boldsymbol{\theta}$ (mol m^{-3})
θ_i^o	i$^{\text{th}}$ element of vector $\boldsymbol{\theta}^{\mathbf{o}}$ (mol m^{-3})
$\boldsymbol{\theta}$	Transformed concentration vector (mol m^{-3})
$\boldsymbol{\theta}^{\mathbf{o}}$	Transformed initial concentration vector (mol m^{-3})
κ_{eff}	Effective electrolyte conductivity (S m^{-1})
λ_i	i$^{\text{th}}$ element of matrix $\boldsymbol{\Lambda}$ (s^{-1})
$\boldsymbol{\Lambda}$	Diagonal eigenvalue matrix of $\mathbf{K}$ (s^{-1})
μ	Electrolyte viscosity (Pa s)
ν	Molar ratio of solvent to fixed ion sites in the membrane
ξ	Dimensionless electro-osmotic coefficient
ρ	Electrolyte density (kg m^{-3})
σ_m	Membrane conductivity (S m^{-1})
Φ_1^h	Electrode potential in half-cell *h* (V)

10. Appendix A: Model simplifications for species crossover

When considering species crossover in the absence of decay reactions, the mass balances are constrained by conservation of mass, as the total moles of species A and species B, m_A and m_B (mol), respectively, is constant across all states of charge in both electrolytes according to **Equations (III.55)** and **(III.56)**.

$$m_A = V^+C_A^{\infty,+} + V^+C_{A^+}^{\infty,+} + V^-C_A^{\infty,-} \tag{III.55}$$

$$m_B = V^-C_B^{\infty,-} + V^-C_{B^+}^{\infty,-} + V^+C_{B^+}^{\infty,+} \tag{III.56}$$

These additional constraints reduces the system of 6 ordinary differential equations (**Equation (13)** in the main text) to a system of only 4 equations, written explicitly in **Equation (III.57)**.

$$\frac{d}{dt}\begin{bmatrix} C_A^{\infty,+} \\ C_{A^+}^{\infty,+} \\ C_B^{\infty,-} \\ C_{B^+}^{\infty,-} \end{bmatrix} = \begin{bmatrix} -\dfrac{I}{V^+F} + k_{c,A}^- \dfrac{m_A}{V^-} \\ \dfrac{I}{V^+F} \\ \dfrac{I}{V^-F} \\ -\dfrac{I}{V^-F} + k_{c,B^+}^+ \dfrac{m_B}{V^+} \end{bmatrix} - \begin{bmatrix} \left(k_{c,A}^+ + k_{c,A}^- \dfrac{V^+}{V^-}\right) & k_{c,A}^- \dfrac{V^+}{V^-} & -k_{c,B}^- & 0 \\ 0 & k_{c,A^+}^+ & k_{c,B}^- & 0 \\ 0 & k_{c,A^+}^+ \dfrac{V^+}{V^-} & k_{c,B}^- \dfrac{V^+}{V^-} & 0 \\ 0 & -k_{c,A^+}^+ \dfrac{V^+}{V^-} & k_{c,B^+}^+ & \left(k_{c,B^+}^- \dfrac{V^+}{V^-} + k_{c,B^+}^+\right) \end{bmatrix} \begin{bmatrix} C_A^{\infty,+} \\ C_{A^+}^{\infty,+} \\ C_B^{\infty,-} \\ C_{B^+}^{\infty,-} \end{bmatrix} \tag{III.57}$$

This system of coupled differential equations can then be solved using the framework outlined in **Section 2.4** of the main text. Incidentally, because the rate constants here comprise a 4 × 4 matrix, the eigenvectors and eigenvalues can be calculated analytically.

Note that the generalized model presented in the main text does not explicitly account for conservation of mass, as the concentration of decay products was not considered and therefore does not present additional constraints. However, when crossover and species decay are incorporated simultaneously, the rate constant terms in **K** should possess similar magnitudes such that the matrix is not singular. For example, if crossover rates are relatively fast and species decomposition is several orders of magnitude slower, the system approaches the mass conservation limit described by **Equations (III.55)** and **(III.56)**, causing **K** to be poorly scaled and potentially leading to errors in computing the eigendecomposition.

IV. Closed-form cell cycling models for predicting redox flow battery performance

1. Background

The generalized zero-dimensional models we have developed thus far are powerful for evaluating connections between material properties and cycling performance, yet they still require some computational knowledge for proper implementation. As exponential decay terms introduce nonlinear terms in the mass balance solution, the zero-dimensional model (**Chapter III**) leverages nonlinear algebraic solvers and numerical integration to predict key performance metrics (i.e., capacities, efficiencies). While these methods do not create large disruptions in simulation time, this can certainly frustrate its usability and may slow more computationally expensive analyses (e.g., optimization, controls). To overcome this limitation, exponential terms can be approximated through Taylor expansions to yield polynomial equations for the mass balance solutions, which can be further solved to give closed-form analytical expressions for capacities and efficiencies. Silcox et al. used an analogous approach for deriving capacity fade metrics for varying species decay rates and cycling conditions, providing closed-form expressions for predicting capacity fade characteristics under variable testing conditions.[44] Using a more generalized zero-dimensional framework, we aim to derive analytical expressions for capacity fade and cycling efficiencies that incorporate multiple failure modes (i.e., crossover, species decay) and voltage losses (i.e., ohmic, kinetic, mass transport). From this simplified model, the key performance metrics can be calculated using relatively basic matrix operations, making simulations possible with less complex numerical methods.

To this end, we sought to expand on the analytical zero-dimensional framework by deriving approximations to the mass balance solutions, enabling fully closed-form solutions for cell cycling metrics. Specifically, we apply Taylor expansions to approximate exponential terms in the mass balances as polynomials, allowing them to be solved algebraically for charge and discharge times. By incorporating these polynomials into expressions for the cell voltage, we also derive analytical expressions for the voltaic efficiency. The resulting simplifications to the model facilitate significant improvements in accessibility while also further reducing the computation time. First, to more rigorously characterize the accuracy of the closed-form expressions, we evaluate varying orders of expansion (i.e., first, second, third order) and compare the root-mean squared error against the complete zero-dimensional model. Second, to demonstrate the accessibility of this framework, we develop a spreadsheet modeling package in Excel, delivering a flexible and easy-to-use simulation tool for broader use by the RFB community. The results of this work expand the utility of zero-dimensional models and may facilitate their use in a wider range of experimental and modeling studies. Further, the availability of easy-to-use spreadsheet models can support efforts to educate new entrants in the RFB field and complement undergraduate curricula in electrochemical engineering.

2. Theoretical framework

The closed-form constitutive equations developed here are derived from simplifications to the generalized zero-dimensional model presented in **Chapter III**. We start from the general mass balance equation, written in **Equations (IV.1) – (IV.3)**.

$$\frac{d}{dt}\begin{bmatrix} C_{A}^{\infty.+} \\ C_{A^+}^{\infty.+} \\ C_{B^+}^{\infty.+} \\ C_{B}^{\infty.-} \\ C_{B^+}^{\infty.-} \\ C_{A}^{\infty.-} \end{bmatrix} = \begin{bmatrix} -\dfrac{I}{V^+F} \\ \dfrac{I}{V^+F} \\ 0 \\ \dfrac{I}{V^-F} \\ -\dfrac{I}{V^-F} \\ 0 \end{bmatrix} - \begin{bmatrix} k_{c,A}^{+} & -f_{A^+}k_{d,A^+} & 0 & -k_{c,B}^{-} & 0 & -k_{c,A}^{-} \\ 0 & k_{d,A^+}+k_{c,A^+}^{+} & 0 & k_{c,B}^{-} & 0 & 0 \\ 0 & 0 & k_{c,B^+}^{+} & -k_{c,B}^{-} & k_{c,B^+}^{-} & 0 \\ 0 & k_{c,A^+}^{+} & 0 & k_{d,B}+k_{c,B}^{-} & 0 & 0 \\ 0 & -k_{c,A^+}^{+} & -k_{c,B^+}^{+} & -f_{B}k_{d,B} & k_{c,B^+}^{-} & 0 \\ -k_{c,A}^{+} & -k_{c,A^+}^{+} & 0 & 0 & 0 & k_{c,A}^{-} \end{bmatrix} \begin{bmatrix} C_{A}^{\infty.+} \\ C_{A^+}^{\infty.+} \\ C_{B^+}^{\infty.+} \\ C_{B}^{\infty.-} \\ C_{B^+}^{\infty.-} \\ C_{A}^{\infty.-} \end{bmatrix} \tag{IV.1}$$

$$\frac{d}{dt}\mathbf{C} = \mathbf{b} - \mathbf{KC} \tag{IV.2}$$

$$\mathbf{C}(t=0) = \mathbf{C^o} \tag{IV.3}$$

Again, the analytical solution to these mass balances is **Equation (IV.4)**.

$$\mathbf{KC} = \mathbf{b} - \exp(-\mathbf{K}t)(\mathbf{b} - \mathbf{KC^o}) \tag{IV.4}$$

Under conditions where the rates of crossover, species decay, and self-discharge are low relative to the charge and discharge times (i.e., $t_c k_i \ll 1$, $t_d k_i \ll 1$, where k_i (s^{-1}) represents a decay or crossover rate constant), then the exponentials can be approximated by a Taylor expansion according to **Equation (IV.5)**.

$$\exp(-\mathbf{K}t) = 1 - \mathbf{K}t + \frac{1}{2}(\mathbf{K}t)^2 - \frac{1}{6}(\mathbf{K}t)^3 + \cdots \tag{IV.5}$$

In the complete analytical solution, solving **Equation (IV.4)** for the charge and discharge times requires numerical methods, as the sum of exponential terms is nonlinear. By approximating these terms as polynomials, the charge and discharge times can instead be derived algebraically. Generally, higher order polynomials provide more accurate solutions but require increasing mathematical complexity; to this end, we derive solutions for first, second, and third order approximations.

A first-order Taylor expansion of the exponential terms yields the solution to the mass balances given by **Equation (IV.6)**.

$$\mathbf{C} = \mathbf{C}^{\mathbf{o}} + \left(\mathbf{b} - \mathbf{K}\mathbf{C}^{\mathbf{o}}\right)t \tag{IV.6}$$

The charge and discharge times are defined by the minimum time required for the reacting species concentrations to reach zero at the electrode surface. For the charging half-cycle, the reacting species are A or B^+, which respectively correspond to the first and fifth elements of **C**. Therefore, the charge time is the result of matrix operations corresponding to those species as given by **Equation (IV.7)**.

$$t_c = \min\begin{Bmatrix} -\left(C_A^{o,+} - \dfrac{I}{FA_{ed}k_m}\right)\left(-\dfrac{I}{V^+F} - k_{c,A}^{+}C_A^{o,+} + f_{A^+}k_{d,A^+}C_{A^+}^{o,+} + k_{c,B}^{-}C_B^{o,-} + k_{c,A}^{-}C_A^{o,-}\right)^{-1} \\ -\left(C_{B^+}^{o,-} - \dfrac{I}{FA_{ed}k_m}\right)\left(-\dfrac{I}{V^-F} + k_{c,A^+}^{+}C_{A^+}^{o,+} + k_{c,B^+}^{+}C_{B^+}^{o,+} + f_B k_{d,B}C_B^{o,-} - k_{c,B^+}^{-}C_{B^+}^{o,-}\right)^{-1} \end{Bmatrix} \tag{IV.7}$$

Similarly, the discharge time is given by **Equation (IV.8)**. Note that during discharge, the current is negative by definition.

$$t_d = \min\begin{Bmatrix} -\left(C_{A^+}^{o,+} + \dfrac{I}{FA_{ed}k_m}\right)\left(\dfrac{I}{V^+F} - \left(k_{d,A^+} + k_{c,A^+}^{+}\right)C_{A^+}^{o,+} - k_{c,B}^{-}C_B^{o,-}\right)^{-1} \\ -\left(C_B^{o,-} + \dfrac{I}{FA_{ed}k_m}\right)\left(\dfrac{I}{V^-F} - k_{c,A^+}^{+}C_{A^+}^{o,+} - \left(k_{d,B} + k_{c,B}^{-}\right)C_B^{o,-}\right)^{-1} \end{Bmatrix} \tag{IV.8}$$

From the charge and discharge times, the coulombic efficiency, CE, can be expressed according to **Equation (IV.9)**.

$$\mathrm{CE}=\frac{t_d}{t_c} \tag{IV.9}$$

Determining the voltaic efficiency requires integration of the cell voltage to determine the average charge and discharge voltage as shown in **Equation (IV.10)**.

$$\mathrm{VE}=\frac{\bar{E}_d}{\bar{E}_c}=\frac{\frac{1}{t_d}\int_0^{t_d}\left(E_{cell}\right)dt}{\frac{1}{t_c}\int_0^{t_c}\left(E_{cell}\right)dt} \tag{IV.10}$$

As the derivations are comparable for charge and discharge, here we focus on the discharge voltage, written explicitly in **Equation (IV.11)**.

$$\bar{E}_d=\frac{1}{t_d}\int_0^{t_d}\left(E^{o,+}-E^{o,-}+I\left(R_m+R_c\right)-\frac{RT}{F}\ln\left(\frac{\left(C_A^s\right)\left(C_{B^+}^s\right)}{\left(C_{A^+}^s\right)\left(C_B^s\right)}\right)\right)dt \tag{IV.11}$$

As the first several terms are assumed constant over the half-cycle, their integrals are fairly straightforward as shown in **Equation (IV.12)**.

$$\frac{1}{t_d}\int_0^{t_d}\left(E^{o,+}-E^{o,-}+I\left(R_m+R_c\right)\right)dt=E^{o,+}-E^{o,-}+I\left(R_m+R_c\right) \tag{IV.12}$$

The logarithmic concentration terms are comparatively more complex, as each surface concentration is given by a polynomial expression. The integral can be simplified by separating the logarithmic terms (**Equation (IV.13)**) and solved generally according to **Equation (IV.14)** for a first-order expansion.

$$-\frac{RT}{Ft_d}\int_0^{t_d}\left(\ln\left(\frac{\left(C_A^s\right)\left(C_{B^+}^s\right)}{\left(C_{A^+}^s\right)\left(C_B^s\right)}\right)\right)dt=-\frac{RT}{Ft_d}\int_0^{t_d}\left(\ln\left(C_A^s\right)+\ln\left(C_{B^+}^s\right)-\ln\left(C_{A^+}^s\right)-\ln\left(C_B^s\right)\right)dt \tag{IV.13}$$

$$\int_0^X\ln\left(Y+Zt\right)dt=\left(X+\frac{Y}{Z}\right)\ln\left(Y+ZX\right)-X-\frac{Y}{Z}\ln\left(Y\right) \tag{IV.14}$$

Here, *X, Y,* and *Z* are constant coefficients. Each concentration term can then be combined with **Equation (IV.12)** to yield a complete closed-form expression for the discharge voltage. Finally, the energy efficiency is the product of the coulombic and voltaic efficiencies as given in **Equation (IV.15)**.

$$\mathrm{EE} = \mathrm{VE} \times \mathrm{CE} \tag{IV.15}$$

For the second-order expansion (**Equation (IV.16)**), we follow the same procedure except that the quadratic formula is used to solve the resulting second-order polynomials.

$$\mathbf{C} = \mathbf{C^o} + \left(\mathbf{b} - \mathbf{K}\mathbf{C^o}\right)t - \frac{1}{2}\left(\mathbf{K}\mathbf{b} - \mathbf{K}^2\mathbf{C^o}\right)t^2 \tag{IV.16}$$

$$t_c = \min\left\{\begin{array}{ll} & R = C_A^{o,+} - \dfrac{I}{FA_{ed}k_m} \\ \dfrac{-S - \sqrt{S^2 - 4RT}}{2R}; & S = -\dfrac{I}{V^+F} - \mathbf{K}_{1,*}\mathbf{C^o} \\ & T = \mathbf{K}_{1,*}\mathbf{b} - \mathbf{K}_{1,*}^2\mathbf{C^o} \\ & \\ & R = C_{B^+}^{o,-} - \dfrac{I}{FA_{ed}k_m} \\ \dfrac{-S - \sqrt{S^2 - 4RT}}{2R}; & S = -\dfrac{I}{V^-F} - \mathbf{K}_{5,*}\mathbf{C^o} \\ & T = \mathbf{K}_{5,*}\mathbf{b} - \mathbf{K}_{5,*}^2\mathbf{C^o} \end{array}\right\} \tag{IV.17}$$

$$t_d = \min\left\{\begin{array}{ll} & R = C_{A^+}^{o,+} + \dfrac{I}{FA_{ed}k_m} \\ \dfrac{-S - \sqrt{S^2 - 4RT}}{2R}; & S = \dfrac{I}{V^+F} - \mathbf{K}_{2,*}\mathbf{C^o} \\ & T = \mathbf{K}_{2,*}\mathbf{b} - \mathbf{K}_{2,*}^2\mathbf{C^o} \\ & \\ & R = C_B^{o,-} + \dfrac{I}{FA_{ed}k_m} \\ \dfrac{-S - \sqrt{S^2 - 4RT}}{2R}; & S = \dfrac{I}{V^-F} - \mathbf{K}_{4,*}\mathbf{C^o} \\ & T = \mathbf{K}_{4,*}\mathbf{b} - \mathbf{K}_{4,*}^2\mathbf{C^o} \end{array}\right\} \tag{IV.18}$$

Note that $\mathbf{K}_{i,*}$ refers to the i^{th} row of matrix **K** and that $\mathbf{K}^2$ is the square of matrix **K**. Interestingly, the lower root of the quadratic approximation always corresponds to the charge / discharge times, as the parabolic concentration-time function for the reacting species is concave upward. Computing the voltaic efficiency requires integration of the logarithms, which now feature second-order polynomials. The general form of this integral is given by **Equation (IV.19)** where W, X, Y, and Z are constant coefficients.

$$\int_{0}^{W} \ln\left(X+Yt+Zt^{2}\right)dt=\left(\frac{1}{2Z}\right)\left[\begin{array}{l} 2\sqrt{Y^{2}-4XZ}\left(\tanh^{-1}\left(\dfrac{Y+2ZW}{\sqrt{Y^{2}-4XZ}}\right)-\tanh^{-1}\left(\dfrac{Y}{\sqrt{Y^{2}-4XZ}}\right)\right) \\ +\left(Y+2ZW\right)\log\left(X+W\left(Y+ZW\right)\right)-\left(Y\right)\log\left(X\right)-4ZW \end{array}\right] \tag{IV.19}$$

For third-order expansions (**Equation (IV.20)**), we apply the cubic formula to solve the resulting third-order polynomials.

$$\mathbf{C}=\mathbf{C}^{\mathbf{o}}+\left(\mathbf{b}-\mathbf{K}\mathbf{C}^{\mathbf{o}}\right)t-\frac{1}{2}\left(\mathbf{K}\mathbf{b}-\mathbf{K}^{2}\mathbf{C}^{\mathbf{o}}\right)t^{2}+\frac{1}{6}\left(\mathbf{K}^{2}\mathbf{b}-\mathbf{K}^{3}\mathbf{C}^{\mathbf{o}}\right)t^{3} \tag{IV.20}$$

However, to our knowledge, a concise analytical solution does not exist for the logarithm of a third-order polynomial, frustrating a closed-form analytical expression for VE. As such, we leverage numerical integration to compute the average charge and discharge voltages. For brevity, the third-order derivations are discussed in **Appendix A**.

3. Assessing error for closed-form approximations

To assess the relative error of the simplified model against the complete solution, we leveraged MATLAB® R2022b; similar to **Chapter III**, eigenvalues and eigenvectors were calculated using the *eig* function, nonlinear algebraic equations were solved implicitly using the *fsolve* function, and numerical integration was performed using the *cumtrapz* function. All simulation results presented throughout this work were performed on a Dell Latitude 7290 laptop computer with an Intel® Core™ i7-8650U processor (quad-core, 1.90 GHz) and a random-access memory of 16 GB. **Figure 1** compares discharge capacities using the "complete 0-D model"—solved using numerical methods—to the second order closed-form approximations for differing diffusion coefficients. Note that the cycling conditions used here are analogous to those used to generate **Figure III-6a**. Qualitatively, the second order approximations capture capacity fade remarkably well across a range of different crossover rates, highlighting the efficacy of using low-order Taylor expansions to simplify the model equations. However, assessing the relative accuracy of these methods requires a more rigorous evaluation of error across a range of model inputs.

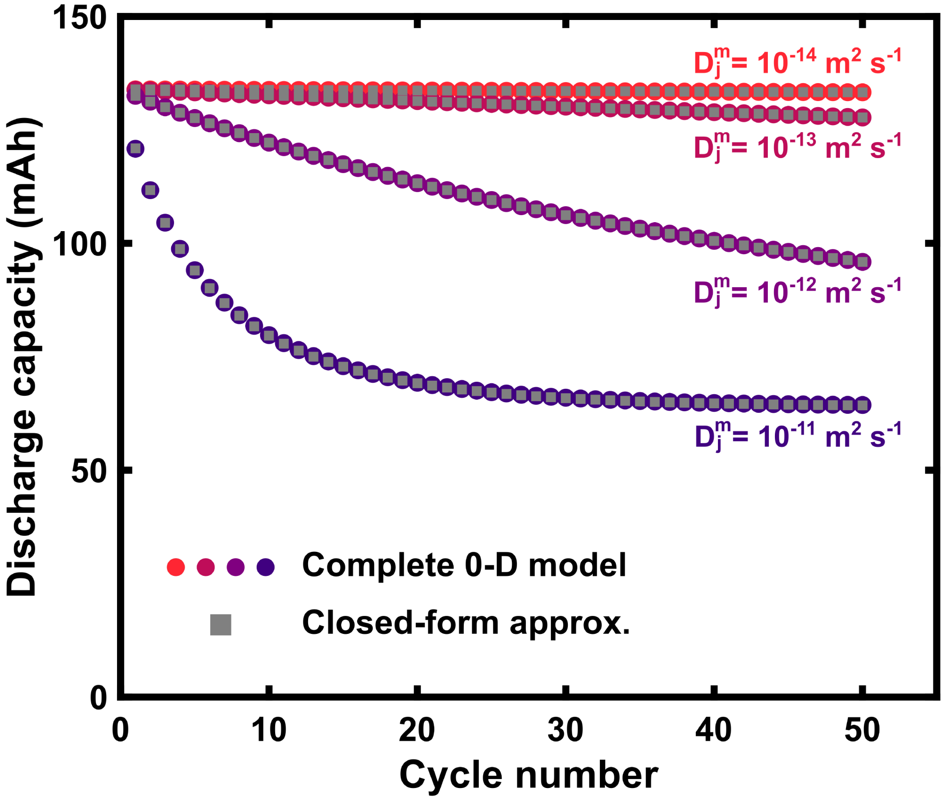

***Figure IV-1**. Comparison of the second-order approximation to results obtained from the complete zero-dimensional model for different membrane diffusion coefficients. All cell conditions for both sets of data are identical to those presented in **Figure III-9**.*

To expedite the process of comparing simulations across a rather excessive set of independently tunable input parameters, we elect to reduce the parameters to a minimum set of scaled parameters, which are provided in **Table IV-1**. For each of these dimensionless groups, we randomly select model inputs across a uniform distribution for physically realistic model conditions, and conducted all simulations for 1000 cycles to provide sufficient time for decay processes to proceed. However, note that the actual time represented by each cycle depends on the dimensional parameters, meaning that the timescales of the simulation may vary depending on input parameters. Additionally, we assume that both half-cell volumes are equal and that the bulk concentration of A and B^+ are initially equal while all other concentrations are zero. We quantify error between the "complete 0-D model" and the closed-form approximations by comparing both parity and root-mean squared error (RMSE) between the capacities and efficiencies predicted by the models. Results are reported for 1000 unique parameter combinations, yielding a total of 10^6 data points.

Table IV-1. *Scaled parameters and their ranges used for comparing model outputs.*

Scaled parameter	Definition	Range
Dimensionless current	$\frac{I}{FA_{ed}k_mC^{\infty}}$	0 – 0.25
OCV (V)	$E^{0,+} - E^{0,-}$	1 – 3
Ohmic losses (V)	$I\left(R_m + R_c\right)$	0 – 0.3
Dimensionless permeability of *A*	$\frac{D_A^m K_A A_m F C_A^o}{Il_m}$	10^{-7} – 10^{-3}
Dimensionless permeability of B^+	$\frac{D_{B^+}^m K_{B^+} A_m F C_{B^+}^o}{Il_m}$	10^{-7} – 10^{-3}
Permeability ratio of A^+	$D_{A^+}^m / D_A^m$	0.1 – 10
Permeability ratio of B	$D_B^m / D_{B^+}^m$	0.1 – 10
Dimensionless electric field	$\frac{FIl_m}{\sigma_m RTA_m}$	10^{-3} – 10
Dimensionless electro-osmotic flux	$\frac{\xi Il_m}{\nu C_{\text{site}} D_j^m A_m}$	0
Dimensionless decay rate of A^+	$\frac{k_{d,A^+} C_A^o V^+ F}{I}$	10^{-7} – 0.01
Dimensionless decay rate of B	$\frac{k_{d,B} C_{B^+}^o V^+ F}{I}$	10^{-7} – 0.01
f_{A^+} (–)	---	0.01 – 0.99
f_B (–)	---	0.01 – 0.99
z_A (–)	---	1
z_{B^+} (–)	---	2

Figure 2 shows parity plots for discharge capacities predicted by first, second, and third order approximations ("predicted values") measured against those calculated from the complete analytical solution ("actual values"). As the randomly generated inputs are dimensionless, we report the capacity as a dimensionless fraction of the theoretical capacity. Beyond the first order approximation, the analytical approximations describe the solution remarkably well over a relatively wide range of input values as indicated by the tight clustering of values around the parity line. The error is further quantified by the RMSE in **Figure 3** for the charge and discharge capacities as well as the coulombic, voltaic, and energy efficiencies. Here, we calculate RMSE for each cycling simulation (1000 cycles) and report the average and standard deviation across all parameter combinations (1000 simulations). Similar trends are observed with respect to the relative accuracy where $< 1\%$ relative error is observed for all model inputs beyond the first order approximation. However, given the wide range of independent parameters, we observe considerable variation in the relative error, especially for the first-order approximation. For instance, the RMSE of the discharge capacity extends as low as ca. 10^{-7} and as high as ca. 0.24. Upon closer inspection, the simulations featuring the largest degree of inaccuracy are those with longer charge / discharge times and faster crossover and decay rates, which is further exacerbated by significant electric field contributions. Migration causes larger differences in crossover rate constants between charge and discharge, leading to compounding errors from cycle to cycle. These phenomena are reflected in the arcing features that extend from the parity line as cycling proceeds and later converges closer to zero (**Figure 2a**).

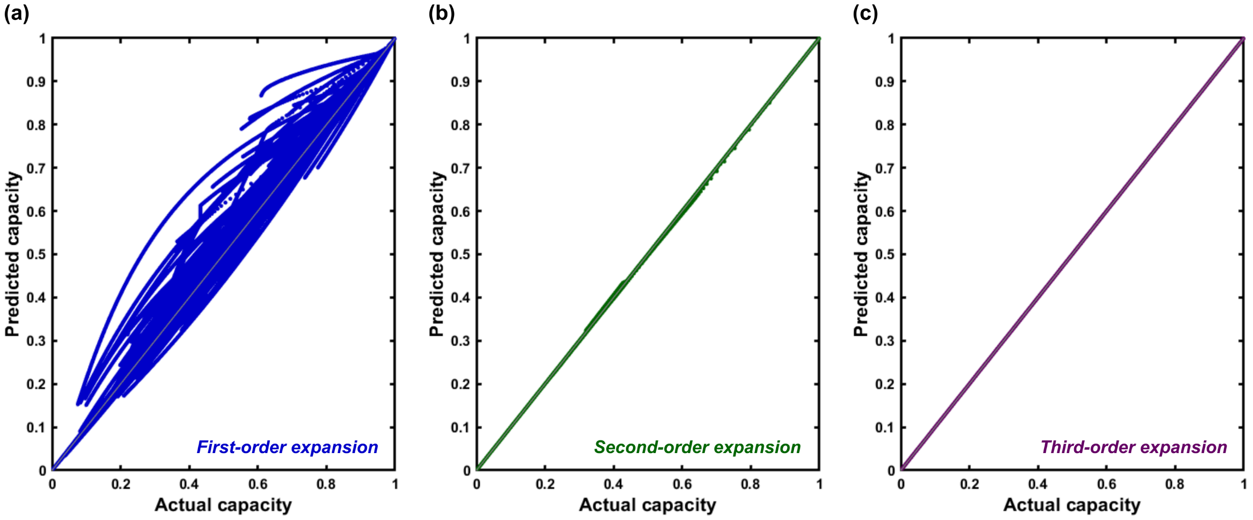

Figure IV-2. *Parity plot comparing dimensionless discharge capacities predicted from closed-form approximations ("predicted capacity") versus those determined from the complete zero-dimensional model ("actual capacity") for (a) first-order expansion, (b) second-order expansion, and (c) third-order expansion. Simulations were conducted over 1000 cycles using randomly-generated inputs and repeated 1000 times.*

As expected, increasing the extent of Taylor expansion improves model accuracy, as the higher order terms better approximate the exponential function at increasing times and with faster decay and crossover rates. This can be seen visually by both the tighter clustering around the parity line (**Figure 2**) and the lower magnitudes of the RMSE observed in the quantitative analysis (**Figure 3**). While there exist some differences between the second- and third-order approximations, the additional accuracy gained is diminishing and likely does not meaningfully affect results. Further, we reiterate that third-order expansions prohibit the derivation of closed-form expressions for VE and EE and introduce considerable difficulty in identifying the polynomial roots needed to predict charge and discharge capacities. Thus, we conclude that second-order approximations are sufficient for predicting performance metrics while providing a reasonably straightforward theoretical framework.

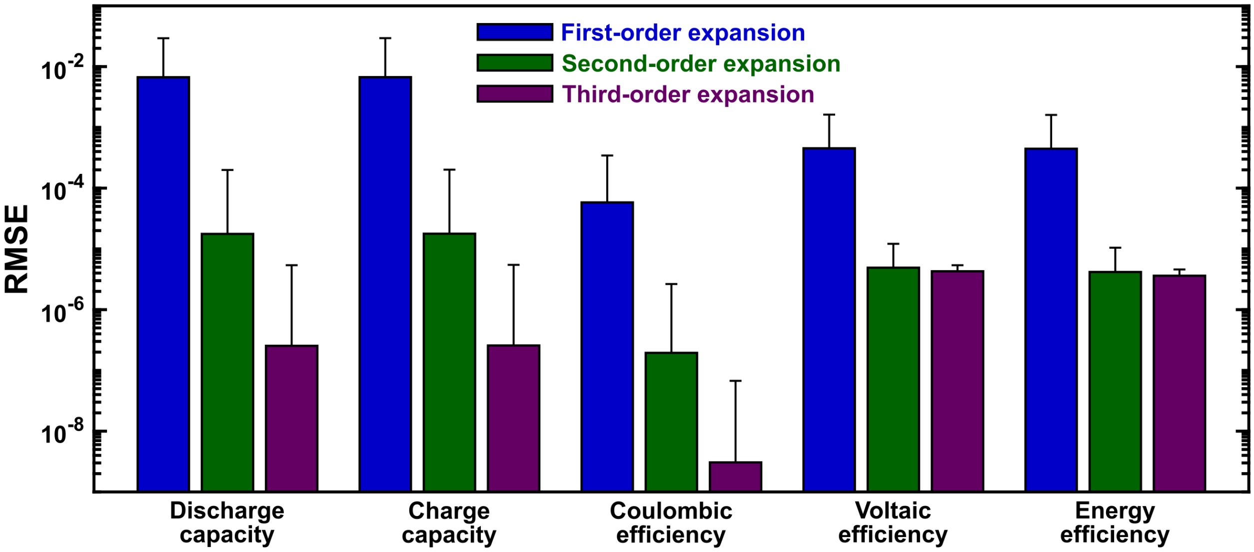

Figure IV-3. *Average root-mean squared error (RMSE) for dimensionless charge and discharge capacities as well as coulombic, voltaic, and energy efficiencies, comparing the values predicted by closed-form approximations and the complete zero-dimensional model. Simulations were conducted over 1000 cycles using randomly-generated inputs and repeated 1000 times. Error bars represent the standard deviation across all of the simulations.*

4. Developing an accessible simulation platform

As described above, a key feature of closed-form analytical expressions is that it enables spreadsheet modeling of redox flow cells, which could support more accessible simulations as well as integration with existing modeling workflows. Considering the second- and third-order expansions provide comparable margins of error, and third-order expansions frustrate closed-form expressions for VE, we elected to leverage the simpler second-order expressions for designing a spreadsheet model. The model is constructed in Excel 2019 and features a wide range of variable input parameters corresponding to electrolyte, electrode, and membrane properties; cell configuration; and operating conditions. Similar to **Chapter III**, we use the empirical correlation derived by Barton et al. to compute mass transfer coefficients, which are assumed to be equal for all species.[125] As such, the results presented here are most relevant for the custom 2.55 cm^2 cell used in that study, although the formula for the mass transfer coefficient may be adapted to other embodiments.

Figure 5 shows a snapshot of the prototype spreadsheet, featuring the input properties and their descriptions as well as representative outputs. The input values can be readily adjusted to simulate different operating conditions, electrolyte formulations, membrane properties, and electrode characteristics, however the model is subject to the same assumptions and limitations presented in **Chapter III**. Note that cells highlighted in blue (membrane resistance, mass transfer coefficient) are computed from other input values, but could be entered manually. Additionally, the cutoff voltages are used to set the voltage at the end of each half-cycle and are not used to determine the charge capacity. Matrix operations are performed in the spreadsheet to compute capacities and efficiencies at each cycle using results from the previous cycle. As a representative case, results are shown for 100 full charge / discharge cycles. For select cycles (here, cycles 1, 10, 20, 40, 60, 80, 100), the concentrations and cell voltage are calculated at multiple time points (here, 1000) throughout each half-cycle to compute charge / discharge voltage profiles.

As expected from the rigorous error analysis, the results here are consistent with behavior obtained using the complete zero-dimensional model. Accordingly, the accuracy of this model as compared with experimental systems is subject to the validity of the overarching zero-dimensional assumption. As noted in **Chapter III**, previous demonstrations have reported suitable accuracy for capturing charge / discharge behavior in vanadium RFBs[66,68] and aqueous organic RFBs,[71] and experimental results described in **Chapter VI** (vide infra) show excellent quantitative agreement. Importantly, performance metrics can be simulated in ~1 s after updating input parameters, meaning that variables can be readily manipulated to explore relationships between material properties and performance outputs. The rapid computations time and accessibility of the model could support educational efforts around RFBs and electrochemical systems. Additionally, the modeling framework may also help enable facile performance predictions prior to cycling experiments, allowing for real-time comparisons between measured characteristics and expected results.

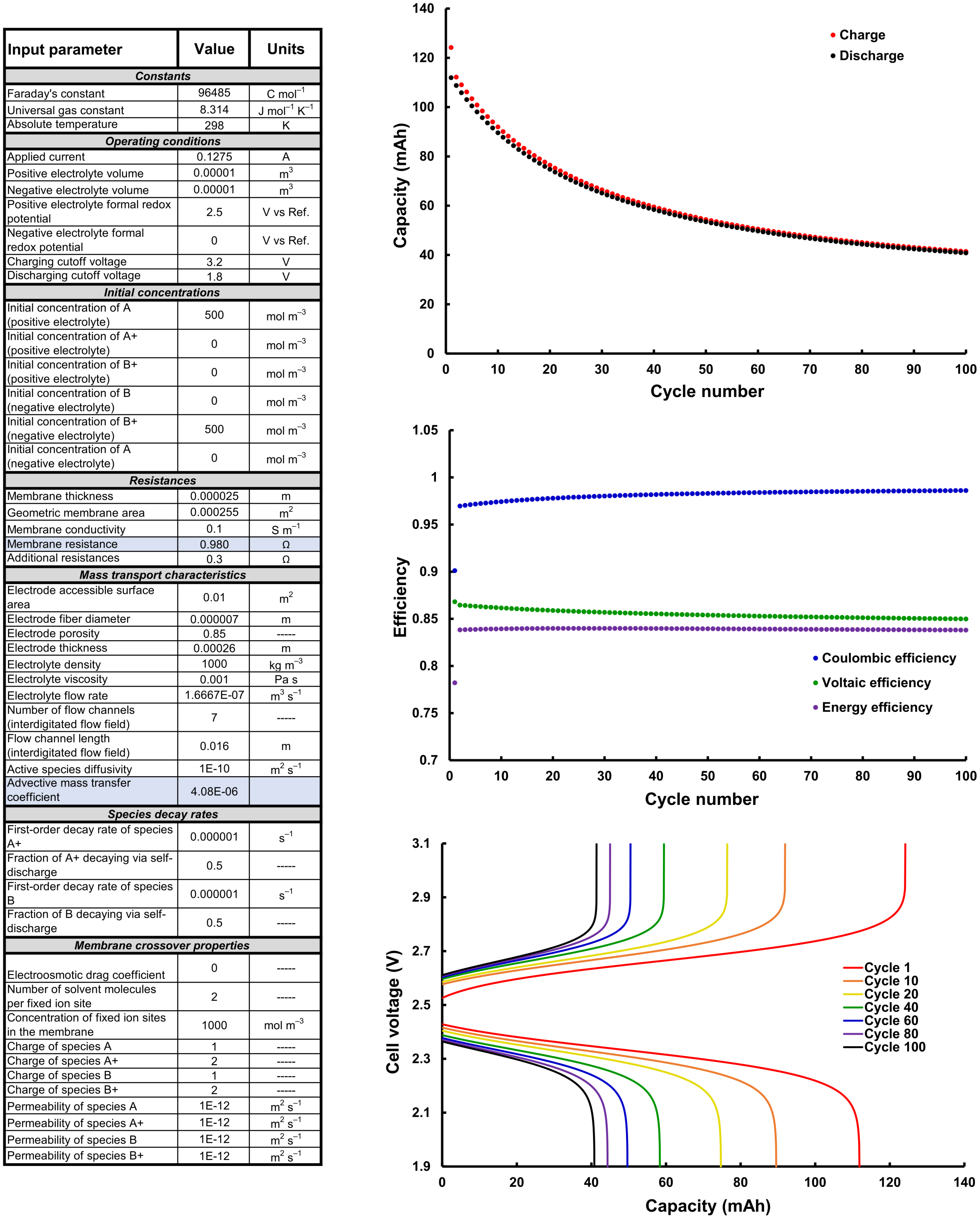

Input parameter	Value	Units
Constants		
Faraday's constant	96485	C mol^{-1}
Universal gas constant	8.314	$\text{J mol}^{-1}\ \text{K}^{-1}$
Absolute temperature	298	K
Operating conditions		
Applied current	0.1275	A
Positive electrolyte volume	0.00001	m^3
Negative electrolyte volume	0.00001	m^3
Positive electrolyte formal redox potential	2.5	V vs Ref.
Negative electrolyte formal redox potential	0	V vs Ref.
Charging cutoff voltage	3.2	V
Discharging cutoff voltage	1.8	V
Initial concentrations		
Initial concentration of A (positive electrolyte)	500	mol m^{-3}
Initial concentration of A+ (positive electrolyte)	0	mol m^{-3}
Initial concentration of B+ (positive electrolyte)	0	mol m^{-3}
Initial concentration of B (negative electrolyte)	0	mol m^{-3}
Initial concentration of B+ (negative electrolyte)	500	mol m^{-3}
Initial concentration of A (negative electrolyte)	0	mol m^{-3}
Resistances		
Membrane thickness	0.000025	m
Geometric membrane area	0.000255	m^2
Membrane conductivity	0.1	S m^{-1}
Membrane resistance	0.980	Ω
Additional resistances	0.3	Ω
Mass transport characteristics		
Electrode accessible surface area	0.01	m^2
Electrode fiber diameter	0.000007	m
Electrode porosity	0.85	-----
Electrode thickness	0.00026	m
Electrolyte density	1000	kg m^{-3}
Electrolyte viscosity	0.001	Pa s
Electrolyte flow rate	1.6667E-07	$\text{m}^3\ \text{s}^{-1}$
Number of flow channels (interdigitated flow field)	7	-----
Flow channel length (interdigitated flow field)	0.016	m
Active species diffusivity	1E-10	$\text{m}^2\ \text{s}^{-1}$
Advective mass transfer coefficient	4.08E-06	
Species decay rates		
First-order decay rate of species A+	0.000001	s^{-1}
Fraction of A+ decaying via self-discharge	0.5	-----
First-order decay rate of species B	0.000001	s^{-1}
Fraction of B decaying via self-discharge	0.5	-----
Membrane crossover properties		
Electroosmotic drag coefficient	0	-----
Number of solvent molecules per fixed ion site	2	-----
Concentration of fixed ion sites in the membrane	1000	mol m^{-3}
Charge of species A	1	-----
Charge of species A+	2	-----
Charge of species B	1	-----
Charge of species B+	2	-----
Permeability of species A	1E-12	$\text{m}^2\ \text{s}^{-1}$
Permeability of species A+	1E-12	$\text{m}^2\ \text{s}^{-1}$
Permeability of species B	1E-12	$\text{m}^2\ \text{s}^{-1}$
Permeability of species B+	1E-12	$\text{m}^2\ \text{s}^{-1}$

***Figure IV-4**. Screenshot of the zero-dimensional spreadsheet model constructed in Excel 2019, showing simulation inputs and representative performance metrics.*

5. Conclusions

In this work, we derived closed-form expressions for galvanostatic zero-dimensional cell cycling models, enabling more explicit connections between material properties and performance characteristics. By comparing error across varying orders of approximation, we showed that second-order Taylor expansions were sufficient for accurately capturing performance metrics under physically-relevant cell cycling conditions without overly complicating the mathematical formulation. Using the second-order expressions, we developed a spreadsheet model in Excel, which can simulate flow cell performance, including the charge / discharge capacity, cycling efficiencies, and charge / discharge profiles. This modeling framework can potentially improve accessibility to RFB simulation tools, providing foundational knowledge to new entrants in the field and supporting broader education efforts in electrochemistry and electrochemical engineering.

6. List of symbols

Roman symbols

A_{ed}	Accessible surface area of the electrode (m^2)
A_m	Geometric membrane area (m^2)
$\mathbf{b}$	Constant reaction rate vector (mol m^{-3} s^{-1})
$\mathbf{C}$	Concentration vector (mol m^{-3})
$\mathbf{C^o}$	Initial concentration vector (mol m^{-3})
$C_j^{\infty,h}$	Bulk concentration of species j in half-cell h (mol m^{-3})
$C_j^{o,h}$	Initial concentration of species j in half-cell h at the beginning of each half-cycle (mol m^{-3})
C_{site}	Concentration of fixed ion sites in the membrane (mol m^{-3})
CE	Fractional coulombic efficiency
D_j^m	Diffusion coefficient of species j in the membrane (m^2 s^{-1})
$E^{o,h}$	Formal redox potential in half-cell h (V)
$\bar{E}_c$	Average charging voltage (V)
$\bar{E}_d$	Average discharging voltage (V)
EE	Fractional energy efficiency
f_j	Fraction of j that decays via self-discharge
F	Faraday's constant (96485 C mol^{-1})
I	Applied current, denoted as positive for charging and negative for discharging (A)
$k_{c,j}^h$	Crossover rate constant for species j in half-cell h (s^{-1})
$k_{d,j}$	Decay rate constant for species j (s^{-1})
$k_{m,j}$	Mass transfer coefficient for species j (m s^{-1})
$\mathbf{K}$	Rate constant matrix (s^{-1})
K_j	Membrane sorption coefficient of species j
l_m	Membrane thickness (m)
OCV	Open-circuit voltage (V)
R	Universal gas constant (8.314 J mol^{-1} K^{-1})
R_c	Additional ohmic resistances (Ω)
R_m	Membrane ohmic resistance (Ω)
t	Time (s)
t_c	Charge time (s)
t_d	Discharge time (s)
T	Temperature (K)
V^h	Total electrolyte volume in half-cell h (m^3)

VE	Fractional voltaic efficiency
z_j	Ionic charge of species *j*

Greek symbols

ν	Molar ratio of solvent to fixed ion sites in the membrane
ξ	Dimensionless electro-osmotic coefficient
σ_m	Membrane conductivity (S m^{-1})

7. Appendix A: Closed-form expressions for third-order expansions

Here, we demonstrate the closed-form solution to the third-order expansion (**Equation (IV.20)** using the cubic formula. For brevity, we show a representative solution for the charging time based on the consumption of A. In general, there are three unique roots for a third-order polynomial, given by **Equation (IV.21)**.

$$\begin{aligned} t_c &= -\frac{1}{3}\left(\frac{T}{U}\right) + \left(W + X\right) \\ t_c &= -\frac{1}{3}\left(\frac{T}{U}\right) - \frac{1}{2}\left(W + X\right) + \frac{1}{2} i\sqrt{3}\left(W - X\right) \\ t_c &= -\frac{1}{3}\left(\frac{T}{U}\right) - \frac{1}{2}\left(W + X\right) - \frac{1}{2} i\sqrt{3}\left(W - X\right) \end{aligned} \tag{IV.21}$$

The placeholder variables are related to the constant coefficients by **Equation (IV.22)**.

$$\begin{aligned} R &= C_{A^+}^{o,+} + \frac{I}{F A_{ed} k_m} \\ S &= -\frac{I}{V^+ F} - \mathbf{K}_{1,*}\mathbf{C}^{\mathbf{o}} \\ T &= \mathbf{K}_{1,*}\mathbf{b} - \mathbf{K}_{1,*}^{2}\mathbf{C}^{\mathbf{o}} \\ U &= \mathbf{K}_{1,*}^{2}\mathbf{b} - \mathbf{K}_{1,*}^{3}\mathbf{C}^{\mathbf{o}} \\ W &= \sqrt[3]{Z + \sqrt{Y^3 + Z^2}} \\ X &= \sqrt[3]{Z + \sqrt{Y^3 - Z^2}} \\ Y &= \frac{1}{3}\left(\frac{S}{U}\right) - \frac{1}{9}\left(\frac{T}{U}\right)^2 \\ Z &= \frac{1}{6}\left(\frac{ST}{U^2}\right) - \frac{1}{2}\left(\frac{R}{U}\right) - \frac{1}{27}\left(\frac{T}{U}\right)^3 \end{aligned} \tag{IV.22}$$

Computing charging and discharging times based on other reacting species only requires manipulation of the terms in *R*, *S*, *T*, and *U* and selection of the minimum time for either half-cycle. The time is represented by any of the roots depending on the curvature of the cubic function.

V. Too much of a good thing? Assessing performance tradeoffs of two-electron compounds for redox flow batteries

1. Background

The development of low-cost redox couples and associated electrolytes is a promising cost-reduction pathway for redox flow batteries (RFBs).[15,23] To this end, organic molecules and metal-coordination complexes are emerging as alternative charge storage species to compete with more traditional inorganic salts. These candidate materials are especially compelling for meeting production demands, as many can be derived from abundant, widely accessible sources and synthesized at-scale using existing process knowledge and infrastructure.[19] Further, their chemical structures can be functionalized to refine key properties, such as the redox potential, electrochemical reversibility, solubility, and stability.[141–143] Of particular note is the possibility for these materials to support multiple electron transfers, which, in principle, may facilitate marked increases in capacity and concomitant decreases in energy-specific electrolyte cost.[18] However, multi-valent redox couples are often chemically irreversible due to the increasing instability and/or decreasing solubility of the charged species.[144] Recent research efforts have led to the advancement of several multi-electron transfer molecular platforms, which have been tuned to mitigate major decomposition pathways and promote solubility across different oxidation states in relevant electrolytes, furthering their viability in practical embodiments.[26,145–147] Despite this progress, the overall impact of the multi-electron approach on cell performance has not been widely explored beyond proof-of-concept demonstrations.[18]

While many molecular engineering challenges (e.g., stability, solubility, etc.) are universal to the design of redox electrolytes, the unique electron transfer mechanisms (sequential vs. concerted) of multi-electron compounds present a characteristic feature that may constrain their design. For example, many redox-active organic molecules that undergo multi-electron transfer in aqueous electrolytes (e.g., phenazines,[37] phenothiazines,[148] and quinones[119,149,150]) typically exhibit multiple redox reactions occurring at similar potentials due to hydrogen bonding interactions present in these environments.[38] Conversely, similar molecules used in nonaqueous electrolytes (e.g., bipyrimidines,[151] bispyridinylidenes,[152] phenazines,[153] phenothiazines,[145,146] quinones,[154] and viologens[155,156]), some used in aqueous electrolytes (e.g., viologens[157–160]), and metal-coordination complexes containing non-innocent ligands[26,161–163] often feature sequential electron transfer events with disparate and easily discernable redox potentials, ranging from 200 – 800 mV. Compared to the concerted mechanism, which presents minimal voltage losses (vide infra), the sequential mechanism imposes significant losses, increasing with the potential difference between redox events. Indeed, prior experimental work has shown that, during galvanostatic cell cycling, there is an asymmetry between voltage-time plateaus during charge and discharge: during the charging step, more time is spent at the higher cell voltage, while during the discharging step, more time is spent at the lower cell voltage.[26,145–147] This augments the difference between the average charge and discharge voltages, lowering both the voltaic and energy efficiencies of the cell. To assess the efficacy of multi-electron compounds, it is necessary to understand the magnitude of these losses, which, in turn, requires a deeper understanding of the extent to which the molecular properties and cell operating conditions contribute to RFB performance.

In this chapter, we develop three electrochemical models (**Figure II-1**) to understand the effect of two-electron compounds on cell cycling and assess their performance tradeoffs in RFBs. To gain initial insight into the underlying physics driving multi-electron transfer, we begin by analyzing the chronopotentiometric response of a one-dimensional planar electrode (**Figure II-1a**), highlighting the influence of thermodynamic and mass transport factors on electrode polarization. Subsequently, using a single half-cell (**Figure II-1b**) to simulate galvanostatic charge / discharge cycling, we show that voltaic efficiency is significantly affected by both the average redox potential and the potential difference between the redox events. To a lesser extent, different mass transfer rates between species, along with comproportionation reaction rates, further alter the cycling behavior. Finally, using a full cell galvanostatic cycling model (**Figure II-1c**), we consider the impact of utilizing two-electron compounds in both half-cells, which results in compounding inefficiencies due to additional voltage losses and charge imbalance. By connecting molecular properties to cell performance, we are able to propose design criteria for more efficient high-capacity redox electrolytes—specifically, lowering the potential difference between redox events through molecular engineering and integrating multi-electron compounds into long-duration applications will greatly improve their viability. More broadly, this approach provides a framework for evaluating the impact of material properties on cell performance, which can be extended to investigate additional sources of inefficiency (e.g., activation and ohmic overpotentials) and other characteristic failure modes (e.g., molecular decomposition, crossover, etc.) for candidate systems.

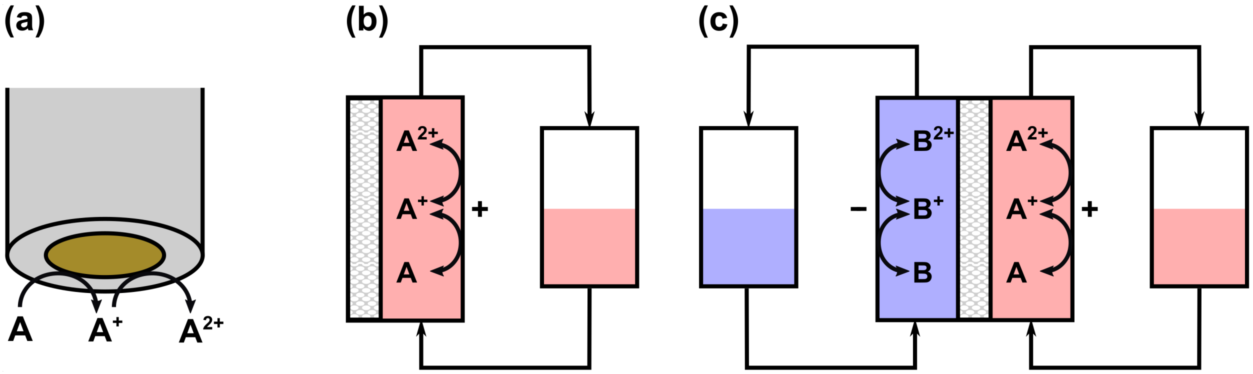

Figure V-1. Schematic of modeling domains for (a) chronopotentiometry at a planar electrode, (b) galvanostatic charging / discharging for a single half-cell with a two-electron compound A, and (c) galvanostatic charging / discharging of a full cell with the two-electron compounds A and B.

2. *Theoretical framework*

The theoretical framework presented here describes concerted and sequential two-electron transfer processes by quantifying the voltage-time relationship typical of galvanostatic processes. Specifically, the sequential two-electron transfer for species *A* is described by **Equations (V.1)** and **(V.2)**.

$$A \rightleftharpoons A^{+} + e^{-} \tag{V.1}$$

$$A^{+} \rightleftharpoons A^{2+} + e^{-} \tag{V.2}$$

In addition to heterogeneous electron transfer on the electrode surface, homogeneous comproportionation and disproportionation (**Equation (V.3)**) in the bulk must be considered when the redox potential of **Equation (V.2)** is more positive than that of **Equation (V.1)**:

$$A + A^{2+} \rightleftharpoons 2A^{+} \tag{V.3}$$

In contrast to **Equations (V.1)-(V.3)**, species *A* may undergo a concerted two-electron transfer in which the oxidation of *A* proceeds directly to A^{2+} according to **Equation (V.4)**.

$$A \rightleftharpoons A^{2+} + 2e^{-} \tag{V.4}$$

The following sections discuss the role of thermodynamics, kinetics, and mass transport effects on the reactions in **Equations (V.1)–(V.4)**, and subsequently describe model nondimensionalization and execution.

2.1. Thermodynamics and reaction kinetics

To simplify the reaction kinetics and the overall theoretical analysis, all electrode reactions are assumed to be electrochemically reversible such that reactive species at the electrode surface are in equilibrium and their concentrations are governed by the Nernst Equation (**Equations (V.5)** and **(V.6)** for the first and second oxidation, respectively). We note this assumption is in agreement with prior experimental literature for many of the organic molecules and metal-coordination complexes under consideration for use in RFBs.[18,23,142]

$$E = E_1^{(A)} + \frac{RT}{F}\ln\left(\frac{C_{A^+}^s}{C_A^s}\right) \tag{V.5}$$

$$E = E_2^{(A)} + \frac{RT}{F}\ln\left(\frac{C_{A^{2+}}^s}{C_{A^+}^s}\right) \tag{V.6}$$

In **Equations (V.5)** and **(V.6)**, E (V) is the potential at the electrode surface, $E_1^{(A)}$ (V) is the formal redox potential of the first oxidation (**Equation (V.1)**), $E_2^{(A)}$ (V) is the formal redox potential of the second oxidation (**Equation (V.2)**), R (8.314 J mol^{-1} K^{-1}) is the universal gas constant, T (K) is the absolute temperature (here, T = 298 K), F (96485 C mol^{-1}) is the Faraday constant, and C_j^s (mol m^{-3}) is the concentration of species j at the electrode surface. It is also convenient to introduce $E_{avg}^{(A)}$ as the arithmetic mean of $E_1^{(A)}$ and $E_2^{(A)}$. Note that throughout this work, all potentials are defined relative to an arbitrary reference electrode.

The rate of bulk comproportionation, r_p (mol m^{-3} s^{-1}), and bulk disproportionation, r_d (mol m^{-3} s^{-1}) are given by **Equations (V.7)** and **(V.8)**, respectively:

$$r_p = k_p C_A^\infty C_{A^{2+}}^\infty \tag{V.7}$$

$$r_d = k_d \left(C_{A^+}^\infty\right)^2 \tag{V.8}$$

Where C_j^∞ (mol m^{-3}) is the concentration of species j in the bulk solution and k_p and k_d (m^3 mol^{-1} s^{-1}) are the comproportionation and disproportionation rate constants, respectively. These rate constants are related by the difference in formal redox potentials, $\Delta E^{(A)} = E_2^{(A)} - E_1^{(A)}$, according to **Equation (V.9)**:

$$k_p = k_d \exp\left(\frac{F}{RT}\Delta E^{(A)}\right) \tag{V.9}$$

For a concerted two-electron transfer (**Equation (V.4)**), equilibrium concentrations at the electrode surface are again described by the Nernst equation as shown in **Equation (V.10)**.

$$E = E_{avg}^{(A)} + \frac{RT}{2F}\ln\left(\frac{C_{A^{2+}}^{s}}{C_{A}^{s}}\right) \tag{V.10}$$

Because the concerted step does not proceed through an intermediate, comproportionation and disproportionation are assumed to be negligible.

2.2. Chronopotentiometry at a planar electrode

To analyze the time-dependent potential response for sequential two-electron transfer at a planar electrode (**Figure II-1a**), a one-dimensional model can be derived from the mass conservation equation in the absence of convection and migration (**Equation (V.11)**):

$$\frac{\partial C_j}{\partial t} = -D\nabla^2 C_j = -D\frac{\partial^2 C_j}{\partial x^2} \tag{V.11}$$

Subject to the following initial and boundary conditions:

$$C_j(t=0,x) = C_j^{\infty} \tag{V.12}$$

$$-D\frac{\partial C_j(t,x=0)}{\partial x} = N_j \tag{V.13}$$

$$C_j(t,x=\infty) = C_j^{\infty} \tag{V.14}$$

Where t (s) is the time, x (m) is the axial position perpendicular to the planar electrode surface, D ($m^2\ s^{-1}$) is the diffusivity, which is assumed to be the same for all species, C_j (mol m^{-3}) is the local concentration of species j, and N_j (mol $m^{-2}\ s^{-1}$) is the molar flux of species j to the electrode surface. The solution to **Equations (V.11)-(V.14)** for the time-dependent concentration of species j is given by **Equation (V.15)**.[164]

$$C_j(x,t) = C_j^\infty - \frac{1}{(\pi D)^{1/2}} \int_0^t \frac{-N_j(\eta)}{(t-\eta)^{1/2}} \exp\left(\frac{-x^2}{4D(t-\eta)} \right) d\eta \tag{V.15}$$

Note that η is an integration variable. To derive the electrode potential as a function of time, **Equation (V.16)** relates the applied current, I (A), to the partial currents, I_1 and I_2 (A), for the reactions given in **Equations (V.1)** and **(V.2)**, respectively:

$$I = I_1 + I_2 \tag{V.16}$$

The partial currents are equivalent to the surface fluxes according to **Equations (V.17)-(V.19)**:

$$N_A = -\frac{I_1}{FS} \tag{V.17}$$

$$N_{A^+} = \frac{I_1}{FS} - \frac{I_2}{FS} \tag{V.18}$$

$$N_{A^{2+}} = \frac{I_2}{FS} \tag{V.19}$$

Here, S (m^2) is the electrode surface area. **Equation (V.15)** can be combined with **Equations (V.16)–(V.19)** for each species to determine the electrode potential as a function of time using **Equations (V.5)** and **(V.6)**. These coupled, nonlinear equations can then be solved implicitly, as discussed below.

2.3. Galvanostatic cell cycling

To describe the effects of sequential two-electron transfers on galvanostatic charge / discharge, a zero-dimensional model is derived (**Figure II-1b**). Similar to the planar electrode case, the model applies a constant charging current (**Equation (V.16)**), which is the sum of the partial currents. Electrode kinetics are again described by **Equations (V.5)** and **(V.6)**, and the relationship between the bulk and surface concentrations of each species can be described by convective mass transfer (**Equations (V.20)** and **(V.21)**) and the flux balance (**Equation (V.22)**):

$$I_1 = FSk_{m,A}\left(C_A^{\infty} - C_A^{s}\right) \tag{V.20}$$

$$I_2 = -FSk_{m,A^{2+}}\left(C_{A^{2+}}^{\infty} - C_{A^{2+}}^{s}\right) \tag{V.21}$$

$$I_1 - I_2 = -FSk_{m,A^{+}}\left(C_{A^{+}}^{\infty} - C_{A^{+}}^{s}\right) \tag{V.22}$$

Here, $k_{m,j}$ (m s^{-1}) is the mass transfer coefficient of species j. **Equations (V.20)–(V.22)** can be combined with the equilibrium expressions in **Equations (V.5)** and **(V.6)** to arrive at an expression for the surface concentration of A^{+} (C_{A+}^{s}):

$$C_{A^{+}}^{s} = \frac{k_{m,A}C_A^{\infty} + k_{m,A^{+}}C_{A^{+}}^{\infty} + k_{m,A^{2+}}C_{A^{2+}}^{\infty}}{k_{m,A}\exp\left(\frac{F}{RT}\left(E_1^{(A)} - E\right)\right) + k_{m,A^{+}} + k_{m,A^{2+}}\exp\left(\frac{F}{RT}\left(E - E_2^{(A)}\right)\right)} \tag{V.23}$$

The surface concentration is then substituted into **Equation (V.16)** to solve for the electrode potential as a function of the time-dependent bulk concentrations (**Equation (V.24)**). Again, the coupled nonlinear algebraic equations (**Equations (V.23)** and **(V.24)**) can be solved implicitly (vide infra).

$$I = FSk_{m,A}\left[C_A^{\infty} - C_{A^{+}}^{s}\exp\left(\frac{F}{RT}\left(E_1^{(A)} - E\right)\right)\right] - FSk_{m,A^{2+}}\left[C_{A^{2+}}^{\infty} - C_{A^{+}}^{s}\exp\left(\frac{F}{RT}\left(E - E_2^{(A)}\right)\right)\right]$$

(V.24)

Finally, to track changes in the bulk concentration, the system is assumed to be well-mixed such that the total current is uniformly distributed throughout the entire volume. Note that the model treats the electrode half-cell, reservoir, and connecting tubing as a single continuous domain. For this treatment, the mass balances on the reactor volume for each species are a system of ordinary differential equations as shown by **Equations (V.25)–(V.28)**,

$$V\frac{dC_A^\infty}{dt}=-\frac{I_1}{F}-Vk_pC_A^\infty C_{A^{2+}}^\infty+Vk_d\left(C_{A^+}^\infty\right)^2 \quad (V.25)$$

$$V\frac{dC_{A^+}^\infty}{dt}=\frac{I_1}{F}-\frac{I_2}{F}+2Vk_pC_A^\infty C_{A^{2+}}^\infty-2Vk_d\left(C_{A^+}^\infty\right)^2 \quad (V.26)$$

$$V\frac{dC_{A^{2+}}^\infty}{dt}=\frac{I_2}{F}-Vk_pC_A^\infty C_{A^{2+}}^\infty+Vk_d\left(C_{A^+}^\infty\right)^2 \quad (V.27)$$

which are subject to the initial conditions:

$$C_j^\infty\left(t=0\right)=C_j^o \quad (V.28)$$

V (m^3) is the total electrolyte volume and C_j^o (mol m^{-3}) is the initial bulk concentration. These coupled ordinary differential equations can be numerically solved to yield changes in bulk concentrations as a function of time, which can be further used to implicitly solve for the electrode potential (**Equations (V.23)** and **(V.24)**).

For concerted electron transfer in the absence of comproportionation, the mass balances can be solved analytically, yielding time-dependent bulk concentrations and the subsequent electrode potential according to **Equations (V.29)–(V.31)**:

$$C_A^\infty=C_A^o-\frac{It}{2FV} \quad (V.29)$$

$$C_{A^{2+}}^\infty=C_{A^{2+}}^o+\frac{It}{2FV} \quad (V.30)$$

$$E=E_{avg}^{(A)}+\frac{RT}{2F}\ln\left(\frac{C_{A^{2+}}^\infty+\dfrac{I}{2FSk_{m,A^{2+}}}}{C_A^\infty-\dfrac{I}{2FSk_{m,A}}}\right) \quad (V.31)$$

2.4. Dimensionless variables and analysis

To reduce the total number of independent model parameters, dimensionless variables are introduced. **Equation (V.32)** defines the dimensionless concentration, θ_j^m, which describes the concentration in state *z* ($z \in \{s, \infty, o\}$) normalized by the total bulk concentration, C_T^∞ (mol m^{-3}), which remains constant:

$$\theta_j^z = \frac{C_j^z}{C_A^\infty + C_{A^+}^\infty + C_{A^{2+}}^\infty} = \frac{C_j^z}{C_T^\infty} \tag{V.32}$$

Equation (V.33) defines the dimensionless charging current, Ψ, which is derived by normalizing the total charging current by the mass transfer limiting current for the oxidation of *A*:

$$\Psi = \frac{I}{Fk_{m,A}SC_T^\infty} \tag{V.33}$$

Similarly, **Equation (V.34)** defines a dimensionless time, *τ*, which normalizes the cycle time by the theoretical charging time for one electron:

$$\tau = \frac{tI}{FVC_T^\infty} \tag{V.34}$$

The mass transfer coefficients are normalized by that of species *A* according to **Equation (V.35)** to yield dimensionless mass transfer coefficients, γ_j:

$$\gamma_j = \frac{k_{m,j}}{k_{m,A}} \tag{V.35}$$

Finally, **Equation (V.36)** scales the rate of comproportionation by the charging current to give a dimensionless rate constant, κ:

$$\kappa = \frac{V k_p \left(C_T^{\infty}\right)^2 F}{I} \tag{V.36}$$

Note that for the discharging step, the current reverses sign, resulting in negative values for Ψ, τ, and κ. To ensure the solutions comprise a consistent time domain ($\tau \in [0,2]$), the sign of τ is reversed.

In this analysis, the coupled ODEs (**Equations (V.25)–(V.28)**) were solved using the *ode15s* function in MATLAB® R2018a, while nonlinear algebraic equations were solved implicitly using the *fsolve* function in the same program. Simulations were performed on a Dell Latitude 7290 laptop computer with an Intel® Core™ i7-8650U processor (quad-core, 1.90 GHz) and random-access memory of 16 GB. Solving each charge / discharge cycle took approximately 20 – 30 seconds. To allow for capacity stabilization during cycling, a total of five complete charge / discharge cycles were simulated and results for the fifth cycle are reported, unless stated otherwise.

3. *Chronopotentiometry at a planar electrode*

To gain insight into the underlying physics of electron transfer in two-electron compounds, we first model this process for a one-dimensional planar electrode (**Figure II-1a**). Chronopotentiometry is a constant-current technique that measures potential at the electrode surface arising from surface redox reactions coupled with boundary layer diffusion, as opposed to galvanostatic cycling, where transport primarily takes place via the convection of bulk species whose concentrations change over time. Although the modes of transport are different, chronopotentiometry displays analogous behavior to galvanostatic cycling and can therefore serve as a basis for interpreting the underlying physics present in both systems. For brevity, we examine only the oxidation of A to A^{2+} via sequential electron transfers, assuming that all species have equal diffusion coefficients and comproportionation reaction rates are negligible. When a constant current is applied to a planar electrode, the reactant species concentration at the surface decreases until inevitably approaching zero, which results in a sharp increase in potential. The time required for this process is commonly referred to as Sand's time,[33] $t_{sand}^{(n)}$ (s), as shown in **Equation (V.37)**:

$$t_{sand}^{(n)} = \frac{\left(nFSC_j^{\infty}\right)^2 \pi D_j}{4I^2} \tag{V.37}$$

n is the number of electrons transferred per redox reaction (here, $n = 1$). **Figure V-2a** shows the time-dependent potential response for a constant current applied to a planar electrode for a two-electron donating species, A, with an exemplary value of $\Delta E^{(A)} = 0.6\text{ V}$. The first plateau, corresponding to the oxidation of A to A^{+} (**Equation (V.1)**), is equivalent to a traditional Sand's time measurement for a one-electron transfer. Then, as A^{+} continues to be oxidized to A^{2+} (**Equation (V.2)**), a much longer second plateau can be observed until eventually reaching another sharp increase in potential. Note that the time required to reach this second asymptote is equivalent to that for a concerted two-electron transfer (**Equation (V.37)**); however, similar to galvanostatic cycling, the time spent at each plateau is unequal.[26,145–147]

Although initially dissimilar plateau durations may seem unintuitive, a closer look at the temporal evolution of the concentration and current distributions reveals this to be a sensible outcome (**Figure V-2b** and **Figure V-2c**). Consistent with conventional Sand's time, the concentration of species A reaches zero at $t = t_{sand}^{(1)}$. However, as current continues to flow, A does not stop diffusing from the bulk; rather, the oxidation of A continues contributing significantly to the current, resulting in an elongation of its concentration profile. Correspondingly, the concentration of A^+ at the surface (**Figure V-2c**) increases sharply as $t \rightarrow t_{sand}^{(1)}$ but decreases more gradually because the partial current (I_2) of the second oxidation remains low as A^+ freely diffuses away from the electrode. Thus, despite the higher potential plateau corresponding to the second oxidation, the first oxidation continues to supply a significant fraction of current (I_1), extending the duration of the second plateau as compared to the first. Although analytically simpler, this illustration of chronopotentiometric reaction-diffusion at a planar electrode is analogous to the physics present during galvanostatic charge / discharge and underpins the combined effects of thermodynamics, kinetics, and mass transfer on two-electron transfer compounds.

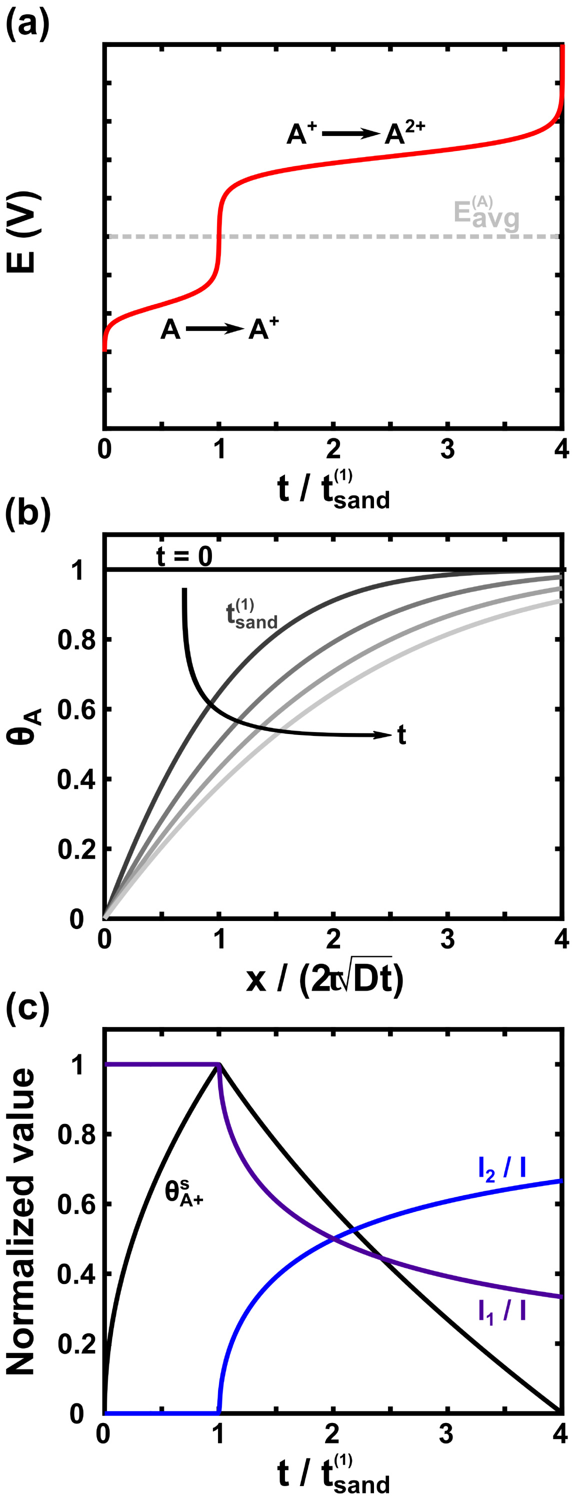

***Figure V-2**. (a) Chronopotentiometry at a planar electrode for a generic $E_{avg}^{(A)}$ and $\Delta E^{(A)}$; the response is independent of the applied current. (b) Temporal evolution of the dimensionless concentration profile for species* A. *(c) Temporal evolution of the dimensionless surface concentration of species* A^+ *and the normalized partial currents.*

4. Two-electron galvanostatic half-cell cycling

With a foundational understanding of the combined factors influencing electrode polarization, we extended our analysis to galvanostatic charging / discharging of two-electron compounds to interrogate their cycling performance. Here, we consider only a single half-cell (**Figure II-1b**), assuming the other half-cell remains at a fixed reference potential of 0 V, and apply a constant, dimensionless charging rate for both charge and discharge (Ψ), which is defined as the applied current relative to the mass transfer limiting current. The resulting potential is a measure of the kinetic and mass transport losses in the half-cell, but note that this model neglects ohmic losses. While these are generally a dominant source of voltage loss in RFBs,[47] they are mostly independent of redox-active material properties, which are the focus of this work. To aid comparison, we initially assume all species have equal mass transfer coefficients ($\gamma_{A^+} = \gamma_{A^{2+}} = 1$) and that comproportionation reaction rates are negligible ($\kappa = 0$); these complicating factors will be introduced subsequently and sequentially to explore their individual effects.

Figure V-3a shows a typical charge / discharge profile for a two-electron transfer process at an intermediate dimensionless current ($\Psi = 0.25$), comparing the response of a concerted electron transfer to that of the more commonly observed sequential electron transfer both with and without a potential difference ($\Delta E^{(A)} = 0.6$ V and $\Delta E^{(A)} = 0$ V, respectively). Because τ is non-dimensionalized by the charging capacity for a one-electron transfer, the theoretical capacity for the two-electron system is, by definition, $\tau = 2$. The accessed capacity (i.e., the maximum value of τ) is directly related to the applied current—in the case of equal mass transfer coefficients, the accessed capacity equals $2(1-\Psi)$. This means that, in the case of $\Psi = 0.25$, the electrolyte undergoes a state of charge (SOC) swing between 12.5% and 87.5% and accesses 75% of the theoretical capacity. Comparing the electrochemical responses, we initially observe a non-negligible difference between the concerted and sequential ($\Delta E^{(A)} = 0 \text{ V}$) electron transfer mechanisms. Specifically, there is a slightly larger difference between average charging and discharging potentials calculated for the sequential mechanism (31.3 mV) compared to the concerted mechanism (19.2 mV), which can be understood by considering that the sequential reaction proceeds through an intermediate, imposing additional mass transfer losses (and thus overpotential).

When a potential difference is applied between the redox events, we observe the formation of two separate plateaus during cycling—during charging, the lower plateau corresponds to the oxidation of A to A^+ (**Equations (V.1)**) and the higher plateau corresponds to the oxidation of A^+ to A^{2+} (**Equation (V.2)**). For very small currents ($\Psi \approx 0.001$), the plateaus are nearly symmetric (i.e., each plateau accounts for almost the same dimensionless time), and the theoretical capacity is accessed. However, increasing currents result in reduced accessible capacity and significant plateau asymmetry (**Figure V-3b**), as demonstrated in earlier bulk electrolysis and cell cycling experiments.[26,145–147] Like the planar electrode case (**Figure V-2c**), species A is not consumed entirely once the second plateau is reached and continues contributing to the current, resulting in a slower consumption of A^+ than if no A remained. At dimensionless currents above $\Psi = 0.5$, the charging profile displays a disappearance in the first plateau—at this point, the oxidation of A on charge and the reduction of A^{2+} on discharge are mass transfer limiting (zero surface concentration) at all points during cycling, meaning the electrode polarization is driven entirely by the second reaction step. Also, because the mass transfer coefficients are assumed to be equal, the resulting charge and discharge curves are symmetric; however, this changes under varying values of γ_{A^+} and $\gamma_{A^{2+}}$ (vide infra), as mass transfer overpotentials contribute unequally to charge and discharge.

While there are several means by which the effects of asymmetry may be quantified, its most significant influence is on voltaic efficiency, which can be expressed as the ratio of the average discharge voltage to the average charge voltage. For reference, under typical cycling conditions, the coulombic efficiency is near unity, thus the voltaic efficiency is a reasonable approximation of the energy efficiency, defined as the product of the coulombic and voltaic efficiencies. In general, the voltaic efficiency decreases with increasing current as the effects of ohmic, kinetic, and mass transport losses become more pronounced, although as mentioned above, we neglect ohmic losses in this study. Additionally, we consider losses from only one half-cell with reversible kinetics, and therefore, these values should be considered as upper bounds for the voltaic efficiency under the specified conditions. Considering these constraints, the results obtained from this model cannot be quantitatively compared to the performance of experimental flow cells; however, we aim not to describe specific systems but rather investigate the phenomenology of multi-electron transfer, which is independent of more complex design features.

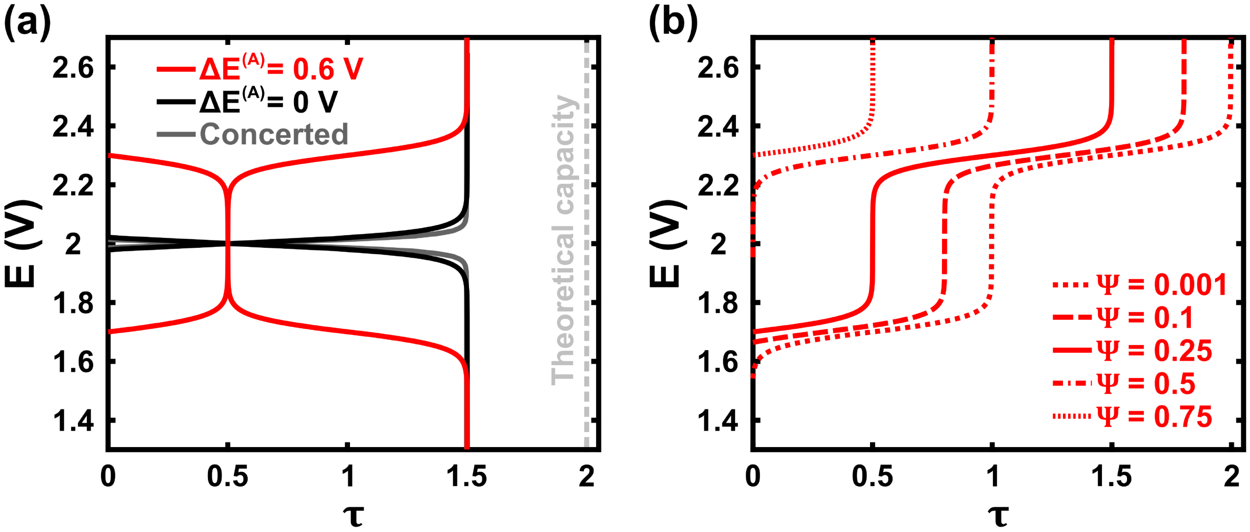

Figure V-3. *(a) Charge / discharge profiles shown for* $\Psi = 0.25$ *and different values of the potential difference (sequential mechanism) compared to the concerted mechanism, and (b) charge profiles for increasing values of dimensionless charging current (*$\Delta E^{(A)} = 0.6\ \mathrm{V}$*). Results shown for* $E_{avg}^{(A)} = 2\ \mathrm{V}$, $\gamma_{A^{+}} = \gamma_{A^{2+}} = 1$, *and* $\kappa = 0$.

Figure V-4 shows the combined effect of dimensionless charging current, potential difference, and average redox potential on the half-cell voltaic efficiency. Ranges chosen for the average redox potential and potential differences reflect values for experimentally reported redox species in aqueous and nonaqueous electrolytes. The curves are characterized by two distinct regions—at low currents, the voltaic efficiency drops rapidly with increasing current due to an imbalance between the two plateaus; at higher currents, where the first plateau disappears completely, the voltaic efficiency slope parallels that of the case where $\Delta E^{(A)} = 0\ \text{V}$ with an offset in magnitude. Importantly, the presence of a potential difference between redox events drastically reduces voltaic efficiency under all conditions, though especially at increasing currents and lower average redox potentials, which are particularly relevant for aqueous chemistries.[165] In general, voltage losses can be compensated with higher average redox potentials, but the half-cell voltaic efficiency for sequential processes may still suffer a 10 – 20% decrease at moderate currents and high cell voltages compared to the concerted process, which represents the maximum voltaic efficiency. These losses in voltaic efficiency are substantial, especially considering they only account for one electrochemically reversible half-cell—additional kinetic (e.g., quasireversible and irreversible behavior,[36] low electrochemically active surface area[166]) and ohmic losses (e.g., electrolyte and membrane resistance[47]) will further reduce overall efficiency.

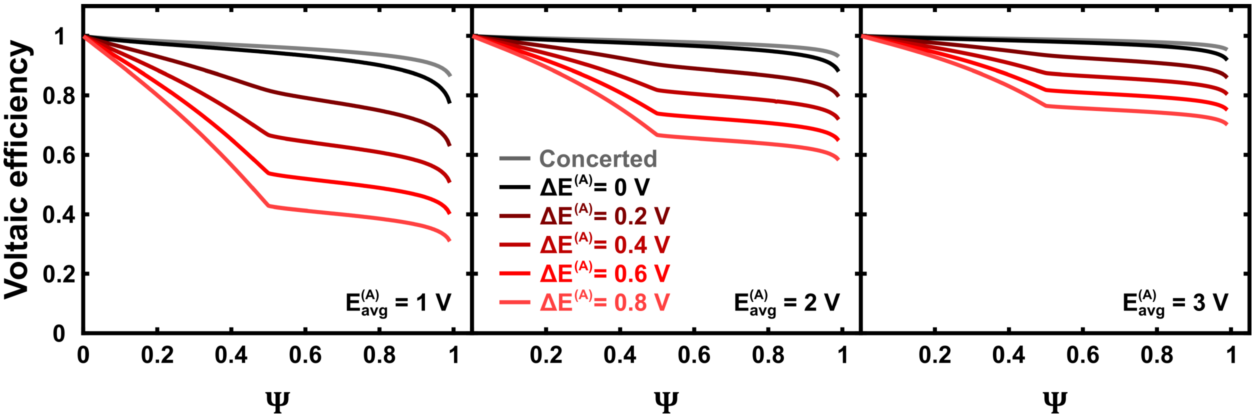

Figure V-4. *Half-cell voltaic efficiency as a function of dimensionless charging current, comparing a concerted two-electron transfer to a sequential two-electron transfer with varied* $\Delta E^{(A)}$ *for increasing values of* $E_{avg}^{(A)}$. *Results shown for* $\gamma_{A^+} = \gamma_{A^{2+}} = 1$ *and* $\kappa = 0$.

Additional mass transfer losses can be evaluated by relaxing the assumption that all species have equal mass transfer coefficients; to simplify our analysis, we will consider cases where the mass transfer rates of A^+ and A^{2+} are equal ($\gamma_{A^+} = \gamma_{A^{2+}}$) but differ from A. The values used here ($\gamma_{A^+} = 0.8, 1.2$) were estimated based on previously reported Sherwood number correlations for RFBs[167] for typical changes in diffusivity for soluble two-electron redox species in differing oxidation states.[26,145] Although the variations in mass transfer are relatively small, the effects can be readily observed from the respective charge / discharge profiles (**Figure V-5a**); specifically, the charging and discharging curves become asymmetric, as differing mass transfer rates affect the relative fluxes and, consequently, the surface concentrations of each species. Similar to the asymmetry between plateaus described already (see **Figure V-4**), this additional asymmetry impacts the half-cell voltaic efficiency (**Figure V-5b**). First, we observe the appearance of an additional change in slope at intermediate dimensionless currents corresponding to the disappearance of a single charge / discharge plateau. For example, when $\gamma_{A^+} = 0.8$, the first plateau on the discharging curve will disappear while the first plateau on the charging curve persists.

Second, as expected, slower mass transfer rates (e.g., reduced flow rates, higher electrolyte viscosity, larger redox-active molecules) correspond to lower voltaic efficiencies at all currents.

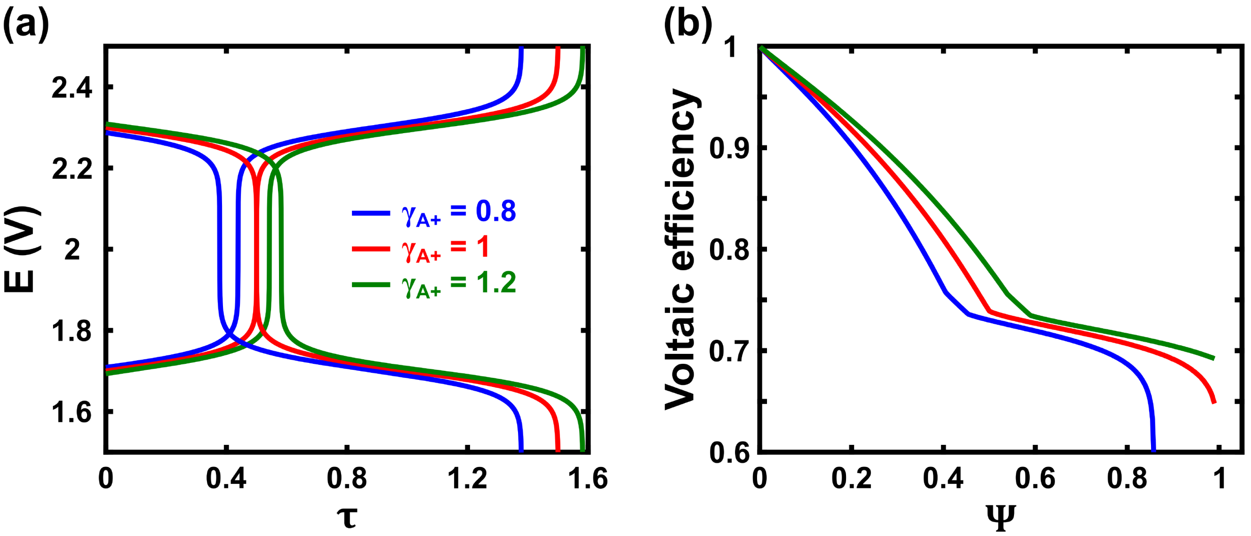

Figure V-5. *(a) Charge / discharge profiles shown for* $\Psi = 0.25$ *and (b) half-cell voltaic efficiency as a function of dimensionless current for varying mass transfer coefficients (*$\gamma_{A^+} = \gamma_{A^{2+}}$*). Results shown for* $E_{avg}^{(A)} = 2\text{ V}$*,* $\Delta E^{(A)} = 0.6\text{ V}$*, and* $\kappa = 0$.

Given the inclusion of variable mass transfer coefficients, the differences between individual species thus necessitates the treatment of comproportionation reactions. When considering sequential electrode reactions of identical kinetic and mass transport conditions, comproportionation does not play a distinguishable role in determining the electrode potential as the species identity does not influence boundary layer fluxes.[168,169] Comproportionation yields a shift in the time-dependent bulk concentrations toward the formation of A^+ (**Figure V-6a**), and with varying mass transport coefficients, this causes charge / discharge curves to become increasingly asymmetric, thus accentuating voltaic efficiency losses that arise from differences in mass transfer (**Figure V-6b**). However, for comproportionation to proceed, both A and A^{2+} must be present in solution concurrently—therefore, this effect only occurs where mass transfer limitations lead to simultaneous oxidation of A and A^+ (charging) or reduction of A^{2+} and A^+

(discharging). These simultaneous reactions only constitute a fraction of the total charging time, which increases with increasing current, meaning that its influence on voltaic efficiency only becomes discernable at dimensionless currents above $\Psi \approx 0.5$. Operation under such low accessible capacity regimes is likely to be impractical and inefficient, and as such, we tentatively conclude that comproportionation for two-electron transfer is negligible under typical galvanostatic conditions. Note that in this treatment, comproportionation and disproportionation reactions are assumed to occur only in the bulk as opposed to the mass transfer boundary layer. This assumption ignores the expected non-linear boundary layer concentrations, although even if the concentrations were to change in the boundary layer, the system is still beholden to the fact that comproportionation reactions only occur alongside the simultaneous oxidation / reduction of both species, so any significant effects will still be restricted to higher currents. As a result, we expect this will have only minor effects on the overall voltaic efficiency and, consequently, the conclusions drawn here are expected to remain valid.

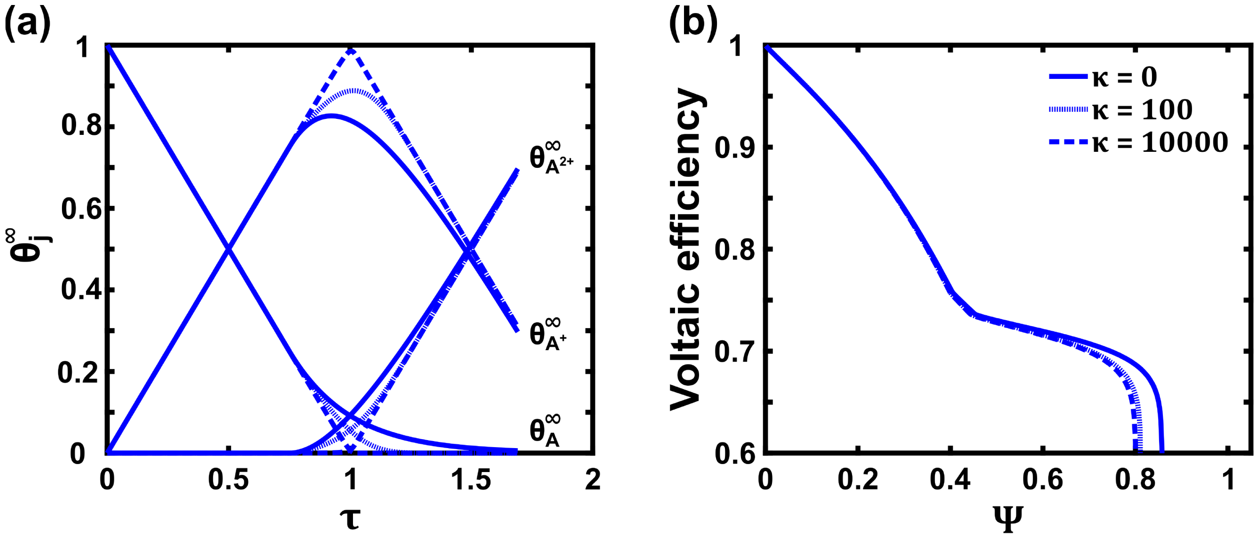

Figure V-6. *(a) Dimensionless concentration profiles as a function of dimensionless time (τ), shown for the first charging step ($\Psi = 0.25$) and (b) half-cell voltaic efficiency as a function of dimensionless charging current (Ψ) for varying values of the dimensionless comproportionation rate constant: $\kappa = 0$, $\kappa = 100$, and $\kappa = 10000$. Results shown for $\gamma_{A^+} = \gamma_{A^{2+}} = 0.8$, $E_{avg}^{(A)} = 2$ V, and $\Delta E^{(A)} = 0.6$ V.*

5. Full cell analysis with two-electron compounds at both electrodes

To this point, we have only considered two-electron compounds in a half-cell, holding the counter half-cell at a constant reference potential (0 V). However, the presence of two-electron reactions in both half-cells presents additional voltage losses. Here, we introduce a second redox-active species, *B*, which undergoes analogous two-electron transfer according to **Equations (V.38)** and **(V.39)** (**Figure II-1c**):

$$B \rightleftharpoons B^{+} + e^{-} \tag{V.38}$$

$$B^{+} \rightleftharpoons B^{2+} + e^{-} \tag{V.39}$$

Species *B* is subject to the same governing equations as species *A*, which are detailed in the **SI**. For simplicity, we once again neglect ohmic losses and assume that mass transfer rates for all species are equal, the latter of which implies comproportionation / disproportionation reactions can also be ignored. In addition, we impose $\Delta E^{(A)} = \Delta E^{(B)} = 0.6\ \mathrm{V}$ and $E_{avg}^{(B)} = 0\ \mathrm{V}$ for all analyses presented here. Note that half-cell reactions proceed in opposite directions—a positive, oxidizing current applied to species *A* corresponds to a negative, reducing current applied to species *B*, and vice versa.

While one would correctly expect voltage losses to double in the case of a full cell if *A* and *B* were symmetric (i.e., equal concentrations, volumes, states of charge, transport properties, cell features), there are additional factors when this symmetry deviates that further hinder performance. In particular, we study charge imbalance (i.e., where the half-cells exist at different states of charge), which may result from self-discharge reactions occurring in the bulk or undesired side reactions (e.g., solvent or supporting salt decomposition, crossover-induced self-discharge, redox species decay). For one-electron compounds, this primarily impacts the accessible capacity because one half-cell becomes capacity-limiting during charge while the other is capacity-limiting during discharge.[31] For two-electron compounds, the effects of charge imbalance become more pronounced, significantly impacting the shape of the charge / discharge curves and the subsequent voltaic efficiency.[146] To quantify charge imbalance between the two half-cells, we vary the initial dimensionless concentration of A (θ_A^o), assuming the initial dimensionless concentration of B^{2+} is 1.

Figure V-7a shows representative cycling profiles for the full cell potential at varying degrees of charge imbalance. Most notably, because each compound features a potential difference ($\Delta E^{(j)}$), the difference between plateaus is doubled for the full cell. In the presence of charge imbalance, an intermediate plateau appears, corresponding to the disappearance of the first potential plateau for one half-cell. For example, during the charging step, species A will be fully oxidized to A^{+} before species B^{2+} can be fully reduced to B^{+}, resulting in the intermediate plateau, which extends with increasing degrees of charge imbalance. **Figure V-7b** shows the resultant effect of these behaviors on voltaic efficiency. Compared to the single half-cell examined in **Figure V-4**, the inclusion of both half-cells doubles the associated losses and further diminishes the voltaic efficiency. Like the case of different mass transfer rates, charge imbalance leads to a characteristic region corresponding to the sequential disappearance of charge / discharge plateaus at increasing dimensionless currents. However, despite the reduction in dimensionless capacity shown in **Figure V-7a**, charge imbalance causes only minor losses in voltaic efficiency at low to moderate currents ($0.2 < \Psi < 0.5$). Overall, the combined effects of two-electron compounds at both electrodes and charge imbalance result in heightened voltaic efficiency losses compared to the single half-cell.

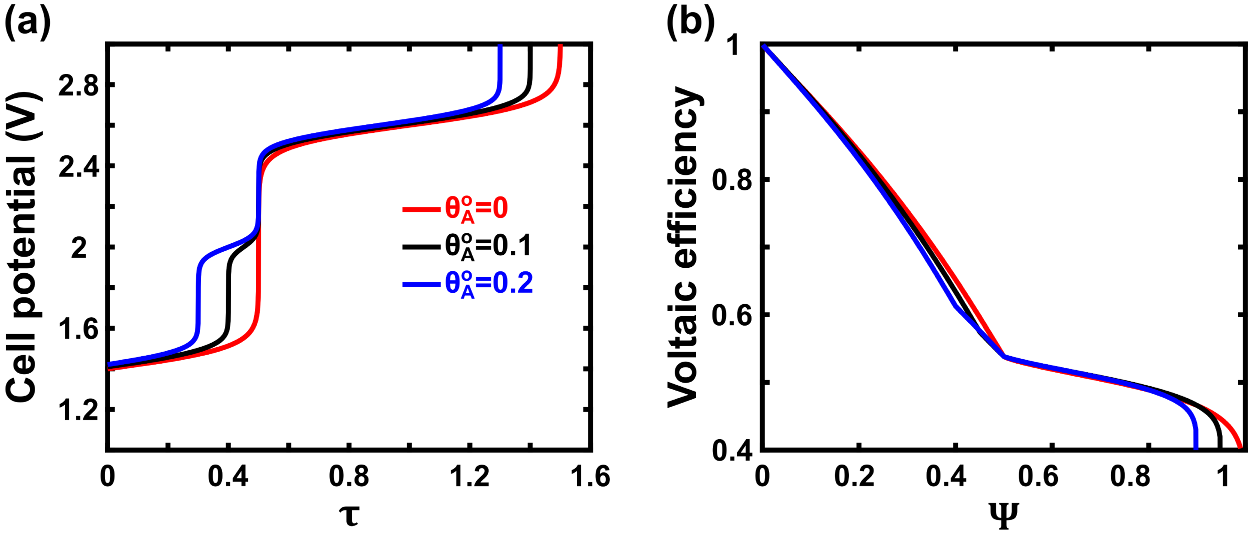

***Figure V-7**. (a) Charge / discharge profiles shown for* $\Psi = 0.25$ *and (b) full cell voltaic efficiency as a function of dimensionless current for varying extents of charge imbalance. Results shown for* $E_{avg}^{(A)} = 2$ V, $E_{avg}^{(B)} = 0$ V, $\Delta E^{(A)} = \Delta E^{(B)} = 0.6$ V, $\gamma_j = 1$, *and* $\kappa = 0$.

6. Design strategies for multi-electron RFBs

The models explored here provide initial evidence that the multi-electron approach, while promising, has significant limitations if operating conditions and molecular design are not carefully considered. Even under optimistic conditions (i.e., losses at one electrode, reversible kinetics, no ohmic losses), we observe 10 – 20% losses in voltaic efficiency at moderate dimensionless currents ($\Psi \approx 0.2$), and these losses grow as the average redox potential decreases and potential difference increases (ca. 30 – 40% losses). Therefore, the advantages of increased charge storage capacity in multi-electron transfer must be weighed against the drawbacks in flow battery performance for a given redox chemistry.

In particular, the losses observed here for two-electron materials are driven primarily by mass transfer, requiring current densities well below the mass transfer limit and / or considerably high mass transfer coefficients to maintain high voltaic efficiency. Such conditions present a complex design tradeoff, where additional stack costs due to increasing cell area and pumping costs due to improving mass transfer rates compete with concomitant advancements in electrochemical performance. This may restrict the viable operating space to applications where costs are less dependent on energy efficiency, as the ability to tolerate voltage losses is closely tied to techno-economics and system specifications. For example, long-duration and/or low current energy storage applications may be comparatively more tolerant of low voltaic efficiencies if other related capital costs are sufficiently low.[170,171] Alternatively, higher cell voltages, enabled by nonaqueous electrolytes[144] and certain aqueous electrolytes,[172] can at least partially offset the increased overpotentials of multi-electron transfer (**Figure V-4**).

To reduce the losses associated with sequential multi-electron transfer, molecular engineering efforts should aim to minimize the potential difference between electron transfer events without sacrificing cell voltage, solubility, or stability. Independently tuning the properties of individual redox events (e.g., potential inversion[173]) is a significant challenge, but future molecular engineering campaigns can build upon previously established examples and strategies, presenting new opportunities for research in this area.[151,152,174–177] For example, Kini et al. demonstrated that nonaqueous anthraquinone derivatives may undergo potential inversion by virtue of successive benzo substitution. Upon functionalization from the tetracyano napthaquinone to the analogous anthraquinone derivative, a shift is observed from sequential one-electron transfer events to a concerted two-electron transfer due to the distorted, non-planar molecular structure of the anthraquinone.[174,177] Similarly, engineering the supporting electrolyte (i.e., solvent and supporting salt) may serve as an additional handle to modulate the properties of multi-electron redox couples.[178–180] These examples highlight the need for a more holistic conceptualization of the combined steric and electronic character of such molecules that influence their electrochemical nature, which should serve to advance fundamental knowledge in molecular electrochemistry and lead to improved nonaqueous RFB chemistries. Conversely, many aqueous organic compounds that undergo proton-coupled electron transfer already exhibit multi-electron reactions with a minimal potential difference,[37,148,149] but these electron transfer reactions should be carefully scrutinized to elucidate gaps between their redox potentials,[29] as the low cell voltages of these systems make them more susceptible to performance losses.

7. Conclusions

The emergence of charge storage materials that support the reversible transfer of multiple electrons provides new pathways toward high energy density, low-cost charge storage. However, depending on the electrochemical and transport properties of the redox electrolyte, these multi-electron compounds face inherent design tradeoffs between improved storage capacity and diminished voltaic efficiency. Here, we have explored various electrochemical models to describe the underlying phenomenology of two-electron transfer in RFBs and to estimate upper bounds for these performance tradeoffs, focusing on the redox electrolyte properties and foregoing more complex geometric constraints. These results reveal that the charging rate (Ψ), average redox potential ($E_{avg}^{(j)}$), and potential difference between redox events ($\Delta E^{(j)}$) primarily drive voltaic efficiency losses, with relative mass transfer rates (γ_j) and comproportionation rates (κ) playing more nuanced roles. Considering the possible limitations, synthetic chemists and material scientists may seek new strategies to tune independent redox events, such as introducing concepts of potential inversion for nonaqueous electrolytes or leveraging existing knowledge of proton-coupled electron transfer for aqueous electrolytes. This low-dimensional modeling approach can further serve as a framework to bound performance for novel charge storage materials, including those with more complex electron transfer mechanisms, and to predict performance prior to embarking on complicated and time-consuming cell cycling studies.

8. *List of symbols*

Roman symbols

C_j^z	Concentration of species *j* in state *z* (mol m^{-3})
C_T^∞	Total bulk species concentration (mol m^{-3})
D	Diffusion coefficient (m^2 s^{-1})
E	Electrode potential (V)
$E_1^{(j)}$	Formal redox potential for the first oxidation of species *j* (V)
$E_2^{(j)}$	Formal redox potential for the second oxidation of species *j* (V)
$E_{avg}^{(j)}$	Average redox potential of species *j* (V)
$\Delta E^{(j)}$	Difference in formal redox potentials of species *j* (V)
F	Faraday's constant (96485 C mol^{-1})
I	Galvanostatic charging current (A)
I_1	Partial current for the first oxidation (A)
I_2	Partial current for the second oxidation (A)
k_d	Disproportionation rate constant (m^3 mol^{-1} s^{-1})
$k_{m,j}$	Convective mass transfer coefficient of species *j* (m s^{-1})
k_p	Comproportionation rate constant (m^3 mol^{-1} s^{-1})
n	Number of electrons transferred per redox reaction
N_j	Molar flux of species *j* (mol m^{-2} s^{-1})
r_d	Bulk disproportionation rate (mol m^{-3} s^{-1})
r_p	Bulk comproportionation rate (mol m^{-3} s^{-1})
R	Universal gas constant (8.314 J mol^{-1} K^{-1})
S	Electrode surface area (m^2)
t	Time (s)
$t_{sand}^{(n)}$	Sand's time for a redox reaction with n electrons (s)
T	Temperature (K)
V	Electrolyte volume (m^3)
x	Axial position perpendicular to the planar electrode surface (m)

Greek symbols

γ_j	Dimensionless mass transfer coefficient of species *j*
η	Integration variable (s)
θ_j^z	Dimensionless concentration of species *j* in state *z*
κ	Dimensionless comproportionation rate
τ	Dimensionless charging time
Ψ	Dimensionless charging current

Superscripts

s	Surface
∞	Bulk solution
o	Initial state

VI. A method for quantifying crossover in redox flow cells through compositionally unbalanced symmetric cell cycling

1. Background

Membrane / separator properties are often measured through a suite of ex situ techniques to quantify permeability and conductivity.[28,136,181] While these properties offer a means to compare different materials, flow cell testing is necessary to evaluate transport under representative RFB conditions—high current densities, time-varying species concentrations. One solution is to simply test the membrane / separator in a flow cell with the redox chemistry of interest and report metrics such as rate-dependent coulombic efficiency, voltaic efficiency, and capacity retention.[138] While this approach offers insight into membrane / separator efficacy, the results are typically obscured by a multitude of confounding factors including other sources of voltage loss (e.g., kinetic and concentration overpotentials) and capacity fade (e.g., species decay, side reactions).[66,182] To isolate membrane / separator contributions, earlier efforts have established methods for monitoring crossover under controlled conditions with applied electric fields.[56,52,57,61,183,60,184] For example, Sing and Meyers previously demonstrated a 4-chamber, 3-membrane redox flow cell design,[56] enabling direct quantification of individual modes of active species transport and leading to adoption by others in the RFB community.[52,57] However, these experiments require a customized cell architecture and continuous electrolyte monitoring, challenging broad implementation and high-throughput experimentation. By instead devising a methodology for measuring crossover in a conventional flow cell configuration, we aim to develop a widely accessible tool for characterizing membranes / separators under well-defined operating conditions.

In this work, we present a technique for quantifying crossover in a traditional zero-gap flow cell (**Figure VI-1**), drawing inspiration from the symmetric cell cycling method commonly used to evaluate redox species stability.[31,42] However, instead of maintaining equal active species concentrations in each half-cell, we introduce a concentration gradient, which promotes a continuous flux of active species through the membrane / separator, from the high concentration half-cell (donor) to the low concentration half-cell (receiver) during cycling. This compositionally unbalanced symmetric cell cycling (CUSCC) allows for characterization of crossover rates under galvanostatic conditions, facilitating quantification of species fluxes as a function of applied current. We first derive a zero-dimensional model to describe the fundamental processes that underpin the technique, establishing characteristic "capacity gain" behavior and examining the impact of varying experimental conditions and transport properties. We then conduct proof-of-concept experiments using a model redox couple ($Fe^{2+/3+}$) with a Nafion™ 117 (N117) cation-exchange membrane, demonstrating the overall utility and accuracy of the approach. Finally, we leverage the zero-dimensional simulations to perform parameter estimation, allowing for property extraction from CUSCC testing that yields values in good agreement with those obtained from independent ex situ measurements. Overall, this methodology provides a facile, easily-implementable approach for measuring crossover in candidate RFB membranes / separators, enabling versatile and informative experimentation across a range of flow cell conditions.

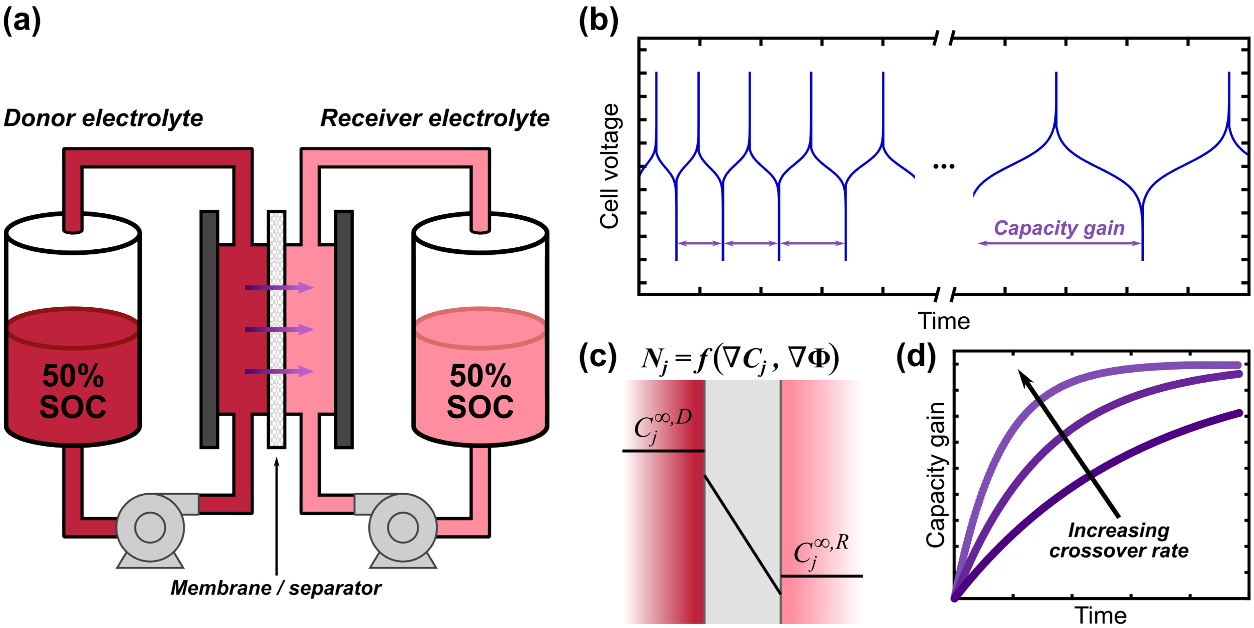

Figure VI-1. *(a) Illustrative schematic of compositionally unbalanced symmetric cell cycling (CUSCC). Both electrolytes are initially prepared at 50% state-of-charge (SOC) and darker colors indicate higher concentrations of active species. The concentration imbalance between half-cells induces a continuous flux of species across the membrane / separator during cycling, as indicated by the purple arrows. (b) Representative charge / discharge profiles, depicting the increase in capacity (i.e., capacity gain) over time due to crossover. (c) Illustrative schematic of species flux through the membrane, which is a function of the concentration and potential gradients. (d) Representative capacity gain profiles over time, highlighting the influence of crossover rate on CUSCC.*

2. *Symmetric cell cycling model*

The theoretical framework used here closely follows **Chapter III**,[182] but is modified to describe a symmetric cell. In general, we consider a single redox species, A, undergoing a one-electron transfer to form A^+ according to **Equation (VI.1)**.

$$A \rightleftharpoons A^+ + e^- \tag{VI.1}$$

The active species A and A^+ have ionic charges, z_j, such that $z_{A^+} = z_A + 1$. Treating each half-cell as one continuous, well-mixed domain, the mass balances for both species can be written according to **Equations (VI.2) – (VI.5)**, where t (s) represents the time from the beginning of each half-cycle (i.e., charge or discharge) and the applied current, I (A) is positive for charge and negative for discharge.

$$\frac{dC_A^{\infty,R}}{dt} = -\frac{I}{V^R F} + \frac{N_A A_m}{V^R} \tag{VI.2}$$

$$\frac{dC_{A^+}^{\infty,R}}{dt} = \frac{I}{V^R F} + \frac{N_{A^+} A_m}{V^R} \tag{VI.3}$$

$$\frac{dC_A^{\infty,D}}{dt} = \frac{I}{V^D F} - \frac{N_A A_m}{V^D} \tag{VI.4}$$

$$m_T = C_{A^+}^{\infty,D} V^D + C_A^{\infty,D} V^D + C_{A^+}^{\infty,R} V^R + C_A^{\infty,R} V^R \tag{VI.5}$$

$C_j^{\infty,h}$ (mol m^{-3}) is the bulk concentration of species j in half-cell h (either the donor electrolyte, D, or the receiver electrolyte, R), V^h (m^3) is the constant electrolyte volume in half-cell h, F (96,485 C mol^{-1}) is the Faraday constant, N_j (mol m^{-2} s^{-1}) is the flux of species j through the membrane / separator (defined as positive for transport from the donor electrolyte to the receiver electrolyte), A_m (m^2) is the membrane / separator geometric area, and m_T (mol) is the total moles of A and A^+, which is constant in the absence of active species decay. Note that **Equation (VI.5)** is an expression of mass conservation. The governing differential equations are subject to the initial condition defined in **Equation (VI.6)**, where $C_j^{o,h}$ is the concentration of species *j* in half-cell *h* at the beginning of the half-cycle.

$$C_j^{\infty,h}\left(t=0\right)=C_j^{o,h} \tag{VI.6}$$

According to Darling et al., the steady-state flux of species *j* from the donor to receiver electrolyte, N_j (mol m^{-2} s^{-1}), can be derived analytically as shown by **Equations (VI.7)** and **(VI.8)** , assuming that transference numbers are given by dilute solution theory, the species fluxes remain at steady-state (i.e., concentration changes in the membrane / separator are fast relative to concentration changes in the donor and receiver compartments), and the active species are minor charge carriers (i.e., excess supporting salt concentration).[48]

$$N_j=\frac{D_j^m K_j}{l_m}\gamma_j\left(\frac{C_j^{\infty,D}\exp(\gamma_j)-C_j^{\infty,R}}{\exp(\gamma_j)-1}\right) \tag{VI.7}$$

$$\gamma_j=-\left(\frac{z_j F}{\kappa_m RT}+\frac{\xi}{\lambda C_{\mathrm{site}} D_j^m F}\right)\frac{I\,l_m}{A_m} \tag{VI.8}$$

D_j^m (m^2 s^{-1}) is the diffusion coefficient of species *j* through the membrane / separator, K_j (dimensionless) is the partition coefficient of species *j*, l_m (m) is the membrane / separator thickness, γ_j (dimensionless) is a flux parameter for species *j*, κ_m (S m^{-1}) is the membrane / separator ionic conductivity, *R* (8.314 J mol^{-1} K^{-1}) is the universal gas constant, and *T* (K) is the absolute temperature. For an ion-selective material, ξ (dimensionless) is the electro-osmotic coefficient, λ (dimensionless) is the molar ratio of solvent to fixed ion sites in the membrane, and C_{site} (mol m^{-3}) is the concentration of fixed ion sites in the membrane. Considering the species flux is linear with respect to concentration, **Equation (VI.7)** can be restated in terms of first-order rate constants as shown in **Equation (VI.9)**.[182]

$$\frac{N_j A_m}{V^R} = k_{c,j}^{D} C_j^{\infty,D} - k_{c,j}^{R} C_j^{\infty,R} \tag{VI.9}$$

$k_{c,j}^{h}$ (s^{-1}) is the crossover rate constant for species j in half-cell h. The mass balances can then be written in matrix form according to **Equations (VI.10)** and **(VI.11)**.

$$\frac{d}{dt}\mathbf{C} = \mathbf{b} - \mathbf{K}\mathbf{C} \tag{VI.10}$$

$$\mathbf{C}(t = 0) = \mathbf{C}^{\mathbf{o}} \tag{VI.11}$$

C (mol m^{-3}) is a column vector containing the 3 bulk species concentrations (i.e., $C_A^{\infty,R}$, $C_{A^+}^{\infty,R}$, $C_A^{\infty,D}$) with $C_{A^+}^{\infty,D}$ given by **Equation (VI.5)**, **b** (mol m^{-3} s^{-1}) is a column vector containing constant terms, **K** (mol m^{-3} s^{-1}) is a matrix containing the first-order rate constants, and $\mathbf{C}^{\mathbf{o}}$ (mol m^{-3}) is a column vector containing the initial concentrations. Because **K** is a positive semi-definite matrix, the mass balances can be solved analytically to yield **Equation (VI.12)**.

$$\mathbf{C} = \mathbf{U}\left(\boldsymbol{\Lambda}^{-1}\mathbf{U}^{-1}\mathbf{b} - \boldsymbol{\Lambda}^{-1}\exp\left(-\boldsymbol{\Lambda}t\right)\left(\mathbf{U}^{-1}\mathbf{b} - \boldsymbol{\Lambda}\mathbf{U}\mathbf{C}^{\mathbf{o}}\right)\right) \tag{VI.12}$$

U (dimensionless) and **Λ** (s^{-1}) are the eigenvector and diagonal eigenvalue matrices of **K**, respectively. The charge and discharge capacities at cycle N—$\mathrm{Cap}_{\mathrm{c}}^{\mathrm{N}}$ and $\mathrm{Cap}_{\mathrm{d}}^{\mathrm{N}}$ (C), respectively—are taken to be the earliest time at which one of the reacting species concentrations at the electrode surface, $C_j^{s,h}$ (mol m^{-3}), reaches zero. To calculate the surface concentrations from the bulk concentrations, we assume that species transport is driven by advection and can be described by **Equation (VI.13)**.

$$I = \pm F A_{ed} k_{m,j} \left(C_j^{\infty,h} - C_j^{s,h} \right) \qquad \text{(VI.13)}$$

A_{ed} (m^2) is the accessible surface area of the porous electrode, $k_{m,j}$ ($m\ s^{-1}$) is the mass transfer coefficient of species j, which is taken to be equal for all species.

All simulations were performed using MATLAB® R2021b on a Dell Latitude 7290 laptop computer with an Intel® Core™ i7-8650U processor (quad-core, 1.90 GHz) and a random-access memory of 16 GB. Eigenvalues and eigenvectors were calculated using the *eig* function and nonlinear algebraic equations were solved implicitly using the *fsolve* function. Each calculation required < 0.05 s per cycle (i.e., charge and discharge).

3. *Experimental procedures*

Unless noted otherwise, all materials preparation, storage, and testing were conducted under ambient conditions. Iron(III) chloride hexahydrate ($FeCl_3 \cdot 6H_2O$, 97%), magnesium chloride hexahydrate ($MgCl_2 \cdot 6H_2O$, 99%), chromium(III) chloride hexahydrate ($CrCl_3 \cdot 6H_2O$, 98%), and hydrochloric acid (HCl, 37% in water) were obtained from Sigma Aldrich. Iron(II) chloride tetrahydrate ($FeCl_2 \cdot 4H_2O$, 98%) was obtained from Alfa-Aesar. All reagents were used as received; $FeCl_2$, $FeCl_3$, $MgCl_2$, and $CrCl_3$ were stored at room temperature in a nitrogen box. Electrolytes were prepared in volumetric flasks using deionized water (Milli-Q Millipore, 18.2 MΩ). For all tests, the donor electrolyte contained 500 mM $FeCl_2$ and 500 mM $FeCl_3$ dissolved in 2 M HCl while the receiver electrolyte contained 50 mM $FeCl_2$, 50 mM $FeCl_3$, 450 mM $CrCl_3$, and 450 mM $MgCl_2$ dissolved in 2 M HCl. Ion-exchange membranes (N117) and porous carbon electrodes (SGL 29AA) were obtained from Fuel Cell Store. Prior to use, SGL 29AA electrodes were cut to 1.4 cm × 1.6 cm using a razor blade and subsequently heat-treated at 400 °C for 30 h to increase physical surface area and improve aqueous electrolyte wetting.[166]

3.1. Sorption measurements

To measure partition coefficients and electrolyte uptake, 4 samples of dry, as-received N117 were cut to 6.25 cm^2 (2.5 cm × 2.5 cm) using a razor blade and soaked in separate 5 mL samples of donor electrolyte for 72 h.[52] Wet masses were recorded after gently drying the samples with a Kimwipe to remove surface droplets. The samples were then soaked in 5 mL of 2 M HCl for 24 h to extract the absorbed species. Leached species concentrations were measured using microelectrode voltammetry (**Figure VI-2**) whereby the plateau currents are proportional to concentration.[181] Voltammograms were recorded on a CH Instruments 760e potentiostat at 10 mV

s^{-1} using a 25-μm diameter gold working electrode (BASi), a platinum wire counter electrode (BASi), and a Ag/AgCl reference electrode (BASi). Prior to use, the microelectrode was polished on a MicroCloth pad containing an aqueous slurry of 0.05 μm alumina powder (Buehler Ltd.), rinsed with deionized water, and gently dried with lens paper.

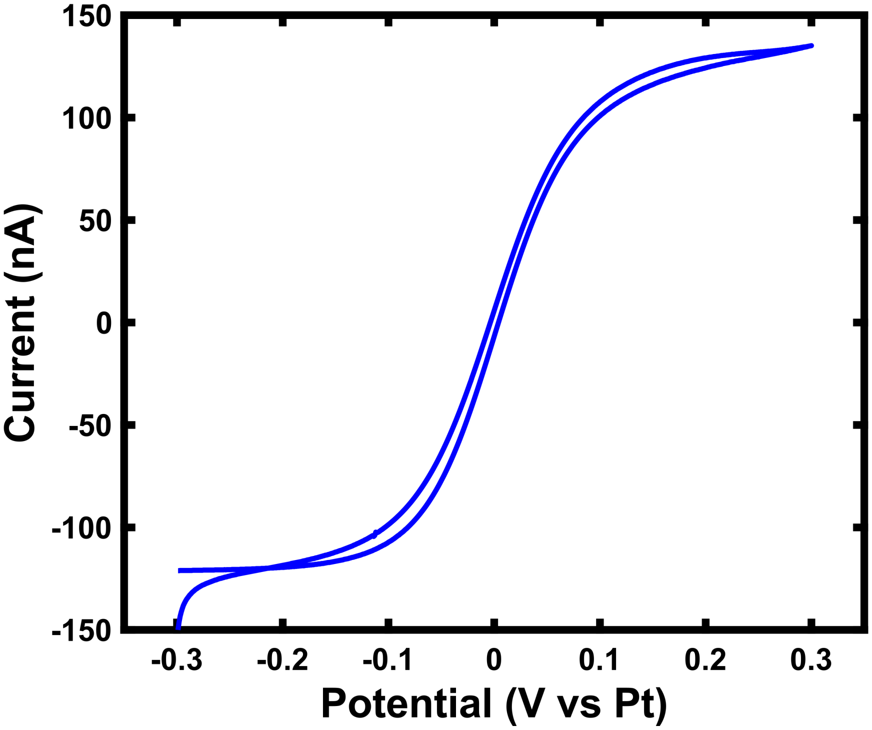

Figure VI-2. *Representative microelectrode voltammograms measured in 50 mM $FeCl_2$, 50 mM $FeCl_3$, and 2 M HCl using a 25-µm diameter gold microelectrode, Pt wire pseudo-reference electrode, and Pt coil counter electrode. Voltammograms were recorded at 10 mV s^{-1} between potentials of ±300 mV vs Pt.*

3.2. H-cell testing

Permeability was measured in an H-cell configuration featuring two ca. 20 mL reservoirs separated by a N117 membrane. Prior to use, N117 was soaked overnight in 2 M HCl. 15 mL of each electrolyte (donor and receiver) was added to their respective reservoirs and stirring was maintained at 600 rpm using 1-cm Teflon stir bars. Both reservoirs were exposed to the atmosphere (ca. 20 °C) throughout the experiment. The receiver electrolyte was equipped with a freshlypolished 25-µm diameter gold microelectrode (working electrode) and two platinum wires (counter and pseudo-reference). Concentrations were measured every hour using chronoamperometry—electrode potentials of ±250 mV vs Pt were held for 10 s and the current was averaged over the final second. Potentials were selected such that the steady-state current was in the plateau region of the voltammogram (**Figure VI-2**). The current was normalized against the initial reading to calculate increases in concentration over time (**Figure VI-3a**).[185] The permeability of each species *j* through the membrane, P_j (m^2 s^{-1}), was determined via linear regression (**Figure VI-3b**) using **Equation (VI.14)**.[186,187]

$$P_j = -\frac{l_m V^R}{2A_m}\left(\frac{d}{dt}\ln\left[1-2\frac{C_j^{\infty,R}(t)}{C_j^{\infty,R}(t)+C_j^{\infty,D}(t)}\right]\right) \tag{VI.14}$$

The diffusion coefficient can be calculated from the permeability and the partition coefficient by **Equation (VI.15)**.

$$P_j = K_j D_j \tag{VI.15}$$

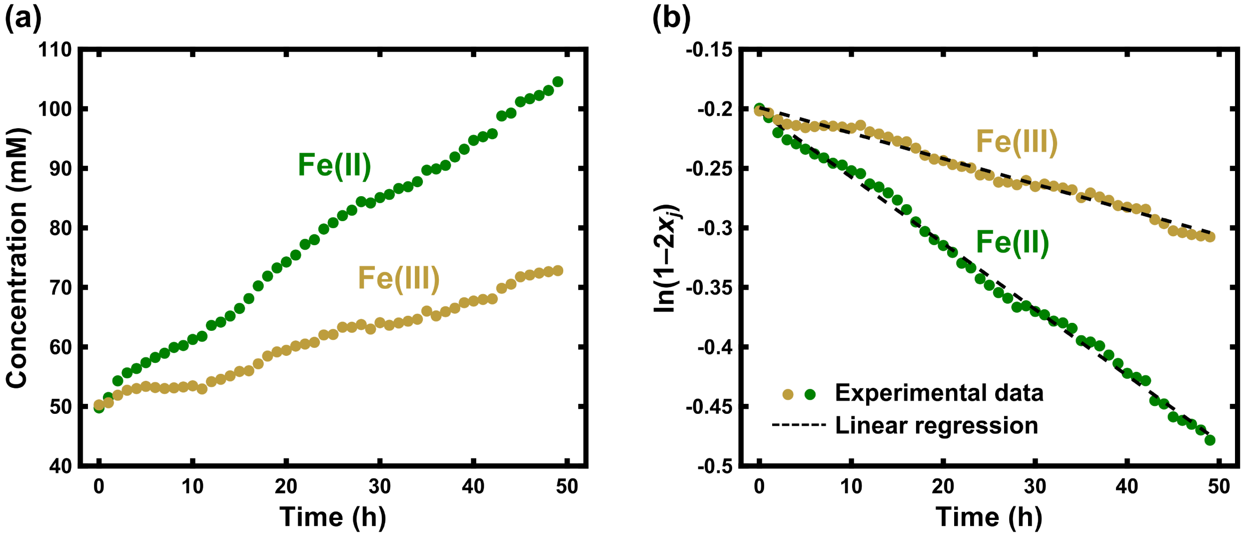

Figure VI-3. *H-cell permeability data. (a) Concentration versus time for Fe(II) and Fe(III) measured over a period of 50 h. (b) Fraction of species j in the receiver electrolyte. The donor electrolyte (15 mL) initially contains 500 mM* $FeCl_2$*, 500 mM* $FeCl_3$*, and 2 M HCl while the receiver electrolyte (15 mL) initially contains 50 mM* $FeCl_2$*, 50 mM* $FeCl_3$*, 450 mM* $MgCl_2$*, 450 mM* $CrCl_3$*, and 2 M HCl.*

3.3. Flow cell testing

Symmetric cell testing was performed on the benchtop in a custom-built, lab-scale 2.55 cm^2 redox flow cell with interdigitated flow fields, 2× SGL 29AA carbon paper electrodes in each half-cell (compressed by ca. 20% using Teflon gaskets), and a single N117 cation-exchange membrane.[42] Prior to cell construction, all membranes were soaked overnight in 2 M HCl. 15 mL of each electrolyte (donor and receiver) were stored in 25 mL media bottles and delivered to the cell at 20 mL min^{-1} through Masterflex L/S 14 Versilon tubing using a Masterflex peristaltic pump. Prior to cycling, electrolyte was circulated for 5 min to promote component wetting and bubble removal, and electrochemical impedance spectroscopy (EIS) was performed at open-circuit potential (200 kHz to 100 mHz, 10 mV amplitude) to determine the high-frequency resistance. Galvanostatic cycling was conducted at varying current densities with voltage cutoffs set to ±400, ±450, and ±550 mV for 20, 50, and 100 mA cm^{-2}, respectively, which were selected such that the ohmically-corrected voltage limits were ca. ±400 mV. Considering the redox potential of $Fe^{2+/3+}$, we do not anticipate nor observe any side reactions for the materials and operating conditions studied here. The current collector in the receiver electrolyte was set as the working electrode to ensure the conditions in the flow cell were consistent with conventions for current in the zero-dimensional model. All electrochemical tests were performed using either a Biologic VMP-3 potentiostat or a Biologic VSP potentiostat.

Membrane conductivity was measured using the same flow cell design in a single-electrolyte configuration. Initially, the cell was assembled with 4× stacked N117 membranes—soaked overnight in 2 M HCl—and donor electrolyte was circulated at 20 mL min^{-1} for 30 min to promote component wetting and bubble removal. EIS was performed every 15 min at open-circuit potential (200 kHz to 100 mHz, 10 mV amplitude) for 2 h to ensure that the high-frequency resistance stabilized. The ohmic resistance was taken to be the high-frequency resistance measured at the end of 2 h. We then disassembled the cell, removed a N117 membrane, reassembled the cell with the same components, and repeated the EIS measurements. Conductivity was determined from the slope of the ohmic resistance versus number of membranes (**Figure VI-4**). Assuming contact resistance between membranes in negligible, the conductivity can be determined from the slope of the resistance versus number of membranes (dR_Ω / dN117) according to **Equation (VI.16)**.

$$\kappa_m = \frac{l_m}{\left(\frac{dR_\Omega}{d\mathrm{N}117}\right)A_m} \tag{VI.16}$$

The slope in **Figure S3** is 0.25 ± 0.02 Ω, yielding a conductivity of 3.6 ± 0.2 S m^{-1}.

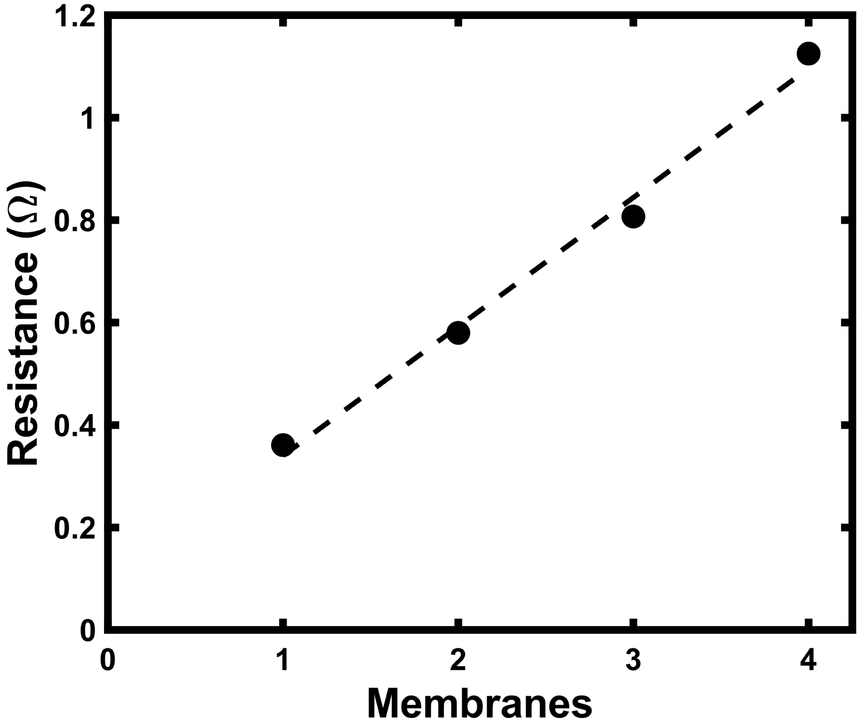

Figure VI-4. Ohmic resistance versus number of N117 membranes determined from electrochemical impedance spectroscopy using the donor electrolyte—500 mM $FeCl_2$, 500 mM $FeCl_3$, and 2 M HCl—in a single electrolyte configuration.

4. Modeling compositionally unbalanced symmetric cell cycling (CUSCC)

To provide theoretical underpinnings for this technique, we first present a representative analysis using a zero-dimensional model, highlighting the characteristic impact of different membrane / separator properties. For this preliminary assessment, we use input parameters (**Table VI-1**) that approximate the cell conditions used in subsequent experimental analyses. **Figure VI-5** shows representative CUSCC simulations, featuring capacity gain profiles as a function of the applied current density for varying membrane / separator conductivities. Here, the capacity gain is the difference between the measured capacity and the initial value of the discharge capacity for the first cycle (i.e., $\mathrm{Cap}_\mathrm{d}^\mathrm{N} - \mathrm{Cap}_\mathrm{d}^1$). Capacity gain is a useful metric for presenting the data in these studies, but note that the absolute magnitude of the accessible capacity depends on mass transport rates and current density (**Figure VI-6**). For context, the initial theoretical capacity in the receiver electrolyte is 40.2 mAh, whereas the accessed capacities in **Figure VI-5a** are 37.6, 30.9, and 19.8 mAh for 20, 50, and 100 mA cm^{-2}, respectively. As crossover progresses, the system eventually approaches an equilibrium state where the electrolytes are fully mixed and concentration gradients across the membrane / separator are diminished. This results in the capacity gain trending toward a plateau region, which represents a conventional symmetric cell. Under the conditions shown in **Figure VI-5**, the theoretical discharge capacity for fully-mixed electrolytes would be 221 mAh, corresponding to capacity rise values of ca. 181 mAh. Note that at lower capacities, the time for each cycle is shorter, resulting in a higher number of data points earlier in the experiment.

***Table VI-1**. Constant input properties used for CUSCC simulations.*

Property	Value
l_m (m)	2×10^{-4}
A_m (m^2)	2.55×10^{-4}
$A_{ed}k_{m,j}$ (m^3 s^{-1})	1×10^{-7}
V^R (m^3)	1.5×10^{-5}
V^D (m^3)	1.5×10^{-5}
z_A (–)	2
z_{A+} (–)	3
K_A (–)	1
K_{A+} (–)	1
ξ (–)	0
$C_A^{o,R}$ (mol m^{-3})	50
$C_{A^+}^{o,R}$ (mol m^{-3})	50
$C_A^{o,D}$ (mol m^{-3})	500
$C_{A^+}^{o,D}$ (mol m^{-3})	500

During the course of cycling, crossover fluxes are driven by spatial gradients in concentration and potential, which gradually increases the receiver electrolyte concentration (i.e., the capacity-limiting side of the symmetric cell) and, consequently, the accessible charge / discharge capacity. Diffusive crossover continuously drives species from the donor electrolyte to the receiver electrolyte, but the flux of each species varies throughout a particular half-cycle due to changing bulk concentrations during charge and discharge. In the absence of migration effects (i.e., zero current, infinite ionic conductivity), the capacity gain has a lower bound determined by the permeability of the active species. This limiting behavior is shown by the gray lines in **Figure VI-5** and **Figure VI-6** and is based on the gains in theoretical capacity calculated from increasing total active species concentration (**Equation (VI.14)**).

The application of current induces a potential gradient across the membrane / separator, altering the rate of ion transport and accelerating capacity gain, as the net crossover of ionic active species is driven by both diffusion and migration. This capacity gain grows larger for less conductive membranes / separators (e.g., **Figure VI-5a**) that incur a larger potential gradient at a given current density, further increasing migration fluxes. Alternating the current between charge and discharge also imposes differences in the relative contributions of diffusion and migration for each half-cycle. Using positively-charged species, the direction of diffusion and migration fluxes are aligned during the discharge half-cycle and opposed during the charge half-cycle (**Equation (VI.7)**). Despite this alternating polarity, the capacity gain still corresponds with changes in the potential gradient strength—growing with increasing current density and decreasing conductivity—as the relatively steady capacity gain via diffusion ensures that the discharge half-cycle is longer than the preceding charge half-cycle, resulting in net crossover via migration.

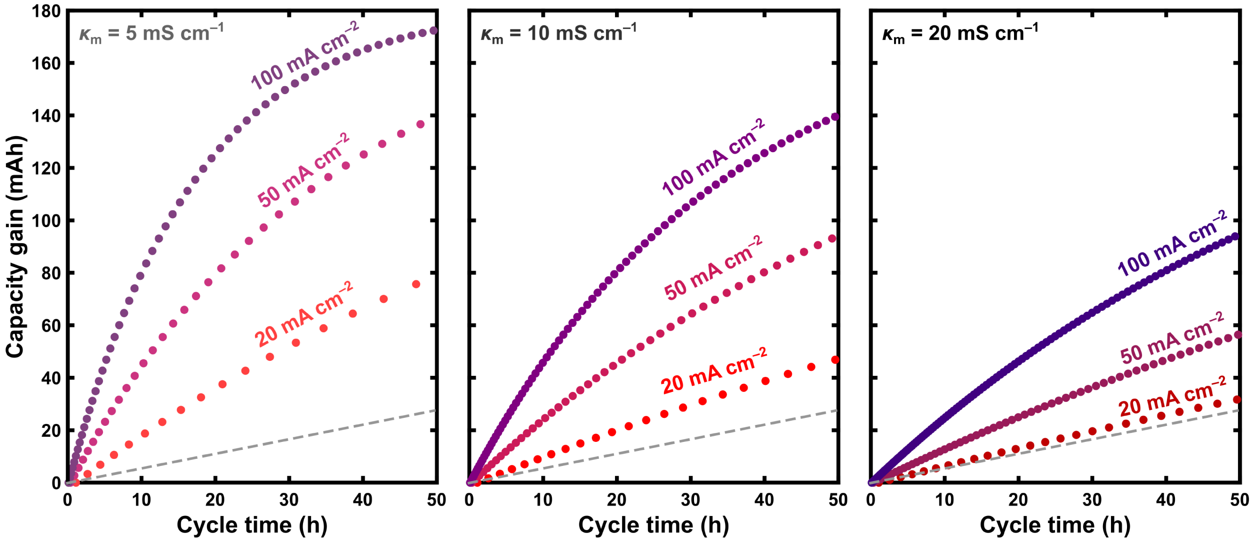

Figure VI-5. *Simulated capacity gain profiles for varying current densities and membrane / separator conductivities. For clarity, only discharge capacities are shown. For all simulations,* $D_A^m = D_{A^+}^m = 5 \times 10^{-12}\ \mathrm{m^2\ s^{-1}}$ *and all other inputs are shown in* ***Table VI-1***. *Gray dashed lines represent the theoretical capacity gain in the absence of an applied current density. Note the theoretical equilibrium capacity for fully mixed electrolytes would be ca. 221 mAh, corresponding to capacity rise values of ca. 181 mAh.*

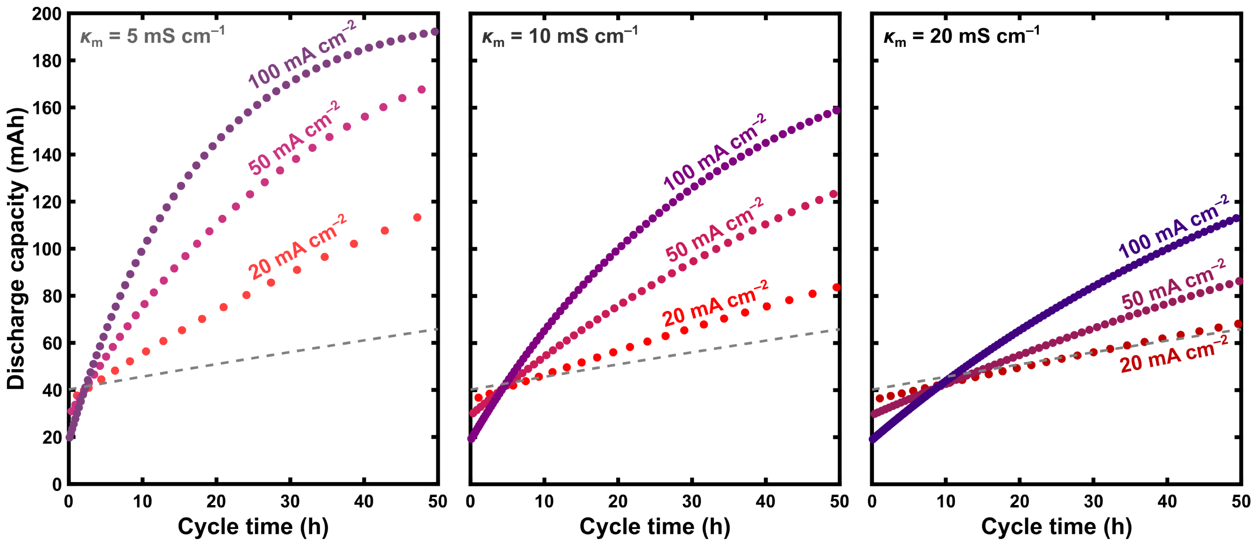

***Figure VI-6**. Simulated discharge capacity at varying current density and membrane / separator conductivity. For all simulations, $D_A^m = D_{A^+}^m = 5 \times 10^{-12}\ \mathrm{m^2\ s^{-1}}$ and all other inputs are shown in **Table VI-1**. Gray dashed lines represent the theoretical capacity gain in the absence of an applied current density. Note the initial theoretical capacity is ca. 41 mAh while the theoretical equilibrium capacity for fully mixed electrolytes would be ca. 221 mAh.*

CUSCC also displays characteristic features that distinguish each species, enabling quantitative disambiguation of their respective transport properties. Specifically, the initial charge capacity is determined by the concentration of A ($C_A^{\infty,R}$), meaning it will only be influenced by the net crossover of that species. The subsequent discharge capacity will depend on the concentration of A$^+$ ($C_{A^+}^{\infty,R}$), which is influenced by the net crossover of both species (A and A$^+$) during the charge half-cycle and by the net crossover of A$^+$ during the discharge half-cycle. As this process repeats itself, the relative contribution of each species to the respective capacity gain propagates from cycle to cycle. For instance, when the crossover rate of A exceeds that of A$^+$, a greater fraction of the net capacity gain is measured by the charge capacity, and, when the crossover rate of A$^+$ exceeds that of A, a greater fraction of the net capacity gain is measured by the discharge capacity.

To highlight these differences, we assess the effect of distinct diffusion coefficients by fixing D_A^m and varying $D_{A^+}^m$. **Figure VI-7** shows capacity gain profiles for a constant current density (100 mA cm^{-2}) with dashed lines provided for discharge to compare against values for charge. When the diffusion coefficients are identical, both capacity gains follow roughly the same trajectory, as the open squares in **Figure VI-7** align with the dashed lines and the fraction of capacity gain measured during charge and discharge are similar, although contributions from migration lead to a slightly larger capacity gain during the discharge half-cycle. Conversely, for $D_A^m > D_{A^+}^m$, the charge capacity initially rises above the discharge capacity and, for $D_A^m < D_{A^+}^m$, the charge capacity falls below the discharge capacity.

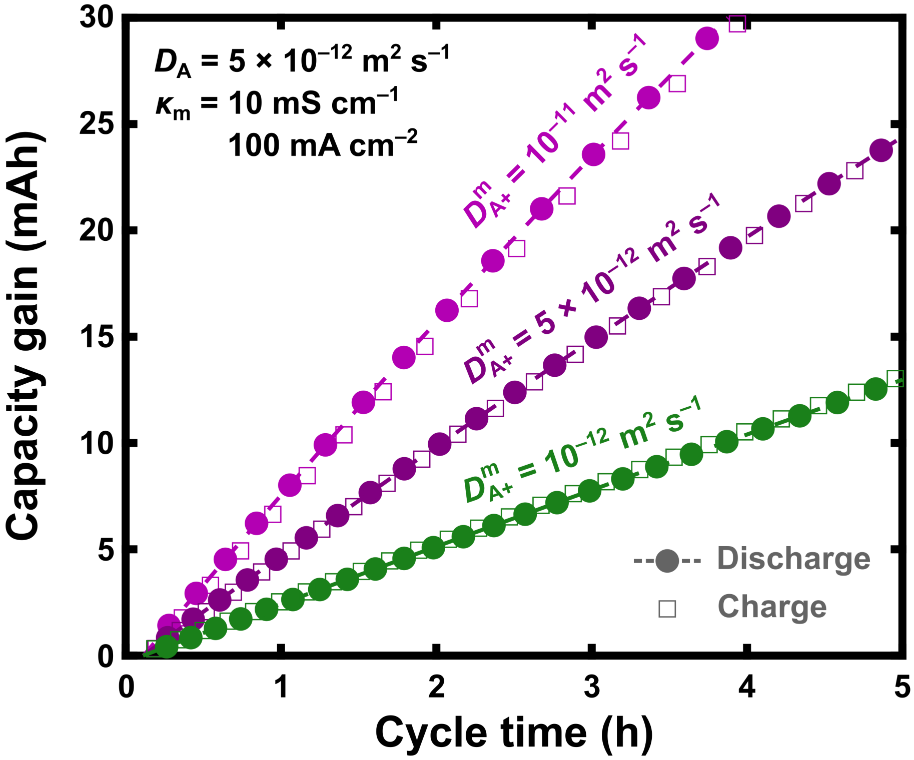

***Figure VI-7**. Simulated capacity gain curves over 5 h at 100 mA cm^{-2} showing both charge and discharge capacities for varying values of $D_{A^+}^m$ with fixed $D_A^m = 5 \times 10^{-12}\ \mathrm{m^2\ s^{-1}}$. Lines alongside the discharge capacities are provided to aid in visual comparison. For all simulations, $\kappa_m = 10\ \mathrm{mS\ cm^{-1}}$ and all other inputs are shown in **Table VI-1**.*

The differences in capacity at this scale are subtle but can be more clearly quantified in terms of the coulombic efficiency (CE), shown graphically in **Figure VI-8a**. As the capacity gain between charge and discharge half-cycles can be non-uniform, it is important to distinguish between the discharge CE—the ratio between the discharge and charge capacity gain in the same cycle—and the charge CE—the ratio between the charge capacity gain and the preceding discharge capacity gain. For the quantitative CE definitions in **Figure VI-8a**, we note again that the capacity gain is the difference between the charge or discharge capacity and the discharge capacity in the first cycle. **Figure VI-8b** and **Figure VI-8c** show the discharge CE and charge CE, respectively, for the same data as **Figure VI-7** extended over 50 h. The y-axes scale on these graphs is constrained to better highlight trends and thus does not show data from earlier cycles. Consistent with **Figure VI-7**, higher values of $D_{A^+}^m$ relative to D_A^m correspond to larger discharge CE (**Figure VI-8b**), as the discharge capacity represents a larger fraction of the net capacity gain. The opposite trend is observed for the charge CE (**Figure VI-8c**), as the relationship between the charge and discharge capacity is inverted. Eventually, all values for the CE tend toward 1 as the capacity gain approaches the equilibrium state corresponding to the plateau region. In the case where $D_{A^+}^m = 10^{-11}\ \mathrm{m^2\ s^{-1}}$, the discharge CE approaches this point faster than when $D_{A^+}^m = 5 \times 10^{-12}\ \mathrm{m^2\ s^{-1}}$ due to the heightened capacity gain rate. Overall, these distinct features indicate that comparisons between the charge and discharge CE for a given set of conditions provide clear insight into the relative transport rates of A and A^+, suggesting that CUSCC can enable simultaneous characterization of both species.

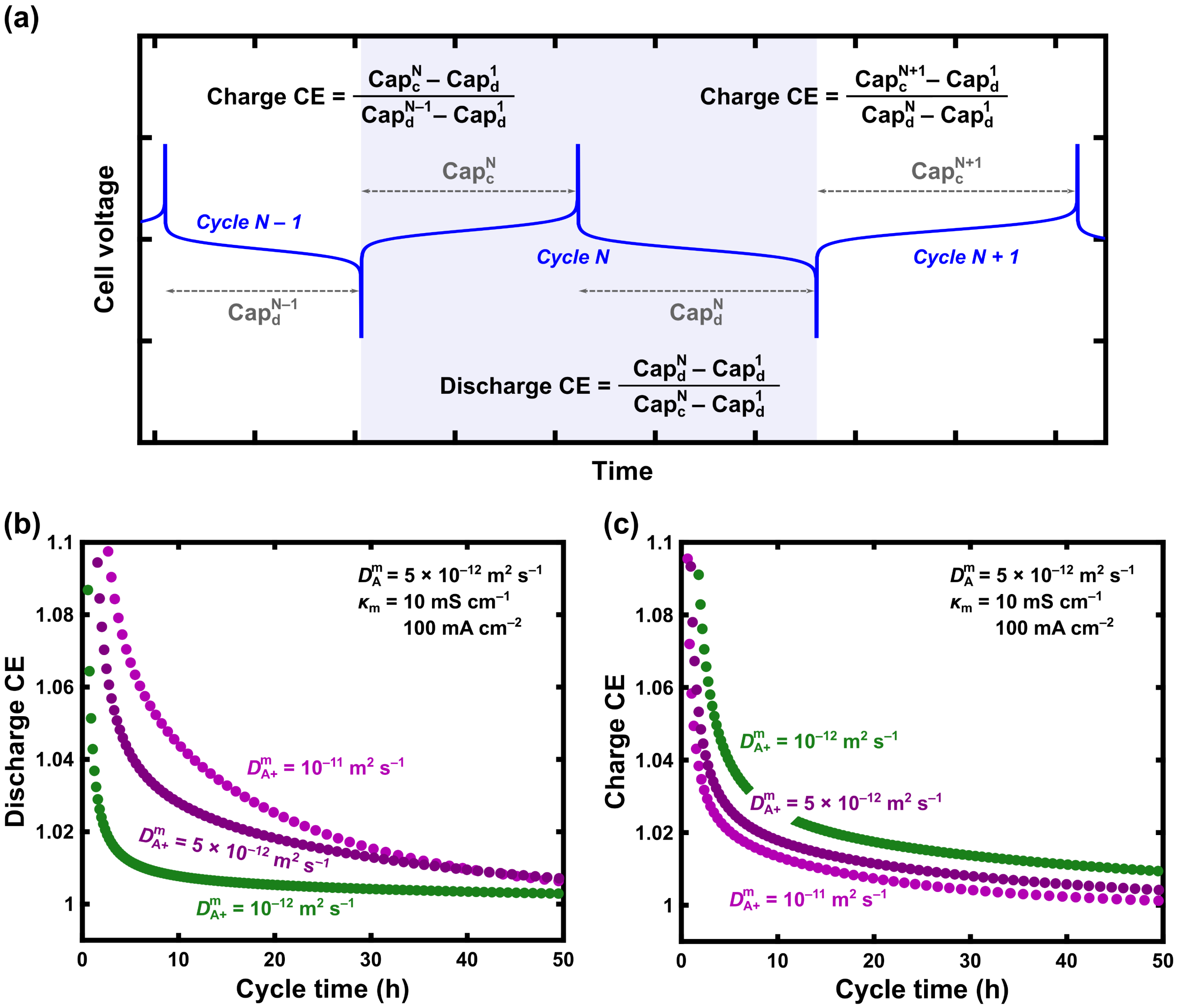

Figure VI-8. *(a) Graphical representation of the charge coulombic efficiency (CE) and the discharge CE with respect to charge / discharge curves. (b) Discharge CE and (c) charge CE for the simulations shown in **Figure VI-7** extended over 50 h. The cycle time corresponds to the end of the discharge step for the discharge CE and the end of the charge step for the charge CE. For the simulations in (b) and (c),* $D_A^m = 5 \times 10^{-12}\ \text{m}^2\ \text{s}^{-1}$, $\kappa_m = 10\ \text{mS cm}^{-1}$*, and all other inputs are shown in **Table VI-1**.*

5. *Experimental validation with a model system*

To demonstrate this technique experimentally, we use a model aqueous redox couple, $Fe^{2+/3+}$, alongside a relatively robust and well-studied cation-exchange membrane—N117. We specifically selected a thicker Nafion variant (nominally, 183 μm) to amplify the potential difference across the membrane, thus inducing a stronger dependence on the applied current density (**Equation (VI.7)**). Considering the order of magnitude concentration difference established between the active species in the donor (1 M $Fe^{2+/3+}$) and receiver (100 mM $Fe^{2+/3+}$) electrolytes, additional "spectator" species must be added to balance the osmotic pressure and mitigate convection through the membrane. To this end, we selected $MgCl_2$ and $CrCl_3$, as they are inactive near the redox potential of $Fe^{2+/3+}$, possess similar ionic charges with Fe^{2+} and Fe^{3+}, respectively, and are stable and fully soluble in the chosen electrolyte (2 M HCl). Concentrations in the receiver solution were selected to minimize the initial starting concentration of $Fe^{2+/3+}$ while ensuring sufficient mass transport rates to support the relatively high current density (vide infra). Note that while the presence of additional species may influence the equilibrium partitioning of species between the electrolytes and the ion-exchange membrane under extended cycling conditions, we do not anticipate that this will adversely impact the crossover rates under these time frames (here, < 50 h). In fact, these conditions may be more representative of those experienced in practical embodiments where there are differing active species in multiple oxidation states.

Prior to cycling, we first measured membrane properties ex situ (**Table VI-2**) using conventional techniques to establish performance expectations and provide baseline values to compare for parameter estimation. Based on the change in mass upon soaking in the donor electrolyte, the membrane exhibits some degree of swelling, resulting in higher internal free volume / porosity. The calculated partition coefficients and permeabilities for both active species in Nafion^{TM} align with prior reports,[188–190] displaying relatively high crossover rates due to efficient cation transport enabled by fluorinated sulfonic acid polymers. Notably, the partition coefficient for Fe^{2+} exceeds that of Fe^{3+}, as more positively-charged species require a comparatively higher number of fixed ion sites to maintain electroneutrality.[49] For context, N117 has a fixed ion site concentration, C_{site}, that is ca. 1.65 M in the dry state (1100 g mol^{-1} equivalent weight); accounting for electrolyte-induced swelling, C_{site} is ca. 1.24 M, indicating Fe^{2+} and Fe^{3+} would account for 21% and 19% of the total available anion sites, respectively. The diffusion coefficient for Fe^{3+} is also lower than Fe^{2+}, as the higher ionic charge likely results in a larger solvated radius, slowing species transport through the membrane.[191] Finally, measured N117 conductivities in the donor electrolyte are also consistent with prior studies.[188]

Table VI-2. *Comparison of membrane properties measured ex situ and predicted using data from the CUSCC technique over 50 h (320 data points).*

Property	Measured ex situ	Predicted from CUSCC
l_m (μm)[a,b]	198 ± 1	-----
$K_{Fe(II)}$[b]	0.27 ± 0.02	-----
$K_{Fe(III)}$[b]	0.16 ± 0.01	-----
$P_{Fe(II)}$ (10^{-11} m^2 s^{-1})	1.15 ± 0.01[c]	1.12
$P_{Fe(III)}$ (10^{-11} m^2 s^{-1})	0.44 ± 0.01[c]	0.30
$D^{m}_{\mathrm{Fe(II)}}$ (10^{-11} m^2 s^{-1})[d]	4.2 ± 0.3	4.2 ± 0.3
$D^{m}_{\mathrm{Fe(III)}}$ (10^{-11} m^2 s^{-1})[d]	2.8 ± 0.1	1.9 ± 0.2
κ_m (S m^{-1})	3.1 ± 0.2[c]	1.96

[a] Electrolyte-swollen membrane thickness
[b] Average and standard deviation determined from 4 independent samples
[c] Average and standard deviation determined from linear regression
[d] Standard deviation determined from error propagation via **Equation (15)**

Using a zero-gap flow cell configuration, we sought to experimentally validate the CUSCC technique for the same model system. Considering the membrane conductivity for N117 is relatively high in this electrolyte, a sufficiently wide range of current densities is needed to generate differences in capacity rise for CUSCC. For less conductive membranes / separators (e.g., those used in nonaqueous RFBs[192] and pH-neutral aqueous RFBs[138]), a smaller range of current densities would likely suffice (**Figure VI-5**). To be consistent with our simulations, we operated cells at 20, 50, and 100 mA cm^{-2} to promote differences in the migration fluxes and thus the capacity gain without exceeding the mass transfer limitations of the receiver electrolyte. The experimental results shown in **Figure VI-9** display similar trends as those predicted by the zero-dimensional modeling and support the theoretical treatment presented earlier. Note that no volume changes were observed in the electrolyte chambers during the cycling experiments, suggesting that the presence of osmotically-balancing species ($MgCl_2$ and $CrCl_3$) obviates any osmotic fluxes and that electro-osmotic fluxes are likely negligible under these conditions (i.e., $\xi \approx 0$).

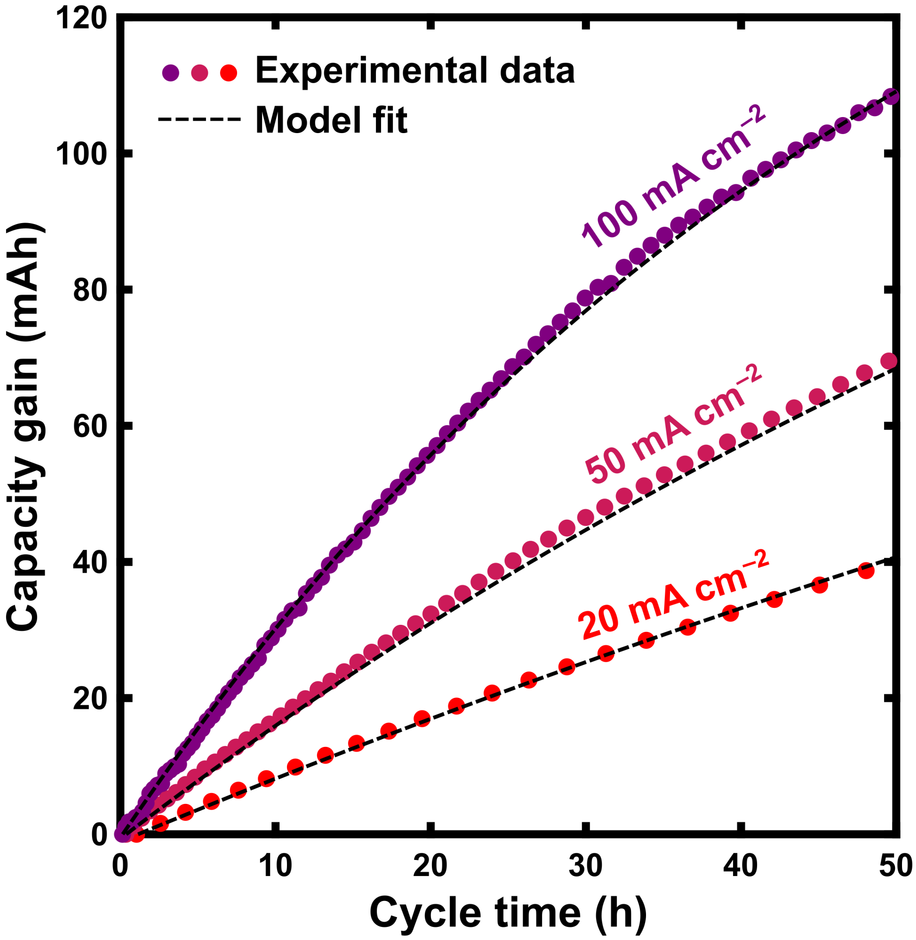

Figure VI-9. *Experimental capacity gain curves for N117 measured at varying current densities (20, 50, and 100 mA cm*$^{-2}$*). For clarity, only discharge capacities are shown. The donor electrolyte (15 mL) contains 500 mM* $FeCl_2$*, 500 mM* $FeCl_3$*, and 2 M HCl while the receiver electrolyte (15 mL) contains 50 mM* $FeCl_2$*, 50 mM* $FeCl_3$*, 450 mM* $MgCl_2$*, 450 mM* $CrCl_3$*, and 2 M HCl. Both electrolytes are prepared at 50% SOC and flow through the cell at 20 mL min*$^{-1}$*. Black dashed lines show simulated data using best-fit values (**Table VI-2**) determined from fitting data to the zero-dimensional model. For all simulations, the partition coefficients and membrane thickness were taken from **Table VI-2** and all other operating parameters were taken from **Table VI-1**. Mass transport coefficients (*$A_{ed}k_{m,j}$*) were estimated as* 1.97×10^{-7} $m^3\ s^{-1}$*,* 1.06×10^{-7} $m^3\ s^{-1}$*, and* 1.41×10^{-7} $m^3\ s^{-1}$ *for experiments performed at 20, 50, and 100 mA cm*$^{-2}$*, respectively.*

The discharge CE (**Figure VI-10a**) and charge CE (**Figure VI-10b**) also provide complementary information to further interpret the transport characteristics of CUSCC data. As expected, all CE values decrease with increasing current density, which is primarily the result of faster cycling resulting in shorter timescales for crossover despite higher fluxes due to migration. Both the charge and discharge CE also tend toward 1 with increasing time, as the capacity gain approaches an equilibrium state corresponding to the plateau region. Values for the discharge CE are also notably lower than those for the charge CE at the same current density. Consistent with observations made in **Figure VI-8**, this behavior implies that the permeability of Fe^{2+} is greater than Fe^{3+}, which aligns with trends in the H-cell data. Finally, it is worth noting that noise in the data is more evident for CE compared to the capacity, which is commonly observed in conventional, compositionally balanced symmetric cell cycling data.[23,31,185] As this is more pronounced at higher current densities and earlier in the experiment when concentrations are lower, the noise is likely due to slight variations in mass transport (e.g., advection, mixing) that alter the accessed capacity. However, considering the expected trends are generally preserved, we posit that this experimental error will not significantly influence the accuracy of extracted parameters.

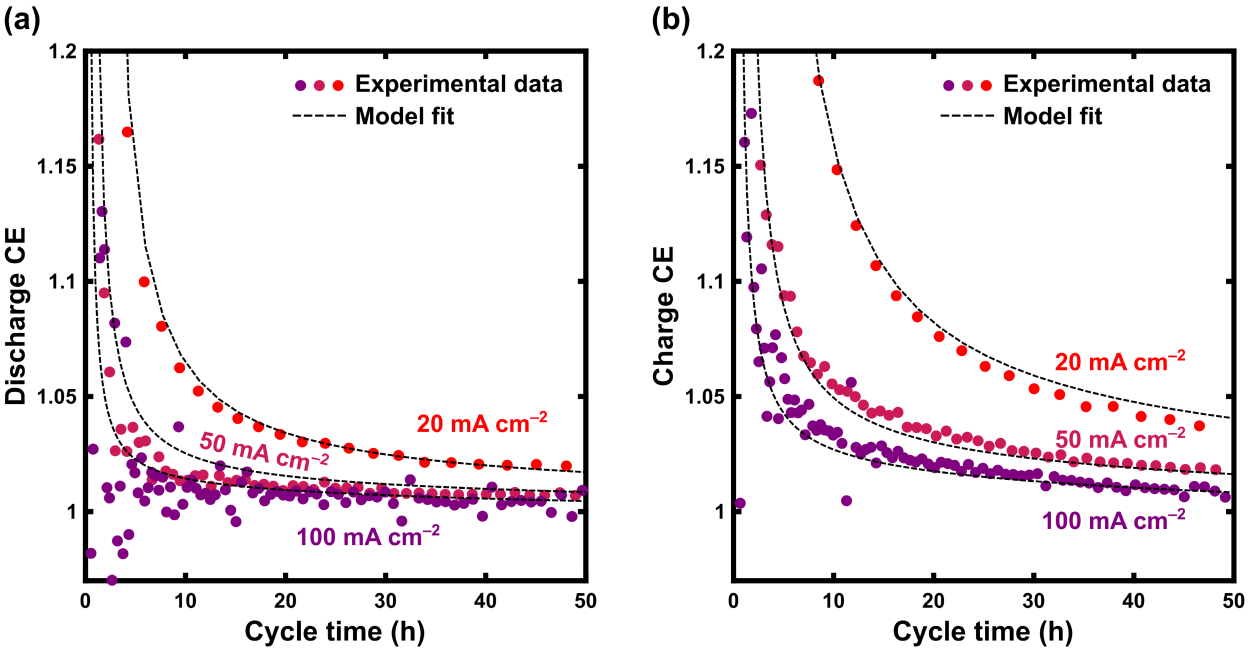

Figure VI-10. *Experimental (a) discharge coulombic efficiency (CE) and (b) charge CE for N117 measured at varying current densities (20, 50, and 100 mA cm^{-2}). The donor electrolyte (15 mL) contains 500 mM $FeCl_2$, 500 mM $FeCl_3$, and 2 M HCl while the receiver electrolyte (15 mL) contains 50 mM $FeCl_2$, 50 mM $FeCl_3$, 450 mM $MgCl_2$, 450 mM $CrCl_3$, and 2 M HCl. Both electrolytes are prepared at 50% SOC and flow through the cell at 20 mL min^{-1}. Black dashed lines show simulated data using best-fit values (**Table VI-2**) determined from fitting data to the zero-dimensional model. For all simulations, the partition coefficients and membrane thickness were taken from **Table VI-2** and all other operating parameters were taken from **Table VI-1**. Mass transport coefficients ($A_{ed}k_{m,j}$) were estimated as 1.97×10^{-7} m^3 s^{-1}, 1.06×10^{-7} m^3 s^{-1}, and 1.41×10^{-7} m^3 s^{-1} for experiments performed at 20, 50, and 100 mA cm^{-2}, respectively.*

6. Parameter extraction from CUSCC data

Although the predicted CUSCC behavior—using properties that are measured ex situ—is somewhat consistent with the experimental capacity gain, we sought to determine whether this technique could independently evaluate membrane / separator properties, which, in turn, could streamline the overall characterization workflow. Considering the zero-dimensional model is computationally efficient—requiring < 0.05 s per cycle on a standard laptop computer—it can be leveraged to rapidly extract parameters from CUSCC experiments. As not all membrane properties are fully decoupled when calculating the flux (**Equation (VI.7)**), we elect to determine the key transport properties—conductivity and diffusivity—using the previously measured equilibrium properties (l_m, K_j) as model inputs. To approximate the mass transfer characteristics (**Equation (VI.13)**), we use the discharge capacity measured during the first cycle. Assuming crossover is negligible and all species have equal mass transport coefficients, the charge and discharge capacities are given by **Equations (VI.17)** and **(VI.18)**, respectively.[182]

$$\mathrm{Cap}_{\mathrm{c}}^{1} = V^{R} F \left(C_{\mathrm{Fe(II)}}^{o,R} - \frac{|I|}{F A_{ed} k_{m,j}} \right) \tag{VI.17}$$

$$\mathrm{Cap}_{\mathrm{d}}^{1} = V^{R} F \left(\left(C_{\mathrm{Fe(II)}}^{o,R} + C_{\mathrm{Fe(III)}}^{o,R} \right) - 2 \frac{|I|}{F A_{ed} k_{m,j}} \right) \tag{VI.18}$$

Here, the initial concentration for the discharge half-cycle has been written in terms of the initial concentrations at the beginning of the experiment. Solving for $A_{ed}k_{m,j}$ in terms of the discharge capacity yields **Equation (VI.19)**.

$$A_{ed}k_{m,j} = \frac{2\left(\frac{|I|}{F}\right)}{\left(C^{o,R}_{\mathrm{Fe(II)}} + C^{o,R}_{\mathrm{Fe(III)}}\right) - \left(\frac{\mathrm{Cap}^{1}_{\mathrm{d}}}{V^{R}F}\right)} \tag{VI.19}$$

Resultant values of $A_{ed}k_{m,j}$ were calculated as 1.97×10^{-7} m^3 s^{-1}, 1.06×10^{-7} m^3 s^{-1}, and 1.41×10^{-7} m^3 s^{-1} for experiments performed at 20, 50, and 100 mA cm^{-2}, respectively, which is consistent with previous studies.[66,71,103] Note that this parameter could potentially be extracted from the fitting routine for the transport properties, however we elected to focus on the membrane characteristics to avoid introducing three additional fitting parameters (i.e., one for each current density).

Using the *fmincon* function in MATLAB, we numerically extract the diffusion coefficients of both species as well as the membrane conductivity by minimizing the sum-squared error, R^2 (dimensionless) between the experimental and simulated values of the charge capacity, discharge capacity, charge CE, and discharge CE according to **Figure VI-11**. Note that we scale the charge and discharge capacity gains by the experimental capacity gain to ensure the order of magnitude and units are comparable to the charge CE and discharge CE. Additionally, as higher current densities provide more data points for fitting (i.e., 87 cycles at 100 mA cm^{-2} vs. 21 cycles at 20 mA cm^{-2}), which could potentially bias the output, the contributions of each data set are normalized by the total number of cycles. We also ignore the charge capacities measured during the first cycle, as small differences in capacity can lead to large errors in the discharge CE. Finally, because the discharge capacity gain for the first cycle is zero, the charge CE cannot be calculated until the third cycle, as the denominator for the second cycle is zero. The *fmincon* function minimizes R^2 by varying $D^{m}_{\mathrm{Fe(II)}}$, $D^{m}_{\mathrm{Fe(III)}}$, and κ_m within a set of lower and upper bounds, given in **Table VI-3**, that are chosen to provide a suitable range of physically realistic values. We use the ex situ properties as initial guesses to the function, although we found no differences in the best-fit values when varying these initial guesses.

$$
\begin{aligned}
R^2 \;=\;& \frac{1}{\mathrm{N_{total}}}\sum_{\mathrm{N}=2}^{\mathrm{N_{total}}}\left(\frac{\mathrm{Cap}_{\mathrm{d,sim}}^{\mathrm{N}}-\mathrm{Cap}_{\mathrm{d,exp}}^{\mathrm{N}}}{\mathrm{Cap}_{\mathrm{d,exp}}^{\mathrm{N}}-\mathrm{Cap}_{\mathrm{d,exp}}^{1}}\right)^2+\cdots && \Bigg\}\ \text{Discharge capacity gain}\\
& \frac{1}{\mathrm{N_{total}}}\sum_{\mathrm{N}=2}^{\mathrm{N_{total}}}\left(\frac{\mathrm{Cap}_{\mathrm{c,sim}}^{\mathrm{N}}-\mathrm{Cap}_{\mathrm{c,exp}}^{\mathrm{N}}}{\mathrm{Cap}_{\mathrm{c,exp}}^{\mathrm{N}}-\mathrm{Cap}_{\mathrm{d,exp}}^{1}}\right)^2+\cdots && \Bigg\}\ \text{Charge capacity gain}\\
& \frac{1}{\mathrm{N_{total}}}\sum_{\mathrm{N}=2}^{\mathrm{N_{total}}}\left(\frac{\mathrm{Cap}_{\mathrm{d,sim}}^{\mathrm{N}}-\mathrm{Cap}_{\mathrm{d,sim}}^{1}}{\mathrm{Cap}_{\mathrm{c,sim}}^{\mathrm{N}}-\mathrm{Cap}_{\mathrm{d,sim}}^{1}}-\frac{\mathrm{Cap}_{\mathrm{d,exp}}^{\mathrm{N}}-\mathrm{Cap}_{\mathrm{d,exp}}^{1}}{\mathrm{Cap}_{\mathrm{c,exp}}^{\mathrm{N}}-\mathrm{Cap}_{\mathrm{d,exp}}^{1}}\right)^2+\cdots && \Bigg\}\ \text{Discharge CE}\\
& \frac{1}{\mathrm{N_{total}}}\sum_{\mathrm{N}=3}^{\mathrm{N_{total}}}\left(\frac{\mathrm{Cap}_{\mathrm{c,sim}}^{\mathrm{N}}-\mathrm{Cap}_{\mathrm{d,sim}}^{1}}{\mathrm{Cap}_{\mathrm{d,sim}}^{\mathrm{N-1}}-\mathrm{Cap}_{\mathrm{d,sim}}^{1}}-\frac{\mathrm{Cap}_{\mathrm{c,exp}}^{\mathrm{N}}-\mathrm{Cap}_{\mathrm{d,exp}}^{1}}{\mathrm{Cap}_{\mathrm{d,exp}}^{\mathrm{N-1}}-\mathrm{Cap}_{\mathrm{d,exp}}^{1}}\right)^2 && \Bigg\}\ \text{Charge CE}
\end{aligned}
$$

Figure VI-11. *Calculation of the sum-squared error, highlighting the contribution of each term used for the parameter extraction procedure. The error from each experiment (i.e., current density) is added together in the nonlinear optimization routine.*

Table VI-3. *Upper and lower bounds and initial guesses used in the parameter extraction routine with fmincon.*

Property	Lower bound	Upper bound	Initial guess
$D^m_{\mathrm{Fe(II)}}$ ($\mathrm{m^2\ s^{-1}}$)	1×10^{-13}	1×10^{-9}	4.2×10^{-11}
$D^m_{\mathrm{Fe(III)}}$ ($\mathrm{m^2\ s^{-1}}$)	1×10^{-13}	1×10^{-9}	2.8×10^{-11}
κ_m ($\mathrm{S\ m^{-1}}$)	0.01	10	3.1

Table VI-2 lists the best-fit values extracted from all of the measured charge and discharge capacities (320 total data points). These results align well with the diffusion coefficients and conductivities measured using ex situ methods, suggesting that the model system behaves as expected under CUSCC conditions. However, we note that consistency between ex situ and in situ methods is not expected for all redox chemistries, as membrane properties may vary with electrolyte SOC and with time.[55,193–195] Thus, we emphasize that the transport characteristics measured by CUSCC are potentially more representative of flow cell conditions, and this technique may better capture non-idealities for less well-behaved chemistries. Using the best-fit parameters as inputs, the dashed lines in **Figure VI-9** show the simulated capacity gain curves overlaid against the experimental data, highlighting the excellent agreement observed between the model and the experimental data and underscoring the robustness of CUSCC to varying operating conditions. Similarly, the dashed lines in **Figure VI-10** show simulated charge and discharge CE using the same set of best-fit parameters. Qualitatively, the relationships between CE and current density as well as between charge and discharge CE are captured by the model. However, the differences between the predicted and measured values are more pronounced. We posit that difficulties in predicting CE likely arise from experimental noise, but do not prohibit accurate parameter extraction, as the estimated values align with expectations and the model describes well the overall CUSCC performance trends.

To this point, we have chosen a relatively arbitrary experimental timeframe (ca. 50 h) to establish the efficacy of the CUSCC method. However, shorter timeframes are advantageous for throughput, so establishing a minimum viable time could reduce barriers to adoption and improve the overall utility. Thus, we further scrutinize the relationships between experiment duration and extracted parameters to determine approximate lower bounds for CUSCC runtime. **Figure VI-12** shows best-fit values as a function of time, ranging from 5 h to 50 h. We observe a continuous, non-negligible drop in the best-fit values for $D^{m}_{\mathrm{Fe(II)}}$, $D^{m}_{\mathrm{Fe(III)}}$, and κ_m with increasing time, suggesting a relatively weak dependence on time after a minimum threshold is reached. We posit that these variations are either the result of changes in transport properties with time or artifacts from compounding experimental error and the fitting procedure. For instance, N117 is initially soaked in 2 M HCl before being exposed to the donor and receiver electrolytes, which may incur changes to conductivity and permeability as the membrane equilibrates. Overall, comparing these best-fit values against the ex situ properties (**Table VI-2**), we see relatively similar characteristics at all times, again confirming that CUSCC can uniquely characterize membrane transport in redox flow cells and further establishing its efficacy for future studies. This analysis suggests that sufficient results are likely attainable within < 24 h of measurement, although we anticipate that the lower bound runtime will likely be system- and chemistry-dependent.

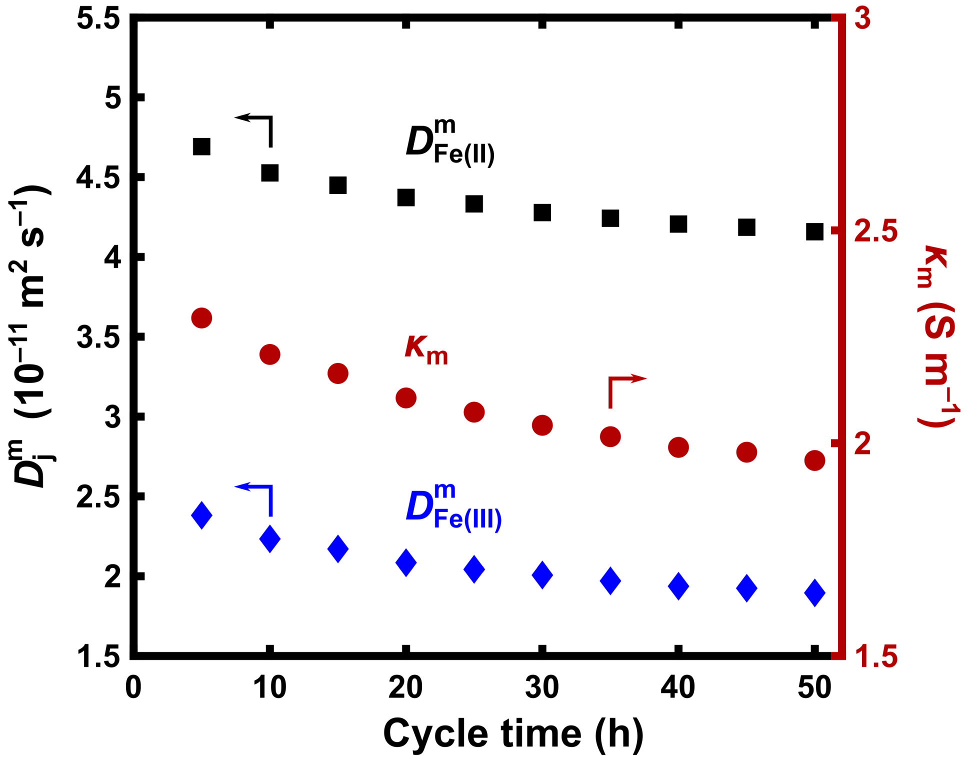

***Figure VI-12**. Comparison of best-fit values ($D^{m}_{Fe(II)}$, $D^{m}_{Fe(III)}$, and κ_m) as a function of experiment run-time. For all simulations, the partition coefficients and membrane thickness were taken from **Table VI-2** and all other operating parameters were taken from **Table VI-1**. Mass transport coefficients ($A_{ed}k_{m,j}$) were estimated as 1.97×10^{-7} m^3 s^{-1}, 1.06×10^{-7} m^3 s^{-1}, and 1.41×10^{-7} m^3 s^{-1} for experiments performed at 20, 50, and 100 mA cm^{-2}, respectively.*

7. Conclusions

Present characterization techniques for RFB membranes are limited in their ability to measure crossover in redox flow cells under dynamic concentrations and with reversing polarity. To this end, we introduced CUSCC as a potential platform for membrane testing in redox flow cells. Using a zero-dimensional model, we first evaluated the fundamental processes that underpin capacity gain and cycling efficiency to develop foundational understanding of the characteristic behaviors. We then investigated a model system—$Fe^{2+/3+}$ and N117—to establish proof-of-concept validations for the methodology. Finally, we leveraged the zero-dimensional model to perform parameter extraction from experimental data, obtaining best-fit values that agree well with those measured by independent techniques and that accurately capture trends in capacity gain and CE. Importantly, the experimental framework described in this work can be easily performed with standard flow cell hardware, making the technique readily accessible to the RFB community.

While this study provides theoretical foundations and proof-of-concept experimental validation, opportunities remain to refine and augment this method. For instance, the examples shown here have focused on galvanostatic operation, yet it may be possible to dynamically raster applied current densities during the operation of a single cell, either across full cycles or within half-cycles, to more quickly extract values of interest. This may be more efficacious under conditions where crossover is slower, enabling more total cycles before reaching equilibrium. Additionally, the mathematical model implemented here assumes that side reactions (e.g., self-discharge, species decay) are negligible, however such processes can be integrated into the existing framework.[182] Finally, we applied a simple data fitting routine to extract parameters from experimental measurements, and we anticipate that deeper analysis of optimization tools could yield more rigorous estimates of uncertainty.

8. List of symbols

Roman symbols

A_{ed}	Accessible surface area of the electrode (m^2)
A_m	Geometric membrane / separator area (m^2)
$\mathbf{b}$	Constant reaction rate vector (mol m^{-3} s^{-1})
$\mathbf{C}$	Concentration vector (mol m^{-3})
$\mathbf{C^o}$	Initial concentration vector (mol m^{-3})
$C_j^{\infty,h}$	Bulk concentration of species *j* in half-cell *h* (mol m^{-3})
$C_j^{o,h}$	Initial concentration of species *j* in half-cell *h* at the beginning of each half-cycle (mol m^{-3})
$C_j^{s,h}$	Electrode surface concentration of species *j* in half-cell *h* (mol m^{-3})
C_{site}	Concentration of fixed ion sites in the membrane (mol m^{-3})
$\mathrm{Cap}_\mathrm{c}^\mathrm{N}$	Charge capacity at cycle N (C)
$\mathrm{Cap}_\mathrm{d}^\mathrm{N}$	Discharge capacity at cycle N (C)
D_j^m	Diffusion coefficient of species *j* in the membrane / separator (m^2 s^{-1})
F	Faraday's constant (96485 C mol^{-1})
I	Applied current, denoted as positive for charging and negative for discharging (A)
$k_{c,j}^h$	Crossover rate constant for species *j* in half-cell *h* (s^{-1})
$k_{m,j}$	Mass transfer coefficient of species *j* (m s^{-1})
$\mathbf{K}$	Rate constant matrix (s^{-1})
K_j	Partition coefficient of species *j*
l_m	Membrane / separator thickness (m)
N_j	Flux of species *j* through the membrane / separator (mol m^{-2} s^{-1})
P_j	Permeability of species *j* in the membrane / separator (m^2 s^{-1})
R	Universal gas constant (8.314 J mol^{-1} K^{-1})
t	Time (s)
T	Temperature (K)
$\mathbf{U}$	Eigenvector matrix of $\mathbf{K}$
V^h	Total electrolyte volume in half-cell *h* (m^3)
z_j	Ionic charge of species *j*

Greek symbols

$\boldsymbol{\beta}$	Transformed constant reaction rate vector (mol m^{-3} s^{-1})
γ_j	Dimensionless flux parameter
κ_m	Membrane conductivity (S m^{-1})
λ	Molar ratio of solvent to fixed ion sites in the membrane
$\mathbf{\Lambda}$	Diagonal eigenvalue matrix of $\mathbf{K}$ (s^{-1})
ξ	Dimensionless electro-osmotic coefficient

VII. Summary and outlook

Redox flow batteries (RFBs) are electrochemical energy storage technologies that hold promise for improving the sustainability, efficiency, resiliency, and service life of the electric grid. In particular, the battery architecture features independently scalable energy and power, modular construction, and simplified maintenance, presenting opportunities for low-cost, long-duration storage. Despite these favorable characteristics, the projected capital costs, driven in large part by the constituent components of the system, prohibit widespread adoption, motivating research efforts to expand the materials repertoire, including novel redox couples, electrolytes, and membranes. Notably, the past decade has seen exciting advances, including the emergence of engineered molecules (e.g., redox-active organics, metal-centered coordination complexes) whose physical and electrochemical properties can be tuned through molecular functionalization. While such materials offer a new means of tuning RFB performance metrics, they also present new complexities for device operation, which include managing an array of parasitic processes (e.g., active species crossover, molecular decay, component degradation, side reactions) that result in heightened capacity fade and reduced cycling efficiencies. This multifaceted parameter space frustrates the articulation of unambiguous design criteria, as the relationships between constituent material properties and cell performance metrics are not yet well-understood.

This thesis has addressed these knowledge gaps by developing theoretical and experimental methods that support the rational design of RFBs. We derived and applied zero-dimensional models to translate material properties to cell cycling performance, establishing clear connections between complex design tradeoffs and enabling more informed decisions about materials selection. We developed and evaluated experimental tools to characterize chemical / electrochemical processes that govern the performance and long-term stability of RFBs. Together, these central aims have provided engineering frameworks for approaching the design process by quantifying essential material characteristics and by presenting constitutive equations for predicting performance based on those properties.

While the work presented here has laid strong foundations for RFB engineering, there remains significant future work to advance these methodologies and to continue developing practical embodiments for energy storage. The microelectrode-based sensor discussed in **Chapter II** offered fundamental advancements for implementing microelectrodes but only pursued a proof-of-concept implementation only in a symmetric flow cell. Further implementation of these tools in practical systems will provide methods to more thoroughly characterize flow cell operation. Ongoing work by Schubert and coworkers has evaluated the statistical accuracy of microelectrodes for continuous SOC and SOH measurements and also applied them to rigorously assess the efficacy of symmetric cell cycling.[100,185,196–198] Jacquemond et al. also recently applied microelectrodes to measure active species crossover for characterizing transport phenomena in nonaqueous RFB membranes.[181] Additionally, combining these operando diagnostics with zero-dimensional modes (**Chapter III**) could provide additional validation for the zero-dimensional models while providing deeper insight into flow cell operation. Beyond traditional RFBs, such in-line sensors may find utility in redox-mediated architectures as well as in electrosynthetic processes.

The models developed in **Chapters III** and **IV** have numerous applications for interrogating experimental data and integrating more complex physical processes into the theoretical framework. Similar to the work by Silcox et al.,[44] these models can be used alongside experimental capacity fade data to extract quantitative assessment of redox species stability, potentially mediating the need for standardized experimental protocols. The methods may also be applied to understand performance losses associated with scale-up—for instance, by combining multiple electrolyte domains and shunt currents, the analytical zero-dimensional framework could potentially be applied to simulate stack performance. Additionally, as closed-form analytical models facilitate the use of simplified simulation tools (e.g., spreadsheets), this framework may serve as a basis for developing modules for educational practice in electrochemical engineering and as platform for providing foundational knowledge to new entrants within the RFB community.

Chapter V discussed future directions for molecular engineering of multi-electron materials, arguing that attention should be directed toward methodologies to reduce the potential difference between redox events. Further development of molecules that display either concerted or energetically-similar sequential electron transfer, similar to many aqueous organic RFB compounds—may also yield more flexible, high-performing organic RFBs. Conversely, some limitations associated with these materials may be overcome through cell and system engineering. For example, operating at sufficiently high flow rates or low current densities can limit the voltaic efficiency associated with multi-electron transfer; however, we posit that the sharp decrease in cell voltage resulting from multiple plateaus may impose practical limitations for energy systems.

The development of CUSCC in **Chapter VI** offers new dimension to the widely used symmetric cell cycling technique, making it largely accessible to the RFB community, and we anticipate significant opportunities in technique advancement and in membrane characterization. As discussed already, there exist pathways for expanding the theoretical framework of CUSCC to incorporate additional failure modes and cycling protocols to more effectively and expeditiously evaluate active species crossover. Application of this method may be particularly useful for interrogating transport phenomena in nonaqueous RFB membranes, where comparatively little attention has been paid to membrane / separator design and characterization. For instance, as high concentration nonaqueous RFBs begin to emerge,[199,200] the effects of active species concentration on membrane / separator properties remains unclear. Additionally, CUSCC may find application in routine membrane / separator characterization workflows for both aqueous organic RFBs and vanadium RFBs, as property tradeoffs continue to frustrate design strategies for these systems.

Overall, while significant achievements have been made in the RFB field over the past several decades, a wide range of opportunities remain for fundamental advancement and technology development. We hope that the methodologies developed in this thesis accelerate those new directions by providing foundational theoretical and experimental tools that improve the depth of materials, reactor, and systems design strategies.

References

(1) Soloveichik, G. L. Battery Technologies for Large-Scale Stationary Energy Storage. *Annu. Rev. Chem. Biomol. Eng.* **2011**, *2*, 503–527. https://doi.org/10.1146/annurev-chembioeng-061010-114116.

(2) Chu, S.; Majumdar, A. Opportunities and Challenges for a Sustainable Energy Future. *Nature* **2012**, *488* (7411), 294–303. https://doi.org/10.1038/nature11475.

(3) Clémençon, R. The Two Sides of the Paris Climate Agreement : Dismal Failure or Historic Breakthrough? **2016**.

(4) Gyuk. US DOE Program Planning Document, 2011.

(5) Byrne, R. H.; Nguyen, T. A.; Copp, D. A.; Chalamala, B. R.; Gyuk, I. Energy Management and Optimization Methods for Grid Energy Storage Systems. *IEEE Access* **2018**, *6*, 13231–13260. https://doi.org/10.1109/ACCESS.2017.2741578.

(6) Yang, Z.; Zhang, J.; Kintner-Meyer, M. C. W.; Lu, X.; Choi, D.; Lemmon, J. P.; Liu, J. Electrochemical Energy Storage for Green Grid. *Chem. Rev.* **2011**, *111* (5), 3577–3613. https://doi.org/10.1021/cr100290v.

(7) Dunn, B.; Kamath, H.; Tarascon, J.-M. Electrical Energy Storage for the Grid: A Battery of Choices. *Science* **2011**, *334* (6058), 928–935. https://doi.org/10.1126/science.1212741.

(8) Blomgren, G. E. The Development and Future of Lithium Ion Batteries. *J. Electrochem. Soc.* **2017**, *164* (1), A5019–A5025. https://doi.org/10.1149/2.0251701jes.

(9) Nitta, N.; Wu, F.; Lee, J. T.; Yushin, G. Li-Ion Battery Materials: Present and Future. *Mater. Today* **2015**, *18* (5), 252–264. https://doi.org/10.1016/j.mattod.2014.10.040.

(10) Sheikh, K.; Chen, B. X.; Penn, I. Lithium-Ion Batteries Work Earns Nobel Prize in Chemistry for 3 Scientists. *The New York Times*. October 9, 2019. https://www.nytimes.com/2019/10/09/science/nobel-prize-chemistry.html (accessed 2019-10-14).

(11) Staffell, I.; Scamman, D.; Abad, A. V.; Balcombe, P.; Dodds, P. E.; Ekins, P.; Shah, N.; Ward, K. R. The Role of Hydrogen and Fuel Cells in the Global Energy System. *Energy Environ. Sci.* **2019**, *12* (2), 463–491. https://doi.org/10.1039/C8EE01157E.

(12) Andersson, J.; Grönkvist, S. Large-Scale Storage of Hydrogen. *Int. J. Hydrog. Energy* **2019**, *44* (23), 11901–11919. https://doi.org/10.1016/j.ijhydene.2019.03.063.

(13) Kim, K. J.; Park, M.-S.; Kim, Y.-J.; Kim, J. H.; Dou, S. X.; Skyllas-Kazacos, M. A Technology Review of Electrodes and Reaction Mechanisms in Vanadium Redox Flow Batteries. *J. Mater. Chem. A* **2015**, *3* (33), 16913–16933. https://doi.org/10.1039/C5TA02613J.

(14) Chalamala, B. R.; Soundappan, T.; Fisher, G. R.; Anstey, M. R.; Viswanathan, V. V.; Perry, M. L. Redox Flow Batteries: An Engineering Perspective. *Proc. IEEE* **2014**, *102* (6), 976–999. https://doi.org/10.1109/JPROC.2014.2320317.

(15) Perry, M. L.; Weber, A. Z. Advanced Redox-Flow Batteries: A Perspective. *J. Electrochem. Soc.* **2016**, *163* (1), A5064–A5067. https://doi.org/10.1149/2.0101601jes.

(16) Perry, M. L.; Saraidaridis, J. D.; Darling, R. M. Crossover Mitigation Strategies for Redox-Flow Batteries. *Curr. Opin. Electrochem.* **2020**, *21*, 311–318. https://doi.org/10.1016/j.coelec.2020.03.024.

(17) Ding, Y.; Zhang, C.; Zhang, L.; Zhou, Y.; Yu, G. Molecular Engineering of Organic Electroactive Materials for Redox Flow Batteries. *Chem. Soc. Rev.* **2018**, *47* (1), 69–103. https://doi.org/10.1039/C7CS00569E.

(18) Li, M.; Rhodes, Z.; Cabrera-Pardo, J. R.; Minteer, S. D. Recent Advancements in Rational Design of Non-Aqueous Organic Redox Flow Batteries. *Sustain. Energy Fuels* **2020**, *4* (9), 4370–4389. https://doi.org/10.1039/D0SE00800A.

(19) Brushett, F. R.; Aziz, M. J.; Rodby, K. E. On Lifetime and Cost of Redox-Active Organics for Aqueous Flow Batteries. *ACS Energy Lett.* **2020**, *5* (3), 879–884. https://doi.org/10.1021/acsenergylett.0c00140.

(20) Rodby, K. E.; Carney, T. J.; Ashraf Gandomi, Y.; Barton, J. L.; Darling, R. M.; Brushett, F. R. Assessing the Levelized Cost of Vanadium Redox Flow Batteries with Capacity Fade and Rebalancing. *J. Power Sources* **2020**, *460*, 227958. https://doi.org/10.1016/j.jpowsour.2020.227958.

(21) Rodby, K. E.; Perry, M. L.; Brushett, F. R. Assessing Capacity Loss Remediation Methods for Asymmetric Redox Flow Battery Chemistries Using Levelized Cost of Storage. *J. Power Sources* **2021**, *506*, 230085. https://doi.org/10.1016/j.jpowsour.2021.230085.

(22) Baran, M. J.; Braten, M. N.; Sahu, S.; Baskin, A.; Meckler, S. M.; Li, L.; Maserati, L.; Carrington, M. E.; Chiang, Y.-M.; Prendergast, D.; Helms, B. A. Design Rules for Membranes from Polymers of Intrinsic Microporosity for Crossover-Free Aqueous Electrochemical Devices. *Joule* **2019**, 2968–2985. https://doi.org/10.1016/j.joule.2019.08.025.

(23) Kwabi, D. G.; Ji, Y.; Aziz, M. J. Electrolyte Lifetime in Aqueous Organic Redox Flow Batteries: A Critical Review. *Chem. Rev.* **2020**, *120* (14), 6467–6489. https://doi.org/10.1021/acs.chemrev.9b00599.

(24) Murali, A.; Nirmalchandar, A.; Krishnamoorthy, S.; Hoober-Burkhardt, L.; Yang, B.; Soloveichik, G.; Prakash, G. K. S.; Narayanan, S. R. Understanding and Mitigating Capacity Fade in Aqueous Organic Redox Flow Batteries. *J. Electrochem. Soc.* **2018**, *165* (7), A1193. https://doi.org/10.1149/2.0161807jes.

(25) Nolte, O.; Volodin, I. A.; Stolze, C.; Hager, M. D.; Schubert, U. S. Trust Is Good, Control Is Better: A Review on Monitoring and Characterization Techniques for Flow Battery Electrolytes. *Mater. Horiz.* **2021**, 1866–1925. https://doi.org/10.1039/D0MH01632B.

(26) Sevov, C. S.; Fisher, S. L.; Thompson, L. T.; Sanford, M. S. Mechanism-Based Development of a Low-Potential, Soluble, and Cyclable Multielectron Anolyte for Nonaqueous Redox Flow Batteries. *J. Am. Chem. Soc.* **2016**, *138* (47), 15378–15384. https://doi.org/10.1021/jacs.6b07638.

(27) Sevov, C. S.; Brooner, R. E. M.; Chénard, E.; Assary, R. S.; Moore, J. S.; Rodríguez-López, J.; Sanford, M. S. Evolutionary Design of Low Molecular Weight Organic Anolyte Materials for Applications in Nonaqueous Redox Flow Batteries. *J. Am. Chem. Soc.* **2015**, *137* (45), 14465–14472. https://doi.org/10.1021/jacs.5b09572.

(28) Gandomi, Y. A.; Aaron, D. S.; Houser, J. R.; Daugherty, M. C.; Clement, J. T.; Pezeshki, A. M.; Ertugrul, T. Y.; Moseley, D. P.; Mench, M. M. Critical Review—Experimental Diagnostics and Material Characterization Techniques Used on Redox Flow Batteries. *J. Electrochem. Soc.* **2018**, *165* (5), A970. https://doi.org/10.1149/2.0601805jes.

(29) Zhao, E. W.; Liu, T.; Jónsson, E.; Lee, J.; Temprano, I.; Jethwa, R. B.; Wang, A.; Smith, H.; Carretero-González, J.; Song, Q.; Grey, C. P. In Situ NMR Metrology Reveals Reaction Mechanisms in Redox Flow Batteries. *Nature* **2020**, *579* (7798), 224–228. https://doi.org/10.1038/s41586-020-2081-7.

(30) Sandford, C.; Edwards, M. A.; Klunder, K. J.; Hickey, D. P.; Li, M.; Barman, K.; Sigman, M. S.; White, H. S.; Minteer, S. D. A Synthetic Chemist's Guide to Electroanalytical Tools for Studying Reaction Mechanisms. *Chem. Sci.* **2019**, *10* (26), 6404–6422. https://doi.org/10.1039/C9SC01545K.

(31) Goulet, M.-A.; Aziz, M. J. Flow Battery Molecular Reactant Stability Determined by Symmetric Cell Cycling Methods. *J. Electrochem. Soc.* **2018**, *165* (7), A1466. https://doi.org/10.1149/2.0891807jes.

(32) Elgrishi, N.; Rountree, K. J.; McCarthy, B. D.; Rountree, E. S.; Eisenhart, T. T.; Dempsey, J. L. A Practical Beginner's Guide to Cyclic Voltammetry. *J. Chem. Educ.* **2018**, *95* (2), 197–206. https://doi.org/10.1021/acs.jchemed.7b00361.

(33) Bard, A. J.; Faulkner, L. R. *Electrochemical Methods: Fundamentals and Applications*; Wiley, 2000.

(34) Compton, R. G.; Banks, C. E. *Understanding Voltammetry*, 2nd ed. edition.; ICP, 2011.

(35) Fuller, T. F.; Harb, J. N. *Electrochemical Engineering*; John Wiley & Sons, 2018.

(36) Wang, H.; Sayed, S. Y.; Luber, E. J.; Olsen, B. C.; Shirurkar, S. M.; Venkatakrishnan, S.; Tefashe, U. M.; Farquhar, A. K.; Smotkin, E. S.; McCreery, R. L.; Buriak, J. M. Redox Flow Batteries: How to Determine Electrochemical Kinetic Parameters. *ACS Nano* **2020**, *14* (3), 2575–2584. https://doi.org/10.1021/acsnano.0c01281.

(37) Wang, C.; Li, X.; Yu, B.; Wang, Y.; Yang, Z.; Wang, H.; Lin, H.; Ma, J.; Li, G.; Jin, Z. Molecular Design of Fused-Ring Phenazine Derivatives for Long-Cycling Alkaline Redox Flow Batteries. *ACS Energy Lett.* **2020**, *5* (2), 411–417. https://doi.org/10.1021/acsenergylett.9b02676.

(38) Quan, M.; Sanchez, D.; Wasylkiw, M. F.; Smith, D. K. Voltammetry of Quinones in Unbuffered Aqueous Solution: Reassessing the Roles of Proton Transfer and Hydrogen Bonding in the Aqueous Electrochemistry of Quinones. *J. Am. Chem. Soc.* **2007**, *129* (42), 12847–12856. https://doi.org/10.1021/ja0743083.

(39) Forner-Cuenca, A.; Brushett, F. R. Engineering Porous Electrodes for Next-Generation Redox Flow Batteries: Recent Progress and Opportunities. *Curr. Opin. Electrochem.* **2019**, *18*, 113–122. https://doi.org/10.1016/j.coelec.2019.11.002.

(40) Barton, J. L.; Milshtein, J. D.; Hinricher, J. J.; Brushett, F. R. Quantifying the Impact of Viscosity on Mass-Transfer Coefficients in Redox Flow Batteries. *J. Power Sources* **2018**, *399*, 133–143. https://doi.org/10.1016/j.jpowsour.2018.07.046.

(41) Kowalski, J. A.; Neyhouse, B. J.; Brushett, F. R. The Impact of Bulk Electrolysis Cycling Conditions on the Perceived Stability of Redox Active Materials. *Electrochem. Commun.* **2020**, *111*, 106625. https://doi.org/10.1016/j.elecom.2019.106625.

(42) Milshtein, J. D.; Kaur, A. P.; Casselman, M. D.; Kowalski, J. A.; Modekrutti, S.; Zhang, P. L.; Attanayake, N. H.; Elliott, C. F.; Parkin, S. R.; Risko, C.; Brushett, F. R.; Odom, S. A. High Current Density, Long Duration Cycling of Soluble Organic Active Species for Non-Aqueous Redox Flow Batteries. *Energy Environ. Sci.* **2016**, *9* (11), 3531–3543. https://doi.org/10.1039/C6EE02027E.

(43) Ertugrul, T. Y.; Clement, J. T.; Gandomi, Y. A.; Aaron, D. S.; Mench, M. M. In-Situ Current Distribution and Mass Transport Analysis via Strip Cell Architecture for a Vanadium Redox Flow Battery. *J. Power Sources* **2019**, *437*, 226920. https://doi.org/10.1016/j.jpowsour.2019.226920.

(44) Silcox, B.; Zhang, J.; Shkrob, I. A.; Thompson, L.; Zhang, L. On Transferability of Performance Metrics for Redox-Active Molecules. *J. Phys. Chem. C* **2019**, *123* (27), 16516–16524. https://doi.org/10.1021/acs.jpcc.9b02230.

(45) Kowalski, J. A.; Fenton, A. M.; Neyhouse, B. J.; Brushett, F. R. A Method for Evaluating Soluble Redox Couple Stability Using Microelectrode Voltammetry. *J. Electrochem. Soc.* **2020**. https://doi.org/10.1149/1945-7111/abb7e9.

(46) Er, S.; Suh, C.; Marshak, M. P.; Aspuru-Guzik, A. Computational Design of Molecules for an All-Quinone Redox Flow Battery. *Chem. Sci.* **2015**, *6* (2), 885–893. https://doi.org/10.1039/C4SC03030C.

(47) Darling, R.; Gallagher, K.; Xie, W.; Su, L.; Brushett, F. Transport Property Requirements for Flow Battery Separators. *J. Electrochem. Soc.* **2016**, *163* (1), A5029–A5040. https://doi.org/10.1149/2.0051601jes.

(48) Darling, R. M.; Weber, A. Z.; Tucker, M. C.; Perry, M. L. The Influence of Electric Field on Crossover in Redox-Flow Batteries. *J. Electrochem. Soc.* **2015**, *163* (1), A5014. https://doi.org/10.1149/2.0031601jes.

(49) Crothers, A. R.; Darling, R. M.; Kusoglu, A.; Radke, C. J.; Weber, A. Z. Theory of Multicomponent Phenomena in Cation-Exchange Membranes: Part I. Thermodynamic Model and Validation. *J. Electrochem. Soc.* **2020**, *167* (1), 013547. https://doi.org/10.1149/1945-7111/ab6723.

(50) Nemani, V. P.; Smith, K. C. Analysis of Crossover-Induced Capacity Fade in Redox Flow Batteries with Non-Selective Separators. *J. Electrochem. Soc.* **2018**, *165* (13), A3144. https://doi.org/10.1149/2.0701813jes.

(51) Kushner, D. I.; Crothers, A. R.; Kusoglu, A.; Weber, A. Z. Transport Phenomena in Flow Battery Ion-Conducting Membranes. *Curr. Opin. Electrochem.* **2020**, *21*, 132–139. https://doi.org/10.1016/j.coelec.2020.01.010.

(52) Darling, R. M.; Saraidaridis, J. D.; Shovlin, C.; Fortin, M. The Influence of Current Density on Transport of Vanadium Acetylacetonate through a Cation-Exchange Membrane. *J. Electrochem. Soc.* **2022**, *169* (3), 030514. https://doi.org/10.1149/1945-7111/ac58cb.

(53) Su, L.; Darling, R. M.; Gallagher, K. G.; Xie, W.; Thelen, J. L.; Badel, A. F.; Barton, J. L.; Cheng, K. J.; Balsara, N. P.; Moore, J. S.; Brushett, F. R. An Investigation of the Ionic Conductivity and Species Crossover of Lithiated Nafion 117 in Nonaqueous Electrolytes. *J. Electrochem. Soc.* **2015**, *163* (1), A5253. https://doi.org/10.1149/2.03211601jes.

(54) Crothers, A. R.; Darling, R. M.; Kushner, D. I.; Perry, M. L.; Weber, A. Z. Theory of Multicomponent Phenomena in Cation-Exchange Membranes: Part III. Transport in Vanadium Redox-Flow-Battery Separators. *J. Electrochem. Soc.* **2020**, *167* (1), 013549. https://doi.org/10.1149/1945-7111/ab6725.

(55) Gigli, M.; Kowalski, J. A.; Neyhouse, B. J.; D'Epifanio, A.; Brushett, F. R.; Licoccia, S. Investigating the Factors That Influence Resistance Rise of PIM-1 Membranes in Nonaqueous Electrolytes. *Electrochem. Commun.* **2019**, *107*, 106530. https://doi.org/10.1016/j.elecom.2019.106530.

(56) Sing, D. C.; Meyers, J. P. Direct Measurement of Vanadium Crossover in an Operating Vanadium Redox Flow Battery. *ECS Trans.* **2013**, *50* (45), 61. https://doi.org/10.1149/05045.0061ecst.

(57) Ashraf Gandomi, Y.; Aaron, D. S.; Mench, M. M. Coupled Membrane Transport Parameters for Ionic Species in All-Vanadium Redox Flow Batteries. *Electrochimica Acta* **2016**, *218*, 174–190. https://doi.org/10.1016/j.electacta.2016.09.087.

(58) Darling, R. M.; Saraidaridis, J. D.; Shovlin, C.; Fortin, M.; Murdock, L. A.; Benicewicz, B. C. The Influence of Current Density on Transport of Vanadium Cations through Membranes with Different Charges. *J. Electrochem. Soc.* **2021**, *168* (4), 040516. https://doi.org/10.1149/1945-7111/abf264.

(59) Saraidaridis, J. D.; Darling, R. M.; Yang, Z.; Shovlin, C.; Fortin, M.; Robb, B. H.; Waters, S. E.; Marshak, M. P. Transport of Ligand Coordinated Iron and Chromium through Cation-Exchange Membranes. *J. Electrochem. Soc.* **2022**, *169* (6), 060532. https://doi.org/10.1149/1945-7111/ac7782.

(60) Luo, Q.; Li, L.; Nie, Z.; Wang, W.; Wei, X.; Li, B.; Chen, B.; Yang, Z. In-Situ Investigation of Vanadium Ion Transport in Redox Flow Battery. *J. Power Sources* **2012**, *218*, 15–20. https://doi.org/10.1016/j.jpowsour.2012.06.066.

(61) Vardner, J. T.; Ye, A. A.; Valdes, D. A.; West, A. C. Current-Driven Vanadium Crossover as a Function of SOC and SOD in the Vanadium Redox Flow Battery. *J. Electrochem. Soc.* **2020**, *167* (8), 080512. https://doi.org/10.1149/1945-7111/ab88bc.

(62) Vardner, J. T.; Edziah, J.-J. S.; West, A. C. Measurement of VO2+ Transference Number in Nafion with Varying Concentrations of Sulfuric Acid. *J. Electrochem. Soc.* **2019**, *166* (6), A848. https://doi.org/10.1149/2.0061906jes.

(63) Kumar Chakrabarti, B.; Kalamaras, E.; Kumar Singh, A.; Bertei, A.; Rubio-Garcia, J.; Yufit, V.; M. Tenny, K.; Wu, B.; Tariq, F.; S. Hajimolana, Y.; P. Brandon, N.; Low, C. T. J.; L. Roberts, E. P.; Chiang, Y.-M.; R. Brushett, F. Modelling of Redox Flow Battery

Electrode Processes at a Range of Length Scales: A Review. *Sustain. Energy Fuels* **2020**, *4* (11), 5433–5468. https://doi.org/10.1039/D0SE00667J.

(64) Tang, A.; Bao, J.; Skyllas-Kazacos, M. Dynamic Modelling of the Effects of Ion Diffusion and Side Reactions on the Capacity Loss for Vanadium Redox Flow Battery. *J. Power Sources* **2011**, *196* (24), 10737–10747. https://doi.org/10.1016/j.jpowsour.2011.09.003.

(65) Skyllas-Kazacos, M.; Goh, L. Modeling of Vanadium Ion Diffusion across the Ion Exchange Membrane in the Vanadium Redox Battery. *J. Membr. Sci.* **2012**, *399–400*, 43–48. https://doi.org/10.1016/j.memsci.2012.01.024.

(66) Pugach, M.; Kondratenko, M.; Briola, S.; Bischi, A. Zero Dimensional Dynamic Model of Vanadium Redox Flow Battery Cell Incorporating All Modes of Vanadium Ions Crossover. *Appl. Energy* **2018**, *226*, 560–569. https://doi.org/10.1016/j.apenergy.2018.05.124.

(67) Pathak, A.; Sharma, A. K.; Gupta, A. K. Dimensional Analysis of a Flow-by Porous Electrode and Demonstration to All-Vanadium Redox Flow Batteries Thereon. *J. Energy Storage* **2021**, *44*, 103258. https://doi.org/10.1016/j.est.2021.103258.

(68) Lee, S. B.; Mitra, K.; Pratt, H. D.; Anderson, T. M.; Ramadesigan, V.; Chalamala, B. R.; Subramanian, V. R. Open Data, Models, and Codes for Vanadium Redox Batch Cell Systems: A Systems Approach Using Zero-Dimensional Models. *J. Electrochem. Energy Convers. Storage* **2020**, *17* (1). https://doi.org/10.1115/1.4044156.

(69) Kapoor, M.; Gautam, R. K.; Ramani, V. K.; Verma, A. Predicting Operational Capacity of Redox Flow Battery Using a Generalized Empirical Correlation Derived from Dimensional Analysis. *Chem. Eng. J.* **2020**, *379*, 122300. https://doi.org/10.1016/j.cej.2019.122300.

(70) Sharma, A. K.; Ling, C. Y.; Birgersson, E.; Vynnycky, M.; Han, M. Verified Reduction of Dimensionality for an All-Vanadium Redox Flow Battery Model. *J. Power Sources* **2015**, *279*, 345–350. https://doi.org/10.1016/j.jpowsour.2015.01.019.

(71) Modak, S.; Kwabi, D. G. A Zero-Dimensional Model for Electrochemical Behavior and Capacity Retention in Organic Flow Cells. *J. Electrochem. Soc.* **2021**, *168* (8), 080528. https://doi.org/10.1149/1945-7111/ac1c1f.

(72) Kaur, A. P.; Holubowitch, N. E.; Ergun, S.; Elliott, C. F.; Odom, S. A. A Highly Soluble Organic Catholyte for Non-Aqueous Redox Flow Batteries. *Energy Technol.* **2015**, *3* (5), 476–480. https://doi.org/10.1002/ente.201500020.

(73) Petchsingh, C.; Quill, N.; Joyce, J. T.; Eidhin, D. N.; Oboroceanu, D.; Lenihan, C.; Gao, X.; Lynch, R. P.; Buckley, D. N. Spectroscopic Measurement of State of Charge in Vanadium Flow Batteries with an Analytical Model of VIV-VV Absorbance. *J. Electrochem. Soc.* **2015**, *163* (1), A5068. https://doi.org/10.1149/2.0091601jes.

(74) Zhao, E. W.; Jónsson, E.; Jethwa, R. B.; Hey, D.; Lyu, D.; Brookfield, A.; Klusener, P. A. A.; Collison, D.; Grey, C. P. Coupled In Situ NMR and EPR Studies Reveal the Electron Transfer Rate and Electrolyte Decomposition in Redox Flow Batteries. *J. Am. Chem. Soc.* **2021**, *143* (4), 1885–1895. https://doi.org/10.1021/jacs.0c10650.

(75) Sevov, C. S.; Hickey, D. P.; Cook, M. E.; Robinson, S. G.; Barnett, S.; Minteer, S. D.; Sigman, M. S.; Sanford, M. S. Physical Organic Approach to Persistent, Cyclable, Low-

Potential Electrolytes for Flow Battery Applications. *J. Am. Chem. Soc.* **2017**, *139* (8), 2924–2927. https://doi.org/10.1021/jacs.7b00147.

(76) Huang, J.; Pan, B.; Duan, W.; Wei, X.; Assary, R. S.; Su, L.; Brushett, F. R.; Cheng, L.; Liao, C.; Ferrandon, M. S.; Wang, W.; Zhang, Z.; Burrell, A. K.; Curtiss, L. A.; Shkrob, I. A.; Moore, J. S.; Zhang, L. The Lightest Organic Radical Cation for Charge Storage in Redox Flow Batteries. *Sci. Rep.* **2016**, *6* (1), 1–9. https://doi.org/10.1038/srep32102.

(77) Zhang, J.; Yang, Z.; Shkrob, I. A.; Assary, R. S.; Tung, S. on; Silcox, B.; Duan, W.; Zhang, J.; Su, C. C.; Hu, B.; Pan, B.; Liao, C.; Zhang, Z.; Wang, W.; Curtiss, L. A.; Thompson, L. T.; Wei, X.; Zhang, L. Annulated Dialkoxybenzenes as Catholyte Materials for Non-Aqueous Redox Flow Batteries: Achieving High Chemical Stability through Bicyclic Substitution. *Adv. Energy Mater.* **2017**, *7* (21), 1701272. https://doi.org/10.1002/aenm.201701272.

(78) Nolte, O.; Geitner, R.; Hager, M. D.; Schubert, U. S. IR Spectroscopy as a Method for Online Electrolyte State Assessment in RFBs. *Adv. Energy Mater.* **2021**, *11* (28), 2100931. https://doi.org/10.1002/aenm.202100931.

(79) Rudolph, S.; Schröder, U.; Bayanov, I. M.; Blenke, K.; Hage, D. High Resolution State of Charge Monitoring of Vanadium Electrolytes with IR Optical Sensor. *J. Electroanal. Chem.* **2013**, *694*, 17–22. https://doi.org/10.1016/j.jelechem.2013.01.042.

(80) Ressel, S.; Bill, F.; Holtz, L.; Janshen, N.; Chica, A.; Flower, T.; Weidlich, C.; Struckmann, T. State of Charge Monitoring of Vanadium Redox Flow Batteries Using Half Cell Potentials and Electrolyte Density. *J. Power Sources* **2018**, *378*, 776–783. https://doi.org/10.1016/j.jpowsour.2018.01.006.

(81) Li, X.; Xiong, J.; Tang, A.; Qin, Y.; Liu, J.; Yan, C. Investigation of the Use of Electrolyte Viscosity for Online State-of-Charge Monitoring Design in Vanadium Redox Flow Battery. *Appl. Energy* **2018**, *211*, 1050–1059. https://doi.org/10.1016/j.apenergy.2017.12.009.

(82) Quill, N.; Oboroceanu, D.; Buckley, D. N.; Lynch, R. P. Conductivity of Vanadium Flow Battery (VFB) Catholytes: Dependence on Sulfur and Vanadium Concentration and Temperature. *ECS Trans.* **2017**, *80* (10), 3. https://doi.org/10.1149/08010.0003ecst.

(83) Zelger, C.; Süßenbacher, M.; Laskos, A.; Gollas, B. State of Charge Indicators for Alkaline Zinc-Air Redox Flow Batteries. *J. Power Sources* **2019**, *424*, 76–81. https://doi.org/10.1016/j.jpowsour.2019.03.099.

(84) Haisch, T.; Ji, H.; Weidlich, C. Monitoring the State of Charge of All-Vanadium Redox Flow Batteries to Identify Crossover of Electrolyte. *Electrochimica Acta* **2020**, *336*, 135573. https://doi.org/10.1016/j.electacta.2019.135573.

(85) Watt-Smith, M. J.; Ridley, P.; Wills, R. G. A.; Shah, A. A.; Walsh, F. C. The Importance of Key Operational Variables and Electrolyte Monitoring to the Performance of an All Vanadium Redox Flow Battery. *J. Chem. Technol. Biotechnol.* **2013**, *88* (1), 126–138. https://doi.org/10.1002/jctb.3870.

(86) Knehr, K. W.; Kumbur, E. C. Open Circuit Voltage of Vanadium Redox Flow Batteries: Discrepancy between Models and Experiments. *Electrochem. Commun.* **2011**, *13* (4), 342–345. https://doi.org/10.1016/j.elecom.2011.01.020.

(87) Hayer, N.; Kohns, M. Thermodynamically Rigorous Description of the Open Circuit Voltage of Redox Flow Batteries. *J. Electrochem. Soc.* **2020**, *167* (11), 110516. https://doi.org/10.1149/1945-7111/ab9e85.

(88) Stolze, C.; Hager, M. D.; Schubert, U. S. State-of-Charge Monitoring for Redox Flow Batteries: A Symmetric Open-Circuit Cell Approach. *J. Power Sources* **2019**, *423*, 60–67. https://doi.org/10.1016/j.jpowsour.2019.03.002.

(89) Struckmann, T.; Kuhn, P.; Ressel, S. A Combined in Situ Monitoring Approach for Half Cell State of Charge and State of Health of Vanadium Redox Flow Batteries. *Electrochimica Acta* **2020**, *362*, 137174. https://doi.org/10.1016/j.electacta.2020.137174.

(90) Yang, Z.; Darling, R. M.; Perry, M. L. Electrolyte Compositions in a Vanadium Redox Flow Battery Measured with a Reference Cell. *J. Electrochem. Soc.* **2019**, *166* (13), A3045. https://doi.org/10.1149/2.1161913jes.

(91) Fenton Jr., A. M.; Brushett, F. R. Using Voltammetry Augmented with Physics-Based Modeling and Bayesian Hypothesis Testing to Identify Analytes in Electrolyte Solutions. *J. Electroanal. Chem.* **2021**, 115751. https://doi.org/10.1016/j.jelechem.2021.115751.

(92) Mirceski, V.; Komorsky-Lovrić, S.; Lovrić, M. *Square-Wave Voltammetry: Theory and Application*; Monographs in Electrochemistry; Springer-Verlag, 2007. https://doi.org/10.1007/978-3-540-73740-7.

(93) Gundry, L.; Guo, S.-X.; Kennedy, G.; Keith, J.; Robinson, M.; Gavaghan, D.; Bond, A. M.; Zhang, J. Recent Advances and Future Perspectives for Automated Parameterisation, Bayesian Inference and Machine Learning in Voltammetry. *Chem. Commun.* **2021**, *57* (15), 1855–1870. https://doi.org/10.1039/D0CC07549C.

(94) Kroner, I.; Becker, M.; Turek, T. Monitoring the State of Charge of the Positive Electrolyte in a Vanadium Redox-Flow Battery with a Novel Amperometric Sensor. *Batteries* **2019**, *5* (1), 5. https://doi.org/10.3390/batteries5010005.

(95) Pahari, S. K.; Gokoglan, T. C.; Visayas, B. R. B.; Woehl, J.; Golen, J. A.; Howland, R.; Mayes, M. L.; Agar, E.; Cappillino, P. J. Designing High Energy Density Flow Batteries by Tuning Active-Material Thermodynamics. *RSC Adv.* **2021**, *11* (10), 5432–5443. https://doi.org/10.1039/D0RA10913D.

(96) Baran, M. J.; Braten, M. N.; Montoto, E. C.; Gossage, Z. T.; Ma, L.; Chénard, E.; Moore, J. S.; Rodríguez-López, J.; Helms, B. A. Designing Redox-Active Oligomers for Crossover-Free, Nonaqueous Redox-Flow Batteries with High Volumetric Energy Density. *Chem. Mater.* **2018**, *30* (11), 3861–3866. https://doi.org/10.1021/acs.chemmater.8b01318.

(97) Montoto, E. C.; Nagarjuna, G.; Moore, J. S.; Rodríguez-López, J. Redox Active Polymers for Non-Aqueous Redox Flow Batteries: Validation of the Size-Exclusion Approach. *J. Electrochem. Soc.* **2017**, *164* (7), A1688–A1694. https://doi.org/10.1149/2.1511707jes.

(98) Kowalski, J. A.; Fenton Jr., A. M.; Neyhouse, B. J.; Brushett, F. R. A Method for Evaluating Soluble Redox Couple Stability Using Microelectrode Voltammetry. *J. Electrochem. Soc.* **2020**, *167* (16), 160513. https://doi.org/10.1149/1945-7111/abb7e9.

(99) Bond, A. M. Past, Present and Future Contributions of Microelectrodes to Analytical Studies Employing Voltammetric Detection. A Review. *Analyst* **1994**, *119* (11), 1R-21R. https://doi.org/10.1039/AN994190001R.

(100) Stolze, C.; Meurer, J. P.; Hager, M. D.; Schubert, U. S. An Amperometric, Temperature-Independent, and Calibration-Free Method for the Real-Time State-of-Charge Monitoring of Redox Flow Battery Electrolytes. *Chem. Mater.* **2019**, *31* (15), 5363–5369. https://doi.org/10.1021/acs.chemmater.9b02376.

(101) Kaur, A. P.; Harris, O. C.; Attanayake, N. H.; Liang, Z.; Parkin, S. R.; Tang, M. H.; Odom, S. A. Quantifying Environmental Effects on the Solution and Solid-State Stability of a Phenothiazine Radical Cation. *Chem. Mater.* **2020**, *32* (7), 3007–3017. https://doi.org/10.1021/acs.chemmater.9b05345.

(102) Milshtein, J. D.; Barton, J. L.; Darling, R. M.; Brushett, F. R. 4-Acetamido-2,2,6,6-Tetramethylpiperidine-1-Oxyl as a Model Organic Redox Active Compound for Nonaqueous Flow Batteries. *J. Power Sources* **2016**, *327*, 151–159. https://doi.org/10.1016/j.jpowsour.2016.06.125.

(103) Milshtein, J. D.; Tenny, K. M.; Barton, J. L.; Drake, J.; Darling, R. M.; Brushett, F. R. Quantifying Mass Transfer Rates in Redox Flow Batteries. *J. Electrochem. Soc.* **2017**, *164* (11), E3265–E3275. https://doi.org/10.1149/2.0201711jes.

(104) Novak, P.; Christensen, P. A.; Iwasita, T.; Vielstich, W. Anodic Oxidation of Propylene Carbonate on Platinum, Glassy Carbon and Polypyrrole: An "in-Situ" FTIR Study. *J. Electroanal. Chem. Interfacial Electrochem.* **1989**, *263* (1), 37–48. https://doi.org/10.1016/0022-0728(89)80122-6.

(105) Deen, W. M. *Analysis of Transport Phenomena*, 2nd edition.; Oxford University Press, 2011.

(106) Wang, Y. (王怡琳); Kaur, A. P.; Attanayake, N. H.; Yu, Z. (于洲); Suduwella, T. M.; Cheng, L. (程蕾); Odom, S. A.; Ewoldt, R. H. Viscous Flow Properties and Hydrodynamic Diameter of Phenothiazine-Based Redox-Active Molecules in Different Supporting Salt Environments. *Phys. Fluids* **2020**, *32* (8), 083108. https://doi.org/10.1063/5.0010168.

(107) Xu, Q.; Zhao, T. S.; Zhang, C. Effects of SOC-Dependent Electrolyte Viscosity on Performance of Vanadium Redox Flow Batteries. *Appl. Energy* **2014**, *130*, 139–147. https://doi.org/10.1016/j.apenergy.2014.05.034.

(108) Neyhouse, B. J.; Fenton Jr., A. M.; Brushett, F. R. Too Much of a Good Thing? Assessing Performance Tradeoffs of Two-Electron Compounds for Redox Flow Batteries. *J. Electrochem. Soc.* **2021**, *168* (5), 050501. https://doi.org/10.1149/1945-7111/abeea3.

(109) Boettcher, P. A.; Agar, E.; Dennison, C. R.; Kumbur, E. C. Modeling of Ion Crossover in Vanadium Redox Flow Batteries: A Computationally-Efficient Lumped Parameter Approach for Extended Cycling. *J. Electrochem. Soc.* **2015**, *163* (1), A5244. https://doi.org/10.1149/2.0311601jes.

(110) Ma, R. X.; Setzler, B. P.; Gong, K.; Gu, S.; Yan, Y. A General, Analytical Model for Flow Battery Costing and Design. *J. Electrochem. Soc.* **2018**, *165* (10), A2209. https://doi.org/10.1149/2.1201809jes.

(111) Trovò, A. Battery Management System for Industrial-Scale Vanadium Redox Flow Batteries: Features and Operation. *J. Power Sources* **2020**, *465*, 228229. https://doi.org/10.1016/j.jpowsour.2020.228229.

(112) Wei, Z.; Tseng, K. J.; Wai, N.; Lim, T. M.; Skyllas-Kazacos, M. Adaptive Estimation of State of Charge and Capacity with Online Identified Battery Model for Vanadium Redox Flow Battery. *J. Power Sources* **2016**, *332*, 389–398. https://doi.org/10.1016/j.jpowsour.2016.09.123.

(113) Clemente, A.; Costa-Castelló, R. Redox Flow Batteries: A Literature Review Oriented to Automatic Control. *Energies* **2020**, *13* (17), 4514. https://doi.org/10.3390/en13174514.

(114) Lee, S. B.; Pratt, H. D.; Anderson, T. M.; Mitra, K.; Chalamala, B. R.; Subramanian, V. R. Estimation of Transport and Kinetic Parameters of Vanadium Redox Batteries Using Static Cells. *ECS Trans.* **2018**, *85* (5), 43. https://doi.org/10.1149/08505.0043ecst.

(115) Tenny, K. M.; Braatz, R. D.; Chiang, Y.-M.; Brushett, F. R. Leveraging Neural Networks and Genetic Algorithms to Refine Electrode Properties in Redox Flow Batteries. *J. Electrochem. Soc.* **2021**, *168* (5), 050547. https://doi.org/10.1149/1945-7111/abf77c.

(116) Severson, K. A.; Attia, P. M.; Jin, N.; Perkins, N.; Jiang, B.; Yang, Z.; Chen, M. H.; Aykol, M.; Herring, P. K.; Fraggedakis, D.; Bazant, M. Z.; Harris, S. J.; Chueh, W. C.; Braatz, R. D. Data-Driven Prediction of Battery Cycle Life before Capacity Degradation. *Nat. Energy* **2019**, *4* (5), 383–391. https://doi.org/10.1038/s41560-019-0356-8.

(117) Wiberg, C.; Carney, T. J.; Brushett, F.; Ahlberg, E.; Wang, E. Dimerization of 9,10-Anthraquinone-2,7-Disulfonic Acid (AQDS). *Electrochimica Acta* **2019**, *317*, 478–485. https://doi.org/10.1016/j.electacta.2019.05.134.

(118) Goulet, M.-A.; Tong, L.; Pollack, D. A.; Tabor, D. P.; Odom, S. A.; Aspuru-Guzik, A.; Kwan, E. E.; Gordon, R. G.; Aziz, M. J. Extending the Lifetime of Organic Flow Batteries via Redox State Management. *J. Am. Chem. Soc.* **2019**, *141* (20), 8014–8019. https://doi.org/10.1021/jacs.8b13295.

(119) Hu, B.; Luo, J.; Hu, M.; Yuan, B.; Liu, T. L. A PH-Neutral, Metal-Free Aqueous Organic Redox Flow Battery Employing an Ammonium Anthraquinone Anolyte. *Angew. Chem.* **2019**, *131* (46), 16782–16789. https://doi.org/10.1002/ange.201907934.

(120) Hoober-Burkhardt, L.; Krishnamoorthy, S.; Yang, B.; Murali, A.; Nirmalchandar, A.; Prakash, G. K. S.; Narayanan, S. R. A New Michael-Reaction-Resistant Benzoquinone for Aqueous Organic Redox Flow Batteries. *J. Electrochem. Soc.* **2017**, *164* (4), A600–A607. https://doi.org/10.1149/2.0351704jes.

(121) Zhang, J.; Shkrob, I. A.; Assary, R. S.; Tung, S. on; Silcox, B.; Curtiss, L. A.; Thompson, L.; Zhang, L. Toward Improved Catholyte Materials for Redox Flow Batteries: What Controls Chemical Stability of Persistent Radical Cations? *J. Phys. Chem. C* **2017**, *121* (42), 23347–23358. https://doi.org/10.1021/acs.jpcc.7b08281.

(122) Wei, J.; Prater, C. D. The Structure and Analysis of Complex Reaction Systems. In *Advances in Catalysis*; Eley, D. D., Selwood, P. W., Weisz, P. B., Balandin, A. A., De Boer, J. H., Debye, P. J., Emmett, P. H., Horiuti, J., Jost, W., Natta, G., Rideal, E. K., Taylor, H.

S., Eds.; Academic Press, 1962; Vol. 13, pp 203–392. https://doi.org/10.1016/S0360-0564(08)60289-8.

(123) You, X.; Ye, Q.; Cheng, P. The Dependence of Mass Transfer Coefficient on the Electrolyte Velocity in Carbon Felt Electrodes: Determination and Validation. *J. Electrochem. Soc.* **2017**, *164* (11), E3386. https://doi.org/10.1149/2.0401711jes.

(124) Schmal, D.; Van Erkel, J.; Van Duin, P. J. Mass Transfer at Carbon Fibre Electrodes. *J. Appl. Electrochem.* **1986**, *16* (3), 422–430. https://doi.org/10.1007/BF01008853.

(125) Barton, J. L.; Milshtein, J. D.; Hinricher, J. J.; Brushett, F. R. Quantifying the Impact of Viscosity on Mass-Transfer Coefficients in Redox Flow Batteries. *J. Power Sources* **2018**, *399*, 133–143. https://doi.org/10.1016/j.jpowsour.2018.07.046.

(126) Attanayake, N. H.; Liang, Z.; Wang, Y.; Kaur, A. P.; Parkin, S. R.; Mobley, J. K.; Ewoldt, R. H.; Landon, J.; Odom, S. A. Dual Function Organic Active Materials for Nonaqueous Redox Flow Batteries. *Mater. Adv.* **2021**, *2* (4), 1390–1401. https://doi.org/10.1039/D0MA00881H.

(127) Garza, G. D. L.; Kaur, A.; Shkrob, I.; Robertson, L.; Odom, S.; McNeil, A. Balancing High Energy Density and Chemical Stability in Redox Flow Batteries with Symmetric Tetrazines. **2021**. https://doi.org/10.26434/chemrxiv-2021-tjb1v.

(128) Yan, Y.; Vogt, D. B.; Vaid, T. P.; Sigman, M. S.; Sanford, M. S. Development of High Energy Density Diaminocyclopropenium-Phenothiazine Hybrid Catholytes for Non-Aqueous Redox Flow Batteries. *Angew. Chem. Int. Ed.* **2021**, *60* (52), 27039–27045. https://doi.org/10.1002/anie.202111939.

(129) Greco, K. V.; Bonesteel, J. K.; Chanut, N.; Tai-Chieh Wan, C.; Chiang, Y.-M.; Brushett, F. R. Limited Accessibility to Surface Area Generated by Thermal Pretreatment of Electrodes Reduces Its Impact on Redox Flow Battery Performance. *ACS Appl. Energy Mater.* **2021**, *4* (12), 13516–13527. https://doi.org/10.1021/acsaem.1c01980.

(130) Forner-Cuenca, A.; Penn, E. E.; Oliveira, A. M.; Brushett, F. R. Exploring the Role of Electrode Microstructure on the Performance of Non-Aqueous Redox Flow Batteries. *J. Electrochem. Soc.* **2019**, *166* (10), A2230–A2241. https://doi.org/10.1149/2.0611910jes.

(131) Burgess, M.; Moore, J. S.; Rodríguez-López, J. Redox Active Polymers as Soluble Nanomaterials for Energy Storage. *Acc. Chem. Res.* **2016**, *49* (11), 2649–2657. https://doi.org/10.1021/acs.accounts.6b00341.

(132) Montoto, E. C.; Nagarjuna, G.; Hui, J.; Burgess, M.; Sekerak, N. M.; Hernández-Burgos, K.; Wei, T.-S.; Kneer, M.; Grolman, J.; Cheng, K. J.; Lewis, J. A.; Moore, J. S.; Rodríguez-López, J. Redox Active Colloids as Discrete Energy Storage Carriers. *J. Am. Chem. Soc.* **2016**, *138* (40), 13230–13237. https://doi.org/10.1021/jacs.6b06365.

(133) Li, M.; Case, J.; Minteer, S. D. Bipolar Redox-Active Molecules in Non-Aqueous Organic Redox Flow Batteries: Status and Challenges. *ChemElectroChem* **2021**, *8* (7), 1215–1232. https://doi.org/10.1002/celc.202001584.

(134) Silcox, B.; Zhang, J.; Tung, S. O.; Shkrob, I. A.; Zhang, L.; Thompson, L. T. Cross-Platform Classifier of Chemical Stability for Charged Redoxmers. *ACS Mater. Lett.* **2021**, 1605–1609. https://doi.org/10.1021/acsmaterialslett.1c00424.

(135) Neyhouse, B. J.; Brushett, F. R. From the Synthesis Vial to the Full Cell: Electrochemical Methods for Characterizing Active Materials for Redox Flow Batteries. In *Encyclopedia of Energy Storage*; Cabeza, L. F., Ed.; Elsevier: Oxford, 2022; pp 453–465. https://doi.org/10.1016/B978-0-12-819723-3.00058-5.

(136) Li, M.; Odom, S. A.; Pancoast, A. R.; Robertson, L. A.; Vaid, T. P.; Agarwal, G.; Doan, H. A.; Wang, Y.; Suduwella, T. M.; Bheemireddy, S. R.; Ewoldt, R. H.; Assary, R. S.; Zhang, L.; Sigman, M. S.; Minteer, S. D. Experimental Protocols for Studying Organic Non-Aqueous Redox Flow Batteries. *ACS Energy Lett.* **2021**, *6* (11), 3932–3943. https://doi.org/10.1021/acsenergylett.1c01675.

(137) Liang, Z.; Attanayake, N. H.; Greco, K. V.; Neyhouse, B. J.; Barton, J. L.; Kaur, A. P.; Eubanks, W. L.; Brushett, F. R.; Landon, J.; Odom, S. A. Comparison of Separators vs Membranes in Nonaqueous Redox Flow Battery Electrolytes Containing Small Molecule Active Materials. *ACS Appl. Energy Mater.* **2021**, *4* (6), 5443–5451. https://doi.org/10.1021/acsaem.1c00017.

(138) Small, L. J.; Pratt, H. D.; Anderson, T. M. Crossover in Membranes for Aqueous Soluble Organic Redox Flow Batteries. *J. Electrochem. Soc.* **2019**, *166* (12), A2536. https://doi.org/10.1149/2.0681912jes.

(139) Orella, M. J.; Brown, S. M.; Leonard, M. E.; Román-Leshkov, Y.; Brushett, F. R. A General Technoeconomic Model for Evaluating Emerging Electrolytic Processes. *Energy Technol.* **2020**, *8* (11), 1900994. https://doi.org/10.1002/ente.201900994.

(140) Driscoll, T. A.; Hale, N.; Trefethen, L. N. *Chebfun Guide*; Pafnuty Publications: Oxford, 2014.

(141) Kowalski, J. A.; Su, L.; Milshtein, J. D.; Brushett, F. R. Recent Advances in Molecular Engineering of Redox Active Organic Molecules for Nonaqueous Flow Batteries. *Curr. Opin. Chem. Eng.* **2016**, *13*, 45–52. https://doi.org/10.1016/j.coche.2016.08.002.

(142) Hogue, R. W.; Toghill, K. E. Metal Coordination Complexes in Nonaqueous Redox Flow Batteries. *Curr. Opin. Electrochem.* **2019**, *18*, 37–45. https://doi.org/10.1016/j.coelec.2019.08.006.

(143) Ruiyong Chen. Redox Flow Batteries for Energy Storage: Recent Advances in Using Organic Active Materials. *Curr. Opin. Electrochem.* **2020**, *21*, 40–45. https://doi.org/10.1016/j.coelec.2020.01.003.

(144) Yan, Y.; Robinson, S. G.; Sigman, M. S.; Sanford, M. S. Mechanism-Based Design of a High-Potential Catholyte Enables a 3.2 V All-Organic Nonaqueous Redox Flow Battery. *J. Am. Chem. Soc.* **2019**, *141* (38), 15301–15306. https://doi.org/10.1021/jacs.9b07345.

(145) Kowalski, J. A.; Casselman, M. D.; Kaur, A. P.; Milshtein, J. D.; Elliott, C. F.; Modekrutti, S.; Attanayake, N. H.; Zhang, N.; Parkin, S. R.; Risko, C.; Brushett, F. R.; Odom, S. A. A Stable Two-Electron-Donating Phenothiazine for Application in Nonaqueous Redox Flow Batteries. *J. Mater. Chem. A* **2017**, *5* (46), 24371–24379. https://doi.org/10.1039/C7TA05883G.

(146) Attanayake, N. H.; Kowalski, J. A.; Greco, K. V.; Casselman, M. D.; Milshtein, J. D.; Chapman, S. J.; Parkin, S. R.; Brushett, F. R.; Odom, S. A. Tailoring Two-Electron-

Donating Phenothiazines To Enable High-Concentration Redox Electrolytes for Use in Nonaqueous Redox Flow Batteries. *Chem. Mater.* **2019**, *31* (12), 4353–4363. https://doi.org/10.1021/acs.chemmater.8b04770.

(147) Hendriks, K. H.; Sevov, C. S.; Cook, M. E.; Sanford, M. S. Multielectron Cycling of a Low-Potential Anolyte in Alkali Metal Electrolytes for Nonaqueous Redox Flow Batteries. *ACS Energy Lett.* **2017**, *2* (10), 2430–2435. https://doi.org/10.1021/acsenergylett.7b00559.

(148) Zhang, C.; Niu, Z.; Peng, S.; Ding, Y.; Zhang, L.; Guo, X.; Zhao, Y.; Yu, G. Phenothiazine-Based Organic Catholyte for High-Capacity and Long-Life Aqueous Redox Flow Batteries. *Adv. Mater.* **2019**, *31* (24), 1901052. https://doi.org/10.1002/adma.201901052.

(149) Yang, B.; Hoober-Burkhardt, L.; Krishnamoorthy, S.; Murali, A.; Prakash, G. K. S.; Narayanan, S. R. High-Performance Aqueous Organic Flow Battery with Quinone-Based Redox Couples at Both Electrodes. *J. Electrochem. Soc.* **2016**, *163* (7), A1442–A1449. https://doi.org/10.1149/2.1371607jes.

(150) Tong, L.; Goulet, M.-A.; Tabor, D. P.; Kerr, E. F.; De Porcellinis, D.; Fell, E. M.; Aspuru-Guzik, A.; Gordon, R. G.; Aziz, M. J. Molecular Engineering of an Alkaline Naphthoquinone Flow Battery. *ACS Energy Lett.* **2019**, *4* (8), 1880–1887. https://doi.org/10.1021/acsenergylett.9b01321.

(151) Griffin, J. D.; Pancoast, A. R.; Sigman, M. S. Interrogation of 2,2′-Bipyrimidines as Low-Potential Two-Electron Electrolytes. *J. Am. Chem. Soc.* **2021**, *143* (2), 992–1004. https://doi.org/10.1021/jacs.0c11267.

(152) Alkhayri, F.; Dyker, C. A. A Two-Electron Bispyridinylidene Anolyte for Non-Aqueous Organic Redox Flow Batteries. *J. Electrochem. Soc.* **2020**, *167* (16), 160548. https://doi.org/10.1149/1945-7111/abd492.

(153) Kwon, G.; Lee, S.; Hwang, J.; Shim, H.-S.; Lee, B.; Lee, M. H.; Ko, Y.; Jung, S.-K.; Ku, K.; Hong, J.; Kang, K. Multi-Redox Molecule for High-Energy Redox Flow Batteries. *Joule* **2018**, *2* (9), 1771–1782. https://doi.org/10.1016/j.joule.2018.05.014.

(154) Huang, J.; Yang, Z.; Vijayakumar, M.; Duan, W.; Hollas, A.; Pan, B.; Wang, W.; Wei, X.; Zhang, L. A Two-Electron Storage Nonaqueous Organic Redox Flow Battery. *Adv. Sustain. Syst.* **2018**, *2* (3), 1700131. https://doi.org/10.1002/adsu.201700131.

(155) Hu, B.; Liu, T. L. Two Electron Utilization of Methyl Viologen Anolyte in Nonaqueous Organic Redox Flow Battery. *J. Energy Chem.* **2018**, *27* (5), 1326–1332. https://doi.org/10.1016/j.jechem.2018.02.014.

(156) Chai, J.; Lashgari, A.; Wang, X.; Jiang, J. “Jimmy.” Extending the Redox Potentials of Metal-Free Anolytes: Towards High Energy Density Redox Flow Batteries. *J. Electrochem. Soc.* **2020**, *167* (10), 100556. https://doi.org/10.1149/1945-7111/ab9e84.

(157) Liu, T.; Wei, X.; Nie, Z.; Sprenkle, V.; Wang, W. A Total Organic Aqueous Redox Flow Battery Employing a Low Cost and Sustainable Methyl Viologen Anolyte and 4-HO-TEMPO Catholyte. *Adv. Energy Mater.* **2016**, *6* (3), 1501449. https://doi.org/10.1002/aenm.201501449.

(158) DeBruler, C.; Hu, B.; Moss, J.; Luo, J.; Liu, T. L. A Sulfonate-Functionalized Viologen Enabling Neutral Cation Exchange, Aqueous Organic Redox Flow Batteries toward

Renewable Energy Storage. *ACS Energy Lett.* **2018**, *3* (3), 663–668. https://doi.org/10.1021/acsenergylett.7b01302.

(159) Luo, J.; Hu, B.; Debruler, C.; Liu, T. L. A π-Conjugation Extended Viologen as a Two-Electron Storage Anolyte for Total Organic Aqueous Redox Flow Batteries. *Angew. Chem. Int. Ed.* **2018**, *57* (1), 231–235. https://doi.org/10.1002/anie.201710517.

(160) Wang, H.; Li, D.; Xu, J.; Wu, Y.; Cui, Y.; Chen, L. An Unsymmetrical Two-Electron Viologens Anolyte for Salt Cavern Redox Flow Battery. *J. Power Sources* **2021**, *492*, 229659. https://doi.org/10.1016/j.jpowsour.2021.229659.

(161) Cabrera, P. J.; Yang, X.; Suttil, J. A.; Hawthorne, K. L.; Brooner, R. E. M.; Sanford, M. S.; Thompson, L. T. Complexes Containing Redox Noninnocent Ligands for Symmetric, Multielectron Transfer Nonaqueous Redox Flow Batteries. *J. Phys. Chem. C* **2015**, *119* (28), 15882–15889. https://doi.org/10.1021/acs.jpcc.5b03582.

(162) Laramie, S. M.; Milshtein, J. D.; Breault, T. M.; Brushett, F. R.; Thompson, L. T. Performance and Cost Characteristics of Multi-Electron Transfer, Common Ion Exchange Non-Aqueous Redox Flow Batteries. *J. Power Sources* **2016**, *327*, 681–692. https://doi.org/10.1016/j.jpowsour.2016.07.015.

(163) Arnold, A.; Dougherty, R. J.; Carr, C. R.; Reynolds, L. C.; Fettinger, J. C.; Augustin, A.; Berben, L. A. A Stable Organo-Aluminum Analyte Enables Multielectron Storage for a Nonaqueous Redox Flow Battery. *J. Phys. Chem. Lett.* **2020**, *11* (19), 8202–8207. https://doi.org/10.1021/acs.jpclett.0c01761.

(164) Savéant, J.-M.; Costentin, C. *Elements of Molecular and Biomolecular Electrochemistry: An Electrochemical Approach to Electron Transfer Chemistry*; John Wiley & Sons, 2019.

(165) Darling, R. M.; Gallagher, K. G.; Kowalski, J. A.; Ha, S.; Brushett, F. R. Pathways to Low-Cost Electrochemical Energy Storage: A Comparison of Aqueous and Nonaqueous Flow Batteries. *Energy Environ. Sci.* **2014**, *7* (11), 3459–3477. https://doi.org/10.1039/C4EE02158D.

(166) Greco, K. V.; Forner-Cuenca, A.; Mularczyk, A.; Eller, J.; Brushett, F. R. Elucidating the Nuanced Effects of Thermal Pretreatment on Carbon Paper Electrodes for Vanadium Redox Flow Batteries. *ACS Appl. Mater. Interfaces* **2018**, *10* (51), 44430–44442. https://doi.org/10.1021/acsami.8b15793.

(167) Barton, J. L.; Milshtein, J. D.; Hinricher, J. J.; Brushett, F. R. Quantifying the Impact of Viscosity on Mass-Transfer Coefficients in Redox Flow Batteries. *J. Power Sources* **2018**, *399*, 133–143. https://doi.org/10.1016/j.jpowsour.2018.07.046.

(168) Evans, D. H. One-Electron and Two-Electron Transfers in Electrochemistry and Homogeneous Solution Reactions. *Chem. Rev.* **2008**, *108* (7), 2113–2144. https://doi.org/10.1021/cr068066l.

(169) Lehmann, M. W.; Evans, D. H. Effect of Comproportionation on Voltammograms for Two-Electron Reactions with an Irreversible Second Electron Transfer. *Anal. Chem.* **1999**, *71* (10), 1947–1950. https://doi.org/10.1021/ac990066g.

(170) Li, Z.; Pan, M. S.; Su, L.; Tsai, P.-C.; Badel, A. F.; Valle, J. M.; Eiler, S. L.; Xiang, K.; Brushett, F. R.; Chiang, Y.-M. Air-Breathing Aqueous Sulfur Flow Battery for Ultralow-

Cost Long-Duration Electrical Storage. *Joule* **2017**, *1* (2), 306–327. https://doi.org/10.1016/j.joule.2017.08.007.

(171) Albertus, P.; Manser, J. S.; Litzelman, S. Long-Duration Electricity Storage Applications, Economics, and Technologies. *Joule* **2020**, *4* (1), 21–32. https://doi.org/10.1016/j.joule.2019.11.009.

(172) Robb, B. H.; Farrell, J. M.; Marshak, M. P. Chelated Chromium Electrolyte Enabling High-Voltage Aqueous Flow Batteries. *Joule* **2019**, *3* (10), 2503–2512. https://doi.org/10.1016/j.joule.2019.07.002.

(173) Evans, D. H.; Hu, K. Inverted Potentials in Two-Electron Processes in Organic Electrochemistry. *J. Chem. Soc. Faraday Trans.* **1996**, *92* (20), 3983–3990. https://doi.org/10.1039/FT9969203983.

(174) Kini, A. M.; Cowan, D. O.; Gerson, F.; Moeckel, R. New Synthesis and Properties of 11,11,12,12-Tetracyano-9,10-Anthraquinodimethane: An Electron Acceptor Displaying a Single-Wave, Two-Electron Reduction and a Coproportionation Pathway to the Radical Anion. *J. Am. Chem. Soc.* **1985**, *107* (3), 556–562. https://doi.org/10.1021/ja00289a006.

(175) Lehmann, M. W.; Singh, P.; Evans, D. H. Potential Inversion in the Reduction of Trans-2,3-Dinitro-2-Butene. *J. Electroanal. Chem.* **2003**, *549*, 137–143. https://doi.org/10.1016/S0022-0728(03)00264-X.

(176) Sampson, M. D.; Nguyen, A. D.; Grice, K. A.; Moore, C. E.; Rheingold, A. L.; Kubiak, C. P. Manganese Catalysts with Bulky Bipyridine Ligands for the Electrocatalytic Reduction of Carbon Dioxide: Eliminating Dimerization and Altering Catalysis. *J. Am. Chem. Soc.* **2014**, *136* (14), 5460–5471. https://doi.org/10.1021/ja501252f.

(177) Wellman, D. E.; West, R. Synthesis and Characterization of a New Polyquinone Exhibiting a Two-Electron, Single-Wave Reduction. *J. Am. Chem. Soc.* **1984**, *106* (2), 355–360. https://doi.org/10.1021/ja00314a019.

(178) Hernández-Burgos, K.; Rodríguez-Calero, G. G.; Zhou, W.; Burkhardt, S. E.; Abruña, H. D. Increasing the Gravimetric Energy Density of Organic Based Secondary Battery Cathodes Using Small Radius Cations (Li+ and Mg2+). *J. Am. Chem. Soc.* **2013**, *135* (39), 14532–14535. https://doi.org/10.1021/ja407273c.

(179) Geiger, W. E.; Barrière, F. Organometallic Electrochemistry Based on Electrolytes Containing Weakly-Coordinating Fluoroarylborate Anions. *Acc. Chem. Res.* **2010**, *43* (7), 1030–1039. https://doi.org/10.1021/ar1000023.

(180) Barrière, F.; Geiger, W. E. Use of Weakly Coordinating Anions to Develop an Integrated Approach to the Tuning of ΔE1/2 Values by Medium Effects. *J. Am. Chem. Soc.* **2006**, *128* (12), 3980–3989. https://doi.org/10.1021/ja058171x.

(181) Jacquemond, R. R.; Geveling, R.; Forner-Cuenca, A.; Nijmeijer, K. On the Characterization of Membrane Transport Phenomena and Ion Exchange Capacity for Non-Aqueous Redox Flow Batteries. *J. Electrochem. Soc.* **2022**. https://doi.org/10.1149/1945-7111/ac8623.

(182) Neyhouse, B. J.; Lee, J.; Brushett, F. R. Connecting Material Properties and Redox Flow Cell Cycling Performance through Zero-Dimensional Models. *J. Electrochem. Soc.* **2022**, *169* (9), 090503. https://doi.org/10.1149/1945-7111/ac86aa.

(183) Mushtaq, K.; Lagarteira, T.; Zaidi, A. A.; Mendes, A. In-Situ Crossover Diagnostics to Assess Membrane Efficacy for Non-Aqueous Redox Flow Battery. *J. Energy Storage* **2021**, *40*, 102713. https://doi.org/10.1016/j.est.2021.102713.

(184) Lagarteira, T.; Pacheco, P.; Almeida, C.; Bentien, A.; Monteiro, R.; Mendes, A. In-Situ Measurement of Vanadium Crossover for the Vanadium Redox Flow Battery. *J. Electrochem. Soc.* **2019**, *166* (16), A4067. https://doi.org/10.1149/2.0331916jes.

(185) Volodin, I. A.; Stolze, C.; Nolte, O.; Rohland, P.; Hager, M. D.; Schubert, U. S. State and Prospects of Unbalanced, Compositionally Symmetric Flow Battery Cycling and Steady-State Amperometry Techniques for Electrolyte Stability Assessment: The Case of Methyl Viologen. *ACS Appl. Energy Mater.* **2023**, *6* (1), 302–316. https://doi.org/10.1021/acsaem.2c02959.

(186) Shin, S.-H.; Yun, S.-H.; Moon, S.-H. A Review of Current Developments in Non-Aqueous Redox Flow Batteries: Characterization of Their Membranes for Design Perspective. *RSC Adv.* **2013**, *3* (24), 9095–9116. https://doi.org/10.1039/C3RA00115F.

(187) Luo, X.; Lu, Z.; Xi, J.; Wu, Z.; Zhu, W.; Chen, L.; Qiu, X. Influences of Permeation of Vanadium Ions through PVDF-g-PSSA Membranes on Performances of Vanadium Redox Flow Batteries. *J. Phys. Chem. B* **2005**, *109* (43), 20310–20314. https://doi.org/10.1021/jp054092w.

(188) Sun, C.-Y.; Zhang, H.; Luo, X.-D.; Chen, N. A Comparative Study of Nafion and Sulfonated Poly(Ether Ether Ketone) Membrane Performance for Iron-Chromium Redox Flow Battery. *Ionics* **2019**, *25* (9), 4219–4229. https://doi.org/10.1007/s11581-019-02971-0.

(189) Kim, Y.-S.; Oh, S.-H.; Kim, E.; Kim, D.; Kim, S.; Chu, C.-H.; Park, K. Iron-Chrome Crossover through Nafion Membrane in Iron-Chrome Redox Flow Battery. *Korean Chem. Eng. Res.* **2018**, *56* (1), 24–28. https://doi.org/10.9713/kcer.2018.56.1.24.

(190) Sun, C.-Y.; Zhang, H. Investigation of Nafion Series Membranes on the Performance of Iron-Chromium Redox Flow Battery. *Int. J. Energy Res.* **2019**, *43* (14), 8739–8752. https://doi.org/10.1002/er.4875.

(191) Hawthorne, K. L.; Wainright, J. S.; Savinell, R. F. Studies of Iron-Ligand Complexes for an All-Iron Flow Battery Application. *J. Electrochem. Soc.* **2014**, *161* (10), A1662. https://doi.org/10.1149/2.0761410jes.

(192) Yuan, J.; Pan, Z.-Z.; Jin, Y.; Qiu, Q.; Zhang, C.; Zhao, Y.; Li, Y. Membranes in Non-Aqueous Redox Flow Battery: A Review. *J. Power Sources* **2021**, *500*, 229983. https://doi.org/10.1016/j.jpowsour.2021.229983.

(193) Saraidaridis, J.; Yang, Z. Electrolyte Takeover Strategy for Performance Recovery in Polysulfide-Permanganate Flow Batteries. *J. Electrochem. Soc.* **2021**, *168* (11), 110556. https://doi.org/10.1149/1945-7111/ac3ab0.

(194) Ashraf Gandomi, Y.; Aaron, D. S.; Nolan, Z. B.; Ahmadi, A.; Mench, M. M. Direct Measurement of Crossover and Interfacial Resistance of Ion-Exchange Membranes in All-Vanadium Redox Flow Batteries. *Membranes* **2020**, *10* (6), 126. https://doi.org/10.3390/membranes10060126.

(195) Xie, W.; Darling, R. M.; Perry, M. L. Processing and Pretreatment Effects on Vanadium Transport in Nafion Membranes. *J. Electrochem. Soc.* **2015**, *163* (1), A5084. https://doi.org/10.1149/2.0111601jes.

(196) Schubert, U. S.; Nolte, O.; Volodin, I.; Stolze, C.; Hager, M. D. Trust Is Good, Control Is Better: A Review on Monitoring and Characterization Techniques for Flow Battery Electrolytes. *Mater. Horiz.* **2021**. https://doi.org/10.1039/D0MH01632B.

(197) Stolze, C.; Rohland, P.; Zub, K.; Nolte, O.; Hager, M. D.; Schubert, U. S. A Low-Cost Amperometric Sensor for the Combined State-of-Charge, Capacity, and State-of-Health Monitoring of Redox Flow Battery Electrolytes. *Energy Convers. Manag. X* **2022**, *14*, 100188. https://doi.org/10.1016/j.ecmx.2022.100188.

(198) Zub, K.; Stolze, C.; Rohland, P.; Stumpf, S.; Hoeppener, S.; Hager, M. D.; Schubert, U. S. Inkjet-Printed Microband Electrodes for a Cost-Efficient State-of-Charge Monitoring in Redox Flow Batteries. *Sens. Actuators B Chem.* **2022**, *369*, 132291. https://doi.org/10.1016/j.snb.2022.132291.

(199) Preet Kaur, A.; Neyhouse, B. J.; Shkrob, I. A.; Wang, Y.; Harsha Attanayake, N.; Kant Jha, R.; Wu, Q.; Zhang, L.; Ewoldt, R. H.; Brushett, F. R.; Odom, S. A. Concentration-Dependent Cycling of Phenothiazine-Based Electrolytes in Nonaqueous Redox Flow Cells. *Chem. – Asian J.* **2023**, *18* (5), e202201171. https://doi.org/10.1002/asia.202201171.

(200) Fenton, A. M.; Jha, R. K.; Neyhouse, B. J.; Kaur, A. P.; Dailey, D. A.; Odom, S. A.; Brushett, F. R. On the Challenges of Materials and Electrochemical Characterization of Concentrated Electrolytes for Redox Flow Batteries. *J. Mater. Chem. A* **2022**, *10* (35), 17988–17999. https://doi.org/10.1039/D2TA00690A.

Permissions

Parts of **Chapter I** were reproduced with permissions from work previously published by Elsevier on behalf of the *Encyclopedia of Energy Storage*: B. J. Neyhouse and F. R. Brushett, From the synthesis vial to the full cell: Electrochemical methods for characterizing active materials for redox flow batteries, *Encyclopedia of Energy Storage,* **2**, 453-465. 2022. **Chapter II** was reproduced with permission from B. J. Neyhouse, K. M. Tenny, Y.-M. Chiang, F. R. Brushett, Microelectrode-Based Sensor for Measuring *Operando* Active Species Concentrations in Redox Flow Cells, *ACS Appl. Energy Mater.* **2021** *4* (12), 13830-13840. Copyright 2021 American Chemical Society. **Chapter III** was adapted from work previously published by IOP Publishing on behalf of the *Journal of the Electrochemical Society*: B. J. Neyhouse, J. Lee, F. R. Brushett, Connecting Material Properties and Redox Flow Cell Cycling Performance through Zero-Dimensional Models, *J. Electrochem. Soc.* **2022** *169* (9), 090503. **Chapter IV** is in preparation for submission to a peer-reviewed journal: B. J. Neyhouse, F. R. Brushett. *In preparation*. **2023**. **Chapter V** was reproduced from work previously published by IOP Publishing on behalf of the *Journal of the Electrochemical Society*: B. J. Neyhouse, A. M. Fenton Jr., F. R. Brushett, Too Much of a Good Thing? Assessing Performance Tradeoffs for Two-Electron Compounds in Redox Flow Cells, *J. Electrochem. Soc.* **2021** *168* (5), 050501. **Chapter VI** is currently under review for consideration in the *Journal of the Electrochemical Society*.